Scuola Internazionale Superiore
di Studi Avanzati

The impact of carbon based materials on hippocampal cells: from neurons to networks

Thesis submitted for the degree of "*Doctor Philosophiae*"

Candidate:

Niccolò Paolo Pampaloni

Supervisor:

Prof. Laura Ballerini

SISSA – Via Bonomea, 265 – 34136 Trieste (Italy)

NOTES

The work described in this thesis was carried out at SISSA, Trieste, between November 2013 and October 2017. The data reported in the present thesis have been published, are submitted, or in preparation, as indicated.

Pampaloni NP, Scaini D, Perissinotto F, Bosi S, Prato M, Ballerini L. Sculpting neurotransmission during synaptic development by 2D nanostructured interfaces. *Nanomedicine* (2017) pii: S1549-9634(17)30082-5. doi: 10.1016/j.nano.2017.01.020. [Epub ahead of print].

Pampaloni NP, Lottner M, Giugliano M, Matruglio A, D'Amico F, Prato M, Garrido JA, Ballerini L, Scaini D. Single-layer graphene modulates neuronal communication and up-regulates membrane ion channels. (Submitted).

Pampaloni NP, Rago I, Calaresu I, Ballerini L, Scaini D. Transparent Carbon Nanotubes (tCNTs) guide the reconnection of lesioned entorhinal hippocampal organotypic cultures. (In preparation).

Reinartz S, **Pampaloni NP**, Ballerini L, Diamond ME. Specific modifications of neuronal threshold by optogenetic (subthreshold) modulations of membrane potential. (In preparation).

Vallejo-Giraldo , **Pampaloni NP**, Pallipurath AR, Mokarian-Tabari P, O'Connell J, D. Holmes J, Trotier A,Krukiewicz K, Orpella-Aceret G, Pugliese E, Ballerini L, Kilcoyne M, Dowd E, Quinlan LR, Pandit A, Kavanagh P, Biggs MJP. Preparation of Cytocompatible ITO Neuroelectrodes with Enhanced Electrochemical Characteristics Using a Facile Anodic Oxidation Process. *Adv Funct Mater.* (2017) 1605035.

CONTENTS

INTRODUCTION

1.1 NANOTECHNOLOGY

1.1.1 Overview

Nanotechnology or Nanoscience, refers to that area of technology or science that deals with the “nano-sized” world, thus the metric prefix identifies a growing area of developments and applications. The Nanoscience era dated back with the design of instruments allowing to observe the matter in its finest details, in a scale well beyond what we can perceive with our senses. The term Nanotechnology was first coined in 1974 from Norio Taniguchi to describe semiconductor processes exhibiting properties in the order of a nanometer: “Nanotechnology mainly consists of the processing of separation, consolidation, and deformation of materials by one atom or by one molecule" (Taniguchi, 1974). Since then, engineering devices and developing methods able to manipulate the matter at the nanometer scale increased dramatically, and nowadays we refer to nanotechnology as the construction, synthesis, consolidation of materials and devices which have a functional organization, in at least one dimension, in the nanometer scale (Silva, 2006).

Nanotechnology has been increasingly applied to biological and medical issues; and the success of such applications reside in the fact that most cell components and processes are in the sub-micrometric and nanometric range (Fig.1). Some examples: the DNA double helix has a diameter which is around 2 nm; ribosomes (20 nm); nuclear pores (50 nm); centrioles (200 nm); cell membrane (7-10 nm thick); the hemoglobin (around 5 x 6 nm). Nanotechnology applications to biology and medicine increased to an extent, in the last decades, that this discipline constitutes by itself an entire sub-field of biology, called Bionanotechnology, or Nanobiotechnology.

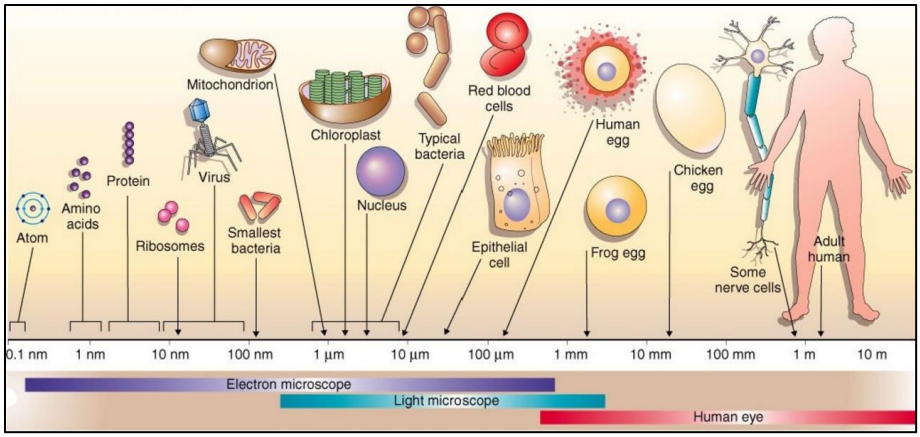

Fig.1 *- Size of different biological elements and structures. Note that most cell components display nano- and micrometric sizes (Copyright © Brooks/Cole - Thomson Learning)*

Nanotechnology related techniques can be organized in two apporaches, named bottom-up and top-down: bottom-up approaches start with one or more defined molecular species, which undergo certain processes that result in a higher-ordered and -organized structure. Examples include templating and scaffolding methods, such as biomineralization, which rely on backbone structures to support and guide the nucleation and growth of a nanomaterial. Top-down approaches instead, begin with a bulk material that incorporates nanoscale details, such as nanolithography and etching techniques. Specific examples include dip-pen nanolithography (in which specific molecules are deposited into desired configurations) and electrostatic atomic force nanolithography, in which molecules are moved around to form desired structures (Silva, 2006).

1.1.2 Nanoscale tools for Neuroscience

Nanoscience began with the ability to “observe” at the atomic scale. In its early stages, between the forties and the sixties, nanotechnology mainly involved the invention of new types of microscopy techniques: the Scanning Tunneling Microscope (STM), able to image

objects at their atomic level (sub-nanometric); the Transmission Electron Microscope (TEM) and the Scanning Electron Microscope (SEM), which are high-resolution microscopes able to resolve images in the nanometric range, exploiting electrons (instead of light) as the radiation source. Later, in 1987, the Atomic Force Microscopy (AFM) was introduced, a microscope consisting of a sharp tip, mounted at the end of a flexible cantilever which is scanned across the sample's surface, that can be used in a variety of configurations, as to resolve the nanotopography of surfaces or to map the spatial distribution of physicochemical forces (Variola, 2014). In the last decades the microscopy field further improved with new methodologies such as the Confocal microscope, the Total Internal reflection Fluorescence Microscope (TIRFM) and others. Recently the Stimulated Emission Depletion (STED; Fig.2) microscopy has been introduced, which through a system of paired synchronized laser pulses, selectively inhibit the fluorescence at its outer part sharpening the fluorescence focal spot, thus enabling to obtain images at resolutions below the diffraction limit (Hell and Wichmann, 1994).

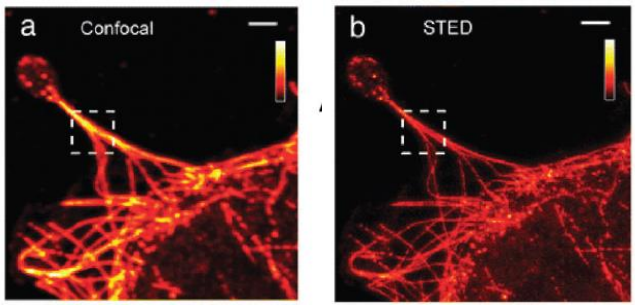

Fig. 2 *- Examples of a (a) classic confocal and (b) STED image of fibroblastic cells. Scale bar: 2 μm. (Variola, 2014).*

Additional nanotechnology-based tools used in basic neuroscience research for their outstanding features are, for example, Quantum Dots (Brus, 1983), semiconductor particles with unique optical and electronic properties (narrow emission spectra, resistant to photobleaching, high quantum yield, easily synthetized) used both for high resolution

imaging and as probes to detect or label specific molecules or tissues (Jaiswal et al, 2004). Furthermore, their spectral properties make them ideal candidate to use as donors in the fluorescence resonance energy transfer (FRET; Cooper & Nadeau, 2009), another important nano-technique which is based on an energy transfer from a donor cromophore to an acceptor cromophore, and is mostly used to investigate molecular dynamics such as protein-protein interactions. Other nanotechnological advances comprehend the DNA nanotechnology, that involves the synthesis of artificial nucleic acids for technological uses (Goodman et al, 2005) or a variety of artificial nanomaterials, such as fullerenes (Kroto et al, 1985), carbon nanotubes (Iijima, 1991), graphene (Novoselov et al, 2004): systems in which desirable electrical and mechanical attributes can be obtained by careful vapor deposition of carbon with accurate control over geometry and bonding (Alivisatos et al, 2013).
Among the promising materials which found application either in biomedical and basic research are the colloidal gold Nanoparticles (AuNPs), which can have a different diameter (they range from 5 to 400 nm), and depending on the size they differentially interact with the visible light, giving rise to a variety of different emission spectra: these properties led their wide employment in the microscopy and bioimaging field. Gold nanoparticles can also be coated with molecules or therapeutic agents, and therefore used as therapeutic agent delivery or sensors in diagnostic.
Recently, the group of Francisco Bezanilla, at the University of Chicago, exploited the AuNPs ability to transduce light into heat to stimulate neurons with light: they employed 20 nm-sized AuNPs coupled them to a synthetic molecule (Ts1) which bind sodium channels without blocking them, and then stimulated the neurons with green laser pulses: the light caused a transient increase in heat that evoked a transient increase in membrane capacitance which caused in turn a depolarization leading to an action potential (Carvalho-de-Souza et al, 2015; Fig. 3). This technique has impressive potential applications, as it would allow the light-driven neuronal stimulation with no need of viral transduction (as in the case of classic Optogenetic), and therefore affecting in a much less invasive manner the natural physiology of neural cells.

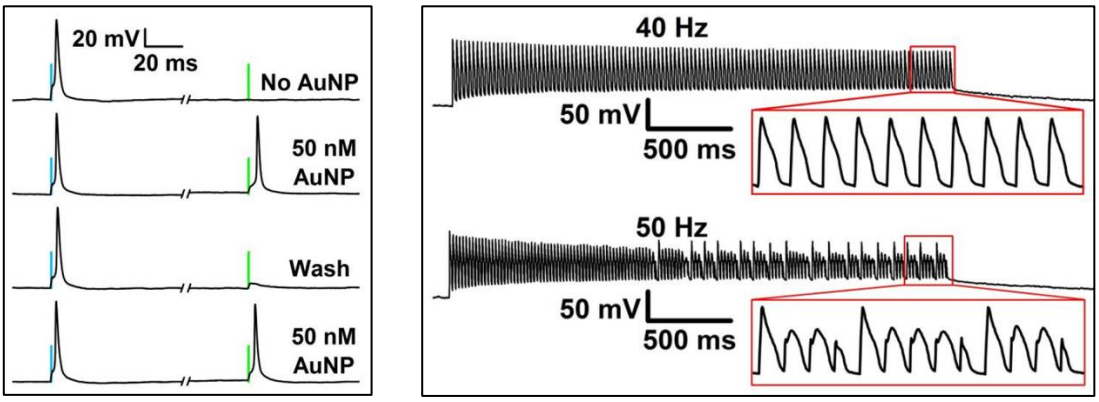

Fig. 3 *- (left) Representative traces of current-clamped DRG cells firing action potentials in response to two different stimuli: a 300 pA, 1 ms current injection (left side, blue bars) and a 174 mW, 1 ms 532 nm laser pulse (right side, green bars). Initially, cells were responsive only to the electrical stimulus, but a bolus of AuNPs sensitized the cells to light. Washing removed enough AuNPs from the cell that the laser effect became insufficient to trigger an action potential. Optical excitability returned when a second bolus was added to the bath. (right) A 40 Hz train of 1 ms laser pulses reliably stimulates an action potential with every laser pulse over a 3 second period (top trace). A comparable train with a pulse frequency of 50 Hz, however, shows some stimuli failing to trigger action potentials toward the end of the pulse train. Following a "miss", the subsequent action potential has increased amplitude due to decreased levels of both sodium channel inactivation and residual potassium channel conduction (bottom trace; Carvalho-de-Souza et al, 2015).*

Optogenetic constitutes indeed one of the most important biological technique achieved in the last decades, allowing the control of neuronal activity through the use of light ("opto"), exploiting genetically encoded light-sensitive proteins ("genetics"; Boyden et al, 2005) called opsins. Due to the possibility of either excite and inhibit target neurons, it has been employed to study a variety of neural states, including fear, anxiety, reward; or diseases, such as Autism or Parkinson (Tye & Deisseroth, 2012). To date, one of the limitations of this technique is given by the low tissue penetrating visible light used to activate the opsins. In this situation, the majority of *in vivo* experiments need to be performed with light sources (lasers or LED) directly connected to the target brain region through optic cables, which are inconvenient to use in experiments with freely moving animals. Also in this context,

nanotechnology came into play to overcome these limitations. In order to exploit the so called “Near Infrared Window”, which is that light range going from 650 nm to 1350 nm where light has its maximum ability to penetrate into biological tissues (Smith et al, 2009), Shah *et al.* took advantage from the Upconversion Nanoparticles (UCNPs), which are a new generation of fluorophores with the ability to convert near infrared radiations with lower energy into visible radiations with higher energy (Wang et al, 2011). They built biocompatible scaffolds mixing together Poly(lactic-co-glycolic acid) (PLGA) and UCNPs and cultured them with hippocampal neurons expressing Channelrhodopsin2 (ChR2, an excitatory opsin commonly used to activate neurons; Fig.4). Then they stimulated neurons using either 470-nm light (the common visible light used to activate ChR2), and 980-nm light (a near infrared light), while neurons were recorded using the whole cell patch clamp technique: in both cases they observed neuronal activation, meaning the UCNP-mediated successful conversion and delivery of near infrared light into visible light (Shah et al, 2015; Fig..).

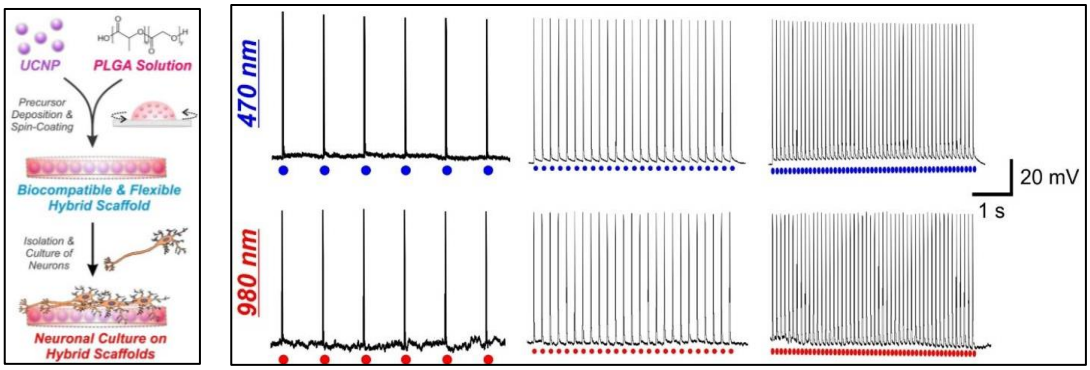

Fig. 4 *- (left) Schematic depicting preparation of PLGA-embedded UCNP hybrid scaffolds for hippocampal neuronal cultures; (right) Representative traces showing repetitive action potentials in a current-clamped hippocampal neuron evoked by 1 Hz, 5 Hz and 10 Hz train of light pulses from 470-nm light (*top*) and 980-nm light (*bottom*; Shah et al, 2015).*

1.1.3 Nanomaterials

Engineered nanomaterials are having a profound impact on a variety of devices employed in diverse field of research. In medicine, for instance, nanomaterials are being investigated for their use in medical diagnostics and implantable devices (Menon et al, 2013; Sahoo et al, 2007; Kumar et al, 2015) such as stents and catheters, which represent a large and critical market in the health care industry (Harris & Graffagnini, 2007). New nanotech-enabled medical devices aim to provide convenient real-time diagnosis of disease that can be done at a clinic rather than at a laboratory, as well as implantable devices that cause less irritation and have improved functionality (Harris & Graffagnini, 2007). In Neuroscience, the increasing ability to design and synthesize nanomaterials has been exploited to implement the potentialities and sensibility of instruments and devices exploited in basic and applied research (Pantic et al, 2015; Veloz-Castillo et al, 2016; Giugliano et al, 2008), pushing forward the potentiality of the field (Berger, 2016). For instance, the employment of nanomaterials has improved the sensitivity and stability of common electrodes used in electrophysiology (Keefer et al, 2008), of optical neural interfaces (Pisanello et al, 2016), and more in general, is strongly challenging the construction of those devices used to monitor neural ensembles on which I will focus in the next paragraph.

1.1.3.1 - Devices

Among the different devices introduced in the last years, such as Metal Nanoelectrodes (Zhu et al, 2014), Functionalized quantum dots (Silva, 2006), or Crabon-Nanofibers-based Micro- and Nanodevices (Zhang et al, 2012), I will focus here on biosensors, nanoneedles and nanowires, and Multielectrode Arrays (MEAs), as in Neuroscience these particular devices have been and still are the most widely employed either in applied and basic research. Furthermore, as they display micro- and nano-sized features, their upgrading goes hand in hand with the development of new nanomaterials.

According to the International Union of Pure and Applied Chemistry (IUPAC) definition, "Biosensors are devices that use specific biochemical reactions mediated by isolated enzymes, immunosystems, tissues, organelles or whole cells to detect chemical compounds usually by electrical, thermal or optical signals" (Nagel et al, 1992). In medical and biological research, biosensors are already widely employed: the DNA chip array technique for instance allow the high-throughput screening of point mutations in a little time; a variety of immune assays, to identify a certain compound through its tagging to specific antibodies which are generally immobilized on a support, as in the case of the Enzyme Linked Immunosorbent Assay (ELISA) technique (Urban, 2009).

A smart and straightforward approach to exploit biosensors to investigate neuronal behavior is given by Nguyen *et al*., who engineered cells to express the M1 muscarinic metabotropic receptor and a genetically encoded fluorescent Ca^{++} sensor: when the M1 receptor was activated by Acetylcholine, the rise in cytosolic Calcium was measured just by measuring the Ca^{++} sensor activity which gave a direct quantitative measure of the muscarinic receptor activation. Through a chronic implantation of this biosensor into the rat frontal cortex, these authors were able to elucidate the action of some neuroleptic drugs on the muscarinic receptor activity (Nguyen *et al*, 2010).

Nanoneedles and Nanowires, are artificial nano- or micrometric sized "needles" which can provide high-fidelity electrophysiological recordings. These devices can perform recordings and stimulation of neurons in a highly scalable fashion *in vitro* and *ex vivo* (Robinson et al, 2012; Alivisatos et al, 2013). Recently, silicon-based three-dimensional vertical nanowires electrode arrays (VNEA) consisting of 16 stimulation/recording sites have been developed, allowing the high fidelity recording and stimulation of hundreds of individual rat cortical neurons (Robinson et al, 2012; Fig. 5).

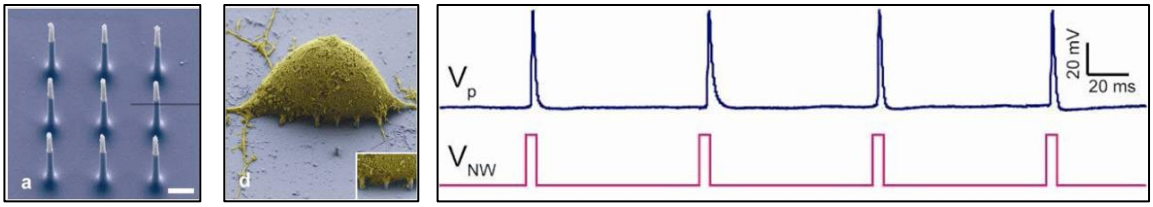

Fig. 5 *- (left) SEM image of the nine silicon nanoneedles that constitutes the active region of the VNEA. Scale bar: 10 μm; (center) SEM micrograph of a rat cortical neuron on top of an electrode pad.; (right) exemple showing that Action potentials (upper blue trace, measured by a patch pipette) could be reliably stimulated by voltage pulses applied to the nanoelectrodes (lower magenta trace; Robinson et al, 2012; Alivisatos et al, 2013).*

Nanoneedles have been found to been useful in a variety of other techniques as in the case of AFM: Obataya *et al* sharpened AFM tips to ultrathin needles of 200-300 nm in diameter, and shown the ability of this needle to penetrate into the cell nucleus, providing a first proof of principle that this technique could be used for fine sub-cellular surgeries in living cells (Obataya et al, 2005). In a more recent study, a tunable array of biodegradable nanoneedles was shown to be able to deliver nucleic acids with an efficiency greater than 90% *in vitro*, and to successfully transfect the angiogenic master regulator gene VEGF-165 *in vivo,* which induced sustained neovascularization and a localized increase in blood perfusion in the target region of the muscle, opening up many possibilities in the field of genetic engineering of the muscle tissue (Chiappini et al, 2015).

MEAs are devices containing multiple electrodes used for the recording and/or stimulation of neurons. MEAs can be used either *in vitro*, to monitor the activity of a cultured network (Gawad et al, 2009; Obien et al, 2014; Hales et al, 2010), and also *in vivo*, implanted into the target region of CNS (Spira & Hai, 2013; Gad et al, 2013). Ideally, all materials used in MEA fabrication should have good biocompatibility, good electrical properties for microelectrodes that can maintain a high signal-to-noise ratio, good transparency for observation of the sample and low cost (Liu et al, 2012). Another important feature that MEAs should display is a good neuron-device electrical coupling (the ratio between the

maximal voltages recorded by the device in response to the maximal voltage generated by an excitable cell; Spira & Hai, 2013). The MEA technology, allow to record multiple extracellular signals from different sites at the same time: for instance, the commercially available MED64 system display 8 x 8 arrays of 64 microelectrodes composed of platinum black, gold and nickel, plated on a glass substrate, and connected to indium tin-oxide (ITO) strip conductors (Liu et al, 2012; Fig. 6).

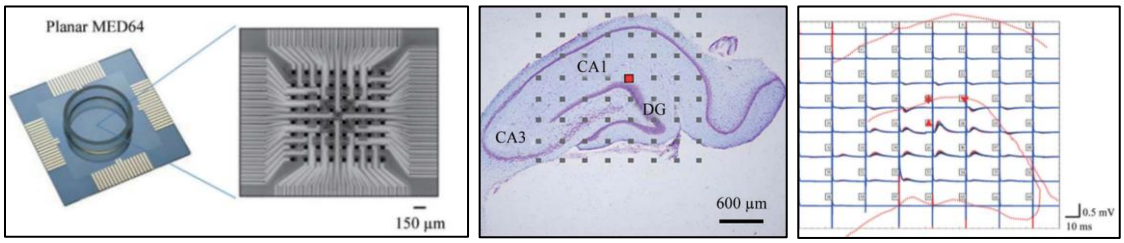

Fig. 6 *- (left) a typical Planar MED64 biochip; highlighted the recording field composed of 64 microelectrodes (center) a rat acute slice of hippocampal formation positioned on a MED64: the red square indicates the site of electrical stimulation (right) real traces of 63 recording electrodes across the dentate gyrus (DG) and the CA1 area in response to the Perforant Pathway stimulation (Liu et al, 2012).*

This system has been widely used to address neuronal network dynamics on both dissociated cultures and brain explants: performing MEA recordings on rat acute slices of the hippocampal formation, Zhao et al were able to correlate a peripheral persistent nociception to changes in temporal and spatial plasticity of synaptic connections and function within the hippocampal formation (Zhao et al, 2009). In another study, Heidemann et al. cultured organotypic co-cultures of rat spinal cords onto MEAs to characterize spatial and temporal activity patterns of spontaneously occurring bursts, as well as the degree of synchronization between the two slices (Heidemann et al, 2015).

The MEA technology can be also coupled to other electrical or optical methods to monitor neuronal ensembles: for instance, El Hady et al combined MEAs electrical recordings and

optical stimulation of channelrhodopsin-2 transduced neurons to study the effect of global activation on synchronized network bursting, and found that whole-field light stimulation of channelrhodopsin-2 transduced neuronal networks induced a change in the bursting dynamics of the network (El Hady et al, 2013). More recently, Pulizzi *et al* were able to induce gamma-like oscillations *in vitro* taking advantage of mammalian cortical dissociated neurons cultured onto MEAs and transfected with Channelrhodopsin fused to mCherry (a red fluorescent protein), and through the simultaneous exploitation of these techinques, they first showed how to induce an oscillatory reverberating network response *in vitro*, and clarified the mechanisms through which the gamma rhythm might emerge *in vivo* (Pulizzi et al, 2016).

1.1.3.2 - Scaffolds

Another important application of nanomaterials which emerged in the last decades is their employment in the scaffold fabrication: scaffolds are three-dimensional synthetic nanostructures used as substrates to interface biological cells or tissues *in vitro* and *in vivo* (Cooper & Nadeau, 2009). Because of their peculiar 3D structure and the possibility to synthesize them in a variety of different forms and materials, from carbon nanotubes (Bosi et al, 2015) to biomaterials (Londono & Badylak, 2015) to hydrogels (Kunze et al, 2009; Nagai et al, 2012), beside the fact that they could be easily functionalized, they turned out to be essential tools in a vast range of fields, from regenerative medicine (Hosseinkhani et al, 2014; Carballo-Molina & Velasco, 2015; Londono & Badylak, 2015), to biomedical applications (Gupta et al, 2014) to neuroscience basic (Chen & Li, 2005; Carlson et al, 2016; Bosi et al, 2015) and applied (Cavallo, 2015) research. In tissue engineering, for instance, biomimetic scaffolds are emerging as a possible treatment after neural tissue degradation or injury (O'Brien, 2011; Tsintou et al, 2015), as it was shown that scaffolds made by hydrogels were able to promote axonal regeneration after a peripheral nerve lesion (Carballo-Molina & Velasco, 2015). In fact, hydrogel scaffolds have properties that could

make them a good alternative as a drug release system: during the gelling process it is possible to incorporate different types of molecules or cells into the gel structure which is facilitated by the high quantity of water that permits the uptake and diffusion of soluble molecules (Carballo-Molina & Velasco, 2015; Nagai et al, 2006).

The most used techniques to generate patterned substrates are the elctrospinning technique and the microcontact printing (Fig. 7). The electrospinning is a fabrication method that uses electric charges to form fine fibers from polymers solution which has been demonstrated either with synthetic (i.e. ploycaprolactone, poly(glycolic acid)) and natural polymers such as collagen. In the process, a polymer solution is passed through a tip where it is subjected to high voltage that charges the conductive liquid. The liquid droplet is stretched beyond the expected shape by electrostatic repulsion, and the resulting surface is known as the Taylor cone. At a critical point, the liquid erupts in a stream. As the jet dries, charge migrates to the surface of the fiber and the mode of current flow changes from ohmic to convective. The jet is then elongated by whipping caused by electrostatic repulsion and is captured on a grounded collector surface. Deposition of the stream onto the edge of a rotating disk produces aligned nanofibers (Fig. 7A; Cooper & Nadeau, 2009).

The microcontact printing on the other hand, is one of the most accessible techniques to produce substrates with controlled patterning: in the first step a “hard stamp” on a Si wafer is created from a printed photolithographic mask containing the pattern of interest. Then, a soft stamp made from poly-dimethylsiloxane (PDMS) is created from this mask. The PDMS may be then enriched with proteins, growth factors or other molecules (Fig..B; Cooper & Nadeau, 2009).

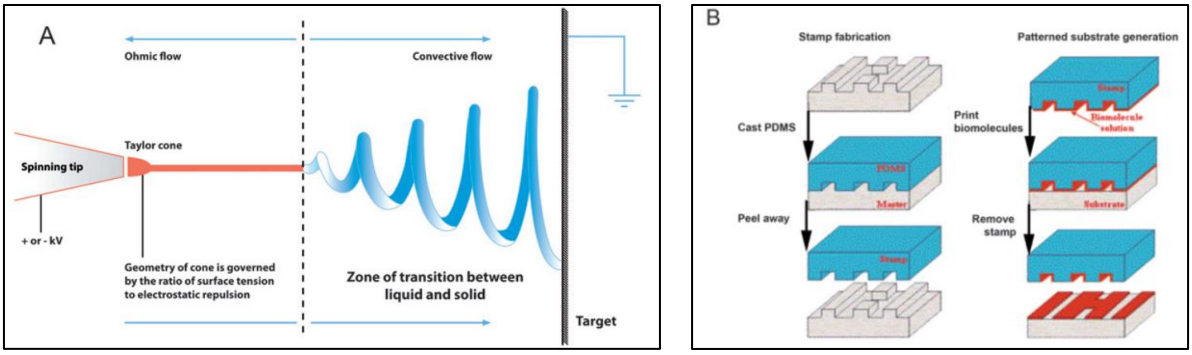

Fig. 7 *- Techniques employed in patterned scaffold generation. (A) Diagram showing the basis of the Electrospinning technique; (B) Schematics of the stemps of microcontact printing, showing the creation of a PDMS mask and the deposition of biomolecules onto a substrate using the stamp (Cooper & Nadeau, 2009).*

As mentioned above, the electrospinning technique is mostly used to produce Nanofibers, which are fibers with a diameter less than 1000 nm mainly used in wound healing and tissue repair (Cetin et al, 2012). Nanofibers have been employed in a variety of scaffolds and interfaced with many different biological samples as electrospun meshes generally comprise of nonwoven fibers with diameters in the hundreds of nanometers, and highly interconnected pores that are tens of micrometers in diameter. The high surface area–volume ratio of these fibrous meshes also ensures abundant area for cell attachment, which allows for a higher density of cells to be cultured as compared with a flat, two-dimensional surface. The morphological resemblance of electrospun nanofibers to native ECM suggests their natural application as a supportive matrix for creating scaffold constructs from stem cells (Lim & Mao, 2009). Electrospun poly(ε-caprolactone) (PCL) scaffolds have been shown to be biocompatible, as they well integrated in the caudate putamen of adult rat brain, with no evidence of microglial encapsulation after 60 days in vivo, with neuronal processes that infiltrated into the scaffold, another evidence of neuronal-scaffold integration (Nisbet et al, 2009).

Hydrogel scaffolds, beside their employment in the field of tissue regeneration, have been also showed to be optimal substrate for neuronal growth: Hanson Shepherd et al.

developed scaffolds of poly(2-hydroxyethyl methacrylate) (pHEMA) with varying architectures on which they grew primary hippocampal neurons, showing that neuronal organization was strongly following the scaffold organization (Fig. 8), and therefore demonstrating that neurons are able to finely sense spatial cues and subsequently re-arrange the network organization /Hanso Shepherd et al, 2011).

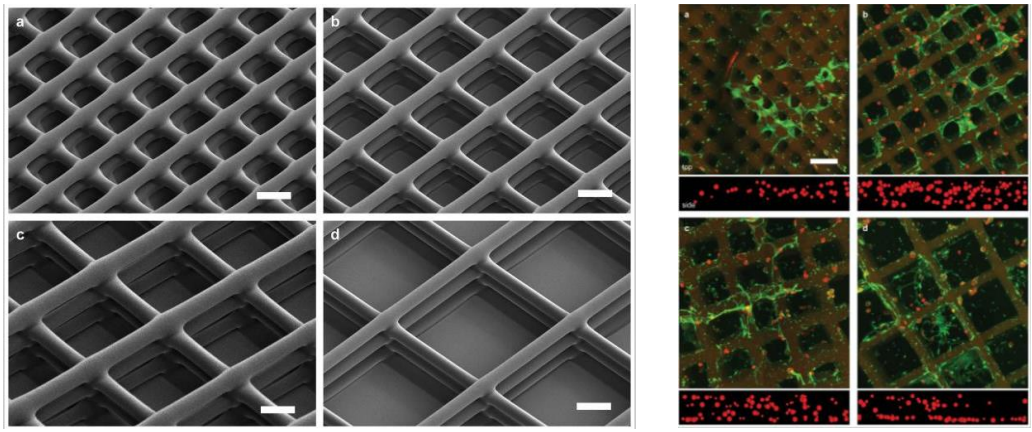

Fig. 8 *- Neurons are able to form networks on 3D scaffolds, forming networks that closely follow the scaffold geometry. (left) SEM micrographs of 3D pHEMA scaffolds of varying architecture, with pitch of a) 30 µm, b) 40 µm, c) 60 µm, and d) 80 µm; scale bars are 20 µm. (right) Confocal images (x-y scans, tiled) of primary rat hippocampal cells distributed within scaffolds of varying pitch: (a) 30 µm, (b) 40 µm, (c) 60 µm, and (d) 80 µm. Actin antibody is used to label the processes (green), while TO-PRO3 is used to label nuclei (red). Side view reconstructions schematically denote the positions (in x-z plane) of the neuronal somata, while their relative size indicates their position along the y-axis. Scale bar, 40 µm (Hanson Shepherd et al, 2011).*

Kunze et al instead developed a microfluidic PDMS-based device with different agarose/alginate parallel layers (thus resembling the cortex neuronal layers) in which dissociated cortical neurons properly grow and extend their neurites across neighboring layers. As the agarose/alginate hydrogel could be potentially implemented with either different cell types or drugs, this three-dimensional scaffold would be an useful tool to address questions either about neural network development and drug testing experiments (Kunze et al, 2009).

In another work, it was shown that laminin-functionalized nanofibers in 3D hyaluronic acid hydrogels enabled a significant alignment of neurites with the nanofibers and significantly increased the distance over which neurites could extend (McMurtrey, 2014). Another example of the potentiality of these substrates as an optimal tool to study neuronal ensembles, is given by Huang et al, who demonstrated that three-dimensional collagen-based scaffolds were able to promote the differentiation of neural stem cell (NSC) into mature neurons at an early stage compared with neurospheres cultured in suspension (Huang et al, 2013). The same kind of cells were shown to grow not only on hydrogel-made scaffolds, but also on porous scaffolds of graphene: in this case, it was seen that not only the scaffold supported the NSC growth, keeping the cells at an active proliferation, but also that cells established a good electrical coupling with the graphene foam, as the authors were able to electrically stimulate the cells through the graphene scaffold (Li et al, 2013).

Three dimension geometries seem to be key features impacting on neuronal network activity (and this is not trivial if we consider the effective brain architecture). It was in fact demonstrated both *in vitro* and *in vivo* (and with different types of materials composing the scaffolds: from carbon nanotubes to different types of polymer fibers; Bosi et al, 2015; Carlson et al, 2016) that neuronal ensembles were much more strongly synchronized and active if interfaced on a 3D scaffolds with respect to bi-dimensional control cultures (Bosi et al, 2015; Carlson et al, 2016; Fig. 9). It was also demonstrated that the transplantation of a scaffold containing Human induced Neuronal (iN) cells into the mouse striatum lead to a percentage of viable cells after 3 weeks of an order-of-magnitude greater than that relative to injection of isolated single cells (Carlson et al, 2016).

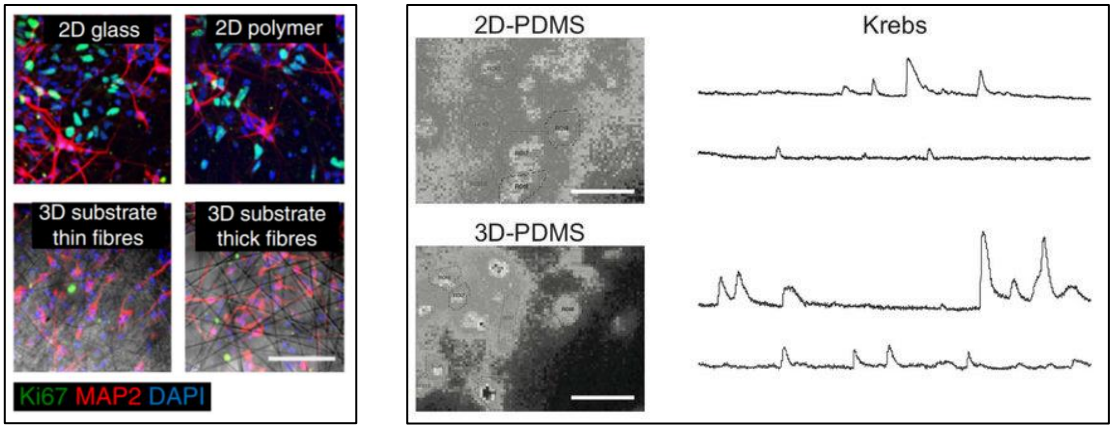

Fig. 9 - (left) Human iN populations robustly express MAP2 in 2D and 3D conditions, while populations of unconverted, proliferative Ki67-expressing iPS cells persist in iN populations plated in 2D conditions. Scale bar, 100 mm (adapted from Carlson et al, 2016). (right) snapshots of representative fields of neuronal cultures grown on 2D-PDMS (top) and 3D-PDMS (bottom) substrates, stained with the Oregon Green 488-BAPTA-1 AM. Scale bar: 50 µm. Repetitive Ca^{2+}-events spontaneously recorded in hippocampal cultures of 9 DIV highlighted an higher frequency and synchronization of events in 3D cultures (adapted from Bosi et al, 2015).

1.2 CARBON BASED MATERIALS

A fundamental key for the successful development of the nanotechnologies emerges from the constant improvement of the materials used to build up the instruments, devices and scaffolds which are exploited in the nanotechnology-related fields. In most cases, also these materials possess spatial features at the nanoscale level (generally from 1 to 100 nanometers), and are therefore called “nanomaterials” (Buzea et al, 2007), whose general charateristics has been introduced previously. In this framework, a particular attention must be given to the “carbon based materials”, materials composed by pure carbon, with different hybridization or structures (Dresselhaus, 2012), which were introduced in the last decades and which role has been fundamental in the development of the nanotechnology based research strategies in Neuroscience. Because of the particular importance and strong impact they had, and still are having, in the Nanotechonology-based research, I will discuss them more in details in the next paragraphs.

1.2.1 General Features

Within the periodic table, the Carbon constitutes the most versatile element, because of the variety of its allotropes and structures, given from the ability of the Carbon valence orbitals to hybridize in sp, sp^2 and sp^3 configurations. To date, three allotropes of carbon which are naturally occurring (diamond, amorphous carbon and graphite) have been described and several carbon allotropes deriving from a synthetic process (such as Graphene, Carbon Nanotubes, Fullerenes, Nanodiamonds) were developed. In nature, if the carbon atoms hybridize with sp^2 bonds, they will generate graphite; if instead the hybridization is purely sp^3, there will be diamond, while amorphous carbon is a mixture of the two. Artificial carbon-based materials, such as graphene and Carbon Nanotubes, display an sp^2 hybridization (Fig. 10): the 2s and two 2p orbitals will form three sp^2 orbitals, able therefore to form three strong covalent bonds, with a trigonal symmetry. It will be the fourth electron, the one in the p_z orbital that did not take part in the sp^2 hybridization, that will form a delocalized π bond in the plane perpendicular to that of the three σ bonds, able to move freely between carbon atoms. It is that electron that confers most interesting features to these materials, such as the high electrical conductivity (Littlejohn, 2014).

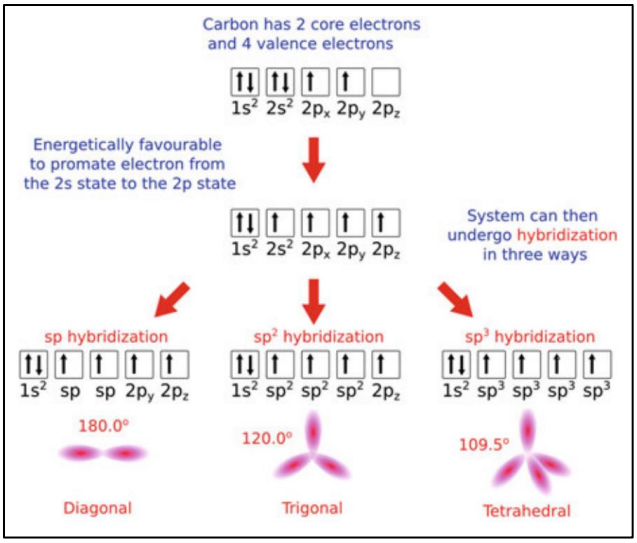

Fig. 10 *- Carbon can undergo three types of hybridization, resulting in different kind of carbon-based materials (Littlejohn, 2014)*

1.2.2 Carbon Nanotubes

Carbon Nanotubes (CNTs) are allotropes of carbon discovered in 1991 (Iijima, 1991) made up of one or more graphene sheets rolled onto themselves forming small cylinders with a diameter ranging from 1 to around 100 nanometers, and lengths that can reach up to around 15 microns. CNTs can be distinguished on the basis of their geometries: from the simplest one of CNTs formed by just one carbon-based sheet, named Single-Walled (SWCNTs); to those composed by two or more graphene sheets, named Multi-Walled (MWCNTs; Fig. 11 ; Choudhary and Gupta, 2011).

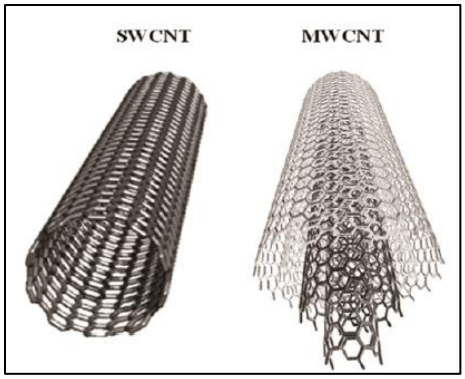

Fig. 11 - *Schematic representation of a SWCNT, composed by just one graphene sheet, compared to a MWCNT, composed by more (three in this cartoon) graphene sheets (Choudhary and Gupta, 2011).*

The chemical bonding of CNTs is composed of sp^2 bonds, like graphene: the chemical bonding of their carbon atoms has sp^2 hybridization, as graphene. This hybridization, not present in other allotropes of carbon, such as the diamond, which has a tetraedric sp^3 hybridization, is fundamental to provide the material with its peculiar strength and electrical conductivity (O'Connell, 2006). The CNT synthesis can be achieved via different chemical techniques such as the Chemical Vapor Deposition (CVD), the laser ablation or the Arc Discharge. Since metal catalysts are employed in all of these processes, in any case the CNT production will lead also to a variable amount of impurities deriving from these metals: purity is a fundamental prerequisite for CNTs employment in biological applications, therefore another step is required to obtain purified CNTs. Purification can be achieved either via acid treatment (which might however affect CNTs length and structure) or, more effectively, by their functionalization which allows CNT to be suspended in various solvents, thus allowing its purification (Prato et al, 2008).

SWCNTs can be either semiconducting or metallic according to the direction in which the graphene sheet is rolled with respect to the hexagonal lattice; if the sheet is rolled horizontally, resulting CNTs (called "zig-zag") will be semiconducting, while if the lattice is rolled at an angle of $\alpha=30°$ relative to the horizontal direction, the nanotube will be a metallic "armchair" (Fig. 12). The remaining types of nanotubes are named according to a

set of indices that correspond to the direction in which the sheet is rolled relative to the origin of the lattice (Boghossian et al., 2011).

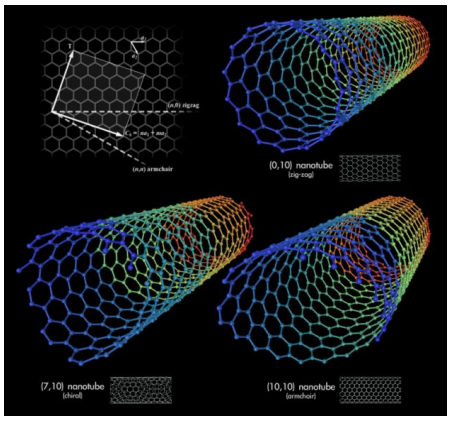

Fig. 12 – *Rolling the graphene in different directions with respect to the hexagonal lattice will give rise to different types of single-walled CNTs (image created by Michael Ströck, released under the Gnu Free Documentation License).*

1.2.3 Graphene

The Graphene is a single atomic layer of crystalline graphite (Fig. 13, left), therefore with a bi-dimensional structure. It has an hybridized sp^2 bonding, with three in-plane σ bonds/atom and π orbitals perpendicular to the plane. (Choi et al, 2010; Fig. 13, right).

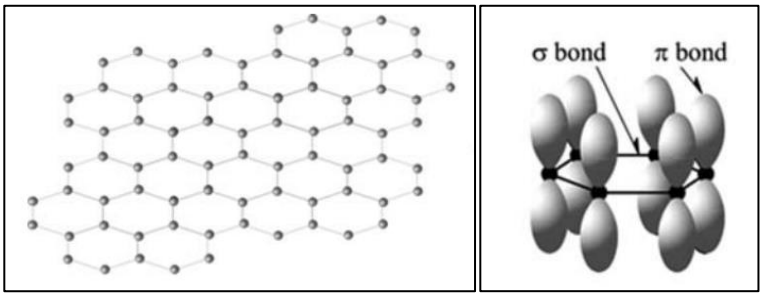

Fig. 13 *– (left) Graphene structure of single-layer two dimensional hexagonal sheet of carbon atoms; (right) schematic of the σ bonds and the π orbitals perpendicular to the plane of the graphene sheet (Choi et al, 2010).*

It was only in 2004 that bi-dimensional graphene was isolated and characterized for the first time (Novoselov et al, 2004); this discovery had a huge impact on various fields of research, from electronics to mechanics to engineering, as this material displays outstanding physical and chemical properties (it was called “miracle material”; Zumdahl & Zumdahl, 2014). For this discovery, in 2010 the graphene “fathers” Andre Geim and Konstantin Novoselov were awarded with the Nobel Prize in Physics. Graphene extraordinary features comprehend: a Young modulus of 1 TPa and intrinsic strength of 130 GPa (200 times stronger than steel, very close to the theoretical limit), a thermal conductivity above 3000 WmK^{-1}, the complete impermeability to any gases, the ability to sustain densities of electric current which are million times higher than copper, and also the easiness to be functionalized (Novoselov et al, 2012).

The graphene synthesis can be achieved via different techniques (Fig. 14) among which the most used are the “Exfoliation and Cleavage” and the “Chemical Vapor Deposition” (CVD). The Exfoliation and Cleavage method starts from the graphite, and use mechanical or chemical energy to break the weak van der Waals forces that bond together the layers of graphene; even though this method is easier and less expensive, it has a poor reproducibility and it often leads to impure graphene, constituted by more than one sheet, and which is less conductive than the graphene synthesized through other methods (Yin et al, 2015). In the CVD technique, a substrate (often Ni or Cu foils) is exposed to volatile precursors, which react on the substrate surface to produce the graphene. This method, also used to synthesize CNTs, leads to a good quality graphene and give the possibility to transfer the graphene on other substrates, such as glass or PDMS (Choi et al, 2010).

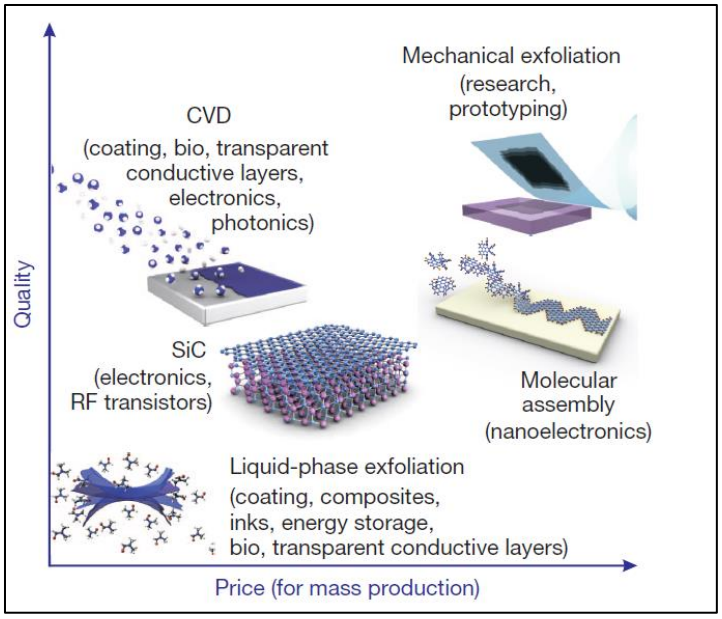

Fig. 14 *- There are several methods used for the graphene synthesis, which allow a choice in terms of size, quality and price (Novoselov et al, 2012).*

Until now, the most common form of graphene used for biomedical purposes has been the "Graphene-Oxide" (GO), which is produced by oxidation of graphite under acidic conditions. The GO has several advantages such as the possibility to disperse it in aqueous media and present hydrophilic functional groups that enable chemical functionalization (Cha et al, 2013).

For instance, when loaded with cancer drugs (after a functionalization with Folic Acid), the GO has been shown to have an improved cancer-targeting capability and anti-cancer activity compared with drugs delivered alone (Zhang et et al, 2010); in another study it was demonstrated that GO conjugated with poly-(ethylene glycol) could be used as a cellular sensor by utilizing the intrinsic photoluminescence property of GO (Sun et al, 2008).

1.2.4 The impact of carbon based materials in neuroscience

The interest in carbon based material increased exponentially in the last decades, first with the discovery of Fullerenes (1985), then with Carbon Nanotubes (1993) and finally with the synthesis of Graphene (2004). The increasing number of scientific publications per year on sp^2 carbon materials provides a measure of the attention that this topic gained in recent years (Fig. 15)

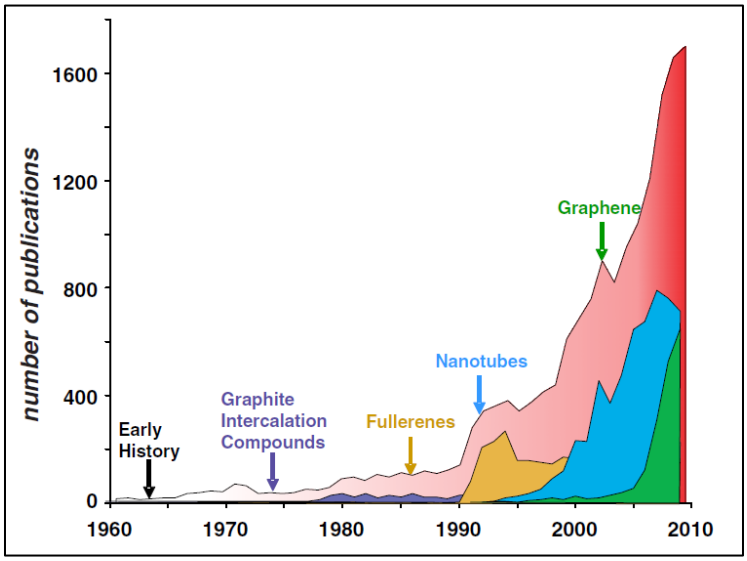

Fig. 15 *- Plot depicting the number of annual scientific publications on sp2 carbon based materials in the last decades (Dresselhaus, 2012).*

Carbon based materials have been widely used both in the clinical and applied neuroscience research. CNTs for instance, have been successfully used as substrates for neuronal growth (Mattson et al, 2000; Lovat et al, 2005): in these early studies it was shown that, not only neuronal cells were growing and surviving well on this material (and the growth could be further improved by slight modifications of CNTs, Mattson et al, 2000), but also that the neurotransmission was strongly potentiated with respect to controls (Fig. 16, left; Lovat et al, 2005). Since then the use of CNTs as substrates for cell growth has increased and further

characterized: we know for instance that CNTs substrates affect neurons both at the single cell level (i.e. increased GABAergic synaptogenesis, different short term plasticity; Fig. 16, middle; Cellot et al, 2009; Cellot et al, 2011), and at the network level (i.e. embryonic spinal cord dorsal root ganglia interfaced with CNTs display increased neurite outgrowth and increased electrical responses to afferent stimulation of ventral interneurons ; Fabbro et al, 2012). Recently, the development of a CNT-based three-dimensional scaffold, demonstrated the ability of this material to increase neuronal signals and synchronization also at the three-dimensional level *in vitro* (Bosi et al, 2015; Fig. 16, right) and to induce a limited scar formation when implanted in the rat primary visual cortex in vivo (Usmani et al, 2016). Also uncoated Graphene-based materials were used as substrate to grow neuronal primary cultures showing to be a permissive interface, on which neurons retained unaltered growth and signaling properties, thus being suitable for carbon-based neural prosthetic devices (Fabbro et al, 2016).

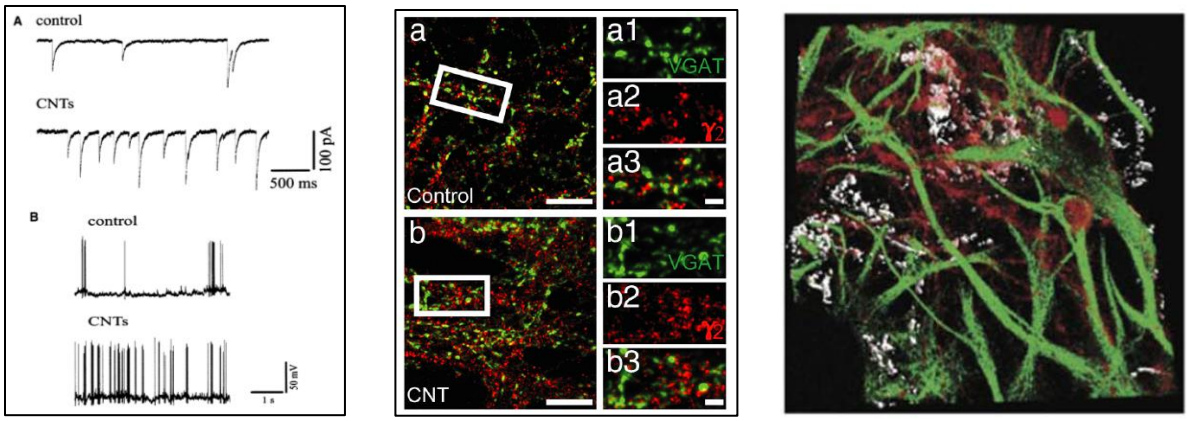

Fig.16 *- Neurons grown on a CNT substrates display (left) increased spontaneous activity and firing (Lovat et al, 2005) and (centre) increased GABAergic synaptogenesis. On the right a confocal reconstruction of a 3D-MWCNT scaffold (in grey) with neurons (in red) grown suspended within a pore, and glia cells (in green) acting as a support (Bosi et al, 2015).*

To prmote CNTs and graphene itnerfacing with biological samples, one of the most prominent issues to be studied is the toxicity of these materials when in contact with cells or entire tissues. First, there are differences between the effects of immobilized platform versus free, unbound CNTs or Graphene particles: in fact, when used as substrates for in vitro studies both uncoated CNT and graphene were shown to have no major toxic effects on either cell lines, dissociated primary cultures or organotypic cultures (Lovat et al, 2005; Fabbro et al, 2012; Lee et al, 2015). Different is the situation regarding unbound particles: for instance free, unbound CNTs (both MWCNT and SWCNT) in their soluble form might instead have toxic effects when they are not properly functionalized, causing asbestos-like pathologies such as granulomas, DNA damage, altered expression of inflammatory genes, oxidative stress, atherosclerotic lesions, (Li et al, 2007). Similarly, it was demonstrated that pristine graphene induces cytotoxicity on murine macrophage-like cells (RAW 264.7 cells) by the depletion of the mitochondrial membrane potential, thus increasing the generation of intracellular ROS, and by triggering apoptosis through the activation of the mitochondrial pathway (Seabra et al, 2014). There are evidences however indicating that appropriate CNTs and graphene chemical modifications can drastically decrease the associated hazard, making these materials biocompatible and, to some extent, even biodegradable. For instance carboxylated CNTs leaved in a hydrogen peroxide-containing medium in the presence of the Horseradish Peroxidase enzyme were almost completely degraded after 10 days, and CNTs with the same functionalization were also found to be degraded by macrophages (probably thanks to the Myeloperoxidase activity; Bianco et al, 2011). Also, Studies based on the uptake of graphene nanosheets coated with polyethylene glycol (PEG) in mice and subsequent photothermal treatment of cancerous tumors did not show any adverse toxic effects (Seabra et al, 2014).

CNTs have been employed not only as substrates but also as detectors and devices: for instance it was created a CNTs based transistor (field-effect transistor coated with SWCNTs) to detect the release of Chromogranin A (CgA) from cultured cortical neurons (Wang et al, 2007). Keefer *et al* employed CNTs to improve the quality of electrophysiological recordings:

coating tungsten as well as stainless steel wire electrodes with CNTs enhanced both the recording and the stimulation quality of cultured neurons, through a decrease in the electrode impedance and an increase in the charge transfer. Also, CNT/gold composite Multi-Electrode-Arrays (MEAs) improved the Field Potential registration at all frequencies (Keefer et al, 2008).

1.2.5 CNTs and Graphene impact on neuronal networks

A variety of works elucidated the outcome of the interaction between neurons and carbon based materials, especially CNTs and Graphene (Lovat et al, 2005; Mazzatenta et al, 2007; Cellot et al, 2009; Cellot et al, 2011; Fabbro et al, 2012; Bosi et al, 2015; Rauti et al, 2016; Usmani et al, 2016). In fact, those two particular carbon based materials, because of their peculiar physicochemical properties, have been shown to best interact and establish a peculiar cross-talk with neuronal cells. To date the knowledge about the neuronal interaction with CNTs is much more exhaustive with respect to the one we have on graphene, as the latter one was introduced more than a decade later, and just in the last years the first reports about the interaction of neuronal cells with graphene based materials were published.

It was back in 2005 that Lovat et al. first reported that dissociated hippocampal cells could healthily grow on a MWCNT carpet, and that this growth was associated to a network potentiation, measured in terms of an increased frequency either of APs and of PSCs (Lovat et al, 2005). Thereafter, many papers came out further clarifying that interaction: it was shown that CNTs carpets were able to induce specific changes on neuronal ensembles, either at the single cell level (probably by establishing a neuronal-substrate electrical coupling) such as the ability to backpropagate APs and to display a different presynaptic plasticity (Mazzatenta et al, 2007; Cellot et al, 2009; Cellot et al, 2011), and major network rearrangements, observed for instance as an increased GABAergic synaptogenesis with

respect to control cultures (Cellot et al, 2011). Also organotypic spinal cord explants were shown to be subjected to major changes induced by CNTs, such as an increased axons outgrowth (Fabbro et al, 2012) when tested as 2D substrates and an increased ability to establish a synchronized cross-talk between spinal organotypic co-cultures (Usmani et al, 2016) when CNTs were tested as 3D scaffolds.

Still, some important questions about this interaction remained unsolved. One major point to be clarified for instance is the mechanism through which CNTs carpet instruct cells, and in particular if the observed potentiation is involving some specific membrane component (especially considering the fact that was shown to occur a tight interaction between CNTs and neuronal membranes; Cellot et al 2009; Fig. 17). Another important point to be addressed is understanding whether the increased activity of neurons grown onto CNTs (see Fig. 16) is a transient rather than a chronic effect, and if it is the result of some pathologic effect (as the increased activity observed in a variety of CNS excitotoxic disorders such as the Schizophrenia or Headaches). Also, the role of the excitatory transmission was not well characterized in previous works, where the attention has been posed on the inhibitory compartment.

In this work I have performed experiments to answer these questions regarding the interaction between neurons and CNTs, to gain deeper knowledge about the effects that this material is having on primary hippocampal cells and synaptic networks.

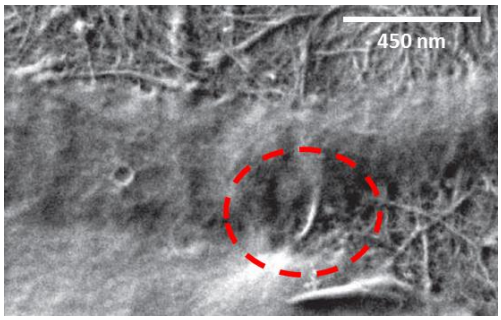

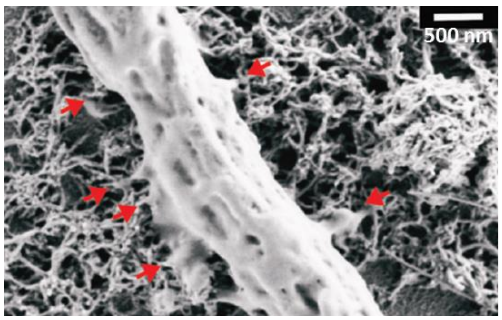

Fig 17 *- CNT carpets establish thight contacts with neural membranes. (left) SEM image depicting hippocampal neuron on a MWCNT substrate; as highlighted by the red circle, CNTs seem to literally "pinching" hippocampal membranes and partially integrate into them, establishing a cell-substrate electrical coupling (Mazzatenta et al, 2007); (right) SEM micrograph showing a peripheral neuronal fiber establishing intimate contacts (red arrows) with the CNT carpet, suggesting that also in the case of spinal explants the ability of CNTs to couple tight to neural membranes (Fabbro et al, 2012). From these observations arose the question if CNTs would somehow stabilize the cell membrane and which membrane structures would have play a major role in this interaction.*

Another part of my work was dedicated to Graphene. The neuronal-Graphene interaction is to date much less characterized, as only in the last years some reports came out about the interaction of graphene based materials and neurons (Fabbro et al, 2016; Rauti et al, 2016). Still, none of those researches dealt with the pure, monomolecular, bi-dimensional foil of Graphene interfaced with primary neurons. We decided to study the possibility of a Graphene/neuronal interfacing, and describe the outcome of this interaction: being a totally new line of research though, we decided to carried out first a general characterization, addressing the basic features of this neuronal/material coupling (such as the cell viability and the basic functional effects), followed by a more focused research in order to explain the observed effects.

In both these developments we used the same experimental paradigm, by culturing on these materials primary neurons obtained from the mammal Hippocampus, in the next paragraph I will introduce the general features of this brain structure.

1.3 THE HIPPOCAMPAL FORMATION

1.3.1 Overview

The hippocampal formation is a CNS structure consisting of the hippocampus proper, the subiculum, pre- and para-subiculum, and the adjacent entorhinal cortex. At the beginning

of the 20th century, this brain region was believed to be part of the olfactory system, because of its proximity to the olfactory areas (Finger, 2001). Only in 1947 the Norwegian anatomist Alf Brodal noticed that dogs, after hippocampal removal, were still able to accomplish tasks based on the olfaction (Brodal, 1947). The ongoing studies with the recently discovered electroencephalogram (EEG) and other evidences coming from clinical and anatomical studies helped in those years to further exclude an hippocampal active role in the olfactory functions, while delineating its fundamental role in memory and attention. For instance, the discovery in 1954 that the hippocampal theta-rhythm (4-7 Hz) was associated with attention and arousal (Green and Arduini, 1954); or the finding that bilateral hippocampal removal lead to anterograde amnesia (Scoville & Milner, 1957). More recently the hippocampus was also found to be fundamental in spatial memory and navigation (O'Keefe and Nadel, 1978).

Anatomically, the hippocampal formation is present in both hemispheres in mammals, at the level of the Medial Temporal Lobe (MTL). Its location within the CNS is well conserved across animals, although there are some differences in its orientation and intrinsic circuit (Fig. 18).

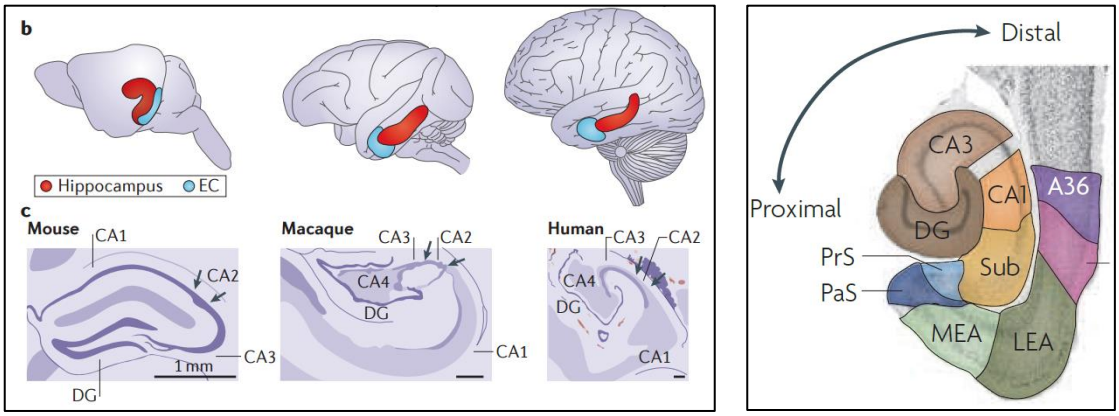

Fig. 18 *– (left) Comparison of the hippocampal formation location within the brain (b; top) and the hippocampal internal circuit (c, bottom) across three different species (mouse, macque and humans).* (Strange et al, 2014); (right) *The hippocampal formation consisting of the Hippocampus proper,*

containing the Dentate Gyrus (DG) and the Cornus Ammonis (CA) regions, the Subiculum (Sub), the Pre-(PrS) and para-Subiculum(PaS), the Medial Entorhinal Crtex (MEC), and the Lateral Entorhinal Cortex (LEC). (van Strien et al, 2009).

1.3.2 The Hippocampus anatomy

The hippocampus proper has been, and still is, one of the most studied cerebral organs within the mammalian CNS and its functional and anatomical connections are well known. Anatomically, consists of an invagination of the cerebral cortex at the level of the medial temporal lobe, present in both hemispheres (Andersen, 2007). To unveil the intrinsic hippocampal circuit we need to visualize a transverse section of the hippocampus; we can appreciate that is composed by one layer of cells (unlike the multilayered Cortex), which are regularly disposed to form the Cornus Ammonis (CA, further divided in CA1, CA2, and CA3) and Dentate Gyrus (DG) regions (Fig. 19, left). The CA region is further subdivided in layers containing different part of the neurons. The *alveus* contains the axons of pyramidal and DG neurons, which altogether form the so called fornix, probably the major output of the hippocampus proper. The *Stratum oriens, next to the Alveus,* mostly contains the somata of the *basket cells* (GABAergic interneurons) forming recurrent collaterals to other neurons; the *Stratum Pyramidale* contains the cell bodies of the pyramidal neurons, the principal excitatory (Glutamatergic) neurons of the hippocampus. Then there is the thin *Stratum lucidum*, only present in the CA3 region, it contains fibers coming from the DG. The *Stratum radiatum* is the thicker one and is composed by various fibers such as the commissural one, some entorhinal afferents in the CA3 region, and the "Schaffer collaterals" (the axons of the CA3 pyramidal neurons). Even some inteneuron can be found in this layer. Finally, the *Stratum lacunosum-moleculare* contains the apical dendrites of pyramidal cells, fibres coming from dentate gyrus and entorhinal afferents (Andersen et al., 2007).

The dentate gyrus consists of the hilus, the granule cells layer, composed by the granule cells somata, and the molecular layer, composed by the granule cells dendrites. The molecular layer is further subdivided in an outer part (OML), and an inner part (IML): the distal dendritic segments composing the OML receive excitatory afferents from the Entorhinal cortex, while contralateral and ipsilateral commissural and associations hippocampal fibers innervate the proximal parts of granule cells dendrites in the IML (Fig. 19, right; Förster et al, 2006).

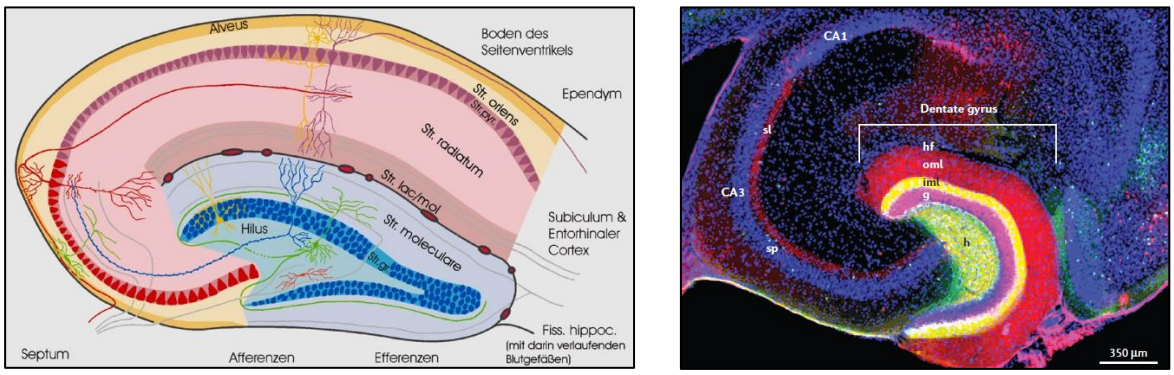

Fig. 19 *- (left) The hippocampal structure* (http://anatomie.vetmed.uni-leipzig.de). (right) *The anatomical organization of the dentate gyrus: mossy cells within the hilus stained with calretinin (green) whose axons project to the contralateral IML, granule cell bodies stained with DAPI (blue) and OML stained with calbindin in red;* (Förster et al, 2006)

The information flow within the hippocampus is unidirectional: afferents coming from the entorhinal cortex contact the DG granule cells, and are then carried along the "tri-synsptic circuit" (DG-CA3-CA1) and exit the hippocampus through the Fornix (Andersen, 1975).
The major output of the hippocampal formation is given by the bundle of fibres arising from the dorsal edge of the hippocampus, called "fimbriae", which in latin means "fringe". This bundle gets thicker and thicker going towards the medial part of the hippocampus, as it collects more and more subicular and temporal hippocampal fibers, until both ipsi- and contralateral fimbriae come together in the midline of the brain, under the corpus callosum,

forming the fornix (from latin, “arch”), that travels further anteriorly towards the anterior commissure, where it divides again. Through the fornix, the hippocampi are connected to the hypothalamic mammillary bodies, septal nuclei and nucleus accumbens, making the hippocampus a major player also in the limbic system, which is involved in emotions, motivation, memories and other cognitive functions (Andersen, 2007).

1.3.3 The Entorhinal Cortex anatomy

The Entorhinal Cortex constitutes the major gateway between the hippocampus and the neocortex, and is located in the posterior temporal lobe of both hemispheres (Fig. 20).

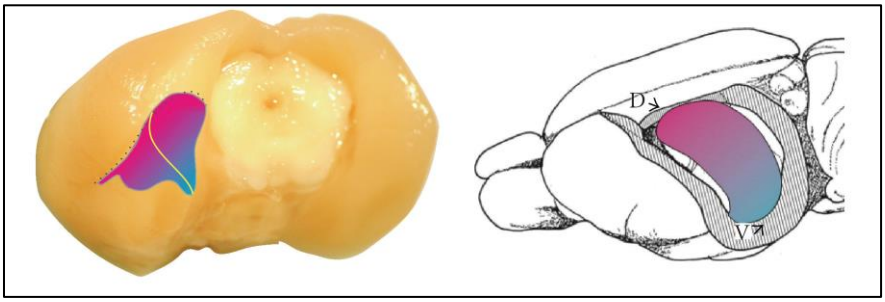

Fig. 20 *- Location of the EC within the (real, left; cartoon, right) rat brain posterior temporal lobe (Canto et al, 2008)*

As part of the CNS cerebral cortex, the EC (its name derives from the fact that it is partially embedded into the rihnal sulcus; ento-rhinal = inside rihnal) has a laminar organization: is organized in different cell layers (VI), each with a peculiar function (Fig. 21). Superficial layers II/III contains the somata of pyramidal neurons which constitutes the main output of the EC towards the hippocampus. Viceversa, the deep layers V/VI contains the cell bodies of

the neurons which receives projection from the hippocampus, constituting the main input to the EC (Fig. 21).

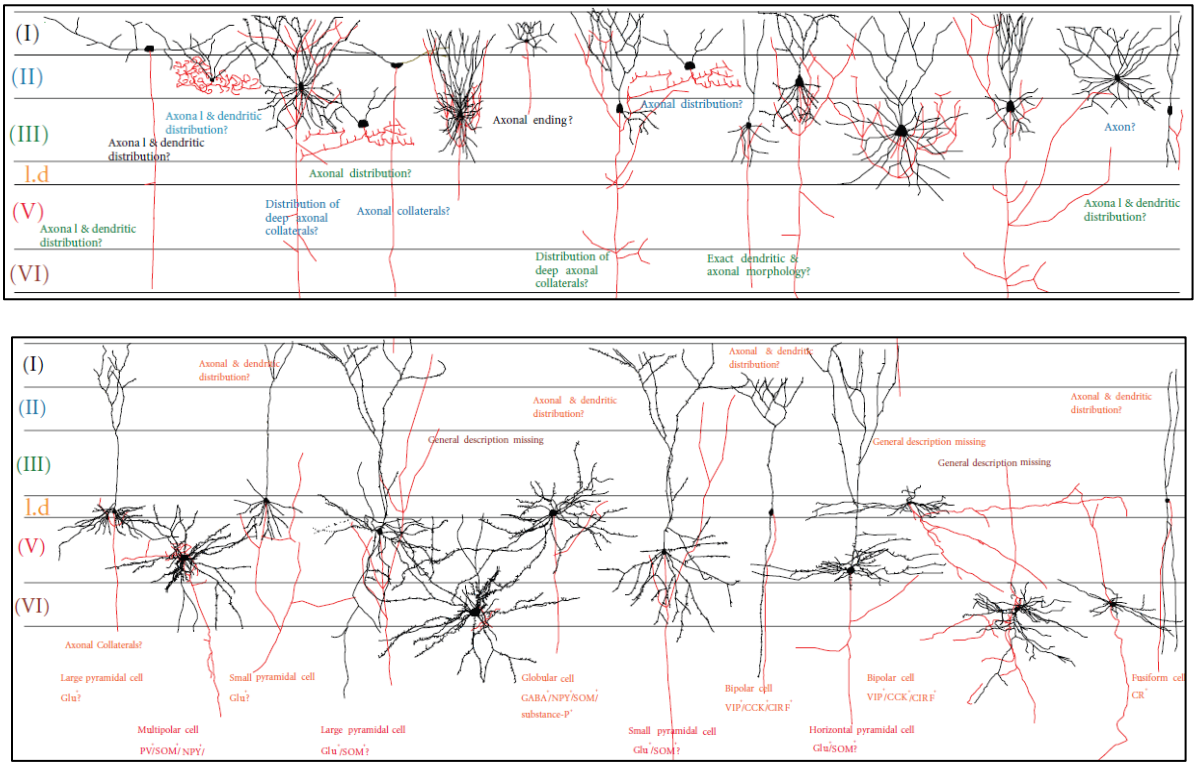

Fig.21 - *Summary diagram of the morphology of main cell types MEC. In the upper panel are represented neurons which have their somata in the superficial layers I/II constituting the main output of the EC; in the bottom panel are instead represented the cell bodies of those neurons located in the deep layers V/VI which constitute the main input to the EC (Canto et al, 2008).*

The EC can be subdivided in a medial part (MEC) and a lateral part (LEC), on the basis of both anatomical and connectivity diversities (Witter and Amaral, 2004; Canto et al, 2008; Fig. 22). The MEC connects preferentially with the postrhinal cortex, presubiculum, occipital cortex and olfactory areas; the LEC instead is connected to the amygdala, perirhinal cortex,

olfactory and insular cortex (Fig. 22). MEC and LEC also connect differentially to the hippocampal formation, both targeting the same neurons in the dentate gyrus and field CA3, while they reciprocally connect to different groups of cells in CA1 and subiculum (Canto et al, 2008).

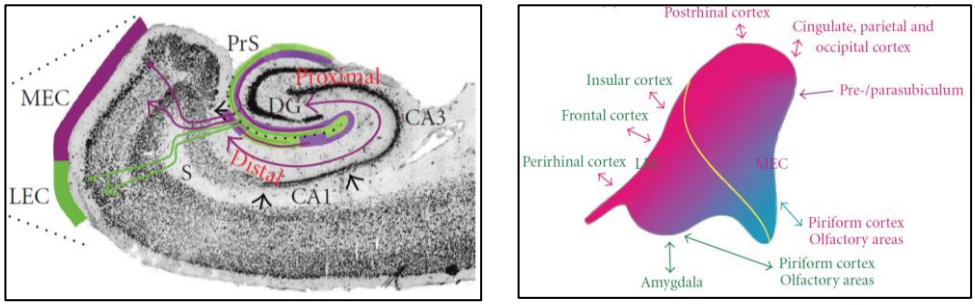

Fig.22 *- Left: Horizontal section of the hippocampal formation illustrating the position of MEC (green) and LEC (purple) and the respective main connections with the hippocampus; right: enlarged entorhinal cortex, indicating the main connectivity of different portions of entorhinal cortex. Brain areas preferentially connected to LEC are printed in green, those connected to MEC are in magenta (Canto et al, 2008).*

1.3.4 Connections and functions

The hippocampal formation seems to be involved in a variety of different functions ranging from emotions to memory to spatial navigation. This variety of functions is supported by its anatomical connectivity (Fig. 23); in fact, the hippocampus establish physical connections with many other brain structures such as the Septum, Hypothalamus, Amygdala, Controlateral Hippocampus and various cortical areas such as the Entorhinal, Cingulate and Olfactory (Bird and Burgess, 2008; Agster and Burwell, 2013; Fig. 23).

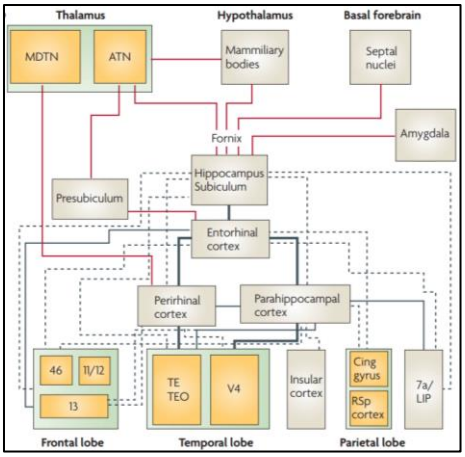

Fig. 23 *- Schematic representation of the hippocampal connections with other brain structure (Bird and Burgess, 2008).*

Among the various connections present within the hippocampal formation (such as the Temporoammonic Pathway or the Alvear Pathway; Witter et al, 2000; Deller et al, 1996), the most well addressed is surely the Perforant Path (PP), that consist of excitatory Glutamatergic projections that from the superficial layers of the Entorhinal Cortex reaches the molecular layer of the Dentate Gyrus and, in a minor portion to the CA3 region, literally perforating the Subiculum (therefore the name “perforant”; Jacobson & Marcus, 2008). From the CA3 region, Mossy fibers relay the information to the CA1 neurons, which then project back their neurites (still through the subiculum) to the deep layers (IV, V mostly) of the Entorhinal cortex (Fig. 24; Neves et al, 2008; van Strien et al, 2009; Jacobson & Marcus, 2008; Witter, 2007).

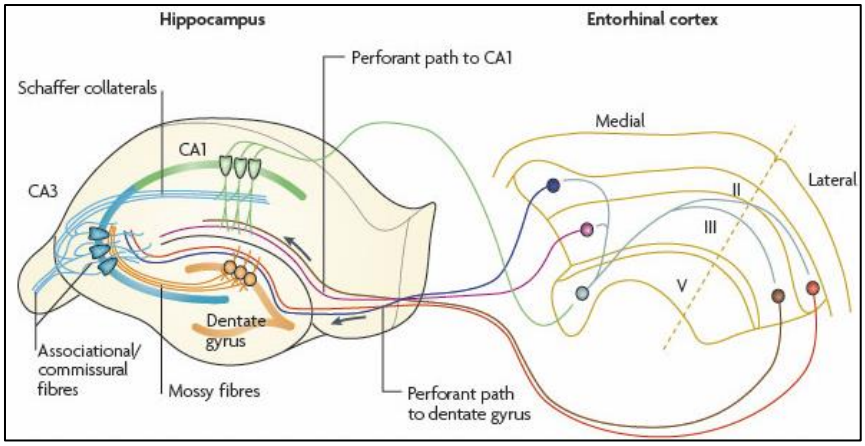

Fig. 24 *- Schematic representation of the Perforant Path connectivity. The PP convey polymodal sensory information from neurons in layer II of the entorhinal cortex to the dentate gyrus. Perforant path axons make excitatory synaptic contact with the dendrites of granule cells: axons from the lateral and medial entorhinal cortices innervate the outer and middle third of the dendritic tree, respectively. Granule cells project, through their axons (the mossy fibres), to the proximal apical dendrites of CA3 pyramidal cells which, in turn, project to ipsilateral CA1 pyramidal cells through Schaffer collaterals and to contralateral CA3 and CA1 pyramidal cells through commissural connections. CA1 neurons project back their axons to entorhinal deep layers (Neves et al, 2008).*

A remarkable example of the importance that the PP had in Neuroscience comes from the discovery of Long Term Potentiation (LTP) in 1973 (Bliss & Lomo, 1973), which was described as an increase in the amplitude of the excitatory post-synaptic potential (EPSP) of the dentate area recorded with extracellular micro-electrodes, after repetitive stimulation of the PP: LTP is to date a well known mechanism, consisting in a long-lasting enhancement of the signal transduction between two neurons, which is required in many cognitive processes, such as memory consolidation and storage (Lynch, 2004).

The PP, which connectivity can be retained *in vitro*, has shown to be the anatomical base of various higher brain processes such as the temporal association memory (Suh et al, 2011; Kitamura et al, 2014) and spatial navigation (Bush et al, 2014).

Another important feature of the hippocampal formation rely on its ability to generate "rhythms": periodically fluctuating waves of neuronal activity observed using local field potential recordings (LFP; Colgin, 2016). These rhythms are characterized by different

frequencies and seem to be associated to different cognitive processes: the “Theta” rhythm (4-12 Hz) for instance, is observed during exploration and rapid eye movement (REM) sleep; the “Sharp Waves Ripples” (110–250 Hz ripples superimposed on 0.01–3 Hz sharp waves) are instead associated to waking immobility and non-REM sleep; “Gamma” rhytms (25-100 Hz) are described also in other brain regions, and in the hippocampus seem to be fundamental in memory retrieval processes (Colgin, 2016).

1.3.5 Culturing the hippocampal formation: *in vitro* models

In vitro neuronal cultures constitute a fundamental tool to address and study neuronal processes and behaviors, as they provide an isolated, controlled system in which cellular features can be easily, if compared to the entire organ, addressed. Different kind of in vitro hippocampal cultures have been developed to date, which can be grouped into three main groups: dissociated cultures, acute slices and organotypic cultures.

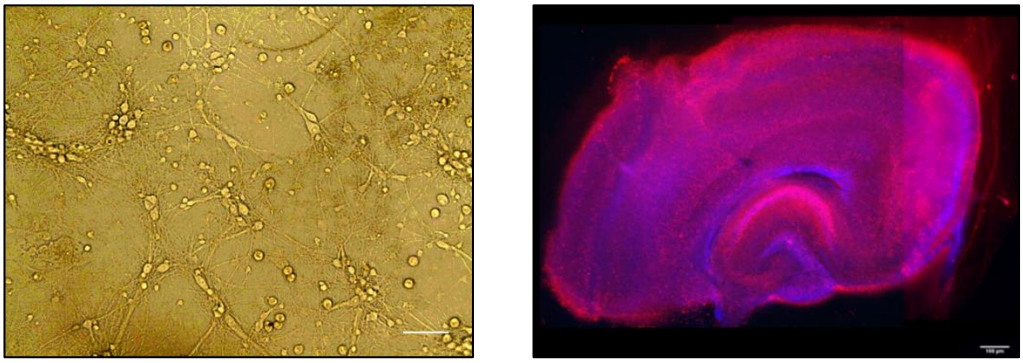

Fig. 25 *- (left) Bright field low magnification micrograph showing dissociated primary hippocampal neurons cultured at DIV 8 cultured onto poly-L-Ornithine coated glass coverslips; individual neurons can be easily visualized; scale bar: 50 μm; (right) low magnification fluorescent micrograph reconstruction of an organotypic entorhinal-hippocampal culture (EHC) fixed at DIV 5 and stained with antibodies againts Map2 (Neuronal marker, red), and with DAPI (nuclear marker, blue). Note the cortex and hippocampus cytoarchitecture neatly maintained within the cultured slice.*

Primary dissociated hippocampal cultures were introduced in the late seventies in the laboratory of Max Cowan at the Washington University in St. Louis (Banker and Cowan, 1977). This protocol relied on the enzymatic dissociation of hippocampi obtained from embryonic rats and subsequent plating on polylisine-treated coverslips in an enriched medium (Banker and Cowan, 1977). Since then, a variety of different protocols to obtain dissociated neurons emerged, because of the wide employment of this advantageous model. In fact, the possibility to have functional neurons spatially segregated each other allowed the study of cellular phenomena which previously couldn't be addressed, such as the network formation and maturation, the synapses physiology, channels and receptors homeostasis, developmental and pharmacological studies.

In nanotechnology, dissociated cell cultures have always been the tool of preference, because they promote a strong physical interaction between neurons and the nanomaterials, which allow a precise characterization of such an interaction, fundamental in the fists steps of the research. If, for instance, we wish to design and manufacture a nanomaterial-based implant able to deliver stimulation at precise locations, it would became crucial to understand the basic interactions of the nanomaterial with single neurons, the stability of such interactions and the functional outcomes in terms of neuronal signaling. In this perspective, there are hundreds of studies addressing single-cell behavior in response to artificial nano-seized cues, that take advantage of this type of in vitro model: Fozdar *et al*, for instance, found that neuronal morphologies could be manipulated using different substrate topographies (Fozdar et al, 2010); Cellot *et al* discovered the potentiating effect of a carbon nanotubes carpet on the synaptic activity of dissociated hippocampal cells (Cellot *et al*, 2009; Cellot *et al*, 2011); Haziza *et al* developed high-brightness photostable fluorescent nanodiamonds (FNDs) that could be tracked inside the branches of dissociated neurons with a spatial resolution of 12 nm and a temporal resolution of 50 ms (Haziza et al, 2016); Blumenthal *et al* exploited hippocampal cells to demonstrate that nanoroughness can modulate the function of neurons and their relationship with astrocytes (Blumenthal et al, 2014; Fig. 26), to name a few.

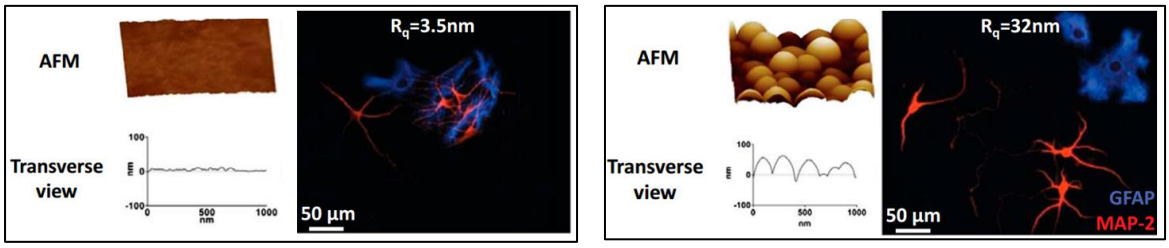

Fig. 26 *- Hippocampal neurons (stained with Map2, red) and astrocytes (stained with GFAP, blue) interact differentially depending on the substrate roughness: if cultured on a barely flat surface (Rq=3.5 nm; left), they tend to aggregate more with respect to rough surfaces (Rq=32 nm; right; adapted from Blumenthal et al, 2014).*

At an increased level of tissue complexity, beyond dissociated primary cultures , we can placethe acute slices and the organotypic cultures. Both these *in vitro* model are constituted by hippocampal transverse explants; but, in the case of acute slices, the hippocampal explants are (more or less, depending on the protocol) directly used for experiments. On the contrary, in the case of organotypic cultures, the slices are cultured and maintained *in vitro* for days/weeks (Gähwiler et al, 1997). From one hand, acute slices are the preferential model used to address many physiological functions, on the other, organotypic cultures give the possibility to address the effects of longer exposures of drugs/materials/substances on the hippocampal tissue, and therefore are generally the most used in Nanotechnology, displaying similar advantages to dissociated cultures in testing chronic growth on artificial substrates, but displaying a higher level of circuit complexity and maintaining the basic cytoarchitecture of the explanted organ. For example, the testing of new generation of recording/stimulating devices often took advantage of organotypic cultures: Yu et al used this *in vitro* model to validate their array made of aligned carbon nanofibers able to record and stimulate the neural tissue (Yu et al, 2007); also Angle & Schaefer, who fabricated small-sized nano-engineered electrodes able to penetrate the plasmamembrane and record transmembrane potentials such as APs, without causing physiological perturbations

(as the change of intracellular biochemistry or the plasmamembrane damage; Angle & Schaefer, 2012).

Due to these motivations, in this work we selected dissociated hippocampal cells to address the basic interactions between CNTs and Graphene, as they gave the possibility to study the effects of these material at the single cell level first (such as the membrane/material interaction, biophysical and electrophysiological basic properties) and how these features are then translated at the network level into different behaviors (such as the observed increase activity or synaptogenesis). Once these features were characterized (and an exhaustive characterization at this level is now achived in the case of CNTs), I wondered how this material would impact on a whole brain organ, thus increasing the complexity of the system. To this purpose I developed the organotypic Hippocampal-Entorhinal cultures (EHCs) to be interfaced with CNTs carpets. CNTs have been shown to possess regenerative cues when interfaced with spinal explants (Fabbro et al, 2012; Usmani et al, 2016; Aurand et al, 2017) but their effects on whole brain structures are not known. As the ultimate goal of CNTs is their employment in the construction of devices/scaffolds to be interfaced with lesioned nerve tissues, we decided to simulate a lesion in the organotypic explant and evaluate the CNTs regenerative effects.

1.3.6 – Lesion approaches

In the neuroscientific field, the “lesion approach” is an accepted and useful tool to elucidate brain functions both *in vivo* (mostly to link the anatomic bases of specific cognitive behaviors; Rorden and Karnath, 2004) and *in vitro* (to understand cellular and molecular functions coupled to specific brain areas; Cassel et al, 1997; Chen et al, 2009). Specific brain lesions, which can be induced both mechanically and pharmacologically, were used for instance to study the role of hippocampus and/or Entorhinal Cortex in memory

consolidation (Kitamura & Inokuchi, 2013; Savage et al, 2004), spatial memory (Clark et al, 2005) and acquisition of place memory (Hales et al, 2014).

As the ultimate purpose of interfacing carbon based materials with neural tissues and cells would be their involvement in the construction of prostheses/devices able either to interact with neurons in a non-pathological manner, and to restore the lost functions both at the spinal and encephalic level, one strategy towards this aim is to test the capability of these materials to interact with the lesioned neural tissue, and evaluate the possible outcomes of this interfacing. To this purpose a variety of *in vitro* lesion approaches has been developed concerning the hippocampal formation (Cassel et al, 1997; Perederiy and Westbrook, 2013), among which the perforant path lesion model present several advantages: the lesion site is distant from the dentate gyrus, and this allow a precise discrimination of local degenerative/inflammatory effects at the lesion site from the regenerative effects of post-lesion circuit reorganization (Perederiy and Westbrook, 2013). Due to this lesion model, several aspects of the hippocampus and more specifically of the dentate gyrus were elucidated. For instance it was observed that in response to de-afferentation, axons of the remaining fiber and dendrites of mature granule cells undergo lamina-specific changes, providing one of the first examples of structural plasticity in the adult brain (Fig. 27; Perederiy and Westbrook, 2013; Vlachos et al, 2012).

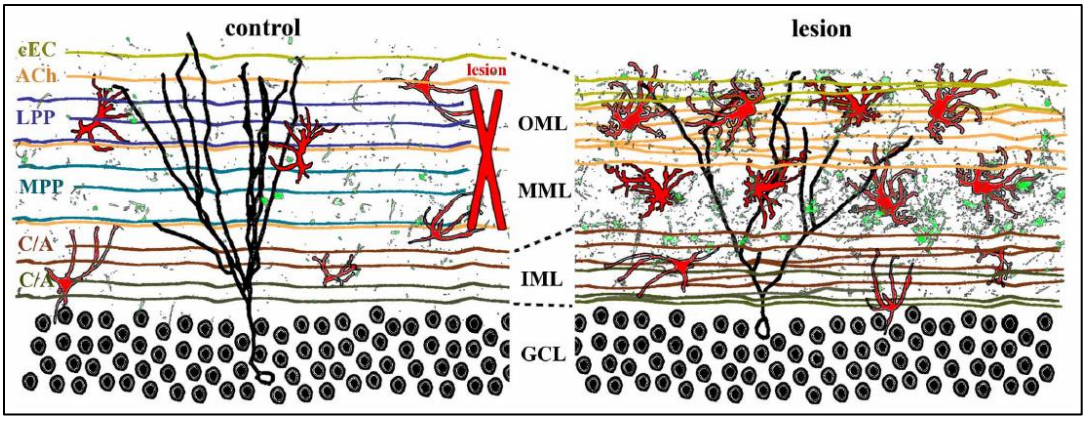

Fig. 27 *- (left) The normal DG structure and innervation from the inner molecular layer (IML) is occupied by the glutamatergic commissural/associational fibers (C/A) that arise from mossy cells in*

the ipsi-or contro-alateral hilus. The middle and outer molecular layer (MML, OML) are occupied predominantly by the glutamatergic performant path (MPP, LPP),which originates in the ipsilateral entorhinal cortex. Cholinergic axons (ACh) from the septal nuclei/diagonal band of Broca are interspersed throughout the molecular layer, as are astrocytes (red) and quiescent microglia (green). (right) Lesion of the entorhinal cortex (red X, in the left panel) transects both medial and lateral performant path, thus eliminating the majority of excitatory input into the dentate gyrus. Degeneration of these axons induces lamina-specific sprouting of the remaining septo hippocampal (ACh), commissural/associational (C/A), and crossed entorhino-dentate (cEC) afferents. In therat, the contralateral entorhino-dentate projection(cEC) partially restores excitatory innervation of the mature granule cells (black trace), however, their dendritic length and complexity are still reduced. The microglia (green) and astrocytes (red) become "activated" following lesion, but this response is limited to the deafferented zone. Note the expansion of the inner molecular layer and shrinkage of the outer layers *(Perederiy and Westbrook, 2013).*

Also, the unilateral PP denervation resulted in a dramatic increase in newly generated granule cells with peculiar features at 14 days post lesion, and this was one of the first piece of evidence of neurogenesis in the adult brain (Lemaire et al, 2012;
Perederiy and Westbrook, 2013). Another advantageous feature of this lesion model, considering the fact that each afferent input terminates in a peculiar lamina of the dentate gyrus molecular layer, is possible to easily discriminate homotypic (i.e., that shares many of the characteristics of the original pathway) versus heterotypic (i.e., that is dissimilar to the original pathway) post-lesion axonal sprouting (Ramirez, 2001; Perederiy and Westbrook, 2013).

Because of these well documented works reporting on the lesioning of the PP, we decided to adopt this model to evaluate the effects of CNTs on the disrupted neural tissue. Still, as CNT-based interfaces would be potentially useful in case of mechanical injuries in which a separation of the CNS structures occurs, we decided to mimic this situation by outdistancing the Entorhinal cortex to the hippocampus 400-600 μm apart and evaluate the potential regenerative effects of this material, compared to a control condition.

AIMS OF THE STUDY

Tissue engineering and regenerative medicine require the constant development of synthetic materials to manufacture scaffolds thatbetter integrate into the target tissues (O'Brien, 2011; Ku et al, 2013; Harrison et al, 2014).

In this framework, newly synthesized nanomaterials made of pure carbon, in particular Carbon Nanotubes (Ijima, 1991) and Graphene (Novoselov et al, 2004) applications to biology received particular attention due to their outstanding physicochemical properties (Hirsch, 2010).

Our team has performed pioneer works during the last decade, about the interactions of neural cells with carbon nanotubes (Lovat et al, 2005; Mazzatenta et al, 2007; Cellot et al, 2009; Cellot et al, 2011; Fabbro et al, 2012; Bosi et al, 2015), and with graphene (Fabbro et al, 2015; Rauti et al, 2016) or, more in general, with synthetic substrates (Cellot et al, 2016).

The major aim of my work has been to use traditional and novel physiology tools to investigate further these "neuro-hybrid systems", and to understand how far Carbon Nanotubes and Graphene can be pushed in neuroscience applications.

With this aim, in the first part of my PhD I further elucidated the behavior of newly formed synapses in primary dissociated neurons when interfaced to bi-dimensional substrates of Multi-walled Carbon Nanotubes. I then addressed the homeostasis of *in-vitro* neural networks interfaced to pure graphene and I characterized for the first time the changes induced by this material in neurons. As last step, I set up a more complex biological *in-vitro* model, consisting of lesioned organotypic Entorhinal-Hippocampal cultures (Perederiy and Westbrook, 2013) and we described the regenerative features of Carbon Nanotubes in this lesion model.

During my PhD I was also involved in two side projects: in the first one, in collaboration with Sebastian Reinhartz and Matthew Diamond (SISSA), we refine the possible

approaches of the optogenetic technique, by manipulating neuronal responses with different light waveforms (Reinhartz et al, MS in preparation, in the appendix). In the second one, in collaboration with the group of Manus Biggs, from the National University of Galway, Ireland, we tested the biocompatibility and addressed the neural behavior of primary neural cells interfaced with Indium Tin Oxide (ITO) substrates with different roughness, thickness and conducting profiles (Vallejo-Giraldo et al, 2017).

ELSEVIER

Nanomedicine: Nanotechnology, Biology, and Medicine
xx (2017) xxx–xxx

nanomedicine
Nanotechnology, Biology, and Medicine

nanomedjournal.com

Special Topic: Two-Dimensional Biomaterials in Regenerative Medicine

Sculpting neurotransmission during synaptic development by 2D nanostructured interfaces

Niccolò Paolo Pampaloni[a], Denis Scaini[b,c,*], Fabio Perissinotto[b,c], Susanna Bosi[d], Maurizio Prato[d,e,f,**], Laura Ballerini[a,***]

[a]*International School for Advanced Studies (SISSA), Trieste, Italy*
[b]*Life Science Department, University of Trieste, Trieste, Italy*
[c]*ELETTRA Synchrotron Light Source, Trieste, Italy*
[d]*Department of Chemical and Pharmaceutical Sciences, University of Trieste, Trieste, Italy*
[e]*Basque Foundation for Science, Ikerbasque, Bilbao, Spain*
[f]*CIC BiomaGUNE, Parque Tecnológico de San Sebastián, San Sebastián (Guipúzcoa), Spain*

Received 4 August 2016; accepted 4 January 2017

Abstract

Carbon nanotube-based biomaterials critically contribute to the design of many prosthetic devices, with a particular impact in the development of bioelectronics components for novel neural interfaces. These nanomaterials combine excellent physical and chemical properties with peculiar nanostructured topography, thought to be crucial to their integration with neural tissue as long-term implants. The junction between carbon nanotubes and neural tissue can be particularly worthy of scientific attention and has been reported to significantly impact synapse construction in cultured neuronal networks. In this framework, the interaction of 2D carbon nanotube platforms with biological membranes is of paramount importance. Here we study carbon nanotube ability to interfere with lipid membrane structure and dynamics in cultured hippocampal neurons. While excluding that carbon nanotubes alter the homeostasis of neuronal membrane lipids, in particular cholesterol, we document in aged cultures an unprecedented functional integration between carbon nanotubes and the physiological maturation of the synaptic circuits.

Key words: Nanostructured materials; Patch clamp; Cholesterol; Synaptic release; Vesicle pools

Neurons are continuously exposed to signals generated by the extracellular environment, including genuine physical cues (such as mechanical or topographical ones) at the nanoscale, able to drive key biological tasks.[1] This ability has been exploited to engineer interfaces with nanostructures with the aim of guiding nerve tissue re-growth.[2–4] Varied strategies have been adopted to decorate bio-interfaces with nano-features[5,6] and incorporating nanomaterials has emerged as a promising one.[5,6] Conductive nanomaterials, such as carbon nanotubes, have received particular attention[7–9] and were shown, when used to interface cultured neurons, to improve the growth of axons[10,11] and to enhance the construction of synaptic connections between

Abbreviations: AFM, atomic force microscopy; CT-B, Cholera Toxin subunit-B; DIV, days in vitro; DOPC, 1,2-Dioleoyl-sn-glycero-3-phosphocholine; MβCD, Methyl-β-Cyclodextrin; mPSCs, miniature post-synaptic currents; MWCNTs, multi-walled carbon nanotubes; PSCs, post-synaptic currents; SLM, artificial lipid membranes; SPM, scanning probe microscopy; TTX, Tetrodotoxin; VGLUT1, vesicular glutamate transporter 1

Financial supports from: This work was supported by the ByAxon n. 737116, NEUROSCAFFOLDS-FP7-NMP-604263 and the PRIN-MIUR n. 2012MYESZW to L.B.

Competing interests: The Authors declare no competing financial interests.

Authors' contributions: NPP performed electrophysiology, immunocytochemistry and confocal microscopy experiments and contributed to the analysis. DS and FP performed SLM experiments and AFM analysis. SB and MP provided the materials. LB and DS conceived the idea and designed the experiments. LB and DS wrote the manuscript. LB provided funding. All authors read and approved the final manuscript.

*Correspondence to: D. Scaini, Life Science Department, University of Trieste, Trieste, Italy.
**Correspondence to: M. Prato, Department of Chemical and Pharmaceutical Sciences, University of Trieste, Trieste, Italy.
***Corresponding author.
E-mail addresses: npampalo@sissa.it (N.P. Pampaloni), dscaini@sissa.it (D. Scaini), fabio.perissinotto@elettra.eu (F. Perissinotto), sbosi@units.it (S. Bosi), prato@units.it (M. Prato), laura.ballerini@sissa.it (L. Ballerini).

http://dx.doi.org/10.1016/j.nano.2017.01.020

neurons.[12–15] More precisely, the extracellular environment, when artificially reconstructed by multi-walled carbon nanotubes (MWCNTs), induced synaptogenesis in cultured hippocampal neurons during early network formation.[12,15,16] Enhancing cell-to-cell communication is crucial in neural circuits' settings,[17] however the role and dynamics of the interactions between MWCNTs and the cellular surfaces (the "nano-bio" interface[18]) are largely unexplored.

The majority of current studies on biological membrane stability in response to nanomaterials are focused on the influence of materials' functionalization or shape/size on cell uptake mechanisms and internalization, to engineer sophisticated drug delivery (nano)-vectors.[19] In this framework, neuronal membranes have been shown to recover even when transiently pierced or deformed by (nano)needles[20] or other intracellular (nano) delivery systems.[21] Water-soluble single-walled carbon nanotubes grafted to poly ethylene glycol impaired, when added to the culturing medium, membrane re-cycling in neurons, presumably by affecting the endocytosis of released vesicles at the pre-synaptic site.[22] However, more specific information about neuronal membrane stability when chronically interfaced to pristine nanomaterial-based growth substrates is lacking. Cell membranes are directly exposed to MWCNTs,[14,23] but there are no reports on the effects that MWCNT interfaces exert on neuronal membrane equilibrium. Recent studies targeted the interaction between lipoid membranes and MWCNTs in suspension.[24,25] Molecular simulations showed that significant changes in the structure of individual lipid molecules, and in their two-dimensional packing, were observed when MWCNTs were adsorbed on cell membranes and subsequently pierced the lipid bilayer.[26,27]

Here, by single cell electrophysiology and immunofluorescence microscopy we monitor the dynamics of glutamate receptor-mediated excitatory transmission in cultured hippocampal neurons interfaced to MWCNTs. We specifically addressed whether MWCNTs, once interfaced to neurons, affected synaptic transmission by modulating lipid membrane structure and dynamics. We focused in particular on cholesterol, a largely represented lipid in neuronal membranes known to regulate presynaptic vesicle release.[28,29] For a first general assessment we used artificial lipid membranes that, when interfaced to MWCNTs, were more stable, in respect to controls, to a cholesterol depleting-agent, i.e. cyclodextrin.[30] Conversely, in cultured neurons, MWCNT interfaces did not alter the membrane cholesterol distribution neither prevented its subsequent depletion by cyclodextrin. Unexpectedly, by cholesterol removal, we unmasked MWCNT ability to shape pre-synaptic vesicle populations at newly formed glutamatergic connections. Finally, we followed up the effects of long term MWCNT interfacing in neural synaptic networks.

Methods

Synthesis of MWCNTs

MWCNTs 20-30 nm in diameter (Nanostructured & Amorphous Materials, Inc.) were used as received and substrates were prepared as described previously.[12,15] Briefly, MWCNT 20-30 nm were functionalized using 1,3-dipolar cycloaddition with heptanal and sarcosine at 130 °C for 120 h in dimethylformammide (DMF) as solvent. For deposition on the coverslips, the DMF solution of functionalized MWCNTs (0.01 mg/mL) was drop casted to uniformly layer the entire substrate and let evaporated at 80 °C, then, the substrates were heated up at 350 °C under N_2 atmosphere to induce the complete re-pristinization of MWCNTs. The uniformity of the deposition was assumed by AFM (Figure 1, *B*) and by scanning electron microscopy (SEM, in Supplementary Figure S1, *D*).

Artificial membrane preparation and characterization

Artificial membranes were prepared by lipid spreading on a supporting glass slide from an organic solvent solution. 1,2-Dioleoyl-sn-glycero-3-phosphocholine (DOPC) and cholesterol molecules (both from Avanti Polar Lipids Inc., US) were dissolved in a 2:1 ratio in chloroform (Sigma Aldrich) at a final concentration of 100 μM. 100 μL of solution were deposited on a glass coverslip, used as control, and on MWCNTs substrates supported by the same glass coverslip (Figure 1).[15] Samples were settled at 37 °C, 80% UR for 30 min, then rinsed in mQ water, dried with a gentle flow of N_2 and mounted on metallic plates using epoxy glue for subsequent atomic force microscopy (AFM) imaging (MFP-3D™, Asylum Research, Santa Barbara, CA, U.S.). Measurements were carried out in buffer solution (HEPES, Sigma Aldrich) at room temperature (RT, 18 to 22 °C) working in dynamic mode. Cantilevers, characterized by a resonant frequency of 69 kHz and force constant of 0.39 nN/nm (OMCL-RC800PSA-1 tips from Olympus Co., Japan), were used working at low oscillation amplitudes with half free-amplitude set-point. Images were acquired at 512 × 512 pixels at 0.75 lines/s scan speed. Artificial membranes for fluorescence experiments were prepared following the same procedure described above but DOPC molecules were mixed with 2% of fluorescent lipid (18:1-06:0 NBD PC, from Avanti Polar Lipids Inc., US). Fluorescent measurements were done by epifluorescence microscopy (Eclipse Ti-U, Nikon Co., Japan; 20× objective, 0.45 NA). Samples were mounted in a liquid cell and the decay in fluorescent signal from both membranes deposited on control and MWCNT substrates were recorded for 60 min after injection of 500 μM Methyl-β-Cyclodextrin (MβCD, Sigma Aldrich) to deplete cholesterol.[30] Decay plots are the average of 3 independent experiments. Values were normalized to the fluorescent signal immediately before MβCD injection. AFM images were analyzed using Gwyddion, open-source modular program for scanning probe microscopy (SPM) data visualization and analysis.[31] Surface roughness was determined as RMS value of the height irregularities on 2.5 μm^2 membrane area. Decays were fitted using a double exponential function using Igor Pro software (Wavemetrics, US). Figure S1, *C* shows the amplitude (error) AFM images of the high magnification reconstructions shown in Figure 1, *A-C*.

Raman characterization

The Raman measurements were performed in the reflection geometry. A 532 nm continuous-wave laser (Cobolt Samba,

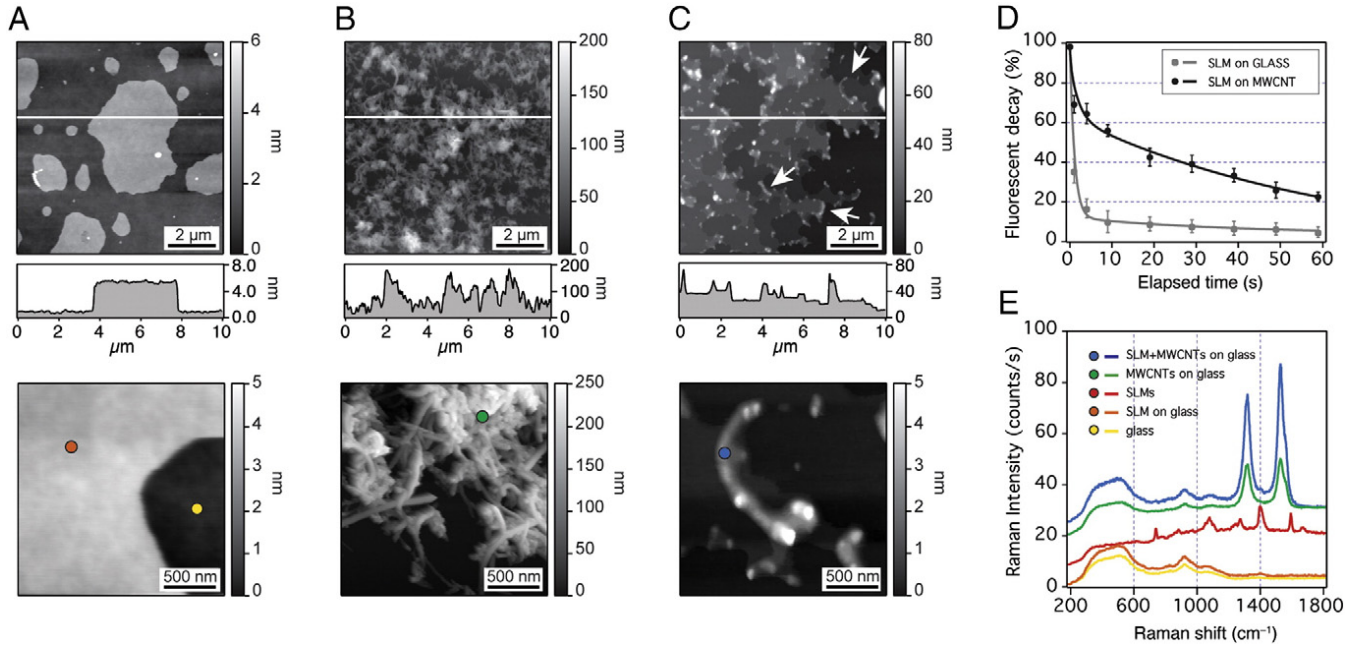

Figure 1. AFM investigation of artificial lipid membranes (SLM). **(A)** Low magnification topographic reconstruction of an incomplete SLM deposited on a control glass surface (on the top). The height profile corresponding to the highlighted line is shown, revealing SLM height of about 5.0 ± 0.2 nm. Higher resolution AFM reconstruction (on the bottom) demonstrates the high uniformity of the so obtained SLB. B. Low magnification topographic reconstruction, corresponding height profile and higher resolution reconstruction of a MWCNTs carpet deposited on glass via drop-casting. Note the high corrugation of the resulting surface pointed out by the top image and single MWCNTs composing the carpet easily distinguishable in the bottom one. **(C)** Low magnification topographic reconstruction, corresponding height profile and higher resolution reconstruction of SLBs deposited on a MWCNTs substrate. It is possible to appreciate (white arrows) MWCNT ability to pierce SLMs, indicated by nanotubes emerging from the upper membrane layer. The altimetric profile reveals flat parts, corresponding to superficial SLBs, from which only MWCNTs apexes protrude. **(D)** Fluorescent decay of SLMs signal after injection of MβCD (500 μM) detected in control (squares) and on MWCNT (circles) membranes. Note that the decay follows a double exponential law characterized by τ values of 1.09 ± 0.02 s and 39.02 ± 9.83 s (gray fitting line) for SLM deposited on glass and 2.02 ± 0.15 s and 63.67 ± 6.92 s for SLM deposited on the MWCNT carpet (black fitting line). Data are averages of 3 independent experiments expressed as mean ± SD. Initial values were normalized before injection of MβCD. E. Raman spectra acquired in the highlighted areas (colored dots) in the bottom panels of A, B and C (glass substrate in yellow, SLM on glass in orange, MWCNTs on glass in green and SLM above MWCNTs in blue). Note that the spectra of MWCNTs with (blue spectrum) and without (green spectrum) SLMs were vertically shifted for illustrative purpose. The reference spectrum of lipids (red spectrum) was acquired on a many-layer membranes sample (MLMs, not shown) in order to minimize Raman signal from the underlying glass surface.

50 mW, bandwidth 1 MHz) was used as excitation source. The beam was focused on the sample by a 100× air objective (NA 0.8, EC EpiPlan, Zeiss) resulting in a diameter of laser spot of about 0.5 μm. A 532 nm RazorEdge Dichroic™ laser-flat beam-splitter and a 532 nm RazorEdge® ultra-steep long-pass edge filter were used to direct the light into microscope and cut Rayleigh scattered light, respectively. The laser power on the sample was controlled by the neutral density filter (Thorlabs) and kept at 100 μW. The acquisition time in all experiments was 60 s. All Raman measurements and analysis were performed by CNR-IOM (TASC Laboratory, Basovizza, Trieste, Italy).

Primary cultures and cell treatment

Hippocampal neurons were obtained from neonatal rats as previously reported.[15] Cells were plated on poly-L-ornithine-coated (Sigma Aldrich) or on MWCNT-coated glass coverslips and incubated at 37 °C, 5% CO_2 in culture medium. Cultured cells were used for experiments either at 8 to 10 and 18 to 21 days in vitro (DIV). To deplete cholesterol from neuronal membranes, cultures were incubated with 1 mM MβCD (Sigma Aldrich) for 1 h at 37 °C.[30] MβCD is a cyclic glucose oligomer with a hydrophobic cavity that is able to bind lipids (especially cholesterol) and make them water-soluble[32] and is commonly used to deplete membrane cholesterol acutely from both leaflets of the bilayer.[33]

Electrophysiology

Patch-clamp, whole cell recordings were obtained with glass micropipettes with a resistance of 4 to 8 MΩ. The intracellular pipette solution was the following (mM): 120 K gluconate, 20 KCl, 10 HEPES, 10 EGTA, 2 $MgCl_2$, 2 Na_2ATP, pH 7.3. The external standard saline solution contained (mM): 150 NaCl, 4 KCl, 1 $MgCl_2$, 2 $CaCl_2$, 10 HEPES, 10 glucose, pH 7.4. All recordings were performed at RT. Cells were voltage clamped at a holding potential set at −56 mV (not corrected for the liquid junction potential, calculated to be 13.7 mV at 20 °C). The uncompensated series resistance had values <8 MΩ. Miniature post-synaptic currents (mPSCs) were recorded in the presence of 1 μM fast-Na^+ channel blocker Tetrodotoxin (TTX; Latoxan). In order to block voltage-gated calcium channels we added 3 mM $CoCl_2$ to the external solution. Data were collected using a Multiclamp 700A Amplifier (Molecular Devices, US), and

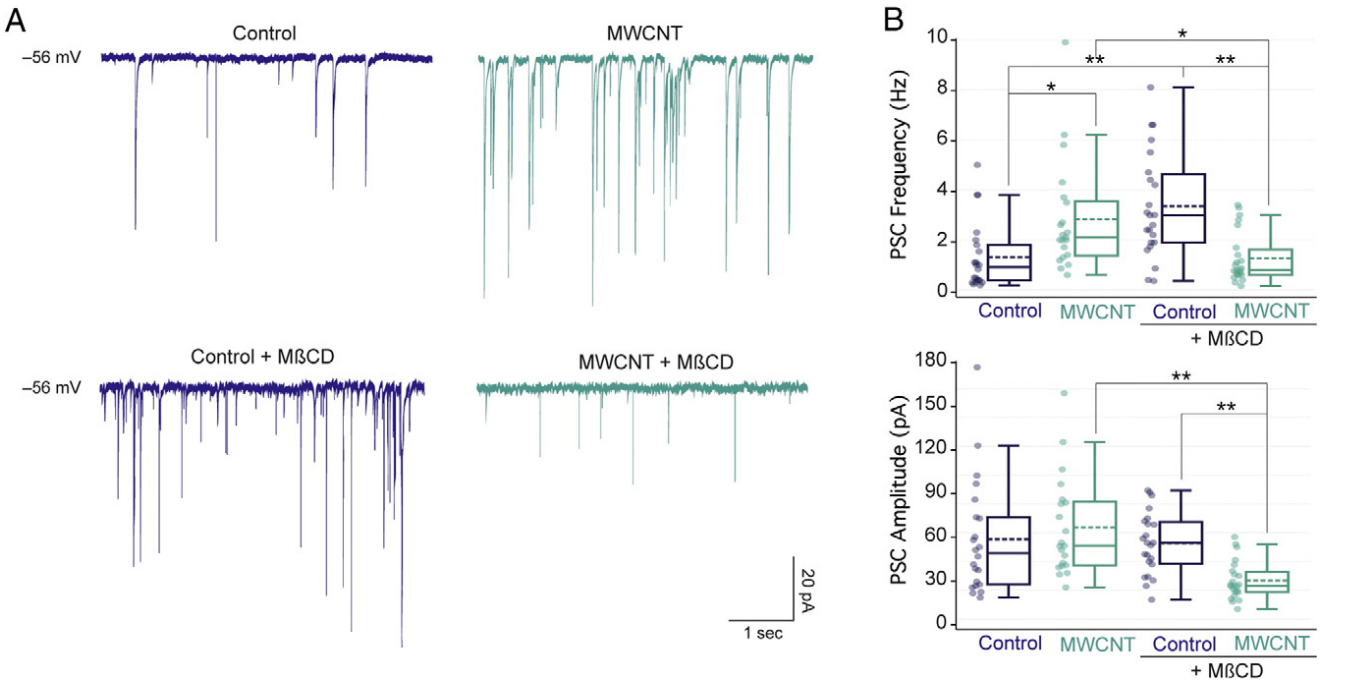

Figure 2. Cholesterol removal by MβCD application in hippocampal cultures. **(A)** Representative traces of spontaneous synaptic activity in control (left) and MWCNT (right) neurons before (top) and after (bottom) MβCD application. **(B)** Box plots summarize pooled data of PSC frequencies (top) and amplitudes (bottom) recorded from control and MWCNTs neurons prior and after MβCD. Note the higher PSC frequency displayed by MWCNT neurons in standard saline and the opposite effects brought about by MβCD in control and MWCNTs.

analyzed using either Clampfit 10.3 (Molecular Devices) or Axograph (Axograph Scientific). Glutamate AMPA-receptor and $GABA_A$-receptor mediated post synaptic currents (PSCs) were isolated offline by building two templates with different kinetic parameters: respectively 0.1 ms rise-time; 3 and 30 ms decay time constant (τ); 10 and 100 ms template length. Previous work[12,15] indicated that in our experimental conditions, the vast majority of fast-decaying ($\tau < 5$ ms) PSCs are mediated by the glutamate AMPA-receptor type; while the slow-decaying ($\tau > 20$ ms) PSCs are mediated by the $GABA_A$-receptor type.

Immunocytochemistry

Cultures were fixed in 4% formaldehyde (prepared from fresh paraformaldehyde) in PBS for 20 min, permeabilized with 0.3% Triton-X-100 and subsequently incubated with primary antibodies for 30 min at RT and after washing in PBS incubated with secondary antibodies for 45 min. Cultures were then mounted with the *Vectashield* (Vector Laboratories) on 1 mm thick microscope glass slides. To visualize neurons and lipid rafts we used the following: rabbit anti-β-tubulin III primary antibody (Sigma T2200, 1:250 dilution) and Alexa 594 goat anti rabbit secondary antibody (Invitrogen, 1:500); Alexa 488 Cholera Toxin subunit-B (CT-B) 1:200 (Molecular Probes) and DAPI, 1:1000 (Invitrogen).

To visualize glutamatergic synapses we co-label neurons with the guinea pig anti-vesicular glutamate transporter 1 (VGLUT1; Millipore, 1:2000) and β-tubulin III (Sigma, 1:250) primary antibodies and Alexa 594 goat anti rabbit (Invitrogen, 1:500) and Alexa 488 goat anti guinea-pig (Invitrogen, 1:500) as secondary antibodies. All images were acquired using an inverted confocal Microscope (Leica Microsystems GmbH, Wetzlar, Germany; 40× oil immersion objective, 1.25 NA).

To quantify VGLUT1 puncta and lipid rafts, n = 20 ± 10 z-stacks (acquired every 0.4 μm) were taken from n = 10 randomly selected fields (240 μm × 240 μm) per coverslip (n = 30, 3 culture series in Control and MWCNTs). To quantify lipid rafts, we selected the CT-B positive objects (<5 μm^3) co-localized to the β-tubulin III positive areas. For each image, the volumes of CT-B positive objects were normalized to the β-tubulin III positive volumes. To quantify VGLUT1 puncta, we selected only VGLUT1-positive puncta (<2 μm3) co-localized to the β-tubulin III positive areas and puncta were normalized to the β-tubulin III positive volumes. Images were analyzed using the Volocity software (Perkin Elmer).

For the filipin labeling of membrane cholesterols[34] cells were fixed, rinsed in PBS and directly incubated for 2 h at RT with 0.05 mg/mL filipin (Sigm-F9765) then mounted and imaged with an Epifluorescence Microscope (DM 6000, Leica; 40× objective, 0.75 NA). We collected 10 fields (355 μm × 265 μm) per coverslip (n = 30, 3 culture series for control and MWCNT) with the same CCD exposure time and illumination intensity. For each image the background fluorescence was subtracted and the fluorescence of four equal squared areas was determined. The average of these four values represented the fluorescence intensity value for each image.[34] Fluorescence signals were quantified using ImageJ software (http://rsb.info.nih.gov/ij/).

Data analysis

All values from samples subjected to the same experimental protocols were pooled together and expressed as mean ± SEM

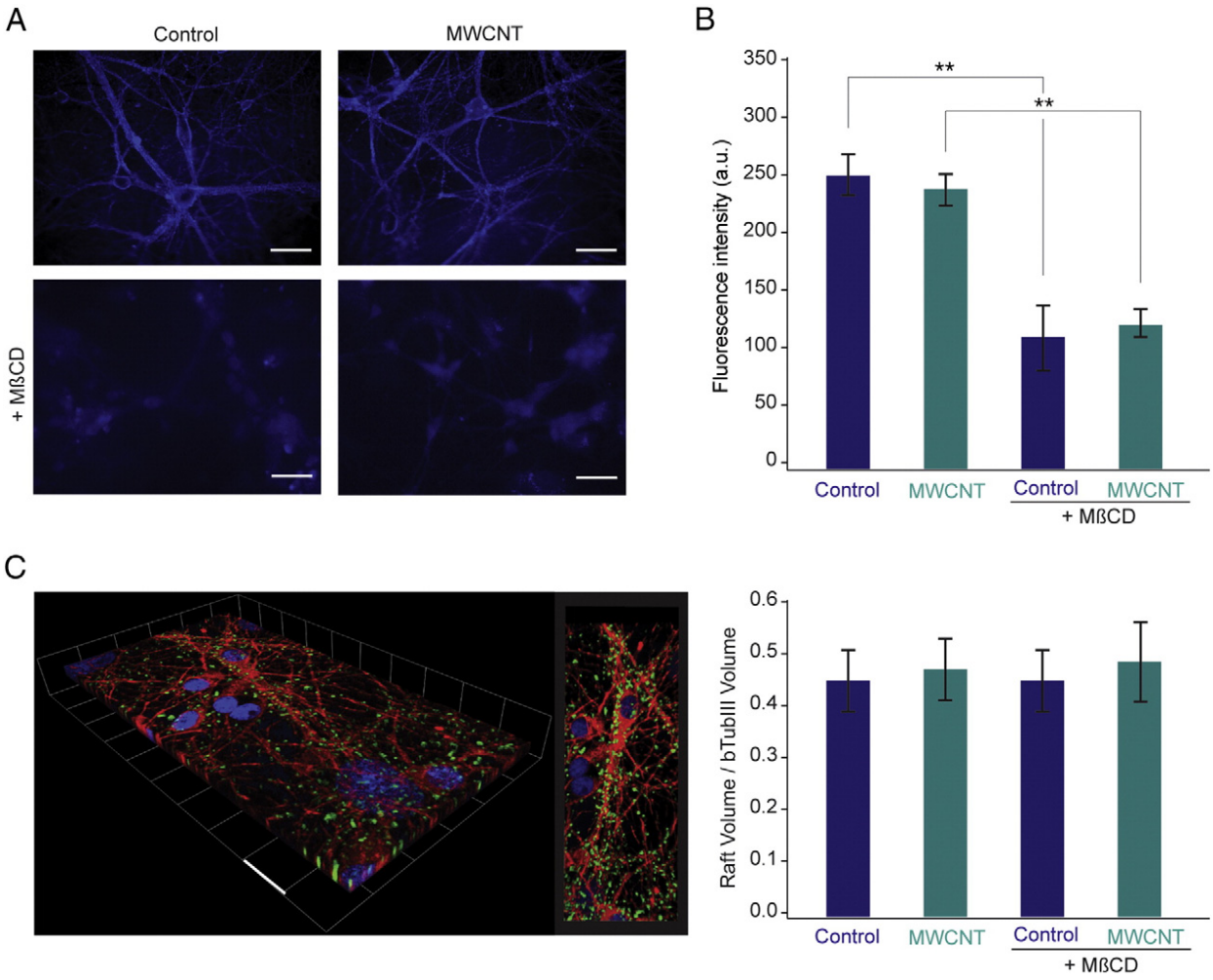

Figure 3. MβCD efficiently removed membrane cholesterol without disrupting lipid rafts. **(A)** Fluorescence micrographs of control and MWCNT hippocampal cells labeled by filipin prior (top) and after (bottom) MβCD treatment. Scale bars 50 μm. **(B)** Bar plot of filipin-derived fluorescence intensity in cultured neurons, note the similar values between control and MWCNT conditions and the comparable reduction upon cholesterol depletion by MβCD. **(C)** Left, 3D and 2D confocal reconstructions of hippocampal cultures immune-labeled with the neuronal marker β-tubulin III (in red) and the lipid-raft marker CT-B (in green), in blue DAPI labeling for nuclei. Scale bars 15 μm. Right, bar plot quantifies the CT-B volume in respect to the β-tubulin III one, note that no differences were observed between controls and MWCNTs before and after the MβCD treatment.

(with n = number of cells, unless otherwise indicated). A statistically significant difference between data sets was assessed by one-way and two-way ANOVA, followed by Bonferroni test. Statistical significance was determined at $P < 0.05$, unless otherwise indicated. Box plots were created using Plotly software (https://plot.ly).

Ethical statement

All animal procedures were conducted in accordance with the National Institutes of Health and with international and institutional standards for the care and use of animals in research, and after consulting with a veterinarian. All experiments were performed in accordance with European Union (EU) guidelines (2010/63/UE) and Italian law (decree 26/14) and were approved by the local authority veterinary service and by our institutional (SISSA-ISAS) ethical committee. All efforts to minimize animal suffering and to reduce the number of animals used were made. Animal use was approved by the Italian Ministry of Health, in agreement with the EU Recommendation 2007/526/CE (http://eur-lex.europa.eu/legal-content/EN/TXT/?uri=uriserv:OJ.L_.2007.197.01.0001.01.ENG&toc=OJ:L:2007:197:TOC).

Results

Artificial lipid membranes interfaced to MWCNTs

In the first set of experiments, we investigated by AFM the appearance of artificial lipid membranes (SLM)[35] interfaced to control substrates or to MWCNTs (Figure 1, *B*; see also[15]). SLM islands grown on control glass coverslips (Figure 1, *A*) and on MWCNTs (Figure 1, *C*) displayed similar morphology (SLM surface roughness 0.38 nm and 0.44 nm when formed on glass and on MWCNT, respectively, Figure 1, *A-C*), however AFM revealed the ability of MWCNTs to pierce membrane layers through SLM entire thickness (Figure 1, *C*, white arrows). These cross interactions induced the occasional appearance of localized

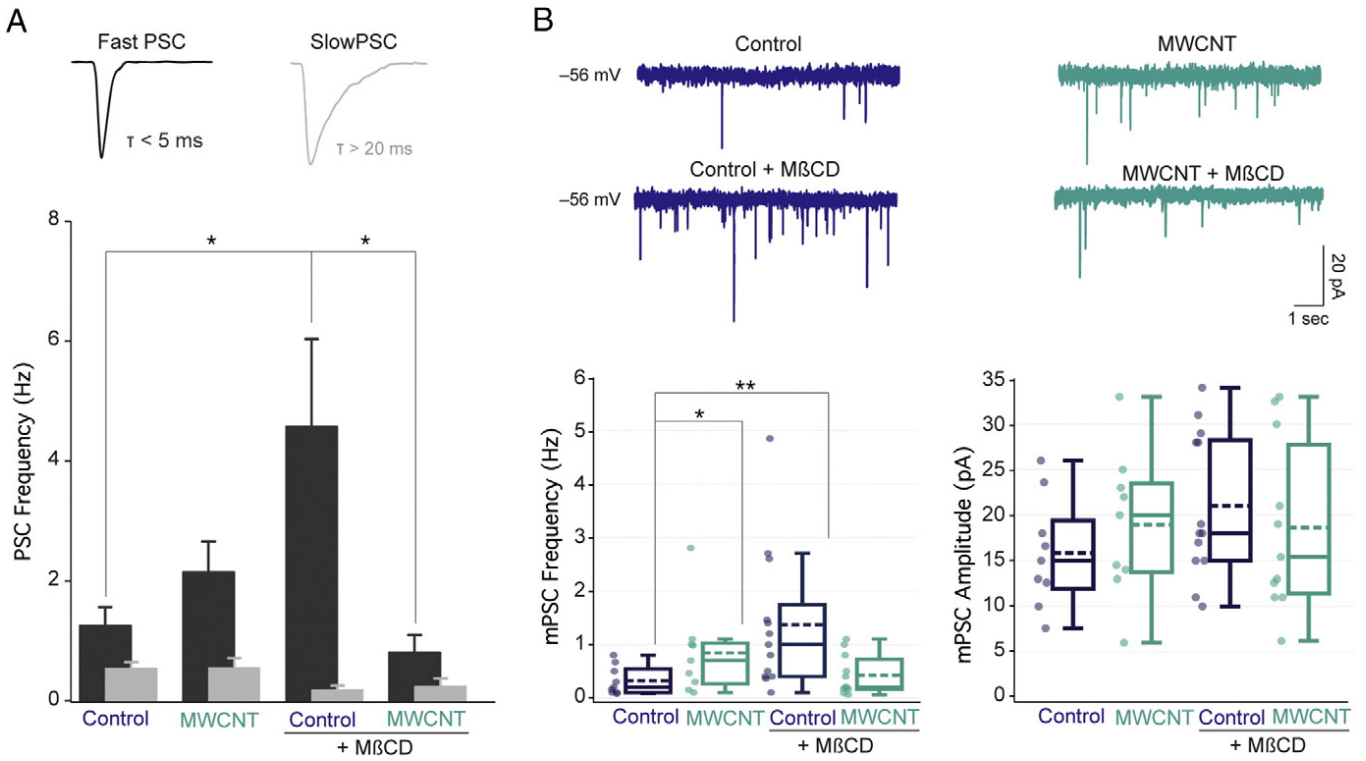

Figure 4. Depletion of cholesterol with MβCD alters fast PSCs occurrence. **(A)** Offline differential analysis of PSC decays (τ) identifies fast and slow events (insets average tracings from the same neurons as in Figure 2, *A*) both in control and MWCNTs. Bar plot summarizes the frequency of fast and slow PSCs in controls and MWCNTs. **(B)** Spontaneous synaptic activity recorded in the presence of TTX; controls and MWCNT mPSC frequency and amplitudes are summarized in the box plots before and after MβCD treatment. Note that mPSC amplitude values are unaffected.

areas where several layers of SLM piled on the surface, due to MWCNTs, a condition rarely observed in controls (Figure 1, *A* and *C*, compare the height profiles).

In Figure 1, *E* the reference Raman spectrum of lipids (in red) is plotted and is characterized by peaks associated with C–N stretch (715 cm^{-1}), C–C stretch (1090 cm^{-1}), CH_2 deformation (1305 cm^{-1} and 1440 cm^{-1}), and C = C stretch (1655 cm^{-1}) vibrations.[36,37] The Raman spectrum of MWCNTs alone on glass substrate (Figure 1, *E*, in green) shows two broad peaks centered at 1350 cm^{-1} and 1590 cm^{-1} that are commonly assigned to the presence of disorder in graphitic materials and to the tangential vibrations of the carbon atoms, respectively.[38,39] The distinguishable shoulder at 1620 cm^{-1} is a double-resonance Raman feature induced by disorder, defects or ion intercalation between the graphitic walls.[38] When SLMs are deposited on glass substrate (Figure 1, *E*, in orange), the strong contribution of the underneath glass is evident, however the lipid peak at 1440 cm^{-1} (CH_2 deformation) is distinguishable in spite of the lower amount of lipids forming the SLM. In SLM on MWCNTs, the characteristic two peaks at 1350 cm^{-1} and 1590 cm^{-1} present on the tubular structures protruding from SLMs (depicted in Figure 1, *C*, bottom panel) confirm that they are MWCNTs, as suggested by the AFM morphology. Interestingly, in this spectrum (in blue in Figure 1, *E*), the peak at 715 cm^{-1} is evident as well. This may be due to the larger laser spot diameter (about 500 nm) compared with MWCNTs (50-250 nm), resulting in a contribution of the surrounding SLBs in the Raman spectrum. Note that broad peaks observed at 400 cm^{-1} and 900 cm^{-1} are due to a photoluminescence in glass substrate, a well-known phenomenon when using a 532 nm excitation wavelength.[40]

Next, we incorporated a fluorescent lipid to SLMs (see Methods) and we compared the efficacy of MβCD treatment (500 μM; 1 h; used to bind and extract cholesterol from the membrane[32,33]) in depleting cholesterol in control and MWCNT SLMs. The plot in Figure 1, *D* summarizes the decay in fluorescence monitored during MβCD application. In order to have comparable measurements, we sampled single SLM layers in both groups. In MWCNTs, SLM lipids appeared more stabilized, as indicated by their significantly slower depletion with respect to controls (decay time constant (τ) average values: $\tau_1 = 1.09 \pm 0.02$ s and $\tau_2 = 39.02 \pm 9.83$ s for control SLMs; $\tau_1 = 12.02 \pm 0.15$ s and $\tau_2 = 63.67 \pm 6.92$ s for SLM deposited on MWCNTs; $P < 0.01$ for τ_1 values; $P < 0.05$ for τ_2; n = 3 different samples each group).

Such results suggest that interfacing with MWCNTs might affect lipid, in particular cholesterol, dynamics in biological membranes.

Acute cholesterol removal in control and MWCNTs hippocampal cultures

To further explore the potential role of MWCNTs in membrane lipid dynamics when interfacing living cells, and in particular in altering cholesterol homeostasis in neurons, we cultured hippocampal cells on control substrates or on meshworks of MWCNTs

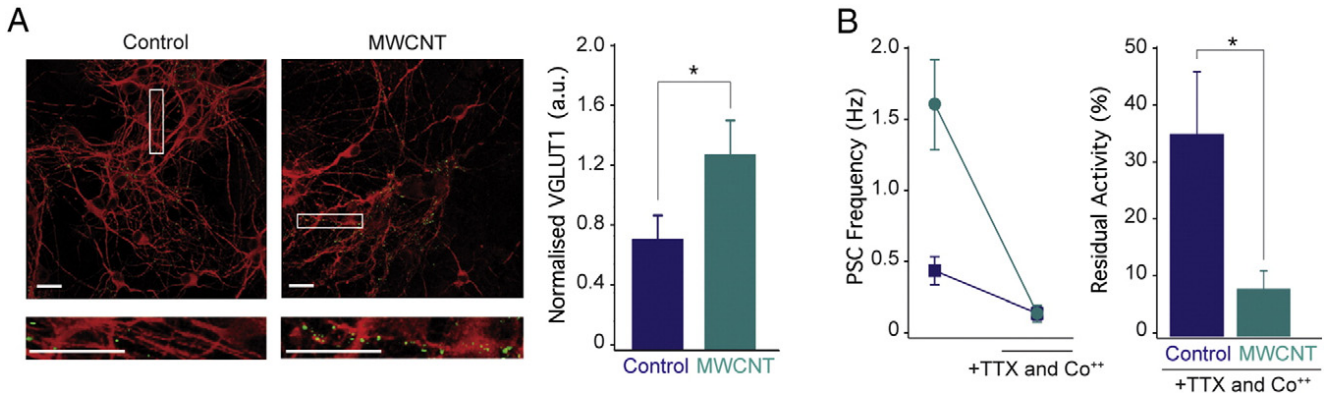

Figure 5. Co-localization of VGLUT1 and β-tubulin III immunostaining in control and MWCNT hippocampal cultures. **(A)** Right, confocal images of hippocampal neurons at 8-10 DIV stained for β-tubulin III (in red) and VGLUT1 (in green). In the insets high magnifications are shown corresponding to the white square areas. Scale bars 20 μm. Left, bar plot summarizes the quantification of VGLUT1 positive puncta, significantly higher in MWCNTs. **(B)** Right, summary graph of the PSCs frequency in standard saline solution and after TTX and Co^{++} application in controls (squares) and MWCNTs (circles). Right, bar plot summarizes the residual activity, in respect to standard saline, after application of TTX and Co^{++}.

(control and MWCNT, respectively). We monitored the synaptic networks before and after cell exposure to MβCD (1 mM; 1 h)[30] by voltage clamp whole-cell recordings, comparing Control neurons with MWCNT ones. The first set of recordings was performed at 8-10 DIV, since at this ages neuronal circuits were reported to display a significant increase in synaptic activity when cultured on MWCNTs.[12,14,15] Figure 2 illustrates this characteristic enhancement in spontaneous synaptic activity brought about by MWCNTs and expressed as a significant ($P < 0.05$) increase (by 133%) in the post synaptic current (PSC) frequency (box plot in Figure 2, *B*, top; control, n = 22; MWCNT, n = 21), leaving PSC amplitudes unperturbed (box plot in Figure 2, *B*, bottom).[12,14,15] Sample tracings of control and MWCNT recordings are shown in Figure 2, *A* (top row).

Exposure to MβCD did not affect neuronal viability and the overall integrity of membranes as estimated by comparing the input resistance values of the recorded neurons before and after treatment (for control: 655 ± 73 MΩ, n = 21, and 694 ± 167 MΩ, n = 23, $P = 0.834$; for MWCNT 487 ± 37 MΩ, n = 22, and 625 ± 90 MΩ, n = 23, $P = 0.117$; prior and after MβCD incubation, respectively) and the values for the cell capacitance (for control: 75 ± 32 pF, n = 21, and 80 ± 7 pF, n = 23, $P = 0.536$; for MWCNT 92 ± 8 pF, n = 22, and 74 ± 7 pF, n = 23,$P = 0.120$; prior and after MβCD incubation, respectively).

Synaptic cholesterol balances spontaneous and evoked neurotransmission by inhibiting spontaneous vesicle turnover and, conversely, by promoting evoked exo-endocytosis.[28] In hippocampal cultures, MβCD-mediated removal of cholesterol has been reported to result in an augmentation of spontaneous synaptic vesicle fusion and recycling.[28]

We measured synaptic activity in these two groups of cultures after cholesterol depletion and, surprisingly, addition of MβCD resulted in two macroscopic, but opposite, changes, illustrated by the sample recordings in Figure 2, *A* (bottom tracings). In control neurons MβCD treatment led to a significant ($P < 0.01$) increase (by 228%) in PSC frequency, without affecting PSC amplitude values; in MWCNTs, on the contrary, MβCD incubation induced a significant reduction in both PSC frequency (by 62%; $P < 0.05$) and PSC amplitude (by 55% $P < 0.01$; summarized in the box plots of Figure 2, *B*). Before analyzing in more details these synaptic changes (see below) we ascertain whether the tight interfacing[14] of neuronal membrane with MWCNTs modulated membrane cholesterol in cultured neurons. Figure 3, *A* shows sample micrographs of cultured neurons (control and MWCNTs) labeled with filipin, used to detect free cholesterol.[41] Cholesterol levels, as measured by filipin fluorescence intensity (see Methods) were similar in the two culture groups (summarized in Figure 3, *A* and *B*). MβCD incubation efficiently removed membrane cholesterol in both culture groups, as documented by the drop in filipin fluorescence intensity after treatments (reduced by 44% in controls and by 52%, in MWCNT, quantified in Figure 3, *B*; n = 30 fields in control and MWCNTs). We further explored the ability of MβCD incubation in altering, in the two neuronal cultures, the integrity of cholesterol/sphingolipid micro-domains (i.e. lipid rafts), expressed by cultured hippocampal neurons.[42] We visualized lipid rafts by double labeling neurons with the raft marker CT-B[43] and the neuronal marker β-tubulin III (Figure 3, *C*). We calculated by confocal analysis the CT-B volume relative to the β-tubulin III one (see Methods) to quantify lipid rafts before and after MβCD incubation. In Figure 3, *C* the bar plot shows the comparable values of the CT-B/β-tubulin III volumes in the two cultures groups, and that apparently MβCD treatment did not deplete CT-B domains in control and MWCNTs. Thus, the used incubation protocol for cholesterol depletion efficiently reduces free cholesterol from neuronal membranes in both cultures, without affecting the integrity of cholesterol-enriched structures, such as lipid rafts.

Despite the similar effects with respect to cholesterol, MβCD affects in an opposite manner PSCs frequency in control and MWCNTs, suggesting the presence of presynaptic terminals where vesicle release is differentially regulated by cholesterol.[44]

Effects of acute cholesterol depletion on glutamatergic synapses

Spontaneous synaptic activity in our recording conditions[15] was manifested as inward currents made up by a mixed population of inhibitory ($GABA_A$-receptor mediated) and

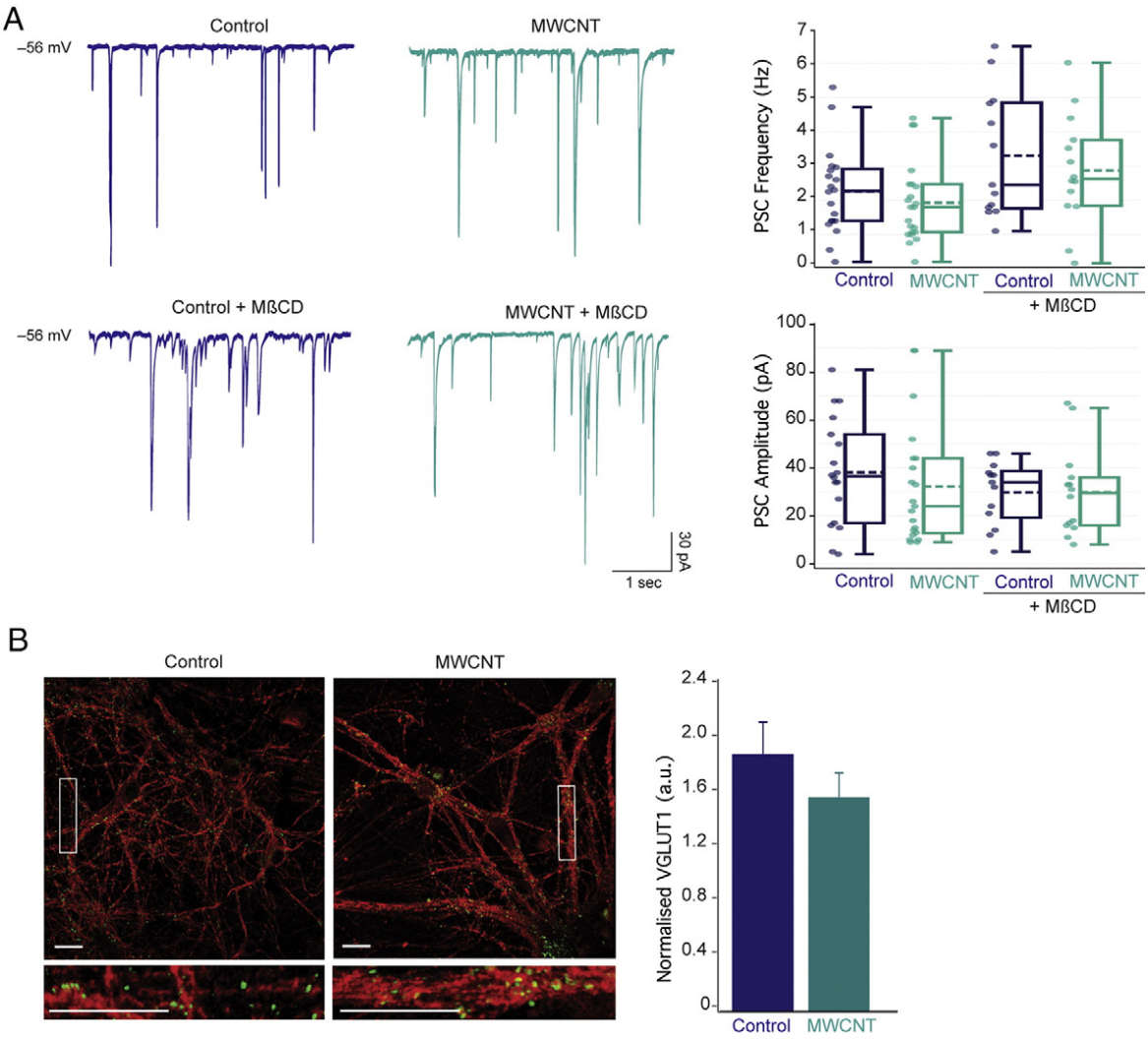

Figure 6. Controls and MWCNTs spontaneous synaptic activity in long-term cultures. **(A)** Left, representative recordings of synaptic activity at 21 DIV in controls and MWCNTs before (top) and after (bottom) MβCD. Box plots (right) summarize the values of PSCs frequency (top) and amplitude (bottom); note the similar values measured in all conditions. **(B)** Confocal micrographs of cultures labeled by β-tubulin III (in red) and VGLUT1 (in green). In the insets high magnifications are shown corresponding to the white square areas. In long-term cultures controls and MWCNTs neurons display similar amount of VGLUT1 puncta, summarized in the bar plot (right). Scale bar, 20 μm.

excitatory (glutamate AMPA-receptor mediated) PSCs, characterized by different kinetics.[15] To gain insights into the MβCD regulation of synaptic activity in the two culture groups, we randomly selected a subset of control (n = 7) and MWCNT (n = 7) neurons to perform offline differential analysis of PSCs kinetic, in particular of their decay.[12,45] By means of their kinetic properties we identified slow decaying PSCs (τ = 22.0 ± 2.0 ms in control; τ = 21.2 ± 1.1 ms in MWCNTs; Figure 4, *A* top right) corresponding to $GABA_A$ receptor-mediated events from fast decaying (τ = 3.1 ± 0.3 ms in control; τ = 3.4 ± 0.4 ms in MWCNTs; Figure 4, *A* top left) events usually corresponding to AMPA-receptor mediated currents.[12,15] The frequency of fast PSCs was upregulated by MβCD in control, but strongly reduced in MWCNT exposed to similar treatments (plot in Figure 4, *A*). Notably, slow PSC frequencies were similarly (and only slightly) reduced in both culture groups when exposed to MβCD.

Cholesterol depletion in neurons is known to increase the rate of spontaneous transmission but it impairs evoked neurotransmission[28,29] and synapses usually segregate, at the presynaptic terminals, the distinct vesicle pools responsible for spontaneous or evoked release.[29,46]

We characterized the effects of cholesterol depletion on spontaneous release by recording miniature PSCs (mPSCs) in the presence of TTX (1 μM). mPSCs, in dissociated hippocampal cultures at this age, comprise virtually only fast events (τ = 4.5 ± 0.6 ms in control, n = 9, and τ = 5 ± 0.9 ms in MWCNT, n = 9; Figure 4, *B*, top tracings) thus representing only excitatory mPSCs.[15] MWCNT mPSCs display, in standard conditions, a significantly ($P < 0.05$) higher frequency (Figure 4, *B*), due to the synaptogenic impact of MWCNTs.[15] The increased number of synapses is further supported in Figure 5, *A* where VGLUT1 labeled presynaptic boutons in β-tubulin III identified neuronal bodies and dendrites, allowed to quantify VGLUT1-positive

puncta, indicating a significant ($P < 0.05$) increase in their density in MWCNT neurons when compared to control ones. MβCD incubation significantly ($P < 0.05$) increased fast mPSCs frequency in control while in MWCNT the frequency of fast minies was only slightly, but not significantly, reduced (plot in Figure 4, *B*); to note, mPSCs amplitudes were not affected by any treatment (box plot in Figure 4, *B*) indicating that the properties of postsynaptic glutamate receptors were not altered by these manipulations.[28]

These results suggest that control and MWCNTs glutamatergic synapses express different release machineries. Namely, control glutamatergic synapses are dominated by spontaneous fusions, on the contrary MWCNT ones preferentially release neurotransmitter in response to action potentials.

To address the expression of heterogeneous populations of presynaptic vesicles, and the different partitioning of synaptic vesicles between the two pools, we estimate the residual activity when PSCs were recorded prior and after the application of TTX and Co^{++} (3 mM; n = 7 control and n = 7 MWCNTs). The block of voltage-gated Ca^{++}-channels impairs the fusion of calcium-dependent vesicles,[47] isolating the calcium-independent "resting pool",[48] mostly involved in spontaneous neurotransmission, namely the component increased by cholesterol removal.[28] In the presence of Co^{++} mPSCs displayed a similar frequency in control and MWCNTs, thus the residual activity in the presence of Ca^{++} channels block, in MWCNTs was significantly smaller ($P < 0.05$; plots in Figure 5, *B*).

This different ratio suggests that synapses in control cultures rely for their basal activity mostly on low calcium-dependent vesicle release.[25]

The effects of acute cholesterol removal in control and MWCNT hippocampal cultures at later stages of synaptic development

Action potential evoked and spontaneous neurotransmitter release modalities involve different molecular machineries regulating segregated vesicle pools at the presynaptic site. Distinct forms of neurotransmission, involving these two modes of release, were reported to change during hippocampal synaptic development in vitro.[49] Immature synapses display high levels of spontaneous release with respect to more mature neurons where evoked release became particularly strong.[49] Indeed, in our experiments the acute removal of cholesterol unmasked an opposite vesicle homeostasis across control and MWCNTs, hinting at a tuning of synaptic maturation.[49] To investigate whether the different synaptic responses to MβCD between control and MWCNTs were related to a transient unbalance toward more mature release phenotype in the newly formed MWCNT synapses, we extended our investigation to neurons in control (n = 20) or interfaced to MWCNTs (n = 22) recorded at 18-21 DIV. In older cultures, the frequency of MWCNT PSCs did not differ from that measured at earlier stages of development under the same growth conditions (compare plots in Figure 2, *B* and in Figure 6, *A*), and was similar to the value measured in aged-matched control neurons, which conversely increased the frequency of PSCs upon in vitro development. Figure 6, *A* shows sample recordings (left) with the pooled values for PSC frequency and amplitude summarized in the box plots (right). The comparable control and MWCNT synaptic activity, suggested by the similar PSC frequency, was supported by immunofluorescence quantification of VGLUT1-positive puncta. As shown in Figure 6, *B* we detected a similar density of positive puncta between the two culture groups. Also in these measures, MWCNT values were equal to those detected at earlier stages of development (compare plots in Figures 5, *A* and 6, *B*), while in control an age dependent increase in puncta was evident. In accordance to these measures, Figure S1A shows that frequency and amplitude of mPSCs did not differ when comparing control and MWCNT at 18-21 DIV.

At 18-21 DIV incubating with MβCD induced a slight and non-significant increase (Figure 6A) in the frequency of PSCs in both cultures groups, without altering PSCs amplitudes, suggesting that in vitro aging leads to an overall balance between synapses expressing different release modes.[49] During the development of hippocampal neurons in culture, the levels of membrane cholesterol usually increase[50] thus we tested the ability of MβCD incubation in depleting cholesterol in 18-21 DIV neurons. Supplemental Figure S1, *B* shows the reduction in filipin fluorescence after MβCD incubation, supporting the efficacy of such a treatment.

These results strengthen the hypothesis that MWCNTs boost the overall network maturation, in terms of number of synapses and efficacy,[15] but in the long-term these effects reach a steady state, probably due to the maximal connectivity homeostatically set by the size of any given neuronal network.[51]

Discussion

Carbon nanotubes are increasingly incorporated in the development of novel two-dimensional biomaterials designed to interface tissue reconstruction and signaling.[16,52] In material science, MWCNTs are adopted in composites to strengthen biomaterial mechanical properties, electrical conductivity or microenvironment-defining moieties.[53] However, MWCNTs are not inert and promote synaptogenesis when interfaced to cultured neurons.[15,54] In the present study we used dissociated cultures to investigate MWCNT ability to alter membrane lipid homeostasis to pinpoint the earliest mechanisms that may contribute in modulating synaptic activity. We also characterized to what extent the MWCNTs driven synaptic enhancement is maintained throughout long-term network development.

The principal finding of the present report is that two-dimensional MWCNT interfaces do not alter the homeostasis of membrane lipids, in particular cholesterol, in neurons. In fact, neurons cultured interfaced to MWCNTs, display a similar membrane cholesterol distribution and, when we used a traditional tool to remove membrane cholesterol, MβCD,[26] this treatment was as effective as in control cells. This result differs from our preliminary observations on artificial lipid membranes, excluding, in living neurons, a decrease mobility of the lipid molecules via preferential interactions with the carbon nanotubes.[21] In this work we confirm the notion that MWCNT microenvironment provide cues instructing the construction of more synapses[15,54] documented by the increase in PSCs frequency, in mPSCs and in VGLUT1-positive labeling; the

latter showing, for the first time directly by confocal microscopy, the higher density of glutamatergic synapses.[15]

The present data show that, in both culture groups, the treatment used to remove cholesterol did not affect cell viability, as sustained by the values of cell input resistance and membrane capacitance.[55,56] In addition, membrane micro-domains enriched in cholesterol such as lipid rafts,[57] involved in the regulation of ionotropic glutamate receptor function,[42] displayed a similar distribution in control and MWCNT neurons when investigated by immunofluorescence labeling and confocal microscopy[58]; these structures where not altered by MβCD treatments and indeed, in both cultures groups, miniature events' analysis suggested the absence of major post synaptic changes due to cholesterol removal.[28]

However, we found that at 8-10 DIV, release at glutamatergic synapses in control and MWCNTs was regulated in an opposite manner by cholesterol reduction.

To understand the reason for the observed difference, we examined the main variable that might conceivably affect release tuning by cholesterol. We had already excluded the possibility of differences in membrane cholesterol distribution and depletion. We thus turned our attention to pre-synaptic process that may be regulated by cholesterol. Removal of cholesterol variably affects spontaneous or evoked neurotransmitter release in cultured neurons, improving spontaneous vesicle fusion and decreasing evoked vesicle recycling.[28]

We thus hypothesized that control synapses display a higher relative amount of spontaneous vesicle pools with respect to MWCNT ones.

In the presence of TTX we observed that in control conditions the frequency of mPSCs was still affected by MβCD, whereas no changes occurred in MWCNT neurons. Our hypothesis was further supported by the block of voltage dependent Ca^{++}-channels by Co^{++} applications.[59] This condition indicated the presence of an opposite ratio between high and low Ca^{++}-dependent vesicle pools in control and MWCNT presynaptic glutamatergic terminals.

Recent reports have shown that the maturation of neurotransmission is accompanied by changes in pre-synaptic release modes; in particular spontaneous vesicle pools are predominant on evoked ones during early stages of development, and these two populations are gradually rebalanced during the synaptic maturation process.[49,60]

It is tempting to speculate that MWCNTs accelerate synaptic network maturation, improving synapse formation and favoring more mature release modes, an effect that is homeostatically regulated upon prolonged interfacing. In fact, in our experiments, control and MWCNTs displayed functional and anatomical similarities after three weeks of growth. We cannot distinguish whether this was due to a progressive shielding of the MWCNTs by extracellular matrix proteins,[61] thus changing the nano-bio interface, or rather by the homeostatic regulation of cultured neuronal networks, constraining the maximal number of synapses[51] and their level of maturation in vitro.

In conclusion, the main finding of the present study is that MWCNTs when used in interfacing neurons can regulate synapse formation and function in a dynamic manner, tuning exquisite neurobiological mechanisms, such as neuronal maturation.[62] This ability is however controlled and limited by the physiological maturation of the synaptic circuit. This functional integration of the MWCNTs within the newly formed neuronal network might represent an attractive property in designing interfaces for neuronal repair.

Brain interfaces of the future require the application of nanomaterial-related technologies to target some of the current ambitions in interfacing neurons: improving the stability, flexibility and durability of the interface, improving the efficacy of the charge transfer to and from neurons, and minimizing the reactivity in the surrounding tissue.[63] The aim is that of realizing high resolution and minimally invasive interfaces between recording probes and biological systems,[64] able to map brain activity and deliver precise stimuli, to interface the brain to an external device or to facilitate recovery of function via engaging neuronal plasticity processes,[65] eventually interfacing the brain to the spinal cord, to regain motor function after spinal cord lesions.[66] In this arena, conductive nano-materials such as carbon nanotubes may be the adequate response to reach miniaturization of the electrodes and neuronal-scale stimulation and recordings, leading to an improved merging between electronic and biosystems.[67] We recently reported low tissue reaction upon implantation in vivo of unmodified MWCNT microsystems, suggesting a biocompatibility crucial to further design of miniaturized platforms based on entirely new materials.[17]

Appendix A. Supplementary data

Supplementary data to this article can be found online at http://dx.doi.org/10.1016/j.nano.2017.01.020.

References

1. Lutolf MP, Hubbell JA. Synthetic biomaterials as instructive extracellular microenvironments for morphogenesis in tissue engineering. *Nat Biotechnol* 2005;**23**:47-55.
2. Dvir T, Timko BP, Kohane DS, Langer R. Nanotechnological strategies for engineering complex tissues. *Nat Nanotechnol* 2011;**6**:13-22.
3. Shao Y, Fu J. Integrated micro/nanoengineered functional biomaterials for cell mechanics and mechanobiology: a materials perspective. *Adv Mater* 2014;**26**:1494-533.
4. Battiston KG, Cheung JW, Jain D, Santerre JP. Biomaterials in co-culture systems: towards optimizing tissue integration and cell signaling within scaffolds. *Biomaterials* 2014;**35**:4465-76.
5. Zhu W, O'Brien C, O'Brien JR, Zhang LG. 3D nano/microfabrication techniques and nanobiomaterials for neural tissue regeneration. *Nanomedicine (Lond)* 2014;**9**:859-75.
6. Seidlits SK, Lee JY, Schmidt CE. Nanostructured scaffolds for neural applications. *Nanomedicine (Lond)* 2008;**3**:183-99.
7. Tian B, Liu J, Dvir T, Jin L, Tsui JH, Qing Q, et al. Macroporous nanowire nanoelectronic scaffolds for synthetic tissues. *Nat Mater* 2012;**11**:986-94.
8. Kotov NA, Winter JO, Clements IP, Jan E, Timko EP, Campidelli S, et al. Nanomaterials for neural interfaces. *Adv Mater* 2009;**21**:3970-4004.
9. Marchesan S, Melchionna M, Prato M. Wire up on carbon nanostructures! How to play a winning game. *ACS Nano* 2015;**9**:9441-50.
10. Mattson MP, Haddon RC, Rao AM. Molecular functionalization of carbon nanotubes and use as substrates for neuronal growth. *J Mol Neurosci* 2000;**14**:175-82.

11. Fabbro A, Villari A, Laishram J, Scaini D, Toma FM, Turco A, et al. Spinal cord explants use carbon nanotube interfaces to enhance neurite outgrowth and to fortify synaptic inputs. *ACS Nano* 2012;**6**:2041-55.
12. Lovat V, Pantarotto D, Lagostena L, Cacciari B, Grandolfo M, Righi M, et al. Carbon nanotube substrates boost neuronal electrical signaling. *Nano Lett* 2005;**5**:1107-10.
13. Mazzatenta A, Giugliano M, Campidelli S, Gambazzi L, Businaro L, Markram H, et al. Interfacing neurons with carbon nanotubes: electrical signal transfer and synaptic stimulation in cultured brain circuits. *J Neurosci* 2007;**27**:6931-6.
14. Cellot G, Cilia E, Cipollone S, Rancic V, Sucapane A, Giordani S, et al. Carbon nanotubes might improve neuronal performance by favouring electrical shortcuts. *Nat Nanotechnol* 2009;**4**:126-33.
15. Cellot G, Toma FM, Varley ZK, Laishram J, Villari A, Quintana M, et al. Carbon nanotube scaffolds tune synaptic strength in cultured neural circuits: novel frontiers in nanomaterial-tissue interactions. *J Neurosci* 2011;**31**:12945-53.
16. Fabbro A, Prato M, Ballerini L. Carbon nanotubes in neuroregeneration and repair. *Adv Drug Deliv Rev* 2013;**65**(15):2034-44.
17. Usmani S, Aurand ER, Medelin M, Fabbro A, Scaini D, Laishram J, et al. 3D meshes of carbon nanotubes guide functional reconnection of segregated spinal explants. *Sci Adv* 2016;**2**(7):e1600087.
18. Nel AE, Mädler L, Velegol D, Xia T, Hoek EM, Somasundaran P, et al. Understanding biophysicochemical interactions at the nano-bio interface. *Nat Mater* 2009;**8**(7):543-57.
19. Lesniak A, Salvati A, Santos-Martinez MJ, Radomski MW, Dawson KA, Åberg C. Nanoparticle adhesion to the cell membrane and its effect on nanoparticle uptake efficiency. *J Am Chem Soc* 2013;**135**(4):1438-44.
20. Wang Y, Yang Y, Yan L, Kwok SY, Li W, Wang Z, et al. Poking cells for efficient vector-free intracellular delivery. *Nat Commun* 2014;**5**:4466.
21. Khanbabaie R, Jahanshahi M. Revolutionary impact of Nanodrug delivery on neuroscience. *Curr Neuropharmacol* 2012;**10**:70-392.
22. Malarkey EB, Reyes RC, Zhao B, Haddon RC, Parpura V. Water soluble single-walled carbon nanotubes inhibit stimulated endocytosis in neurons. *Nano Lett* 2008;**8**:3538-42.
23. Aldinucci A, Turco A, Biagioli T, Toma FM, Bani D, Guasti D, et al. Carbon nanotube scaffolds instruct human dendritic cells: modulating immune responses by contacts at the nanoscale. *Nano Lett* 2013;**13**:6098-105.
24. Dayani Y, Malmstadt N. Lipid bilayers covalently anchored to carbon nanotubes. *Langmuir* 2012;**28**:8174-82.
25. Baoukina S, Monticelli L, Tieleman DP. Interaction of pristine and functionalized carbon nanotubes with lipid membranes. *J Phys Chem B* 2013;**117**:12113-23.
26. Lopez CF, Nielsen SO, Moore PB, Klein LM. Understanding nature's design for a nanosyringe. *S A* 2004;**101**:4431-4.
27. Monticelli L, Salonen E, Chun Ke P, Vattulainen I. Effects of carbon nanoparticles on lipid membranes: a molecular simulation perspective. *Soft Matter* 2009;**5**:4433-45.
28. Wasser CR, Ertunc M, Liu X, Kavalali ET. Cholesterol-dependent balance between evoked and spontaneous synaptic vesicle recycling. *J Physiol* 2007;**579**(2):413-29.
29. Ramirez DM, Kavalali ET. Differential regulation of spontaneous and evoked neurotransmitter release at central synapses. *Curr Opin Neurobiol* 2011;**21**:275-82.
30. Zidovetzki R, Levitan I. Use of cyclodextrins to manipulate plasma membrane cholesterol content: evidence, misconceptions and control strategies. *Biochim Biophys Acta* 2007;**1768**:1311-24.
31. Nečas D, Klapetek P. Gwyddion: an open-source software for SPM data analysis. *Phys* 2012;**10**:181-8.
32. Christian AE, Haynes MP, Phillips MC, Rothblat GH. Use of cyclodextrins for manipulating cellular cholesterol content. *J Lipid Res* 1997;**38**:2264-72.
33. Steck TL, Ye J, Lange Y. Probing red cell membrane cholesterol movement with cyclodextrin. *Biophys J* 2002;**83**:2118-25.
34. Hissa B, Duarte JG, Kelles LF, Santos FP, del Puerto HL, Gazzinelli-Guimaraes PH, et al. Membrane cholesterol regulates lysosome-plasma membrane fusion events and modulates Trypanosoma cruzi invasion of host cells. *PLoS Negl Trop Dis* 2012;**6**:e1583.
35. Richter RP, Brisson A. Characterization of lipid bilayers and protein assemblies supported on rough surfaces by atomic force microscopy. *Langmuir* 2003;**19**:1632-40.
36. Stone N, Kendall C, Smith J, Crow P, Barr H. Raman spectroscopy for identification of epithelial cancers. *Faraday Discuss* 2004;**126**:141-57.
37. Bergholt MS, Zheng W, Ho KY, Teh M, Yeoh KG, So JBY, et al. Fiber-optic Raman spectroscopy probes gastric carcinogenesis in vivo at endoscopy. *J Biophotonics* 2013;**6**:49-59.
38. Osswald S, Havel M, Gogotsi Y. Monitoring oxidation of multiwalled carbon nanotubes by Raman spectroscopy. *J Raman Spectrosc* 2007;**38**:728-36.
39. Lehman JH, Terrones M, Mansfield E, Hurst KE, Meunier V. Evaluating the characteristics of multiwall carbon nanotubes. *Carbon* 2011;**49**:2581-602.
40. Lepot L, De Wael K, Gason F, Gilbert B. Application of Raman spectroscopy to forensic fibre cases. *Sci Justice* 2008;**48**:109-17.
41. Fünfschilling U, Jockusch WJ, Sivakumar N, Möbius W, Corthals K, Li S, et al. Critical time window of neuronal cholesterol synthesis during neurite outgrowth. *J Neurosci* 2012;**32**:7632-45.
42. Hering H, Lin CC, Sheng M. Lipid rafts in the maintenance of synapses, dendritic spines, and surface AMPA receptor stability. *J Neurosci* 2003;**23**:3262-71.
43. Blank N, Schiller M, Krienke S, Wabnitz G, Ho AD, Lorenz HM. Cholera toxin binds to lipid rafts but has a limited specificity for ganglioside GM1. *Immunol Cell Biol* 2007;**85**:378-82.
44. Moulder KL, Jiang X, Taylor AA, Shin W, Gillis KD, Mennerick S. Vesicle pool heterogeneity at hippocampal glutamate and GABA synapses. *J Neurosci* 2007;**27**:9846-54.
45. Clements JD, Bekkers JM. Detection of spontaneous synaptic events with an optimally scaled template. *Biophys J* 1997;**73**:220-9.
46. Melom JE, Akbergenova Y, Gavornik JP, Littleton JT. Spontaneous and evoked release are independently regulated at individual active zones. *J Neurosci* 2013;**33**:17253-63.
47. Ermolyuk YS, Alder FG, Surges R, Pavlov IY, Timofeeva Y, Kullmann DM, et al. Differential triggering of spontaneous glutamate release by P/Q-, N- and R-type Ca2+ channels. *Nat Neurosci* 2013;**16**:1754-63.
48. Fredj NB, Burrone J. A resting pool of vesicles is responsible for spontaneous vesicle fusion at the synapse. *Nat Neurosci* 2009;**12**:751-8.
49. Andreae LC, Fredj NB, Burrone J. Independent vesicle pools underlie different modes of release during neuronal development. *J Neurosci* 2012;**32**:1867-74.
50. Nicholson AM, Ferreira A. Increased membrane cholesterol might render mature hippocampal neurons more susceptible to beta-amyloid-induced calpain activation and tau toxicity. *J Neurosci* 2009;**29**:4640-51.
51. Boyer C, Schikorski T, Stevens CF. Comparison of hippocampal dendritic spines in culture and in brain. *Neuroscience* 1998;**18**:5294-300.
52. Harrison BS, Atala A. Carbon nanotube applications for tissue engineering. *Biomaterials* 2007;**28**:344-53.
53. Bosi S, Ballerini L, Prato M. Carbon nanotubes in tissue engineering. *Top Curr Chem* 2014;**348**:181-204.
54. Kim YG, Kim JW, Pyeon HJ, Hyun JK, Hwang JY, Choi SJ, et al. Differential stimulation of neurotrophin release by the biocompatible nano-material (carbon nanotube) in primary cultured neurons. *J Biomater Appl* 2014;**28**:790-7.
55. Carp JS. Physiological properties of primate lumbar Motoneurons. *J Neurophysiol* 1992;**68**:1121-32.
56. Gao Y, Liu L, Li Q, Wang Y. Differential alterations in the morphology and electrophysiology of layer II pyramidal cells in the primary visual cortex of a mouse model prenatally exposed to LPS. *Neurosci Lett* 2015;**591**:138-43.
57. Allen JA, Halverson-Tamboli RA, Rasenick MM. Lipid raft microdomains and neurotransmitter signalling. *Nat Rev Neurosci* 2007;**8**:128-40.
58. Webb RH. Confocal optical microscopy. *Rep Prog Phys* 1996;**59**:427-71.
59. Mitterdorfer J, Bean BP. Potassium currents during the action potential of hippocampal CA3 neurons. *J Neurosci* 2002;**22**:10106-15.

60. Andreae LC, Burrone J. Spontaneous neurotransmitter release shapes dendritic arbors via long-range activation of NMDA receptors. *Cell Rep* 2015;**10**(6):873-82.
61. Barros CS, Franco SJ, Müller U. Extracellular matrix: functions in the nervous system. *Cold Spring Harb Perspect Biol* 2011;**3**:a005108.
62. Fabbro A, Sucapane A, Toma FM, Calura E, Rizzetto L, Carrieri C, et al. Adhesion to carbon nanotube conductive scaffolds forces action-potential appearance in immature rat spinal neurons. *PLoS One* 2013;**8**(8):e73621.
63. Fattahi P, Yang G, Kim G, Abidian MR. A review of organic and inorganic biomaterials for neural interfaces. *Adv Mater* 2014;**26**:1846-85.
64. Duan X, Lieber CM. Nanoelectronics meets biology: from new nanoscale devices for live-cell recording to 3D innervated tissues. *Chem Asian J* 2013;**8**(10):2304-14.
65. Moorjani S. Miniaturized technologies for enhancement of motor plasticity. *Front Bioeng Biotechnol* 2016;**18**(4):30.
66. Capogrosso M, Milekovic T, Borton D, Wagner F, Moraud EM, Mignardot JB, et al. A brain-spine interface alleviating gait deficits after spinal cord injury in primates. *Nature* 2016;**539**:284-8.
67. Vitale F, Summerson SR, Aazhang B, Kemere C, Pasquali M. Neural stimulation and recording with bidirectional, soft carbon nanotube fiber microelectrodes. *ACS Nano* 2015;**9**(4):4465-74.

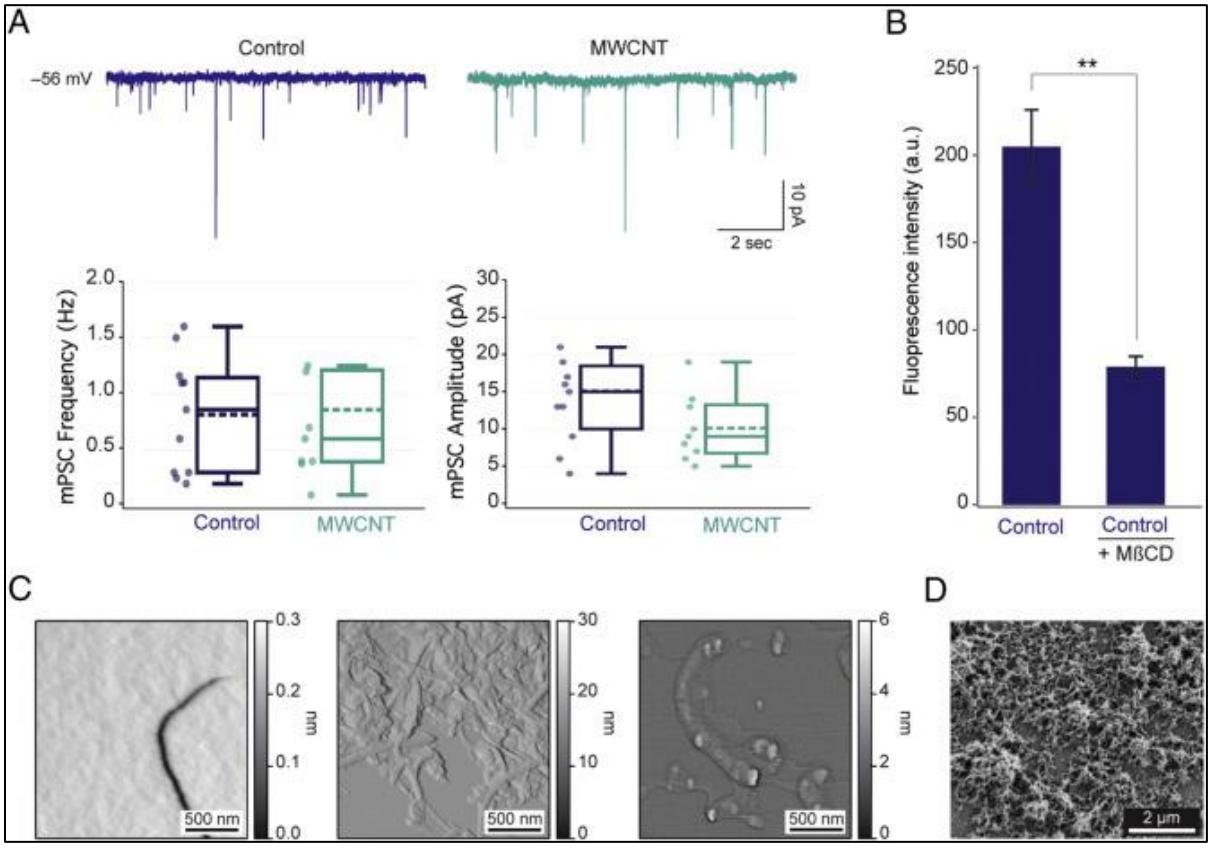

Supplementary Figure S1

A. Representative traces (top) depicting the spontaneous synaptic activity in presence of TTX of controls (n=11) and CNT (n=9) cultures. As shown by the box plots (bottom), at this time of growth in vitro either frequency or amplitude of miniature events was found to be similar between the two groups. B. The MβCD efficacy in reducing membrane cholesterol was assessed in control cultures at 3 weeks of growth in vitro: is evident a significant reduction in the filipin fluorescent signal after the MβCD treatment indicating a significant cholesterol reduction on neuronal membranes. C. Error (amplitude) AFM images of the high magnification reconstructions shown in Figure 1 pointing out details of SLM (left), MWCNTs (middle) and SLM deposited on MWCNTs (right). D. SEM image of a portion of the pristine MWCNT carpet deposited on a glass support pointing out nanotubes morphology and film uniformity.

Single-layer graphene modulates neuronal communication and up-regulates membrane ion channels

Niccolò Paolo Pampaloni[1a], Martin Lottner[2a], Michele Giugliano[3,4,5], Alessia Matruglio[6b], Francesco D'Amico[7], Maurizio Prato[8,9,10], Josè Antonio Garrido[11,12*], Laura Ballerini[1*], Denis Scaini[1,7*]

[1] International School for Advanced Studies (SISSA), Trieste, Italy

[2] Walter Schottky Institut and Physik-Department, Technische Universität München, Am Coulombwall, Garching, Germany

[3] Theoretical Neurobiology & Neuroengineering Laboratory, Department of Biomedical Sciences, Universiteit Antwerpen, Antwerpen, Belgium

[4] Department of Computer Science, University of Sheffield, S1 4DP Sheffield, UK;

[5] Lab of Neural Microcircuitry, Brain Mind Institute, EPFL, CH-1015 Lausanne, Switzerland

[6] CNR-IOM - Istituto Officina dei Materiali, Area Science Park – Basovizza, S.S. 14 km 163,5 Trieste - Italy

[7] Elettra Sincrotrone Trieste S.C.p.A., S.S. 14 Km 163.5 in Area Science Park, I-34149 Trieste, Italy

[8]Department of Chemical and Pharmaceutical Sciences, University of Trieste, Trieste, Italy

[9]Nanobiotechnology Laboratory, CIC biomaGUNE, -San Sebastiàn, Spain

[10]Ikerbasque, Basque Foundation for Science, Bilbao, Spain

[11]Catalan Institute of Nanoscience and Nanotechnology (ICN2), CSIC and The Barcelona Institute of Science and Technology, Campus UAB, Bellaterra, 08193 Barcelona, Spain

[12]ICREA, Pg. Lluís Companys 23, 08010 Barcelona, Spain

[a] these authors equally contributed to the work

[b] Present address: CERIC-ERIC (Central European Research Infrastructure Consortium), Area Science Park, Basovizza, S.S. 14 km 163,5 Trieste, Italy

Abstract

The use of graphene-based materials to engineer sophisticated bio-sensing interfaces adaptable to the central nervous system, requires a detailed comprehension of the behavior of such materials in a biological context. Graphene peculiar properties may cause various cellular changes, but the underlying mechanisms remain unclear. Here, we show that single-layer graphene increases neuronal firing of action potentials *via* altering membrane-associated functions in cultured cells. Graphene directly and selectively tunes extracellular potassium ions distribution at the interface with neurons, a key regulator of neuronal excitability. The resulting membrane biophysical change is represented by an up-regulation in potassium ion channels expression, which significantly shifts the fraction of neuronal firing phenotypes from *adapting* to *tonically firing*. By experimental and theoretical approaches we hypothesize that crucial to these effects are the graphene-ion interactions maximized by single layer graphene deposited on electrically insulating substrates.

Graphene is a highly versatile two-dimensional nanomaterial widely adopted in many domains of science and technology, including advanced biomedical applications, due to its important electrical, optical and mechanical properties [1,2,3]. The combination of these features and, in particular, its remarkable electro-conductivity, makes graphene extremely appealing in neuroengineering, with reference to invasive implant technologies for brain biosensors and electrodes [4,5,6]. Despite

the great interest and hopes raised by late development in graphene applications, the understanding of the functional interactions between graphene and brain tissue is still limited, particularly concerning the close proximity of a single plain layer of carbon atoms and the nervous cells' membrane ion fluxes in a biological milieu. So far, reports have shown that graphene-based materials can be safely interfaced with active neuronal cells [7,8,9], however an in-depth study focused on the influence of single-layer graphene (SLG) on the biophysics of neurons and *ex vivo* neuronal microcircuits upon is missing. In numerous electroceuticals applications [10,11], graphene is in contact with the extracellular environment that surrounds the excitable cell membranes. We thus asked: can SLG directly or indirectly alter neuronal activity? Which manipulations of graphene might be adopted to regulate *ad hoc* these interactions? The answers to these questions appear pivotal in designing future research in bio-hybrid electronic devices and, more in general, will provide important insights on the deep interactions of technology with nature. Here, SLG obtained by Chemical Vapor Deposition (CVD) was used to interface mammalian neurons dissociated from the rat hippocampi as a culture substrate. We employed different architectures of a single atomic layer graphene: (i) suspended or (ii) in contact with electrically insulating or conductive substrates. By these arrangements, we studied the collective electrical activity of neuronal networks coupled on graphene and demonstrated that, when isolated, SLG increased neuronal excitability via inducing specific changes in membrane biophysics. These consist in a significant shift of the fraction of neuronal firing phenotypes in the network from *adapting* to *tonically* firing. We then propose that graphene selectively modifies membrane-

associated neuronal functions and we hypothesize a specific interaction between graphene and potassium ions in the extracellular solution, crucially regulating cell excitability.

Single and multi-layer graphene and gold substrates

Glass supported films of SLG and multi-layer graphene (MLG) were tested as substrates interfacing neuronal growth. The topography of SLG and MLG was characterized by atomic force microscopy (AFM) and compared to control pristine (glass) and gold (Au) metalized glass samples (Fig. 1a). AFM topographies documented a surface roughness of the materials that varied from 0.23±0.02 nm in control, 1.5±0.5 nm in SLG, 20±10 nm for MLG and 0.47±0.1 nm for Au. The quality of CVD grown SLG and MLG samples was assessed by Raman and X-Ray photo-electron analysis. The recorded Raman spectra (Fig. 1b) supported the high quality of the SLG and MLG by showing low I_D/I_G ratios, indicating a low amount of sp^3 hybridized carbon atoms at grain boundaries or binding surface moieties [12]. The shape of the 2D peak, as well as the I_{2D}/I_G ratios are indicative of a low bilayer content in the case of SLG [13] and turbostratic graphite in the case of MLG [14] (Fig. 1b). A graphitic Raman signature is to be expected as the MLG samples have a typical thickness of a few hundreds of layers (data not shown). The higher noise in the SLG Raman spectrum is typical for the lower Raman back scattering intensity of SLG in comparison with MLG. X-Ray photo-electron spectroscopy (XPS) analysis of SLG and MLG on Si_3N_4 reveals that both SLG and MLG samples contain a low degree of process related Cu contamination (Fig. 1c).

SLG potentiates cell signaling in neuronal networks

Large films of SLG, MLG and Au were fabricated and transferred onto bare glass coverslips. To probe the electrical behavior of excitable biological cells, we used hippocampal neurons, which were dissociated from the rat hippocampi and plated directly on graphene- and Au-coated coverslips. As in our previous work with different carbon-based nanomaterial (e.g. carbon nanotubes) [15,16,17], we did not pre-treat the culture substrates with any additional adhesion molecules, which might mask the effects of graphene. Recently, several reports described the successful growth of different cell types on graphene and graphene-based materials [8,18,19], but none reported the *ex vivo* development of primary mammalian cells and neuronal microcircuits on uncoated monolayer of graphene. Neurons plated on glass coverslips were instead used as control cultures [15,16,17]. Direct contact between neurons and SLG, MLG and Au, could be then directly examined, and it was found to allow the growth of cells whose mature morphology was comparable to control ones (Fig. 2a). We further probed neuronal networks viability by quantifying network size and the ratio between neuronal and glial cells after 8-10 *days in vitro* (DIV), using immunofluorescence markers for neurons (class III β-tubulin) and astrocytes (GFAP; Fig. 2b). The histograms in Fig. 2b (right) show the surface density of cells (top) and the neuron/glia ratio (bottom) across all four conditions, which did not significantly differ (culture series used in all conditions n = 3, see Methods). These observations, combined to the similarity of membrane passive electrical properties (see Methods) measured by single-cell intracellular electrophysiology, indicated the

homogeneous growth of healthy neurons [16] across substrates, with comparable levels of cellular composition and maturation.

When cultured *in vitro*, neurons develop *ex vivo* functional synaptic connections and organize their collective electrical activity as a result of recurrently interconnected networks. To assess the possible changes caused by SLG, MLG or Au on neuronal network functions, we focused on synaptic signaling and recorded spontaneous synaptic activity after 8-10 DIV. This is indirectly informative of the combined effect of existence, number, transfer gain of neuronal connections, and intensity of collective interactions between neurons. Heterogeneous post-synaptic currents (PSC) were indeed detected intracellularly as inward currents of variable amplitudes [15] in all conditions, as shown by the sample traces in Figure 2c. While the amplitude of PSCs recorded from neurons growing on SLG (n = 45), MLG (n = 20) and Au (n = 20) were similar to control conditions (n = 40) (top histogram in Fig. 2c), the PSCs frequency (bottom histogram) was significantly higher in SLG than in other conditions (i.e.: control 1.53 ± 0.22 Hz; SLG 3.21 ± 0.41 Hz; p=0.0010). Instead, both MLG, (chemically similar to SLG), and Au, (chemically different but characterized by high electrical conductivity), did not affect neuronal network activity. This suggests the mechanistic involvement of specific properties of the plain sheet of carbon atoms, only when assembled as a monolayer, in the modulation of neuronal PSCs frequency.

SLG and MLG samples were prepared by film transfer either through polystyrene (PS) or polymethyl methacrylate (PMMA) supporting polymer (see Methods). PSCs measured in neurons showed however similar behavior when

carbon based films were transferred through PMMA or PS (Supplementary Fig. 1a). This indicates that the observed effect on PSCs is independent of the carbon film transfer method.

SLG changes intrinsic neuronal firing pattern

Miniature synaptic currents (mPSCs; Fig. 3a) were recorded in a subset of control (n = 11) and SLG (n = 11) neurons by further application of the fast-inactivating voltage-gated sodium channel blocker, tetrodotoxin (TTX, 1 µM). As this treatment impairs the generation of action potentials (APs) and thus blocks overall network activity, recording mPSCs allows disambiguating dynamical from structural components of emerging network activity. In particular, mPSCs reflect the stochastic release of vesicles from the presynaptic terminals at individual synapses reaching the recorded neuron: their frequency depends on the pre-synaptic release probability and on the number of synaptic contacts, while their amplitude depends on postsynaptic receptor sensitivity [20,12]. As pointed out by the histograms in Figure 3a, we found significant difference neither in the frequency nor the amplitude of mPSCs, when recorded in control or SLG conditions. This suggests that the increased PSCs activity described earlier in SLG does not involve structural changes in the number or in the properties of synaptic connections. This is further supported by immune-labeling experiments performed on neurons grown in control and SLG conditions. Figure 3b shows that the number of VGlut1-positive *puncta*, used to label and identify glutamatergic presynaptic terminals, was not altered by the presence of SLG.

Thus, the SLG-mediated increase in neuronal signaling does not involve major network synaptic rearrangements, such as an increased synaptogenesis or a (de)potentiation of synaptic efficacy.

To ultimately clarify the biophysical mechanisms leading to the boost in activity exhibited only by SLG circuits, we examined directly single cell excitability by current-clamp intracellular recordings. Control and SLG neurons displayed similar resting membrane potentials (–52 ± 10 mV in SLG; –50 ± 7 mV in Control) and AP threshold (–35.5 ± 1.2 mV in SLG, n = 21; -34.2 ± 1.5 mV Control, n = 19; see Methods). AP amplitudes were measured from threshold to peak [21], in control (n = 19) and SLG conditions (n = 21) and were similar in the two groups (amplitude: 56.4 ± 3.5 mV for controls and 59 ± 3.1 mV in SLG, p = 0.57; width: 3.5 ± 0.25 ms for controls and 3.7 ± 0.38 ms for SLG, p = 0.59). This indicates that SLG did not alter the expression of voltage-gated fast-inactivating Na^+ channel [22, 23].

To quantify and compare spontaneous APs frequency (Fig. 4a) we recorded control (n = 19) and SLG (n = 21) neurons kept at -60 mV resting membrane potential by injection of negative current. In agreement with the PSCs observations, we detected a significantly higher AP frequency in SLG neurons than in control ones (2.60 ± 0.36 Hz in SLG; 1.37 ± 0.26 Hz in control; p = 0.0054). In addition, when brief and sufficiently strong depolarizing current pulses (2-4 ms; 1 nA) were injected through the glass pipette electrode, single APs could be easily evoked in SLG (n = 25) and control (n = 20). However, the membrane voltage trajectory of evoked single APs was followed by a transient after-hyperpolarizing (AHP) in SLG neurons while only by a small after depolarization (ADP) in control (Fig. 4b). When quantified in terms of

the area below such trajectories with reference to the resting potential (see the histogram in Fig. 4b), the AHP in SLG neurons was significantly different than the ADP detected in control neurons (– 86.96 ± 23.60 pA·ms in SLG; + 107.12 ± 21.85 pA·ms in control; p = 0.0010). Interestingly, the AHP was reduced (by 88%) by bath applying Ba^{++} ($BaCl_2$, 2 mM; n = 3), which is known to block K_{ir} and K_{Ca} membrane channels [24, 25, 26, 27]. The AHP was also reduced (by 58%) by bath applying tetra-ethylammonium (TEA, 1 mM; n = 9) a non-selective blocker of the large majority of voltage gated K^+ membrane channels (Kv; [28], including BK_{Ca} channels [29]. Finally, Apamin (200 μM; n = 5), a specific inhibitor of SK_{Ca} membrane channels [30], also strongly affected (47% reduction) the AHP (Fig. 4b, K^+ channel blockade). All these observations demonstrate that the AHP detected in SLG neurons was likely mediated by K^+ conductances, and particularly by those activated by intracellular accumulation of free Ca^{++} ions [28,31]. The expression of these membrane ion channels is functionally related to the phenomenon of spike-frequency adaptation, where sustained APs discharge progressively slows down in time. We then further examined the sustained discharge patterns of control (n = 13) and SLG (n = 15) neurons, by injecting longer (1 s; 200 pA) depolarizing current pulses (Fig. 4c). In the majority (81.8%) of control neurons, sustained AP firing was dominated by spike frequency adaptation, which we named *adapting* discharge phenotype and which often even resulted in an early burst of closely spaced APs followed by progressive adaptation. On the contrary, SLG neurons (83.3%) showed no APs slowdown, which we named *tonic* discharge phenotype, where cells continuously and more regularly fired APs without apparent accommodation [32, 33].

Taken together, all these data hint at a complex homeostasis in the potassium membrane currents expressed by neurons when coupled to SLG substrates. This hypothesis was reinforced by results obtained under voltage-clamp from control (n = 13) and SLG (n = 15) neurons, where depolarizing voltage pulses starting from a –60 mV holding potential baseline evoked an outward current (Fig. 4d), presumably due to the activation of a mixed population of K^+ channels. When examined under these conditions, SLG neurons were characterized by a significantly larger outward current at positive potentials, shown in the steady-state current/voltage (I/V) plot of Figure 4d, likely consequence of an up-regulation of mixed K^+ currents.

Our pieces of evidence therefore strongly indicate that SLG substrates induce active changes in the electrical properties of growing neurons, presumably related to altered homeostasis of K^+ membrane channels and leading to a modulation of the single-cell firing phenotypes and ultimately to an increased network activity.

Modeling the impact of firing phenotypes on network activity

The observed correlations between single-cell properties, resulting phenotype, and network effects were further investigated by mathematical modeling and computer simulations. We specifically addressed the causality between neuronal firing patterns and network activity, and we studied an established spike-rate mathematical model of the electrical activity emerging in populations of cultured neurons with recurrent synaptic connections (Fig. 5a). This model [34, 35, 36] reproduces *in silico* the spontaneous periodic occurrence of “bursts” of APs (Fig. 5b and 5c), synchronized across the network [36]. These spontaneous events are the

network-level correlates of the PSCs as well as of the spontaneous AP firing, observed in single-cell experiments. In the model, the ignition of each episode of spontaneous firing is a direct consequence of recurrent glutamatergic synaptic transmission (i.e. acting as a positive feedback) and of random spontaneous release events at synaptic terminals (i.e. as in mPSCs). The termination of each spontaneous firing episode is instead determined in the model by the combined effect (i.e. acting as a negative feedback) of inhibitory synaptic connections, transient synaptic pool exhaustion underlying communication between neurons, and spike-frequency adaptation in excitatory neurons. The last mechanism does in fact slow down the repetitive (spontaneous) firing and thus decrease the synaptic net currents to downstream neurons.

We simulated a network of 1600 model neurons with a fraction of excitatory to inhibitory neurons equal to 80/20, reminiscent of the neuronal composition *in vitro* [37]. As most of inhibitory neurons are known from the literature to display only a tonic electrical phenotype, we hypothesized that the change in the ratio between adapting and tonically firing neurons observed in our experiments, occurred in excitatory neurons only. We therefore included in the model two subpopulations of excitatory neurons: one displaying *adapting* phenotype and one displaying *tonic* phenotype. We then found that the higher the relative fraction of *tonic* firing neurons, the higher the rate of occurrence of synchronized bursts (Fig. 5b and 5c). This supports the conclusion that the experimentally observed increase in the frequency of spontaneous (PSCs/APs) activity (Fig. 2c, SLG) is caused by the different ratio of cells with adapting/non-adapting neuronal electrical phenotypes.

The potassium ions hypothesis

By a more biophysically-detailed modeling approach, we then asked at the single-neuron level whether an increase in the total outward ionic conductance or, alternatively, a small reduction in the extracellular concentration of K^+ ions were responsible for the observed changes in single-cell firing activity. To that aim we studied *in silico* the effects on excitability of (i) an increased total outward potassium conductance or of (ii) a modest depletion of extracellular potassium. The rationale behind these computer simulations is that either SLG induced a chronic increase in channel expression involved in firing activity regulation, or SLG acutely altered cell firing by changing ion mobility. The two hypotheses are not mutually exclusive.

As a proof of concept, we considered the simplest possible model of AP generation, as proposed by Hodgkin and Huxley (HH) [38]. This model describes the generation of a (train of) AP(s) in terms of the known interplay between *fast-inactivating* (~1 ms) inward Na^+ currents and *delayed rectifier* outward K^+ potassium currents (Fig. 5d). Of course, by no means these are the only membrane currents underlying the electrophysiological behavior of rat hippocampal neurons [39]. Nonetheless, by stripping down excitability to its bare essential we could explore whether stronger outward potassium currents may favor excitability and not always oppose to it, as intuitively expected. We found that the progressive sodium current inactivation (Fig. 5d, lower left, green traces) – occurring in the HH model only over *fast* and not slow time scales – could be counterbalanced and reversed by strong K^+ currents (Fig. 5d, lower right, red traces). This results in a sustained, tonic, response to an external

current stimulus (i.e. compare Fig. 5d to Fig. 4c), instead of a progressive inactivation of the firing. While this effect is reversed by simulating an overexpression of Na^+ channels (e.g. at the axon initial segment – not shown), it serves us here only as a proof of concept. Figure 5e further illustrates this phenomenon, across distinct stimulus current amplitudes and over three levels of K^+ conductances. Therefore, in the model the more K^+ channels (i.e. same type or distinct type) the higher the excitability, in those regimes where progressive sodium inactivation affects neuronal firing.

However, as outward K^+ currents also depend on the ionic driving force beyond on the maximal conductance (i.e. in our model, $I_K \sim G_K\ (E_K - V)$ - see Methods), theoretically a change in the local ionic composition might reverse sodium inactivation too. In fact, the Nernst equilibrium potential E_K is determined by the K^+ concentration gradients outside and inside the neuronal membranes and it assumes negative values under physiological condition [40]. Should SLG interfere extracellularly with K^+ bulk diffusion in its proximity (see below) then a depletion of K^+ (e.g. 10÷20%, as $[K^+]_{EX} \rightarrow \delta \cdot [K^+]_{EX}$, $\delta = 0.8 \div 0.9$), would lead to increase in the ionic driving force, because E_K would then decrease accordingly (i.e. ~2÷5 mV). By definition

$$E_K = \frac{RT}{zF} \cdot ln\left(\frac{\delta \cdot [K^+]_{EX}}{[K^+]_{IN}}\right) = E_{K\ control} + \Delta$$

where T is the absolute temperature, R the universal gas constant, F the Faraday constant, and z = 1 K^+ valence (i.e. $RT/zF \sim 25\ mV$ at room temperature), and $\Delta = RT/zF \cdot ln(\delta)$ is a negative quantity measured in mV. By numerical simulations

(Fig. 5f), we found that a modest decrease in E_K in the model (e.g. from –75 to –77.6 mV) could indeed counterbalance sodium inactivation, at least for an intermediate external current stimulus intensity and without altering significantly the resting membrane potential.

All in all, this last part of our modeling effort suggests a specific involvement of the extracellular concentration of K^+ in neuronal excitability: the less extracellular K^+ the higher the excitability, at least in those regimes where progressive sodium inactivation affects neuronal firing disfavoring sustained *tonic* response.

It is therefore tempting to speculate that changes in excitability of cells coupled to SLG might be caused by an extracellular reduced mobility of K^+ at the interface between the nanomaterial and the extracellular solution, leading to a K^+ depletion at the neuronal membranes. *Per se*, this would explain directly the change in neuronal phenotype, but indirectly could account for a homeostatic re-arrangement of neuronal excitability by up-regulating number or conductance of K^+ channels.

Localized potassium ions depletion in cell-substrate cleft

Within these proposed mechanisms, it is still unclear how SLG might actually modify K^+ ion mobility while MLG (or Au) do not. It is well known that carbon-based π electron-rich surfaces in ionic solutions show a significant surface enrichment of cations due to specific cation-π interactions [41,42,43,44]. Because of its size, in solution, K^+ ions are more weakly solvated by water, when compared to other species (e.g. Li^+ or Na^+ ions), but are still good π binders. This feature makes K^+ the best alkali metal binder to carbon-based surfaces in aqueous solutions [43,44]. This

implies that, in nanoscale-confined systems, cation trapping occurring at the carbon surface level may lead to a significant local depletion of potassium ions at the neuronal membrane surface level.

In order to address this point Raman spectroscopy was performed on glass supported SLG and MLG samples in wet condition without and in the presence of KCl and NaCl at physiological concentrations (4 mM and 150 mM, respectively). Graphene-related G vibrational peak [13] was evaluated in wavenumber position for both SLG (Fig. 6a, left) and MLG substrates (Fig. 6a, right) with samples immersed in pure deuterium oxide (D_2O), in D_2O solution containing 4 mM KCl, and in D_2O solution containing 150 mM NaCl. The wavenumber maximum position relative to the G-peak Raman shift for control SLG sample is collocated at 1599 ± 0.5 cm^{-1}. It exhibits an increase to 1600 ± 0.5 cm^{-1} and to 1602 ± 0.5 cm^{-1} in the presence of NaCl and KCl D_2O solutions, respectively (Fig. 6a, left, inset). Conversely, in MLG samples G peak maximum position did not change (Fig. 6a, right, inset). The observed positive shift in the G Raman band of graphene together with the narrowing of the G band detected in SLG when in the presence of KCL could result from charge doping [45] or internal strain [46]. The shifts in G band position exhibited by SLG samples in the presence of salt solutions could be indicative of its specific cation interaction, not measured in the case of MLG. The larger G band Raman shift in KCl treated samples (3 ± 0.5 cm^{-1}) than in the presence of NaCl (1 ± 0.5 cm^{-1}) correlates well with a larger SLG affinity for K^+ when compared to Na^+. This result, observed here for the first time, strongly supports theoretical studies on cation-π interaction in solvated conditions [43,44]. Raman analysis of SLG substrates in dry

condition (see Supplementary Fig. 1b) points out, as predicted by gas-phase simulation, a stronger graphene–Na^+ interaction (G peak shift of about 4 ± 1 cm^{-1} than control SLG) than graphene–K^+, confirming the role of cations and the specificity of potassium in the wet condition [43,44].

In our experimental settings, cultured neurons are characterized by a cell body displaying a “disk-like” shape with average diameters of about 10 μm (Fig. 2a and 2b and Fig. 3b). Studies of cell/electrode interfaces in culture showed typical cleft thicknesses between 40-100 nm [47], corresponding to a cell-substrate cleft volume of about 3-8 μm^3. At an extracellular KCl concentration of 4 mM (see Methods), ~7-20·10^6 K^+ ions would occupy such a volume in the bulk. Under these conditions, the specific cation-π interaction at surface level could result in partial K^+ depletion from the extracellular solution facing the cell membrane. Taking into account, in first approximation, a 40:1 ratio between Na^+/K^+ cations in solution, and considering the contribution of both inner and outer hydration shells [48] to evaluate a reasonable cross-section of interaction between K^+ and graphene, we can assume that at least 2·10^6 K^+ will be strongly adsorbed on the surface. This could be translated in a theoretical local depletion of potassium ions of about 10-20% (Fig. 6b), this value is in accordance with what examined by our single-cell neuron model (Fig. 5e and 5f). Such a depletion profile has been inferred mesoscopically by the steady-state diffusion equation with *ad hoc* boundary conditions.

Substrate modulation of graphene cation-π interaction

In our hand, SLG behaved differently from MLG in respect to the K^+ homeostasis of neurons and subsequent improved excitability. The two nanomaterials culturing platforms, SLG and MLG, differ only in the conductive properties of the supporting structure immediately below the first mono atomic carbon layer exposed to the biological milieu (i.e. from one side glass and from the other multiple layers of graphene/graphite). MLG can be regarded, form the point of view of a neuron growing on its top, as a SLG film layered on the underlying, electrically conductive, MLG. It is then tempting to speculate, that graphene efficiency in trapping K^+ ions is tuned or influenced by the electrical properties of the supporting structure [49,50].

In this framework, we investigated if the electrical properties of the supporting material might *per se* tune SLG ability to affect neurons. We compared PSCs in neurons directly grown on glass (Control), on free-standing SLG (Suspended SLG, see Methods) and on SLG transferred on an insulating substrate (SLG on glass) and on a conductive substrate of indium tin-oxide (SLG on ITO). The last is an optically transparent and smooth film with well-defined electrically conductive properties and topography [17]. In Figure 6c the results of such experiments are summarized and are in full accordance to our hypothesis: the PSCs frequency was boosted by SLG on glass (3.11 ± 0.35 Hz *vs.* 1.72 ± 0.21 Hz, p=0.031) and even more by suspended SLG (4.22 ± 0.35 Hz *vs.* controls, p=0.001), while no effects were detected when SLG was layered on ITO. Notably, in suspended SLG, PSCs amplitude is also significantly increased (59.2 ± 5.8 pA *vs.* 35.9 ± 4.9 pA, p=0.017) when compared to control cultures.

It is not trivial to understand the exact mechanism underlying this phenomenon but, in the absence of any theoretical model describing the dependency of graphene π-cation interaction on supporting surface properties, we speculate that surface conductivity is playing a key role. In particular, in suspended SLG, environmental disturbances are minimized allowing access to the intrinsic properties of graphene close to the unperturbed Dirac point. Superficial charge inhomogeneity is reduced in this case compared to supported samples giving rise to a “close-to-theory” system [1,51] (Fig. 6d, left) that will fit better to cation-π simulations’ results [42,43,44]. SLG laying on metal surfaces usually undergo electron-doping resulting in a down-shift of graphene Dirac point [52] (Fig. 6d, middle). This will promote a flattening of the charge-distribution [53] and could result in a reduction of graphene cation-π interaction force. On the other hand, in SLG transferred on insulating substrates as, for example, glass or SiO_2, there are in general local fluctuations in surface potential [54,55] inducing charge jeopardisation on graphene surface where neutral areas, where SLG band structure is basically unperturbed as in the case of suspended graphene, and p-doped areas, coexist [56,57]. In the latter case, the interaction of graphene with potassium will be still present even if its net effect is less pronounced than on suspended SLG.

In this picture, MLG behavior can be described as that of SLG when laying on a (semi)-metallic graphite substrate [58] falling, in this case, in the second case we previously discussed [59].

We conclude that SLG modifies neuronal excitability and we propose that this effect is mediated by graphene ability to restrict K^+ ions mobility in close proximity to

the material surface, but only when the monolayer is deposited on electrically insulating substrates.

We provided multiple lines of evidence to demonstrate that graphene, when engineered in isolated single layer and laid on an insulating glass substrate, is able to tune neuronal excitability. Our physiological experiments demonstrate that the detected increase in neuronal synaptic activity is caused by increased cell firing, rather than to changes in network size or synaptic density [60,61,62]. We also demonstrated that neurons, when exposed to SLG, up-regulate outward currents, in particular potassium ones and switch to functionally-tonic firing phenotypes. Our computer simulations support the notion that changes in the ratio of adapting/firing neurons will impact the global network activity [63,64] and suggest the key contribution of up-regulated potassium conductance in driving this change. All these effects are not mimicked by MLG or other bare conductive substrates such as Au. We propose that, due to the cation-π interactions of graphene, cations, and K^+ in particular [42,43,44], will be trapped at the graphene surface, resulting in a graded depletion of such ions at a distance from the material compatible with the nanometer scale characterizing cell adhesion mechanisms [65,66]. This hypothesis is grounded in earlier molecular dynamics simulations at the equilibrium [42], where ionic enrichment occurs at the interface. As in a random-walk with a “sticky/viscous” wall, free potassium ions at the interface would be largely depleted, while their concentration would be unaffected in the bulk, i.e. far from the graphene surface. Therefore, at the nanoscale, at a distance compatible with realistic cell membrane proximity, a vertical K^+ spatial gradient may not be compensated entirely, as it is

likely to be restricted at the interface with graphene by the tortuosity of the extracellular microenvironment, densely packed with macromolecules for cell adhesion as well as cell membranes of neighboring cells [67]. This will translate in a slight but effective reduction of free extracellular potassium in the sub-micrometrical extracellular space confined between graphene and the underlying neuronal membrane. The effectiveness of such a K^+ depletion in altering cell excitability is grounded by our mathematical single-cell biophysical model. We cannot exclude that the up-regulation of K^+ outward currents and the switch in firing patterns could be induced by other chemical or physical features of SLG, yet unknown. However, on the basis of our experimental evidences, we suggest that the changes in K^+ mobility and in neuron excitability triggered the expression of potassium ionic channels, further modulating neuronal firing. Indeed, adaptive trait in neurons, termed homeostatic plasticity, has been well documented both for plasticity of intrinsic excitability via changing ionic conductance [68], as well as for changes in chemical synaptic strength [69, 70, 71].

The precise mechanisms for the observed effects of SLG substrates in this study are still elusive. We put forward a novel hypothesis based on the specific properties of the materials characterized by π electron-rich one plain layer of carbon atoms and we focused in particular on the specific cation-π interactions [39].
We further postulated that in the case of single layer graphene, the more unperturbed its band structure is, the larger is its ability to deplete potassium ions at the interface with neuronal membrane. Naturally, we cannot exclude alternative possibilities, but our results with suspended and ITO–supported SLG is consistent

with our hypothesis. Despite these considerations on hypothetical mechanisms, the results reported here indicate that graphene properties might affect neuronal information processing *in virtue* of the physical interactions of such a nanomaterial with the biological environment. Novel and outstanding materials might then represent, in general, unconventional and exciting tools to gain insights into genuine biological processes.

METHODS

Substrate fabrication

SLG was CVD grown on ultraflat Cu surfaces and transferred, as previously described [72], onto SiO_2 and Si_3N_4 substrates for subsequent Raman and XPS characterization. In short, after annealing the Cu foil in a 400 sccm :100 sccm argon and hydrogen atmosphere at 100 mbar and 1015°C, a SLG layer is nucleated at 15 mbar with 0.2 sccm methane, and closed by successively increasing the methane content to 0.5 sccm. The graphene is transferred using PMMA (PMMA 950K A2, MicroChem, USA) or PS (Polystyrene MW ~192k, Sigma-Aldrich, USA). For neuronal culturing, SLG was transferred to glass coverslips or indium tin oxide (ITO). Before the transfer procedure, hosting substrates were ultrasonicated in acetone and isopropanol to assure the required cleanness. Glass and ITO coverslips followed an additionally cleaning step in concentrated HCl overnight. MLG sheets were CVD grown on Ni ultraflat surfaces as described previously [73] and transferred on hosting substrates following the same procedure adopted for SLG.

Briefly, the Ni foil was annealed as described before, at a temperature of 900°C. After annealing, a methane flow of 10 sccm at 50 mbar enabled to the diffusion of carbon into the foil, which then, during the following slow cooling step, precipitated to a layer of MLG on the surface.

Gold samples have been prepared starting from glass rectangular slides (24 mm x 12 mm, 0.2 mm thick), cleaned previously in Piranha solution (H_2SO_4:H_2O_2, 5:5 ratio in volume) in order to remove eventually present organic contaminants. Subsequently, 15 nm of Au were thermally evaporated at a rate of 0.5 Å/s. A thin adhesion layer of 5 nm of Cr was used in order to improve Au/glass adhesion. A quartz crystal microbalance was used as thickness control.

To obtain suspended graphene structures, graphene is transferred on patterned substrates obtained using OrmoComp® (micro resist technology, GmbH), a flexible and biocompatible inorganic-organic material. The OrmoComp® substrates have been prepared on circular glasses (5 mm of diameter, 0.12 mm-thick), previously cleaned in Piranha solution (H_2SO_4:H_2O_2 5:5 % v/v) in order to remove organic contaminants. Subsequently, a poly-dimethylsiloxane (PDMS) master is prepared with replica molding process starting from a silicon stamp which is patterned with an array of parallel lines of width and periodicity of 10 μm and 20 μm, respectively. The OrmoComp® master is used to press a drop of OrmoComp® on the circular glass in order to transfer the micropattern. Finally, the OrmoComp® is cured with UV light and the PDMS master is released. Commercially available single-layer CVD graphene on copper (Cu; GRAPHENEA – San Sebastián, Spain) is wet-transferred on the OrmoComp® substrates following the protocol described by Matruglio *et al.*

[74]. Briefly, a layer of 250 nm of mr-I 7020 (a thermoplastic polymer of Micro Resist technology GmbH) is used as sacrificial layer and spin coated on the graphene/Cu. The polymer/graphene/Cu membrane is placed in a copper etching solution ($FeCl_3$:H_2O 3:7 % v/v), etched overnight and finally washed in DI water in order to remove any residual due to the etching solution. The transfer of graphene is performed fishing the polymer/graphene/Cu membrane into the water directly on the OrmoComp® substrate. The water is left to evaporate at room temperature for 2 h, and mr-I 7020 is dissolved in cold acetone for 5 minutes. Critical point drying process is performed in order to avoid the collapse of the suspended structures.

Cell culture and electrophysiology

Isolation of primary brain tissue was carried out in accordance with the recommendations in the Guide for the Care and Use of Laboratory Animals of the National Institutes of Health and the appropriate international and institutional standards for the care and use of animals in research (Italian Ministry of Health, in agreement with the EU Recommendation 2007/526/CE). The protocols in this study and all performed experiments are approved by the local veterinary service and the institutional (SISSA) ethical committee, in accordance with the EU guidelines (2010/63/UE) and Italian law (decree 26/14).

Dissociated hippocampal cultures were obtained from neonatal rats (P0–2) as previously described [15,16,17], and were plated on poly-L-Ornithine coated (SIGMA; Control), SLG-, MLG- or Au-covered glass coverslips. Cultured cells were incubated at 37 °C, 5% CO_2 in culture medium composed of Neurobasal-A (Thermo

Fischer) containing B27 2% (Gibco) Glutamax 10 mM and Gentamycin 0.5 μM (Gibco), and used for experiments at 8–10 days *in vitro* (DIV).

Somatic whole-cell patch clamp recordings were performed at room temperature (20÷22 °C) with pipettes (4÷7MΩ) containing: 105 mM K gluconate, 20 mM KCl, 10 mM HEPES, 4 mM MgATP, 0.3 mM GTP, pH 7.35. The external saline solution contained: 150 mM NaCl, 4 mM KCl, 1 mM $MgCl_2$, 2 mM $CaCl_2$, 10 mM HEPES, 10 mM Glucose, pH 7.4. Under voltage-clamp mode we measured the neuronal passive membrane properties: input resistance and cell capacitance did not significantly differ between the four groups (in control 592 ± 51 MΩ, 74 ± 5 pF, n = 47; in SLG 664 ± 57 MΩ, 83 ± 4 pF, n = 54; in MLG 614 ± 74 MΩ, 85 ± 5 pF, n = 18; in Au 656 ± 65 MΩ, 80 ± 6 pF, n = 17). In voltage clamp experiments, the holding potential (V_h) was –56 mV, not corrected for liquid junction potential, that was calculated to be –14 mV in our experimental conditions; the uncompensated value for series resistance (Rs) was < 8-11 MΩ.

Single spontaneous synaptic events (PSCs) and miniature PSCs (mPSCs) were detected by the use of the AxoGraph X (Axograph Scientific) event detection program [75] and by the Clampfit 10 software (pClamp suite, Axon Instruments). On average, ≥ 400 events were analyzed from each cell in order to obtain mean frequency and amplitude parameters.

Current-voltage relations (I/V plots) were obtained by applying hyperpolarizing or depolarizing voltage steps (15 steps of ΔV = 10 mV; 500 ms duration) from –110 mV to + 30 mV (values corrected for liquid junction potential) in the presence of 1 μM Tetrodotoxin (TTX; Latoxan). A least square routine was fitted to the linear part of

the I/V curve, the slope of which was used to calculate leak conductance. Assuming that a leak conductance is time and voltage independent, the I/V plot were corrected for leak currents by subtracting the observed currents from the extrapolated leak currents at the same level of test potential and the current values were then normalized to the cell capacitance [76].

In current clamp recordings, bridge balancing was continuously monitored and adjusted. Action potentials (APs) were isolated off line by setting an appropriate threshold (30 mV). The fast voltage transients that crossed this threshold were identified as APs and the spontaneous firing frequency for each neuron was calculated on a sample of at least 5 min of continuous recording at -60 mV resting membrane potential. APs threshold was experimentally determined by depolarizing current steps [77].

In evoked APs, the AHP was quantified over a window of 100 ms by calculating the area below or above the voltage curve, starting 20 ms after the beginning of the AP. AP discharge patterns were investigated by delivering depolarizing current steps (1 s) of 200 pA while keeping the cells at –60 mV resting potential with steady intracellular current injection. “Adapting” and “tonic” responses were identified as previously described [33].

Beside the monitoring of the spontaneous firing frequency, all the current clamp experiments were carried out in presence of the synaptic blockers (all from Sigma) CNQX (10 μM), Gabazine (5 μM) and APV (50 μM) added to the external solution. Current and voltage clamp responses were digitized at 20 kHz with the pCLAMP 10 software (Molecular Devices) and stored for further analysis.

Immunohistochemistry

Hippocampal neurons were fixed with 4% paraformaldehyde in PBS for 20 min, permeabilized with 0.3% Triton-X-100 for 10 min and subsequently incubated with primary antibodies for 30 min at RT. After washing in PBS cultures were then incubated with secondary antibodies for 45 min and then mounted in *Vectashield* (Vector Laboratories) on 1 mm thick microscope glass slides. As primary antibodies were used rabbit polyclonal anti-β-tubulin III (Sigma T2200, 1:250 dilution), mouse monoclonal anti-GFAP (Sigma-Aldrich, 1:200 dilution), and guinea pig anti-vesicular glutamate transporter 1 (VGLUT1; Millipore, 1:2000). As secondary antibodies were used Alexa 594 goat anti rabbit (Invitrogen, dilution 1:500), Alexa 488 goat anti mouse (Invitrogen, dilution 1:500), and Alexa 488 goat anti guinea-pig (Invitrogen, 1:500). To stain cells nuclei, we used DAPI (Invitrogen, 1:200 dilution). To quantify cell density, images were acquired with an Epifluorescence Microscope (DM 6000, Leica; 10× objective). We collected 10 fields (1000 μm × 500 μm) per coverslip (n = 30, 3 culture series for control, MLG and Au) and analyzed fluorescence signals using ImageJ software (http://rsb.info.nih.gov/ij/).

To quantify VGlut1 puncta, n = 20 ± 10 z-stacks (acquired every 0.4 μm) were taken from n = 10 randomly selected fields (160 μm × 80 μm) per coverslip (n = 30, 3 culture series in Control and SLG) using an inverted confocal Microscope (Nikon Eclipse Ti-E; 40x oil immersion objective, 1.3 NA). To quantify VGlut1 puncta, we selected only VGlut1-positive puncta (< 2 μm^3) touching the β-tubulin III positive signal; for each image VGlut1 puncta were normalized to the β-tubulin III positive volume. Images were analyzed using the Volocity software (Perkin Elmer).

Electron microscopy (EM)

Scanning EM imaging was conducted using collecting secondary electrons on a Gemini SUPRA 40 SEM (Carl Zeiss NTS GmbH, Oberkochen). Before SEM imaging, neuronal cells grown on the different substrates were fixed in 3% Glutaraldehyde in 0.1 M Sodium Cacodylate Buffer (pH 7.4), then dehydrated sequentially in ethanol solutions of 50, 75, 95, 99 and 100% (vol/vol in H_2O, 3 minutes each, 4 °C). After overnight drying in the fridge, and before imaging samples were metalized with a 5 nm thick layer of platinum-iridium allowing using a metal sputter coater (Polaron SC7620). In order to prevent electron induced surface charging, low accelerating voltages (0.8÷1.5 keV) were used for brain slices visualization.

Substrate characterization

AFM topography data (MFP-3D, Asylum Research, Santa Barbara, California, USA) was acquired in tapping mode, using silicon cantilevers in ambient conditions. The roughness estimates were calculated using the standard deviation of elevation in mapped surface areas with sizes of 10µm x 10µm. XPS spectra were recorded in ultra-high vacuum conditions using a monochromatic SPECS XR-50 Mg Kα X-Ray source ($E_{K\alpha}$ = 1253.6 eV) and a hemispherical energy analyzer (Phoibos 100/150, Specs, Berlin, Germany). µ-Raman spectra were recorded with an in-house built system using an Ar-ion laser at 514.5 nm and operating with a spectral resolution of 0.75 cm^{-1}.

Raman measurements in wet conditions have been carried out at on the IUVS beamline at Elettra synchrotron radiation facility (Trieste, Italy). A complete

description of the experimental apparatus can be found elsewhere [10.1016/j.nima.2012.11.037]. A 532 nm laser source, with a beam power near 5 mW, has been employed as excitation source. The scattered radiation was collected in a backscattering geometrical configuration. A 750 mm focal length Czerny-Turner spectrometer, equipped with an holographic reflection grating of 1800 g/mm and coupled with a Peltier-cooled back-thinned CCD, has been used to get the final Raman spectra.

Data Analysis

All values from samples subjected to the same experimental protocols were pooled together and expressed as mean ± SEM (with n = number of cells, unless otherwise indicated). A statistically significant difference among multiple data sets was assessed by One-way ANOVA, followed by Bonferroni test. Statistically significant difference between two data sets was assessed by Student's t test (after validation of variances homogeneity by Levene's test) for parametric data and by Mann-Whitney for non-parametric ones. Statistical significance was determined at $p<0.05$, unless otherwise indicated.

Mathematical model of the neuronal network

A Wilson-Cowan-like model, accounting for the spontaneous electrical activity observed in cultured neuronal networks, was defined and computer-simulated. It aimed at supporting the interpretation of the *in vitro* recordings and at linking (phenomenologically) single-cell properties to spontaneously emerging network activity. The model describes at the population level, the instantaneous firing rates

$\nu_{E1}(t)$, $\nu_{E2}(t)$ and $\nu_I(t)$ of a heterogeneous ensemble of excitatory (E) and inhibitory (I) neurons, respectively. Three populations were in fact considered (i.e. two excitatory and one inhibitory), each defined by a characteristic time scale (i.e. τ_E and τ_I), by single-cell *f-I* curve (i.e. $\phi(I_{syn})$) and by the specific recurrent connectivity [34,35,36,78].

$$\tau_E \frac{d\nu_{E1}}{dt} = -\nu_{E1} + \phi_{E1}(\mu_{E1}, \sigma_{E1})$$

$$\tau_E \frac{d\nu_{E2}}{dt} = -\nu_{E2} + \phi_{E2}(\mu_{E1} - g_{SFA}\, x_{SFA}\, \nu_{E2}, \sigma_{E2})$$

$$\tau_I \frac{d\nu_I}{dt} = -\nu_I + \phi_I(\mu_I, \sigma_I) \qquad (1)$$

The *f-I* curves were described by an identical transfer function of a *leaky Integrate-and-Fire* model neuron, expressed – under the hypotheses of the diffusion approximation [79]– by an analytical formula (see Supplemental Method). Here only the (infinitesimal) mean μ and variance σ^2 of the incoming average synaptic inputs are considered. These statistical parameters reflected the recurrent synaptic connectivity and of external inputs, as sketched in Fig. 5a, through the size of presynaptic populations (i.e. N_{ext}, N_{E1}, N_{E2}, N_I), the probability of recurrent connectivity (i.e. c), and the average of synaptic couplings (i.e. the charge associated to each postsynaptic potential; Δ_{EE}, Δ_{EI}, Δ_{IE}, Δ_{II}) and their standard deviations (i.e. $s\Delta_{EE}$, $s\Delta_{EI}$, $s\Delta_{IE}$, $s\Delta_{II}$)

$$\mu_{E1} = N_{ext}\Delta_{ext}\nu_{ext} + c\, N_{E1}\Delta_{EE}r_{E1}\nu_{E1} + c\, N_{E2}\Delta_{EE}r_{E2}\nu_{E2} + c\, N_I\Delta_{EI}\nu_I \qquad (2)$$

$$\mu_{E2} = N_{ext}\Delta_{ext}\nu_{ext} + c\, N_{E1}\Delta_{EE}r_{E1}\nu_{E1} + c\, N_{E2}\Delta_{EE}r_{E2}\nu_{E2} + c\, N_I\Delta_{EI}\nu_I$$

$$\mu_I = N_{ext}\Delta_{ext}\nu_{ext} + c\, N_{E1}\Delta_{IE}r_{E1}\nu_{E1} + c\, N_{E2}\Delta_{IE}r_{E2}\nu_{E2} + c\, N_I\Delta_{II}\nu_I$$

$$\sigma^2{}_{E1} = N_{ext}(\Delta^2_{ext} + s\Delta^2_{ext})\nu_{ext} + c\,N_{E1}(\Delta^2_{EE} + s\Delta^2_{EE}){r_{E1}}^2\nu_{E1} + c\,N_{E2}(\Delta^2_{EE} + s\Delta^2_{EE}){r_{E2}}^2\nu_{E2} + c\,N_I(\Delta^2_{EI} + s\Delta^2_{EI})\nu_I \quad (3)$$

$$\sigma^2{}_{E2} = N_{ext}(\Delta^2_{ext} + s\Delta^2_{ext})\nu_{ext} + c\,N_{E1}(\Delta^2_{EE} + s\Delta^2_{EE}){r_{E1}}^2\nu_{E1} + c\,N_{E2}(\Delta^2_{EE} + s\Delta^2_{EE}){r_{E2}}^2\nu_{E2} + c\,N_I(\Delta^2_{EI} + s\Delta^2_{EI})\nu_I$$

$$\sigma^2{}_{I} = N_{ext}(\Delta^2_{ext} + s\Delta^2_{ext})\nu_{ext} + c\,N_{E1}(\Delta^2_{IE} + s\Delta^2_{IE}){r_{E1}}^2\nu_{E1} + c\,N_{E2}(\Delta^2_{IE} + s\Delta^2_{IE}){r_{E2}}^2\nu_{E2} + c\,N_I(\Delta^2_{II} + s\Delta^2_{II})\nu_I$$

Following closely (33), to approximately capture the dynamical filtering effects of AMPAr- and GABAr-mediated synapses, each presynaptic mean firing rate ν in equations. 4-5 was replaced by its low-passed version $\hat{\nu}$ which also included the finite-size fluctuations [34]:

$$\tau_{AMPA}\frac{d\hat{\nu}_{E1}}{dt} = -\hat{\nu}_{E1} + Poisson[N_{E1}\nu_{E1}\Delta t]/(N_{E1}\Delta t)$$

$$\tau_{AMPA}\frac{d\hat{\nu}_{E2}}{dt} = -\hat{\nu}_{E2} + Poisson[N_{E1}\nu_{E1}\Delta t]/(N_{E1}\Delta t)$$

$$\tau_{GABA}\frac{d\hat{\nu}_{I}}{dt} = -\hat{\nu}_{I} + Poisson[N_{E1}\nu_{E1}\Delta t]/(N_{E1}\Delta t) \quad (4)$$

where, for each time *t*, $Poisson[x]$ indicates a new realization of a pseudo-random number, drawn form a Poisson distribution with mean x, and where Δt is the numerical integration step.

The effects of homosynaptic short-term depression at excitatory synapses and spike frequency adaptation in just one of the two excitatory populations, were finally described by three additional equations

$$\tau_{SFA}\frac{dx_{SFA}}{dt} = -x_{SFA} + Poisson[N_{E1}\nu_{E1}\Delta t]/(N_{E1}\Delta t)$$

$$\tau_{STD}\frac{dr_{E1}}{dt} = 1 - r_{E1} - U\ r_{E1}\,\tau_{STD}\,\hat{v}_{E1}$$

$$\tau_{STD}\frac{dr_{E2}}{dt} = 1 - r_{E2} - U\ r_{E2}\,\tau_{STD}\,\hat{v}_{E2} \qquad (5)$$

and by replacing including short-term synaptic depression, intrinsic spike frequency adaptation, and the effects to the finite size of the network [34].

Model parameter	**Value**
$N_{E1} + N_{E2}$	1280
N_I	400
τ_E	20 ms
τ_I	20 ms
τ_{AMPA}	10 ms
τ_{GABA}	2 ms
τ_{STD}	800 ms
τ_{SFA}	1500 ms
g_{SFA}	10 a.u.
U	0.2
$\Delta_{ext} \pm s\Delta_{ext}$	(0.416 $\pm$ 0.104) / C_m mV
$\Delta_{EE} \pm s\Delta_{EE}$	(0.809 $\pm$ 0.202) / C_m mV
$\Delta_{EI} \pm s\Delta_{EI}$	(-0.34 $\pm$ 0.085) / C_m mV
$\Delta_{IE} \pm s\Delta_{IE}$	(1.23 $\pm$ 0.307) / C_m mV
$\Delta_{II} \pm s\Delta_{II}$	(-0.358 $\pm$ 0.0894) / C_m mV
$N_{ext}\nu_{ext}$	1.25 kHz
c	0.25
C_m	20 pF
R_m	1 $k\Omega$
E_m	-70 mV
V_θ	-55 mV
V_H	-70 mV
τ_{arp}	2 ms

Table 1: Numerical values employed in the simulations of Figure 5.

Additional details are provided in Supplemental materials and full model details and the source code are provided as a ModelDB entry [80].

(https://senselab.med.yale.edu/ModelDB; accession number 230930, temporary password 1234).

Conductance based model

A minimal model of neuronal excitability was considered by studying the classic single-compartmental conductance-based description proposed by Hodgkin and Huxley (1952). Therein, the electrical potential *V* across the cell membrane, satisfies the conservation of charge

$$C_m \frac{dV}{dt} = I_{Na} + I_K + I_{leak} + I_{stim}$$

where the sum of externally applied currents (I_{stim}), capacitive displacement currents ($C_m dV/dt$), and ionic transport currents across the membrane (I_{Na}, I_K, I_{leak}) are always balanced. The model is completely described by additional three state variables (i.e. *m, h, n*), expressing the voltage- and time-dependent fractions of inward and outward ionic currents, $I_{Na} = G_{Na} m^3 h\,(E_{Na} - V)$, $I_K = G_K n^4\,(E_K - V)$, $I_{leak} = G_{leak}\,(E_{leak} - V)$ as a first-order kinetic process:

$\frac{dx}{dt} = \alpha_x\,(1 - x) - \beta_x\,x$, with $x \in \{m, h, n\}$

Model parameters are indicated in Table 1, unless noted otherwise.

Parameter	Description	Value
C_m	*Specific cell capacitance*	0.01 μF/mm^2
E_{Na}	*Nernst potential for Na^+ ions*	30 mV
E_K	*Nernst potential for K^+ ions*	-75 mV
E_{leak}	*Nernst potential for "leak" ionic currents*	-80 mV
G_{Na}	*Maximal conductance for Na^+ ions*	0.333 mS/mm^2
G_K	*Maximal conductance for K^+ ions*	0.012 mS/mm^2
G_{leak}	*Maximal conductance for "leak" currents*	0.003 mS/mm^2

I_{stim}	*External DC current stimulus amplitude*	15 nA/mm^2
$\alpha_m(V)$	*Kinetic rate of Na^+ current activation*	0.1 F(0.1,V+35)
$\beta_m(V)$	*Kinetic rate of Na^+ current activation*	4 exp(-(V+60)/18) ms
$\alpha_h(V)$	*Kinetic rate of Na^+ current inactivation*	0.07 exp(-(V+60)/20) ms
$\beta_h(V)$	*Kinetic rate of Na^+ current inactivation*	[exp(-(V+30)/10)+1]$^{-1}$ ms
$\alpha_n(V)$	*Kinetic rate of K^+ current activation*	0.01 F(0.1,V+50) ms
$\beta_n(V)$	*Kinetic rate of K^+ current activation*	0.125 exp(-(V+60)/80) ms
$F(x,y)$	*Boltzman sigmoid function*	y / [1 - exp(x * y)] ms
Δt	Numerical solution time-step	0.001 ms

Table 1– Parameters employed in the simulations of the Hodgkin-Huxley (HH) model. The standard HH mathematical model was numerically simulated as a minimal description of neuronal excitability to gain insight on current-clamp experimental recordings.

FIGURE LEGENDS

Figure 1 | Characterization of the substrates. a, AFM topography reconstructions of glass control, SLG, MLG and gold plated glass surfaces. Scale bar: 5 μm. **b**, Spatial maps of the 2D/G and D/G peak amplitude ratio maps. Scale bar: 10 μm. The single punctual Raman spectra of SLG (in red) and MLG (in blue) represent mapping data points with the corresponding average peak amplitude ratios. To the right, relative spatial 2D/G and D/G ratio maps. **c**, XPS spectrum (X-Ray source: Mg Kα) of SLG (in red) and MLG (in blue). Dotted lines highlight the relevant elements, while the unlabeled features around 750 eV and 980 eV correspond to the oxygen KL_1L_1 and the carbon KVV Auger lines respectively.

Figure 2 | Single-Layer graphene increase neuronal network activity. a, Representative SEM micrographs depicting hippocampal neuron morphology after 10 DIV-growth supported by the different substrates. Scale bar: 10 μm. **b**, Representative fluorescent microscopy images showing dissociated hippocampal networks labeled with class III β-tubulin (for neurons) in red and GFAP (for astrocytes) in green. Scale bar: 100 μm. Cultures grown on the different materials displayed a comparable number of cells, quantified as DAPI-positive nuclei (upper right histograms) and a similar fraction of glial and neuronal cells (lower right histograms). **c**, Representative traces of the spontaneous network activity of neurons grown on the different substrates are shown (left), the corresponding isolated PSCs are shown superimposed (middle; in black the average values). The

histograms summarize the average PSC amplitude values (right, top) and the average PSC frequency ones (right, bottom) in all experimental conditions. Note the significant increase in PSC frequency in SLG when compared to all the other substrates.

Figure 3 | Single-layer graphene does not increase the number of synapses. a, Exemplificative spontaneous traces of synaptic activity recorded in the presence of TTX are shown together with their superimposed mPSCs (right, in black the average values); Control and SLG mPSC frequency and amplitude are summarized in the histograms, note that no differences were detected in these parameters. **b**, Confocal images of neuronal cultures (10 DIV) in Control and SLG identifying the presynaptic VGlut1 (in green) in III β-tubulin positive cells (orange). Scale bar: 20 μm. Higher magnifications of the region highlighted by white boxes are displayed for clarification. Scale bar: 5 μm. The histograms summarize VGlut1 puncta densities in the two conditions (right).

Figure 4 | SLG triggers changes in single cell intrinsic excitability. a, Current-clamp recordings of hippocampal neurons in culture (10 DIV) in Control and SLG. The spontaneous occurrence of APs is summarized in the histograms (right). Note the significant increase of AP frequency in SLG. **b**, Evoked single AP in control (left) and SLG (middle). Note the pronounced AHP in SLG neurons, that was partially abolished by each of the treatments shown, BaCl, TEA or Apamin (right). The histogram at the right quantifies the area below the control and SLG post-AP voltage trajectories with respect to the resting membrane potential. **c**, Current-clamp

recordings from hippocampal neurons in control and SLG induced different discharge patterns that identified two cell categories: *Tonic* or *Adapting*. Bar charts illustrate probability distributions (expressed as percentage of sampled population) of each cell type in control and SLG cultures. **d**, Representative records of voltage-activated outward currents evoked by depolarizing current steps in control and SLG (capacitive transients were not removed). Plot summarizes the I/V relation in control and SLG neurons obtained upon subtraction of leak currents. Note that SLG outward currents were significantly larger than control ones.

Figure 5 | Spike-rate "extended mean-field" model. The model, describing mathematically the electrical activity of excitatory and inhibitory recurrently interacting neurons, was defined and computer simulated (see Supplemental Methods). **a**, The increase in the fraction of non-adapting neurons, observed *in vitr*o on graphene substrates, predicts *in silic*o a higher rate of occurrence for spontaneous synchronized "bursts" of spikes across the entire network. These bursts are presynaptic correlates of the spontaneous compound synaptic potentials, observed experimentally by voltage-clamp. **b** and **c**, Samples of the simulated time series, analysed in **a**, are shown for two values of the fraction of non-adapting neurons, *i.e.* 20% and 80%, out of the total of excitatory neurons. **d**, A counter-intuitive effects of outward potassium currents on cell excitability are explored in a minimal mathematical model. The Hodgkin-Huxley model was numerically integrated (parameters as in Table 2) to simulate membrane potential responses (black traces) to an external step current comparable to experiments (see Methods). **d** and **e**, Plots

within each panel exemplify how an increase (from left subpanels to right subpanels) of the maximal K^+ conductance or, in **f**, its driving force, through a depletion of extracellular K^+ ions, may to some extent reverse the progressive inactivation of inward Na^+ currents (green traces in **d**). Then, inactivating neuronal responses may turn into sustained firing thereby increasing cell excitability (as in **c**). Parameters: in **d**, G_K in {0.012; 0.0216} mS/mm^2; in **e**, G_K in {0.012, 0.04, 0.06} mS/mm^2 from left to right, I_{stim} 5 nA/mm^2; in **f**, I_{stim} as in **e**, while E_K in {-75, -77.6, -80.5} mV from left to right, corresponding to a {0%, 10%, 20%} depletion of extracellular K^+ ions.

Figure 6 | Graphene deplete potassium at the cell/substrate cleft. a, The Raman spectra of graphene G band in wet condition are shown for SLG (left) and MLG (right). Control condition (D_2O, in black) is compared with spectra of graphene immersed in 4 mM D_2O solution (in red) of KCl and 150 mM solution of NaCl (in green). Note that high concentrated NaCl induce in SLG a smaller shift in G-Peak position than KCl while no shifts are detectable in MLG as outlined in the insets. **b**, Sketch of the local amount of K^+ depletion in the membrane/surface cleft due to graphene trapping as function of cleft thickness. In light green the extrapolated values of such a distance (40÷100 nm) [46]. **c**, Histograms summarize the average PSC frequency values (left) and the average PSC amplitudes ones (right) for neurons developed on glass control (in grey), on glass supported SLG (in red), on free-standing SLG (in green) and on SLG deposited on ITO (in blue). Note the significant increase in PSC frequency in SLG laying on insulating glass or, even more, when grown on suspended SLG. SLG on conductive ITO does not change

neuronal activity. **d**, Hypothesis of Dirac point and Fermi level rearrangement as function of SLG supporting material (bottom), and an exemplification of the possible charge distribution in graphene layer as function of electrical characteristics of the underlying surface (top). Blue areas represent more positive regions (e.g. depletion of electrons), red areas represent more negative ones (e.g. persistency of electrons).

REFERENCES

[1] Novoselov, K. S. et al. Electric Field Effect in Atomically Thin Carbon Films. Science 306, 666-669 (2004).

[2] Geim, A. K. & Novoselov, K. S. The rise of graphene. Nat Mater. 6, 183-191 (2007).

[3] Yang, Y. et al. Graphene based materials for biomedical applications. Mat Today 16, 365-373 (2013).

[4] Shin, S. R. et al. Graphene-based materials for tissue engineering. Adv Drug Deliv Rev. 105, 255-274 (2016).

[5] Lu, Y. et al. Flexible Neural Electrode Array Based-on Porous Graphene for Cortical Microstimulation and Sensing. Sci Rep. 6, 33526 (2016).

[6] Blanschke, B. M. et al. Mapping brain activity with flexible graphene micro-transistors. 2D Mater. 4, 025040 (2017).

[7] Kim, J. et al. Monolayer Graphene-Directed Growth and Neuronal Differentiation of Mesenchymal Stem Cells. J Biomed Nanotechnol. 11, 2024-2033 (2015).

[8] Fabbro, A. et al. Graphene-Based Interfaces Do Not Alter Target Nerve Cells. ACS Nano 10, 615-623 (2016).

[9] Rauti, R. et al. Graphene Oxide Nanosheets Reshape Synaptic Function in Cultured Brain Networks. ACS Nano 10, 4459-4471 (2016).

[10] Famm, K. et al. Drug discovery: a jump-start for electroceuticals. Nature 496, 159-161 (2013).

[11] Rivnay, J. et al. Next-generation probes, particles, and proteins for neural interfacing. Sci Advances 3, e1601649 (2017).

[12] Cançado, L.G. et al. Quantifying defects in graphene via Raman spectroscopy at different excitation energies. Nano lett. 11, 3190-3196 (2011).

[13] Ferrari A. C. et al. Raman spectrum of graphene and graphene layers. Phys. Rev. Lett. 97, 187401 (2006).

[14] Cançado, L. G. et al. Measuring the degree of stacking order in graphite by Raman spectroscopy. Carbon 46, 272-275 (2008).

[15] Lovat, V. et al. Carbon nanotube substrates boost neuronal electrical signaling. Nano lett. 5, 1107-1110 (2005).

[16] Cellot, G. et al. Carbon nanotubes might improve neuronal performance by favouring electrical shortcuts. Nat. Nanotechnol. 4, 126-133 (2009).

[17] Cellot, G. et al, Carbon nanotube scaffolds tune synaptic strength in cultured neural circuits: novel frontiers in nanomaterial-tissue interactions. J. Neurosci. 31, 12945-12953 (2011).

[18] Kim, J. et al, Monolayer Graphene-Directed Growth and Neuronal Differentiation of Mesenchymal Stem Cells. J Biomed. Nanotechnol. 11, 2024-2033 (2015).

[19] Baldrighi, M. et al, Carbon Nanomaterials Interfacing with Neurons: An In vivo Perspective. Front. Neurosci. 10, 260 (2016).

[20] Raastad, M. et al. Putative Single Quantum and Single Fibre Excitatory Postsynaptic Currents Show Similar Amplitude Range and Variability in Rat Hippocampal Slices. Eur J Neurosci. 4, 113-117 (1992).

[21] Routh, B. N. et al. Anatomical and Electrophysiological Comparison of CA1 Pyramidal Neurons of the Rat and Mouse. J Neurophysiol. 102, 2288–2302 (2009).

[22] Platkiewicz, J. & Brette, R. Impact of Fast Sodium Channel Inactivation on Spike Threshold Dynamics and Synaptic Integration. PLoS Comput Biol. 7, e1001129 (2011).

[23] Kress, G. J. et al. Axonal sodium channel distribution shapes the depolarized action potential threshold of dentate granule neurons. Hippocampus 20, 558-571 (2016).

[24] Alagem, N. et al, Mechanism of Ba(2+) block of a mouse inwardly rectifying K+ channel: differential contribution by two discrete residues. J Physiol. 534, 381-393 (2001).

[25] Alger, B. E. & Nicoll, R. A. Epileptiform burst afterhyperolarization: calcium-dependent potassium potential in hippocampal CA1 pyramidal cells. Science 210, 1122-1124 (1980).

[26] Jiang, Y. & MacKinnon, R. The barium site in a potassium channel by x-ray crystallography. J Gen Physiol. 115, 269-272 (2000).

[27] Nisenmbaum, E. S. & Wilson, C. J. Potassium currents responsible for inward and outward rectification in rat neostriatal spiny projection neurons. J Neurosci. 15, 4449-4463 (1995).

[28] Storm, J. F. Action potential repolarization and a fast after-hyperpolarization in rat hippocampal pyramidal cells. J Physiol. 385, 733-759 (1987).

[29] Pisirowski, R. & Aldrich, R. W. Calcium activation of BK(Ca) potassium channels lacking the calcium bowl and RCK domains. Nature 420, 499-502 (2002).

[30] Stocker, M. et al, An apamin-sensitive Ca2+-activated K+ current in hippocampal pyramidal neurons. Prot Nat Acad Sci. 96, 4662-4667(1999).

[31] Sah, P. & Faber, E. S. Channels underlying neuronal calcium-activated potassium currents. Prog Neurobiol. 66, 345-353 (2002).

[32] Dégenètais, E. et al. Electrophysiological properties of pyramidal neurons in the rat prefrontal cortex: an in vivo intracellular recording study. Cereb Cortex 12, 1-16 (2002).

[33] Furlan, F. et al. ERG conductance expression modulates the excitability of ventral horn GABAergic interneurons that control rhythmic oscillations in the developing mouse spinal cord. J. Neurosci. 27, 919-928 (2007).

[34] Gigante, G. et al. Network Events on Multiple Space and Time Scales in Cultured Neural Networks and in a Stochastic Rate Model. PLoS Comput Biol. 11, e1004547 (2015).

[35] Gambazzi, L. et al. Diminished activity-dependent brain-derived neurotrophic factor expression underlies cortical neuron microcircuit hypoconnectivity resulting from exposure to mutant huntingtin fragments. J. Pharmacol Exp Ther. 335, 13-22 (2010).

[36] Giugliano, M. et al. Single-neuron discharge properties and network activity in dissociated cultures of neocortex. J Neurophysiol. 92, 977-996 (2004).

[37] Marom, S. & Shahaf, G. Development, learning and memory in large random networks of cortical neurons: lessons beyond anatomy. Q Rev Biophys. 35, 63-87 (2002).

[38] Hodgkin, A. L. & Huxley, A. F. A quantitative description of membrane current and its application to conduction and excitation in nerve. J Physiol. 117, 500-544 (1952).

[39] French, C. R. et al. Properties of an intermediate-duration inactivation process of the voltage-gated sodium conductance in rat hippocampal CA1 neurons. J Neurophysiol. 115, 790-802 (2016).

[40] Sterratt, D. Principles of computational modelling in neuroscience. Cambridge University Press(2011).

[41] Kumpf R A, & Dougherty D A. A mechanism for ion selectivity in potassium channels: computational studies of cation-pi interactions. Science. 261, 1708-10 (1993).

[42] Shi, G,et al. Ion enrichment on the hydrophobic carbon-based surface in aqueous salt solutions due to cation-π interactions. Sci Rep., 3, 3436 (2013).

[43] Pham T A, et al. J. Phys. Chem. C, 120,7332–7338 (2016).

[44] Williams, C D, et al. P, J. Phys. Chem. Lett., 8,703–708 (2017)

[45] Dong, X et al. Doping single-layer graphene with aromatic molecules. Small. 5,1422-6 (2009)

[46] Chacón-Torres, JC, Wirtz, L, Pichler, T. Manifestation of charged and strained
graphene layers in the Raman response of graphite intercalation compounds. ACS
Nano. 7, 9249-59 (2013).

[47] Spira ME, Hai A. Multi-electrode array technologies for neuroscience and cardiology. Nat Nanotechnol. 8,83-94 (2013).

[48] Pestova, O.N.et al. X-ray Phase Analysis of Structure of Water-Salt Systems: NaCl-H2O and KCl-H2O. Russian J of Appl Chem. 77,1066-1069 (2004)

[49] Novák M, et al. Solvent effects on ion-receptor interactions in the presence of an external electric field. Phys Chem Chem Phys. 18,30754-30760 (2016).

[50] Chen, K. et al, Electronic Properties of Graphene Altered by Substrate Surface Chemistry and Externally Applied Electric Field. J. Phys. Chem. C,, 116,6259–6267 (2012)

[51] Novoselov, K. et al., Two-dimensional gas of massless Dirac fermions in graphene. Nature.438, 197-200 (2005).

[52] González-Herrero, H et al. Graphene Tunable Transparency to Tunneling Electrons: A Direct Tool To Measure the Local Coupling. ACS Nano. 10,5131-44 (2016).

[53] Praveen, C. S. et al., Adsorption of alkali adatoms on graphene supported by the Au/Ni(111) surface, Phys Rev. B 92, 075403 (2015).

[54] Kang, Y-J. et al. Electronic structure of graphene and doping effect on SiO2 Phys Rev. B 78, 115404 (2008).

[55] Miwa, R. H. et al. Doping of graphene adsorbed on the a-SiO2 surface.Appl Phys Lett99, 163108 (2011).

[56] Ao, Z. et al. Density functional theory calculations on graphene/α-SiO2(0001) interface. Nanoscale Res Lett. 7,158 (2012).

[57] Fan, X. F. et al. Interaction between graphene and the surface of SiO2. J Phys Condens Matter. 24:305004 (2012).

[58] Terrones, M., et al. Graphene and graphite nanoribbons: Morphology, properties, synthesis, defects and applications. Nano Today, 5,351-372 (2010).

[59] Nezich, D. et al. Electrical characterization of graphene synthesized by chemical vapor deposition using Ni substrate. Nanotechnology 23, 015701 (2012).

[60] Slomowitz, E. et al. Interplay between population firing stability and single neuron dynamics in hippocampal networks. eLife 4: e04378 (2015).

[61] Bogaard, A. et al. Interaction of cellular and network mechanisms in spatiotemporal pattern formation in neuronal networks. J Neurosci. 29, 1677-1687 (2009).

[62] Sahasranamam, A. et al. Dynamical state of the network determines the efficacy of single neuron properties in shaping the network activity. Sci Rep. 6, 26029 (2016).

[63] Radulescu, R.A. Mechanisms Explaining Transitions between Tonic and Phasic Firing in Neuronal Populations as Predicted by a Low Dimensional Firing Rate Model. PLoS One 5:e12695 (2010).

[64] Naud, R. et al. Firing patterns in the adaptive exponential integrate-and-fire model. Biol Cybern. 99, 335-347 (2008).

[65] Wrobel G, Höller M, Ingebrandt S, Dieluweit S, Sommerhage F, Bochem HP, Offenhäusser A. Transmission electron microscopy study of the cell-sensor interface. J R Soc Interface. 5, 213-222. (2008).

[66] Braun, D. & Fromherz, P. Fluorescence interference-contrast microscopy of cell adhesion on oxidized silicon. Appl Phys A 65: 341-348 (1997).

[67] Nicholson, C, Phillips, J. M. Ion diffusion modified by tortuosity and volume fraction in the extracellular microenvironment of the rat cerebellum. J Physiol. 321, 225-57 (1981).

[68] Turrigiano, G. et al. Activity-dependent changes in the intrinsic properties of cultured neurons. Science 264, 974-977 (1994).

[69] Desai, N. S. et al. Critical periods for experience-dependent synaptic scaling in visual cortex. Nature Neurosci. 5, 783–789 (2002).

[70] Galante, M. et al. Opposite changes in synaptic activity of organotypic rat spinal cord cultures after chronic block of AMPA/kainate or glycine and GABAA receptors. J Physiol. 523, 639-651 (2000).

[71] Turrigiano, G. Homeostatic synaptic plasticity: local and global mechanisms for stabilizing neuronal function. Cold Spring Harb Perspect Biol. 4, a005736 (2012).

[72] Drieschner, S. et al. Frequency response of electrolyte-gated graphene electrodes and transistors. Journal of Physics D: Applied Physics 50, 095304 (2017).

[73] Drieschner, S. et al. High surface area graphene foams by chemical vapor deposition. 2D Materials 3, 045013 (2016).

[74] Matruglio, A. et al.Contamination-free suspended graphene structures by a Ti-based transfer method Carbon, 103, 305-310 (2016).

[75] Clements, J. D. & Bekkers, J. M. Detection of spontaneous synaptic events with an optimally scaled template. Biophys J. 73, 220-229 (1997).

[76] Sontheimer, H. & Ransom, C. Whole-Cell Patch-Clamp Recordings. Neuromethods 35, 35-67 Humana Press Inc., (2007).

[77] Ruscheweyh, R. & Sandkuhler, J. Lamina-specific membrane and discharge properties of rat spinal dorsal horn neurones in vitro. J Physiol. 541, 231-244 (2002).

[78] La Camera G, et al The response of cortical neurons to in vivo-like input current: theory and experiment: I. Noisy inputs with stationary statistics. Biol Cybern 99:279–301(2008).

[79] Ricciardi, L. M. Diffusion Processes and Related Topics in Biology. Lecture notes in Biomathematics. Springer-Verlag (1977).

[80] Hines, M. L. et al. Model DB: A Database to Support Computational Neuroscience. J Comput Neurosci. 17, 7-11 (2004).

Acknowledgement

We are grateful to M. Lazzarino for experimental assistance in the fabrication of suspended SLG. We thank A. Laio, G. Scoles and B. Cortés-Llanos for helpful discussion. This paper is based on work supported by the European Union Seventh Framework Program under grant agreement no. 696656 Graphene Flagship and by the Flanders Research Foundation (grant no. G0F1517N). MP, as the recipient of the AXA Chair, is grateful to the AXA Research Fund for financial support. MP was also supported by the Spanish Ministry of Economy and Competitiveness MINECO (project CTQ2016-76721-R), by the University of Trieste and by Diputación Foral de Gipuzkoa program Red (101).

Contributions

N.P.P. performed electrophysiological experiments, immunochemistry, confocal microscopy and all the related analysis; M.L. fabricated supported SLG and MLG

and performed all material characterization; M.G. performed mathematical simulations and analysis and contributed to the writing of the manuscript; A.M. fabricate suspended SLG and gold plated samples; F.D.A. and A.M. performed Raman experiments and data analysis on SLG and MLG in wet and dried conditions; M. P., D.S. and L.B. conceived the study; D.S., L.B., and J.A.G. designed the experimental strategy, interpreted the results and wrote the manuscript.

Additional information

Supplementary information is available in the online version of the paper.

Correspondence and requests for materials should be addressed to Denis Scaini dscaini@sissa.it; Josè Antonio Garrido joseantonio.garrido@icn2.cat; Laura Ballerini laura.ballerini@sissa.it

Competing financial interests

The authors declare no competing financial interests.

Data availability

All the data that support the findings of this study are available within the article and in its Supplementary Information, and these data are available from the corresponding author on request.

SUPPLEMENTARY INFORMATION

Supplemental methods in neuronal network simulation

In our numerical simulations of a networks of interacting excitatory and inhibitory neurons, the electrical response properties of each cell are approximated by those of a *leaky* Integrate-and-Fire unit. In this model, characterized by a lumped membrane capacitance C_m and R_m, the membrane potential of the neuron *V(t)* passively integrates incoming synaptic input currents I_{syn}, around a resting membrane potential E_m and while below the excitability threshold V_θ:

$$C_m \frac{dV}{dt} = \frac{(E_m - V)}{R_m} + I_{syn} \qquad V < V_\theta \tag{S1}$$

As *V* reaches V_θ, the unit is said to *fire* a spike and *V* is reset and hold to a hyperpolarized voltage V_H, for the entire duration of an absolute refractory period τ_{arp}:

$$V(t^*) = V_\theta \qquad V(t) \to V_H \;\; t \in (t^*;\; t^* + \tau_{arp}] \tag{S2}$$

Synaptic interactions are described as current-driven impulsive inputs, where a (train of) presynaptic spike occurring at time t_k is received postsynaptically as a (train of) Dirac's Delta function with a net charge of Δ:

$$I_{syn} = \sum_k \Delta\, \delta(t - t_k) \tag{S3}$$

When the occurrence times $\{t_k\}$ are statistically independent and occurring as stochastic Poisson-distributed events with mean frequency λ, the mean spiking rate ν of a generic unit of the network can be approximated by an analytical expression (Ricciardi, 1977) that is valid as long as λ is very large and Δ is very small (i.e. while the product $\lambda\Delta$ remains finite):

$$\nu = \phi(\mu, \sigma) = [\tau_{arp} + R_m C_m \int_A^B \sqrt{\pi} e^{x^2} (1 + \mathrm{erf}(x)) dx]^{-1} \tag{S4}$$

where $A = \frac{V_\theta - E_m - R_m\mu}{\sigma\sqrt{R_m/C_m}}$ and $B = \frac{V_H - E_m - R_m\mu}{\sigma\sqrt{R_m/C_m}}$, with $\mu = \Delta\,\lambda$ and $\sigma = \Delta\sqrt{\lambda}$.

This expression can be included in a rate-based model, where the activity of individual units is however accounted for implicitly: if synaptic inputs can be considered as statistically identical, then only one equation can be used for describing the evolution in time of the

$$\tau\frac{d\nu}{dt} = -\nu + \phi(\mu, \sigma) \qquad \text{(S5)}$$

Supplementary Figure S1 a, Histograms summarizing the average PSC frequency values (left) and the average PSC amplitudes ones (right) for neurons developed on supported SLG transferred using PMMA (in grey), or PS (in red). SLG induce in neurons' PSCs similar effects when the carbon film is transferred through PMMA or PS. **b**, SLG Raman spectra of G band in dry condition. Control condition (air, in black) is compared with spectra of graphene previously immersed in 4 mM D_2O of KCl (in red) and 150 mM solution of NaCl (in green). Note that, differently from the wet experiments depicted in Figure 6a, NaCl induce now in SLG a larger shift in G-Peak position than KCl (see inset).

Figure 1

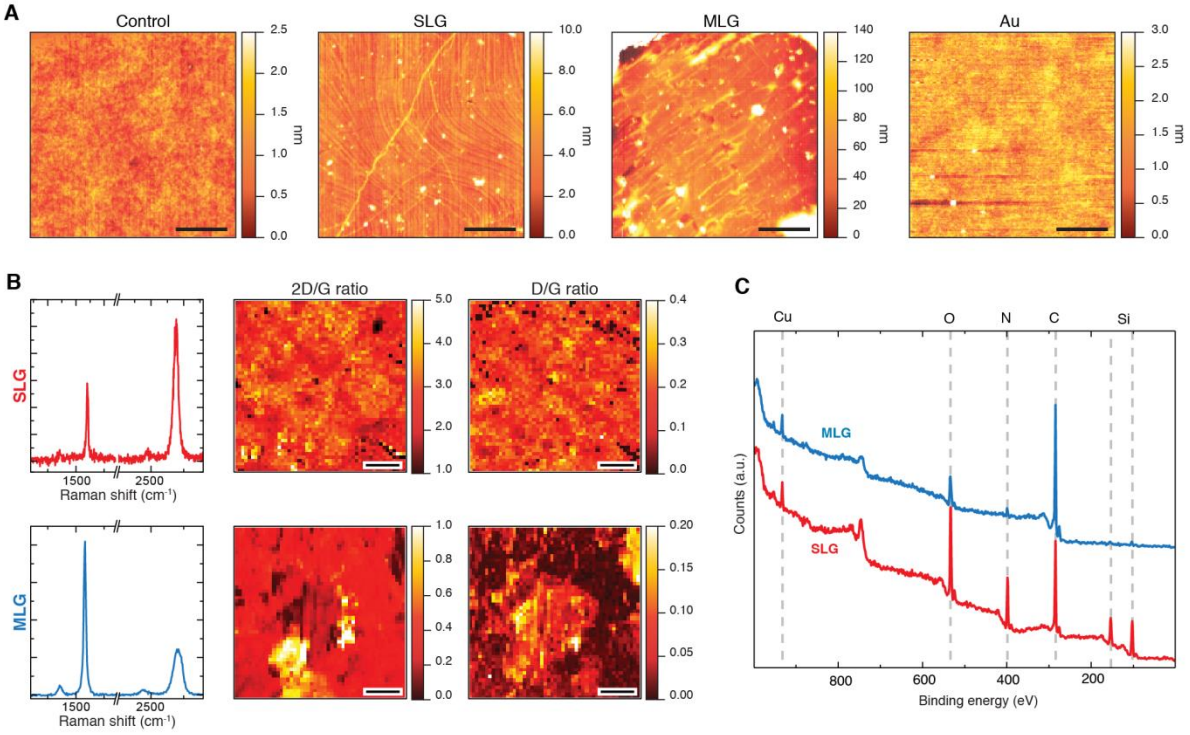
A
Control
SLG
MLG
Au
nm
B
SLG
MLG
2D/G ratio
D/G ratio
Raman shift (cm⁻¹)
1500
2500
C
Cu
O
N
C
Si
MLG
SLG
Counts (a.u.)
Binding energy (eV)
800
600
400
200

Figure 2

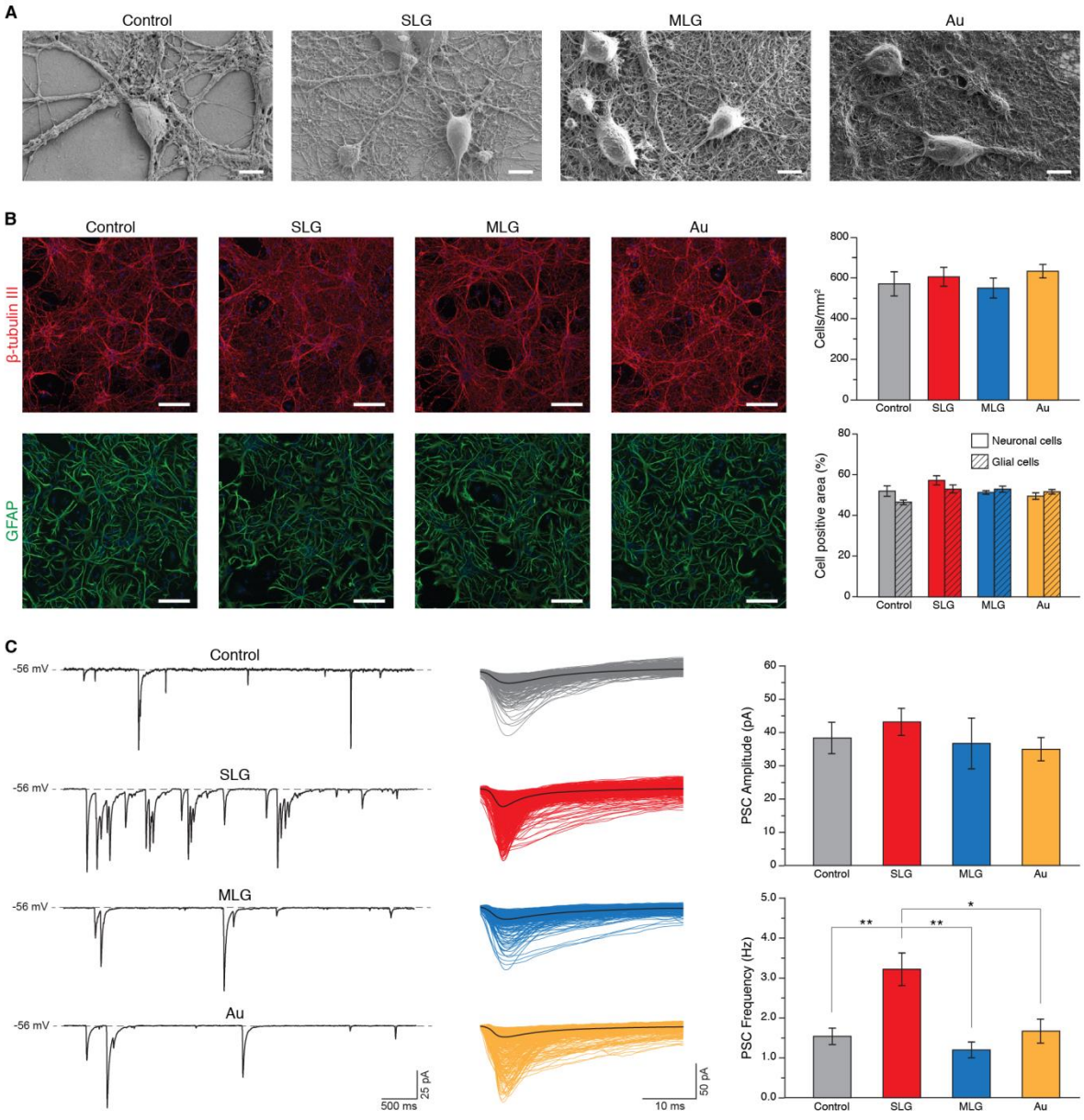
A
Control
SLG
MLG
Au
B
Control
SLG
MLG
Au
β-tubulin III
GFAP
Cells/mm²
Control
SLG
MLG
Au
Neuronal cells
Glial cells
Cell positive area (%)
C
Control
-56 mV
SLG
-56 mV
MLG
-56 mV
Au
-56 mV
25 pA
500 ms
50 pA
10 ms
PSC Amplitude (pA)
PSC Frequency (Hz)
**
**
*

Figure 3

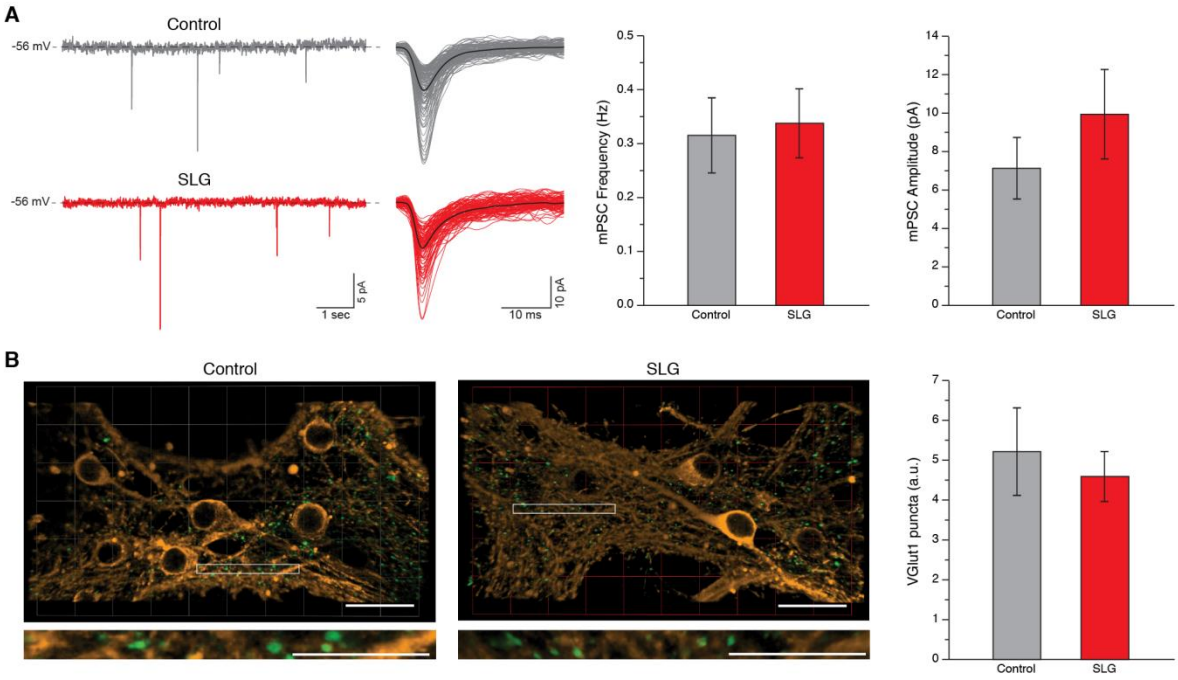
A
Control
-56 mV
SLG
-56 mV
5 pA
1 sec
10 pA
10 ms
mPSC Frequency (Hz)
0.5
0.4
0.3
0.2
0.1
0.0
Control
SLG
mPSC Amplitude (pA)
14
12
10
8
6
4
2
0
Control
SLG
B
Control
SLG
VGlut1 puncta (a.u.)
7
6
5
4
3
2
1
0
Control
SLG

Figure 4

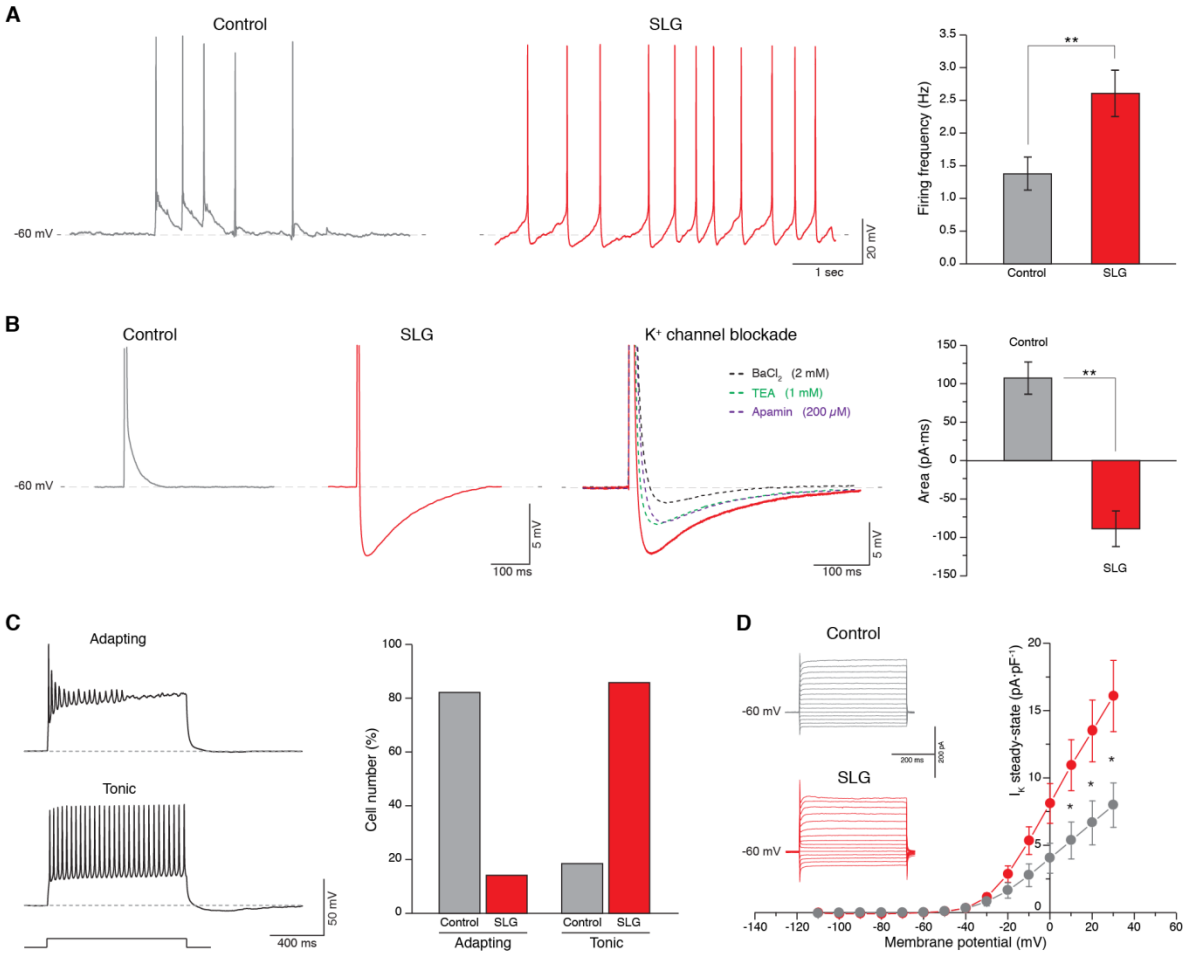
A
Control
SLG
-60 mV
1 sec
20 mV
Firing frequency (Hz)
Control
SLG
B
Control
SLG
K+ channel blockade
BaCl2 (2 mM)
TEA (1 mM)
Apamin (200 μM)
-60 mV
5 mV
100 ms
Area (pA·ms)
C
Adapting
Tonic
50 mV
400 ms
Cell number (%)
Control
SLG
Adapting
Tonic
D
Control
SLG
-60 mV
200 ms
200 pA
Ik steady-state (pA·pF-1)
Membrane potential (mV)

Figure 5

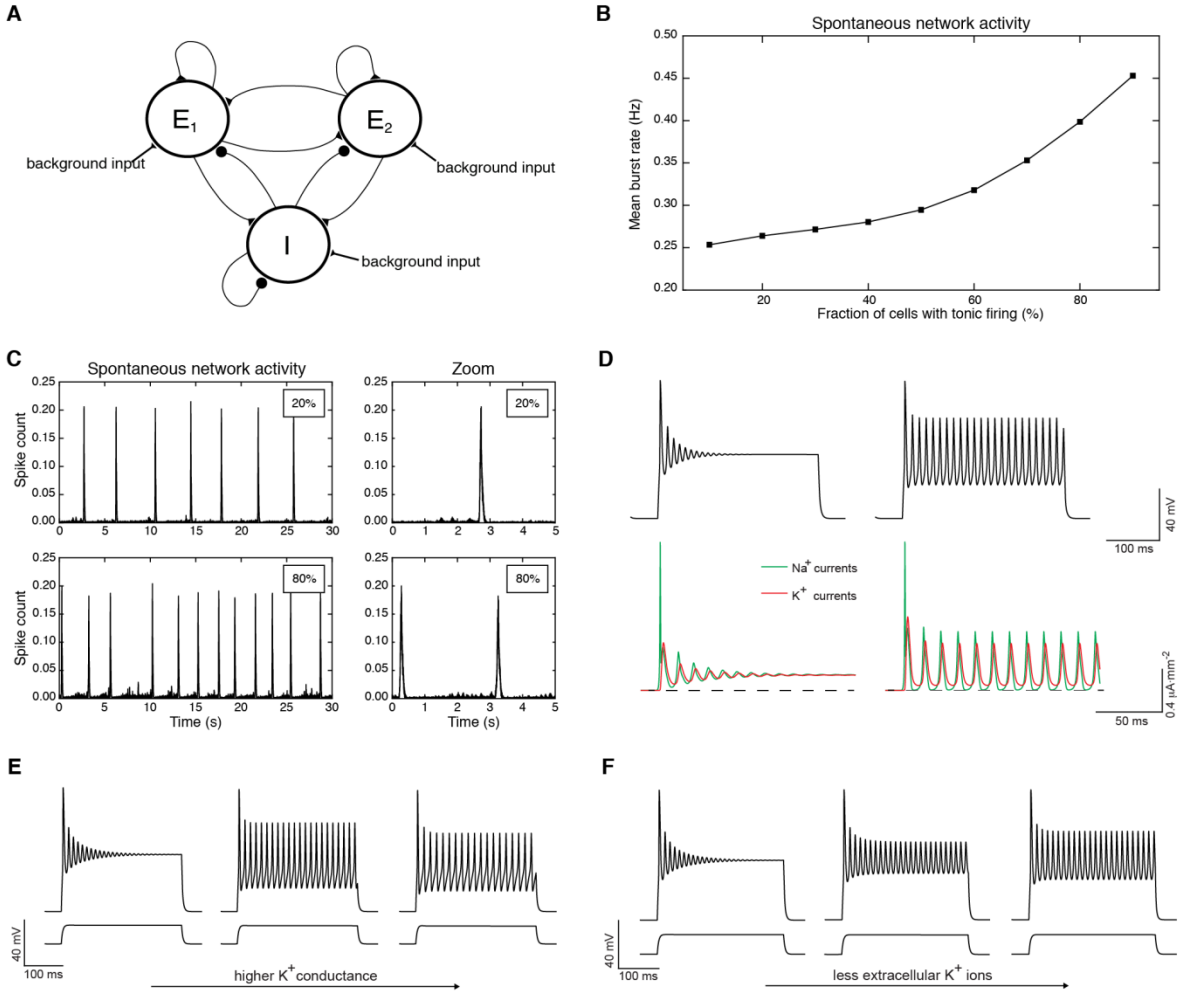
A
E1
E2
I
background input
background input
background input
B
Spontaneous network activity
Mean burst rate (Hz)
Fraction of cells with tonic firing (%)
C
Spontaneous network activity
Zoom
Spike count
20%
80%
Time (s)
D
Na+ currents
K+ currents
40 mV
100 ms
50 ms
0.4 µA mm-2
E
40 mV
100 ms
higher K+ conductance
F
40 mV
100 ms
less extracellular K+ ions

Figure 6

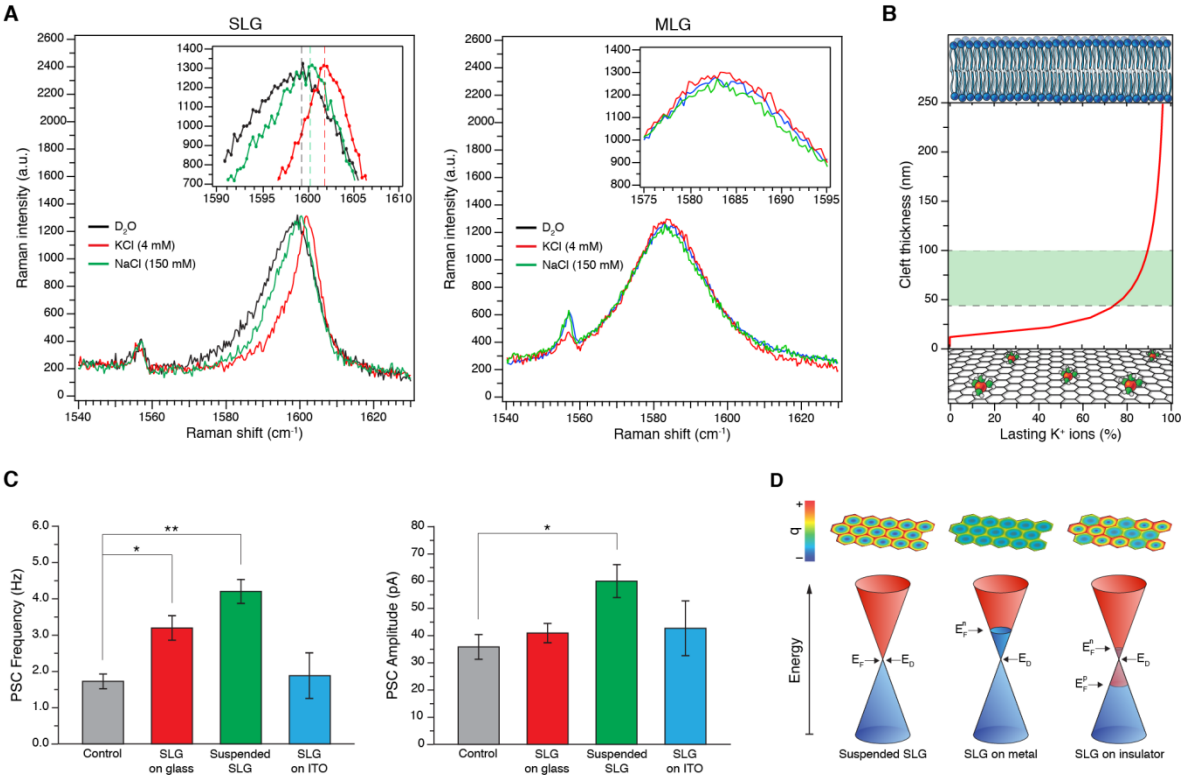

Figure S1:

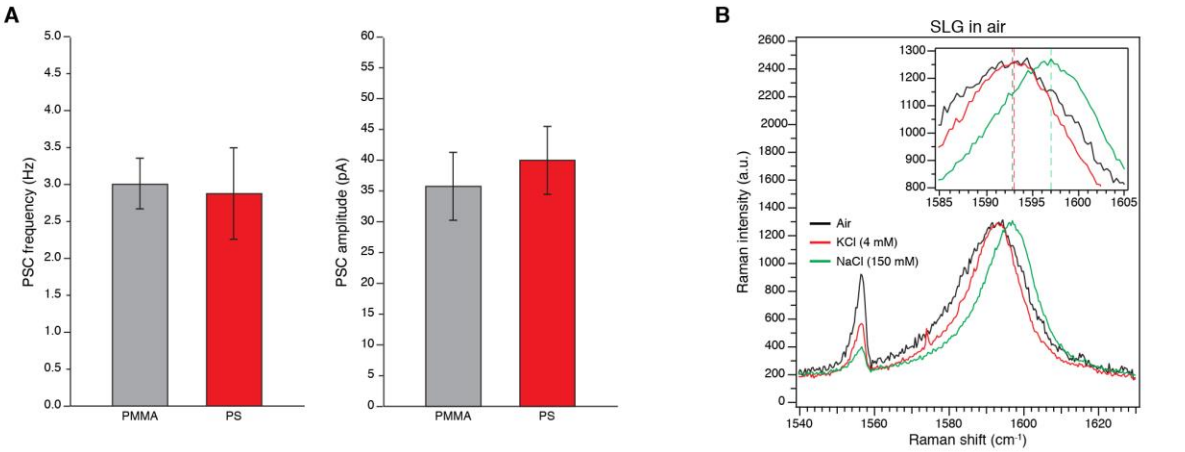

Transparent Carbon Nanotubes (tCNTs) guide the reconnection of lesioned entorhinal hippocampal organotypic cultures

Niccolò P. Pampaloni[1a], Ilaria Rago[2a], Ivo Calaresu[1a], Laura Ballerini[1*], Denis Scaini[1,2*].

[1] International School for Advanced Studies (SISSA), Trieste, Italy.

[2] ELETTRA Synchrotron Light Source, Trieste, Italy

[a] these authors equally contributed to the work

ABSTRACT

In the field of medical engineering and tissue regeneration, nanomaterials are increasingly employed in manufacturing bio-interfaces with controlled physico-chemical cues at the nano-scale. Carbon Nanotubes (CNTs) have been employed to build a variety of neurodevices because of their promising physical properties, in particular the high electrical conductivity; to note, CNT carpets have also shown their unique ability to safely interact and potentiate neuronal networks. The major limitation in further developments based on CNTs, is their relative scarse transparency, not allowing, for example, direct tissue illumination when adopted as growth scaffolds. In the present work, we developed a new method to fabricate CNTs by growing them on a fused silica surface, which result in a transparent CNT-based substrate (tCNTs). After testing the tCNTs biocompatibility as growth substrates for cultured brain cells, we further exploit them to support the growth of intact and lesioned Entorhinal-Hippocampal slice cultures (EHCs). We combined Immunofluorescence microscopy and electrophysiological field potential recordings, to show that tCNTs platform are suitable substrates for the growth of EHCs. In lesioned preparations, we unmask tCNTs ability to significantly increase the signal synchronization and fiber sprouting between the cortex and the hippocampus with respect to controls. The transparency alongside their ability to enhance the reconnection of lesioned brain tissue

areas, make tCNTs optimal candidates to be employed in the new generation of implantable devices in regenerative medicine and tissue engineering.

INTRODUCTION

In medical Neuroscience, the treatment of a variety of pathologic conditions, ranging from Neurodegenerative diseases [1] to Traumatic Brain Injuries (TBI; [2] [3] [4]) to Psychiatric disorders [1], involve the use of assistive implantable devices that are inserted into target brian areas, with the aim to restore the loss functions [5]. In this framework, the Nanotechnology development carried huge advances [6], by allowing the construction of artificial prosthetic devices and scaffolds with nano-sized features, able to instruct the interfaced neural tissue at the cellular and subcellular level [7] [8] [9]. Among the various materials used to build up nano-devices, a great interest was recently received by Carbon based materials such as Carbon Nanotubes (CNTs; [10]), because of their suitable physico-chemical features [11] and their peculiar ability to finely interact with neuronal cells [12] [13] and neural tissues [14] [15]. CNTs have been employed in the fabrication of a variety of neural interfaces [16] [17], such as retinal implants [18] or deep brain stimulators [19]. Furthermore, CNTs have shown a strong regenerative impact on the reconnection of mammal spinal cord explants *in vitro* [20] [14] [15], but their ability on other explanted araes of the central nervous system (CNS) has not been tested yet. This is also due to the fact that CNTs carpets are dark structures which do not allow the passage of visible light, thus preventing the exploitation of all the techniques and methods which require “to see” through the specimens, such as electrophysiology or bright field microscopy, or any application requiring to illuminate the specimens. In this study we developed a new method of fabricating CNTs on fused Silica, which result in a transparent CNT (tCNTs) platform: by means of electrophysiology and immunocytochemistry experiments, we show that this new CNT carpet is able to induce the reported synaptic potentiation in hippocampal cells [12] [13] [21], alongside with a correct maturation of dissociated neurons and glial cells. Furthermore, in order to understand the possible regenerative effects of this material with

a more complex brain structure, we interfaced for the first time this substrate with Entorhinal-Hippocampal organotypic cultures (EHCs). We exploited the Perforant Pathway lesion model, which was further modified by the outdistancing of the Hippocmapus from the Entorhinal Cortex roughly 0.5 mm apart. This condidion better resembles the mechanical injuries of the CNS in which the trauma would cause a separation of previously nearby tissues, [4]. We report here a tremendous impact of tCNTs carpets on the EHCs fiber sprouting ability, which ultimately lead to a functional and anatomical reconnection of the two brain structures. The results presented here, make tCNTs excellent candidates as the material to be employed in future neural prostheses and implantable neural interfaces.

RESULTS

tCNTs synthesis and characterization.

tCNTs were synthesized via catalytic chemical vapor deposition (CCVD) directly on an iron thin film deposited on fused silica substrates (without the employment of any adhesion layer) and running the growth for just 90 sec. In CCVD synthesis of CNTs, catalyst plays a crucial role since the nanoparticles resulting from the annealing treatment act as starting sites for the subsequent CNTs growth [22]. Size and density of these nanoparticles are strongly related to annealing treatment parameters (i.e. temperature and duration) and to the features of the initial catalyst layer (i.e. thickness and adhesion to the underneath substrate; [23]). In the attempt of enhancing nanotubes yield, other research groups have previously adopted one or even more intermediate metallic layers as adhesion and/or anti-diffusion layer between the catalyst and the underneath support [24] [25]. Moreover, it was reported that by setting the annealing treatment conditions at 720 °C for 3 hours and the growth parameters at 720 °C for 1 hour, it is possible to obtain vertically aligned CNTs (VACNTs) on various supports [26]. A huge asset of our synthesis method is that although no

adhesion metal was employed and even if the growth time was limited to merely 90 sec, the yield, reproducibility, and density of the as-produced CNTs are comparable with that of similar carbon nanostructures produced by using more time-consuming methods. FE-SEM imaging was performed on CNTs mat in order to investigate the tubes diameter, length, uniformity and density. Analysis of side view SEM micrograph (Fig. 1a) showed vertical aligned CNTs, oriented perpendicularly to the surface substrate. Instead, the TOP view revealed a random orientation (Fig. 1b). Such morphology is driven by the proximity effect of densely distributed catalyst nanoparticles forcing the initially randomly oriented CNTs into a vertical alignment [27]. TEM characterization was conducted on carbon nanotubes to explore their structure and crystallinity. It has been found that CNTs consist of multi-walled nanotubes (MWCNTs) with different wall number. Specifically, Fig. 1c shows an isolated MWNT with an outer diameter (OD) of less than 20 nm and an inner diameter (ID) of approximately 10 nm. These measurements are consistent with 15 nanotube walls (Fig. 1d). In addition, TEM analysis revealed the presence of structural defects (Fig. 1c), generally imperfections of conjugated sp2 carbon along the tubes, such as breaks, sp3 hybridized carbon atoms, Stone-Wales defects (i.e., two heptagons and two pentagons), probably ascribed to the low growth temperature (730 °C). [28] [29] .The degree of structural ordering and the quality of CVD-grown CNTs were evaluated by Raman spectroscopy. The two main bands typical of all graphite-like materials, including MWCNTs, present in Raman spectra (Fig. 1f) correspond to: the G band at ~1583 cm-1 related to the in-plane tangential vibration of sp2 carbon atoms resulting from the graphitic nature of CNTs and the D band at ~1330 cm-1 indicating the presence of amorphous and/or low ordered carbon structure (carbonaceous impurities with sp^3 bonding, and broken sp^2 bonds in the sidewalls [30]). The ratio between the D (ID) and G (IG) band integral intensities was usually adopted as indicator of CNTs quality. Specifically, similar intensities of these bands [31], as in our case, suggested the presence of non-graphitic carbon in nanotubes, typical for low temperature CVD-grown CNTs [32]. Together with the G band, the second-order Raman peak G' is characteristic of graphitic sp2 materials and is located at ~2700 cm-1. The G' band, an overtone mode of the D band [33], is associated with defect density, but not as crucially as

the first order mode. It was also reported that the intensity of this peak depends significantly on the metallicity of CNTs [34]. Other peaks located at ~1698 cm-1 and at ~1759 cm-1 are related to ν C=O vibration [35] [36], and indicate a possible partial oxidation of MWCNTs.

From the XPS survey spectrum of CNTs (Fig. 1e) three elements can be discriminated: carbon (C1s), oxygen (O1s) and silicon (Si2s, 2p). The amount of C and O are 87.6 at% and 10 at%, respectively. Moreover, a small amount (2.4 at%) of Si was detected. The presence of oxygen on CNTs surface is intrinsically related to the CVD method and, in particular, to defects formed during CNTs synthesis which show a tendency to adsorb oxygen when exposed to air. Fig. 1g indicates the C1s core level for ~ 8 μm-long CNTs. A Shirley background has been subtracted. The most intense peaks located at 284.7 eV and 285.8 eV can be assigned to sp2-hybridized graphitic carbon atoms located on CNTs walls and to amorphous carbon (sp^3-hybridized carbon atoms), respectively [37] [38]. The amorphous carbon is likely due to the CNTs synthesis process, as confirmed by the structural defects identified via TEM (Fig.1c) and Raman spectroscopy (Fig. 1f); the peak at 290.8 eV corresponds to the electron energy loss peak due to π-plasmon excitations. These three peaks are characteristics of C1s core level from CNTs [39]. The additional small peaks at 287.15 eV and 288.4 eV are assigned to the presence of oxygen [39].

tCNTs interfacing dissociated primary neurons

Carbon Nanotubes carpets have been widely characterized as platforms to grow neural cultures, and their effects on hippocampal primary cells are well described [12] [21] [13]. Being the result of a new synthetic process, our first concern was to understand if tCNTs were suitable substrates for neural growth and if they would modulate synaptic activity similarly to what reported for traditional, dark MWCNTs [12] [21]. To this aim, we cultured dissociated primary hippocampal neurons onto tCNTs. By immunofluorescence experiments, we visualized neurons and glial cells, targeted respectively with βTubIII and

GFAP antibodies, to evaluate the network morphology, which was found to be similar in tCNTs and control cultures (Fig. 2a). We further quantified the neuronal and glial cell density after 8-10 days of growth in vitro: as shown in the histograms of Fig.2b, we found comparable numbers of neurons and astrocytes developed in controls and tCNTs substrates, indicating that tCNTs are allowing a correct growth of cells, and are not inducing major toxic effects. We next compared the activity of neurons by means of whole cell patch clamp recordings. Since the appearance of PSCs provides clear evidence of functional synapse formation and is a widely accepted index of network efficacy, we monitored the occurrence of spontaneous postsynaptic currents (PSCs) in both conditions. The activity recorded from hippocampal neurons plated onto tCNTs carpets was found to be significantly enhanced compared to controls (controls: 1.3 ± 0.1 Hz; n=40; tCNTs: n=59; 1.8 ± 0.1 Hz; p=0.03; data from n=7 culture series), while amplitudes were not affected significantly by the tCNT substrate (controls: 30 ± 2.8 pA; tCNTs 44 ± 5 pA; p=0.10; Fig..), as membrane passive properties Input resistance (controls = 790 ± 104 MΩ; tCNTs =587 ± 67 MΩ; p=0.10) and membrane capacitance (control = 34 ± 2 pF; tCNTs 39 ± 3 pF p=0.20). As the increased PSC frequency, associated with similar values of either PSC amplitudes and passive membrane properties, is the widely addressed hallmark of classic CNTs substrates on dissociated hippocampal neurons [12] [21] [13], we concluded that tCNTs are comparable, in terms of functional effects induced in neurons, to the previously tested dark MWCNTs [12] [21], and we therefore decided to test their effects on a more complex brain in vitro model, such as the EHCs organotypic cultures.

Organotypic Entorhinal-Hippocampal cultures growth onto tCNTs

We know from previous studies that CNT-based substrates possess, to a certain extent, regenerative features for spinal cord organotypic cultures [14] [15], and we therefore wondered if tCNTs would preserve these effects when tested on brain areas such as the cortical ones. As shown in Fig.3, intact (top panels) EHC successfully grew onto tCNTs substrates, similarly to controls. We then simulated a lesion at the subicular level and

outdistanced the cortex from the hippocampus 400 to 600 μm apart, (Fig. 3, lower panels) to mimic *in vitro* a traumatic event in which the cortical areas undergo to a separation due to mechanical injury. Transecting the hippocampal formation at the subicular level leads to the disruption of the main excitatory pathway that from the cortical areas reaches the hippocampus, known as the Perforant Pathway (PP; [40]). Lesioning the PP at the subicular level has already been exploited as a lesion model model [41] [42] [43] because, as the lesion site is relatively distant from the Dentate Gyrus, degenerative/inflammatory effects due to the lesion itself are easily discriminated from the regenerative effects of post-lesion circuit re-organization observed in the hippocampus [41]. Furthermore, it is known that the de-afferentation caused by the PP interruption, lead to a lamina-specific re-arrangement of the fibers and dendrites of mature granule cells [41] [43], which may potentially be instructed by a certain artificial cues provided by the physico-chemical features of a certain material, such as CNTs. As shown in Fig. 3, transected EHCs were successfully grown either on control and tCNTs substrates, and no major morphological differences were observed with respect to their un-lesioned counterparts (Fig.3).

tCNTs favours synchronized entorhinal-hippocampal activity

We next evaluated the electrical activity of the slices by extracellular Local Field Potentials (LFPs) simultaneous co-recordings. Under microscopy, we placed one electrode in the molecular layer of the DG (a major hippocampal hub of the Perforant Pathway), while a second electrode was positioned within the deep layer (IV/V) of the EC, where the Pathway should end (sketched in Figure 4a for control and 4d for tCNT). In all recordings, spontaneous LFPs were detecetd by both electrodes before and after adding bicuculline, a blocker of ionotropic $GABA_A$ receptors used to enhance the signal synchronization. We observed no significant changes in LFP frequency in tCNT-interfaced cultures, when compared to controls, in whole (control: DG = 0.3 ± 0.05 Hz and EC = 0.22 ± 0.08 Hz, n=7;

tCNT: DG = 0.25 ± 0.05 Hz and EC = 0.21 ± 0.04 Hz; n=5; p = 0.75 and p = 0.89 respectively; n=8 number of slices for controls and n=5 for tCNTs) and in lesioned slices (control: DG = 0.1 ± 0.03 Hz and EC = 0.05 ± 0.01 Hz, n=9; tCNT: DG = 0.2 ± 0.03 Hz and EC = 0.1 ± 0.01 Hz, n=4; p = 0.16 and p = 0.55; Fig. 4b, 4e; n=9 for controls and n=4 for tCNTs). Bicuculline application is known to induce in hippocampal slices a low-frequency oscillation (LFO) activity, manifested as a slow pace highly synchronized occurrence of LFPs [44] [45]. Indeed, a similar decrease in the frequency of LFPs was observed either in whole (control: DG = 0.23 ± 0.06 Hz and EC = 0.15 ± 0.04 Hz; tCNTs: DG = 0.08 ± 00.02 Hz and EC = 0.09 ± 0.03 Hz; p = 0.67 and p = 0.17 respectively; n=) and lesioned cultures (control: DG = 0.05 ± 0.01 Hz and EC = 0.03 ± 0.01; tCNTs: DG = 0.07 ± 0.01 Hz and EC = 0.08 ± 0.01 Hz; p = 0.59 and p = 0.13; Fig. 4b, 4e). Furthermore, when we measured the Entorhinal-Hippocampal LFP synchronization we found a profound impact of the tCNTs substrates, that induced a strong increase in the signal synchronization, measured as Pearson correlation coefficient (CCF) which statistical significance was determined by a permutation test (see methods). In unlesioned cultures, 43% of controls displayed Entorhinal-Hippocampal synchronized activity in standard krebs with a mean CCF of 0.34 ± 0.1. In the presence of Bicuculline, this value increased to the 86% of samples (mean CCF of 0.52 ± 0.11; Fig. 4c). Interestingly, 100 % of tCNT cultures were synchronized (mean CCF = 0.55 ± 0.18) when already in standard extracellular solution, and this percentage did not change in the presence of bicuculline (mean CCF = 0.67 ± 0.13; p=0.01; Fig. 4f). Still, the most striking impact of tCNTs substrates on the signal synchronization degree between the EC and the DG was found when interfaced with lesioned slices. As shown in Fig. 4e, control lesioned cultures displayed correlated signals only in the 11% of cases in standard Krebs (mean CCF = 0.39 ± 0.11); a value which increased to 33% of correlated signals upon Bicuculline application (with a mean CCF = 0.66 ± 0.11). Since this measures reflect a condition in which the PP had been transected and the resulting slices were outdistanced, we expected at least a decrease (if not a total absence) of the DG-EC signal synchronization with respect to unlesioned slices, because of the anatomical lack of fibers needed to carry the signals. The observed presence of a synchronized activity, even if lowered, should reflect the slice ability to sprout new

fibers able to re-connect the two parts of the organ. Lesioned EHCs interfaced to tCNTs carpets displayed a synchronization degree of 50% when recorded in standard krebs (mean CCF = 0.58 ± 0.21; Fig. 4e); surprisingly this value raised to a full synchronization (100% of signals were correlated; mean CCF = 0.9 ± 0.06; Fig. 4e) of the recorded signals, when $GABA_A$ receptors were blocked with Bicuculline. This result is particularly important because is reflecting an increased ability of the nervous tissue, if interfaced with tCNTs, to functionally re-connect after a sort of lesion.

tCNTs induce an increased axonal sprouting in lesioned cultures

To further assess the functionality of the "crossing-fibers" in lesioned slices, we next decided to stimulate the Perforant Pathway [46]: the recording electrodes were left in the same configuration used for LFPs co-recordings (one into the DG and the other into the EC deep), while the stimulating electrode was placed in the superficial layers of the EC (see Fig.5b, cartoon inset), where the Perforant Path is known to begin [47] [48]. To have a further confirm that this pathway was well preserved in our culture conditions, we first decided to label it by the injection of Chorera Toxin subunit B (CTB), a well known retrograde tracer [49] [50], into the molecular layer of the DG. As Shown in Fig.5a, 24 hours post-injection, we found a large majority of CTX-labelled nuclei into the superficial layers of the EC, confirming that in our intact preparations, the PP was well preserved. We therefore proceeded with the PP stimulation (see methods), and we classified three major classes of responses (Fig.5b): detection of evoked LFPs exclusively in the DG, or in the EC or in both areas. As shown in Fig.5b, we always detected a response in both DG and EC in entire slices either in controls and tCNTs, while in the case of lesioned ones, we found marked differences between the two groups. In control slices we found a dual response both in DG and EC only in the 12.5% of cases, while in tCNTs-interfaced cultures we always found a response in both areas. This evidence further strengthens the hypothesis that the slices are functionally connected when cultured onto tCNT platforms. Finally, we wondered whether the tCNT-related increased activity synchronization was also reflecting an increased re-

generation of axons which would be able to carry the electro-chemical signals. In fact, at time 0, that is immediately after the lesion, there are no fibers crossing the gap, while, along with the culturing, sparse fibers tend to regrowth (Figure 5c). By immunofluorescence we visualised SMI32-positive axons (see methods) crossing the gap between the two cortical structures ("crossing-fibers"): as shown in Fig.5c, we found that cultures grown on tCNT displayed a significant increase of SMI32-positive fibers sprouting into the lesioned area with respect to the control counterparts (control: n=7 number of slices, tCNT: n=6; p=0.02; Fig.5c, right). Considering the previously described increase in LFP synchronization observed in tCNT-lesioned slices compared to controls, this result would strongly indicate the tCNT platforms are able to induce on EHCs cultures an increased expression of functionally-active neural processes that are able to establish an active cross-talk between the two parts of the organ.

DISCUSSION

CNTs have received an increasing attention during the last decade in the field of tissue engineering [51] and nanomedicine [52] [53] as they present unique features [11] which could be exploited to build up nano-devices and neural interfaces [54] [16]. In this study we report for the first time the development of a CNT composite which is not optically dark [55], as the usual CNT scaffolds, but allows the passage of visible light and possess the potentiating [12] [21]and regenerative [15] [14] effects previously observed on neurons grown onto "standard" CNTs carpets. In particular, we showed that the growth of dissociated hippocampal onto tCNTs carpet is comparable, in terms of neuronal and glial density, to the one of controls cultures, and that neurons grown onto tCNTs meshworks display a significantly higher synaptic activity, measured as an increase in PSCs frequency. These results are in line with previous work in which we showed comparable effects of the

standard CNTs on the same kind of in vitro model, and therefore (as the CNT-related "landmark effects" in terms of boosting the network activity were maintained [21] [13] [12]) we proceeded with the interfacing of a more complex brain structure. Because the understanding of the regenerative effects of this material is of fundamental need in case of its involvement in the construction of implantable neural devices, we interfaced it for the first time with organotypic EHCs cultures, a complex 3D explant of the CNS in which the functional and anatomical connections are preserved [56] [57]. We observed the effect induced by the substrate in entire and lesioned slices: in the latter case, by mechanically lesioning the cultures at the subicular level and outdistancing the resulting parts $\simeq$ 0.5 mm apart, we simulated a severe traumatic injury of the CNS. As CNT scaffolds were shown to induce regenerative features on spinal cord segments [14] [15], we were interested to understand if those benefits would have maintained even on complex structures of the brain itself, such as the cortical and sub-cortical ones. We show here that tCNTs allow a correct growing of the whole EHCs explants and increased the degree of synchronization between the hippocampus and the entorhinal cortex. Surprisingly, the regenerative effects of tCNTs were most clear when interfaced with lesioned EHCs cultures, as in this latter case we observed a 4-fold increase in the percentage of correlated signals (50 % of the cultures, against the 11 % in controls) between the hippocampal DG and the EC in standard Krebs, which raised to the 100 % of the slices, when cultures were superfused with the $GABA_A$ antagonist Bicuculline. This result strongly suggests that tCNT promote successful re-innervation between the two excised explants after the lesion. Our hypothesis was further confirmed by the experiments on lesioned slices in which we evoked LFPs by artificially stimulating the PP: in the case of lesioned slices interfaced to tCNTs in fact, we always detected a dual response (both in the DG and EC), while regarding control cultures, a concomitant response in the DG and EC was observed only in the 12.5% of cases. Finally, we demonstrated that changes in axonal regrowth may account for the enhanced correlated activity observed in tCNT cultures, as tCNT-related cultures displayed a significantly higher amount of SMI32-positive fibers between the Hippocampal and Entorhinal explants.

By introducing a new method to synthesize CTN and demonstrating for the first time the benefits that this substrate is bringing to lesioned organotypic EHCs cultures, we strengthened the current knowledge of the CNT effects on neuronal ensembles: tCNTs, with their peculiar transparency coupled to the regenerative effects they induce on the CNS-derived tissue, stand as a promising material to be exploited in a broad range of application in modern neuroscience, ranging from the construction of research tools to the building of medical devices and neural prostheses.

METHODS

tCNTs synthesis

Multi-walled carbon nanotubes were synthesized by the catalytic decomposition of acetylene (carbon source) over an iron catalyst thin layer using fused silica (SiO_2) wafer chips as supporting substrates [58]. The wafers were manually cleaved into 15x15 mm^2 samples using a diamond scribe and cleaned by Radio Corporation of America (RCA) method [59]. This was followed by the deposition of thin iron layer (0.2–1 nm in thickness) directly on the SiO_2 chips using electron beam (e-beam) evaporation. Iron film thickness was monitored with an in-situ quartz crystal microbalance. Since the uniformity of the catalyst layer is crucial for CNTs growth, an average deposition rate of 0.2 Å/sec was adopted. Subsequently, the as-evaporated substrates were located on the heating element inside the high vacuum reaction chamber. An annealing treatment (4 min at 650–670°C in H_2 atmosphere) was performed to reduce iron oxides possibly present on film surface, as a result of the exposition to atmospheric air conditions during transfer from the metal deposition system to the CCVD reactor, and to break down the continuous iron layer into nanoparticles which subsequently act as nucleation sites for CNTs growth. Once the pre-treatment process was over, the carbon source was immediately introduced in the reaction chamber up to a partial pressure of 10–20 mbar. Sample temperature was increased to

730°C and reaction time was limited to 90 sec, resulting in the formation of a uniform carpet of CNTs of less than 10 µm in thickness. After that, the samples were cooled down to room temperature and employed as removed from the reaction chamber.

tCNTs characterization

Field Emission Scanning Electron Microscopy (FE-SEM) imaging was performed on the as-produced CNTs using a Gemini SUPRA 40 SEM (Carl Zeiss NTS GmbH, Oberkochen, Germany) operating at an accelerating voltage of 5 keV. Transmission electron microscopy (TEM) of CNT carpets was performed using an EM 208-Philips TEM system equipped with Quemesa (Olympus Soft Imaging Solutions) camera. Before TEM imaging, samples were released from the substrates, dispersed in ethanol and a drop of the solution was deposited onto a commercial lacey-carbon grid. Raman spectroscopy was conducted on the as-produced CNTs at room temperature employing a Renishaw inVia Raman microscope with a 60x objective lens at 632.8 nm laser excitation and a laser power of 2 mW. In order to evaluate the CNTs surface composition, X-ray Photoelectron Spectroscopy (XPS) was carried out using a commercial Xray photoelectron spectrometer (VG-ESCALAB-II) equipped with a monochromatic Al Kα X-ray source (1486.6 eV) and a hemispherical energy analyzer with a base pressure below 1×10^{-10} mbar. Core-level XPS data analysis was performed after the removal of nonlinear Shirley background and deconvolution into Gaussian/Lorentzian components using Casa-XPS software.

Primary cultures

Hippocampal neurons were obtained from neonatal rats as previously reported [12] [21]. Briefly, cells were plated either on poly-L-ornithine-coated (Sigma Aldrich; controls) or on tCNTs-coated glass coverslips and incubated at 37 °C, 5% CO2 in Neurobasal-A (Thermo

Fischer) medium containing B27 2% (Gibco), Glutamax 10 mM and Gentamycin 0.5 μM (Gibco). Cultured neurons were used for experiments at 8–10 days in vitro (DIV).

Organotypic cultures

Organotypic-entorhinal slice cultures were prepared according to the roller-tube technique, previously described [60] [61]. Briefly, 400 μm thick entorhinal-hippocmpal slices were obtained from P6 to P8 old Wistar rats (because the Perforant Pathway is described to be fully developed from the postnatal day 6 in rats [62]) by means of a tissue Chopper (McIlwan) and stored for 1h in cold (4°C) GBSS enriched with Glucose and Kinurenic Acid to limit excitotoxic processes. The slices were then placed onto glass or tCNTs coverslips embedded in chicken plasma (16 μl; SIGMA), which was coagulated with the addition of a drop of thrombin (23 μl). The lesion was made at the subicular level and the EC was outdistanced from the hippocampus 400 to 600 μm apart, by placing a millimeter graph paper below the coverslips. Cultures were then left 1h at RT and then placed in Nunc tubes filled with were incubated at 37 °C in a roller drum rotating 10 times per hour, in 750 mL of Neurobasal-A (Thermo Fischer) medium containing B27 2% (Gibco), Glutamax 10 mM and Gentamycin 0.5 μM (Gibco), and used for experiments at 8–10 days in vitro (DIV). The medium was completely replaced every 3 days.

Patch clamp

Patch-clamp, whole cell recordings were achieved with glass micropipettes with a resistance of 4 to 7 MΩ. The intracellular pipette solution was the following (mM): 120 K gluconate, 20 KCl, 10 HEPES, 10 EGTA, 2 $MgCl_2$, 2 Na_2ATP, pH 7.3. Cultures were positioned in a custom-made chamber mounted on an inverted microscope (Eclipse TE-200, Nikon, Japan), and continuously superfused with external solution at a rate of 5 mL/min. The external saline solution contained (mM): 150 NaCl, 4 KCl, 1 $MgCl_2$, 2 $CaCl_2$, 10 HEPES, 10 glucose, pH 7.4.

Cells were voltage clamped at a holding potential of −56 mV mV (not corrected for liquid junction potential, that was calculated to be 13.7 mV at 20 °C in these experimental conditions). The uncompensated series resistance had values <8 MΩ. All recordings were performed at RT. Data were collected using a Multiclamp 700A Amplifier (Molecular Devices, US), and analyzed using Clampfit 10.4 (Molecular Devices).

Field potential recordings

Extracellular field potential co-recordings from the visually identified molecular layer of the DG and the superficial layers of the EC were performed on slices at 8-10 DIV at RT (20-22 °C) using low resistance (4-6 MΩ) glass micropipettes filled with extracellular solution. For each experiment, the organotypic slices mounted onto control and tCNT coverslips were positioned into a recording chamber, mounted onto an upright microscope, and superfused with standard Krebs solution containing (in mM): 152 NaCl, 4 KCl, 1 $MgCl_2$, 2 $CaCl_2$,10 HEPES, and 10 glucose. The pH was adjusted to 7.4 with NaOH. A period (45') of stabilization, was followed by the recordings of the Spontaneous activity (45') in standard Krebs, after which Bicuculline (30'; 10 μM) was added to the extracellular solution to weaken synaptic inhibition and induce synchronization between the two recorded areas. As last step, we added CNQX (15'; 10 μM) in which no LFPs were detected, and this was a further indication of the excitatory nature of the recorded signals. All recordings were performed at RT. Data were collected using a Multiclamp 700A Amplifier (Molecular Devices, US),digitized at 10kHz, and analyzed using Clampfit 10.4 (Molecular Devices). To evaluate the frequency of voltage transients, only the events with a minimum peak of three times the baseline signal were included.

The CCF between each voltage pair was calculated in Clampfit 10.4 (Molecular Devices, US). The synchrony between hippocampal and entorhinal LFPs was assessed through a MATLAB custom made script, as previously described [20] [15]. Briefly, for each pair of voltage time series, the Pearson correlation coefficient was assessed and its statistical significance

(P=0.05) was determined by performing a permutation test that allowed to measure the distribution of correlation coefficients that one would expect to observe if the voltage signals recorded from a pair of explants happened to correlate purely by chance. By measuring how likely it was for the values of this null distribution to be larger or equal than the real correlation coefficient, it was possible to understand whether the correlation between the pair of time series was significantly larger than expected by chance. This procedure allowed for determining what fraction of cocultured slices exhibited a significantly synchronous bursting activity, for all the tested conditions [20].

To stimulate the performant pathway we placed Bipolar electrodes made by a low-resistance patch pipette containing normal Krebs into the EC superficial layers. Voltage pulses (200 to1000 μs) of increasing amplitude (1 to 20 V) were delivered by an isolated Voltage stimulator (DS2A; Digitimer ltd.) until a response was detected.

Immunocytochemistry and Microscopy

To visualized dissociated hippocampal neurons, we fixed cultures in 4% formaldehyde in PBS for 20 min, permeabilized with 0.3% Triton-X-100 and incubated with primary antibodies for 30 min at RT. After washing in PBS, cultures were incubated with secondary antibodies for 45 min and then mounted with Vectashield (Vector Laboratories) on 1 mm thick microscope glass slides. To visualize neurons and glial cells we used the following: rabbit anti-β-tubulin III primary antibody (Sigma T2200, 1:250 dilution) and Alexa 594 goat anti rabbit secondary antibody (Thermo-Fisher, 1:500); anti-GFAP mouse primary antibody (SIGMA, 1:250) and Alexa 488 goat anti mouse secondary antibody (Thermo-Fisher, 1:500). Cell nuclei were visualized with the nuclear marker DAPI (1:1000). Cultures were imaged with an Epifluorescence Microscope (DM 6000, Leica; 10× and 20x objectives), and analyzed with the software ImageJ (http://rsb.info.nih.gov/ij/).

To stain Organotypic cultures we fixed them for 1h at RT with PFA (4%). After PBS washes, cultures were incubated with mouse SMI32 (1:250) and rabbit NeuN (SIGMA; 1:200) primary antibodies, and Alexa 594 goat anti rabbit (Invitrogen, 1:500), Alexa 488 goat anti mouse (Invitrogen, 1:500) secondary antibodies and Hoechst (Invitrogen; 1:1000). Cultures were then mounted with Vectashield (Vector Laboratories) on 1 mm thick microscope glass slides, visualized with a Confocal Microscope (Nikon Eclipse Ti-E; 10x objective) and analyzed with the Volocity Software (Perkin Elmer). To quantify the SMI32-positive "crossing-fibers", we selected a same 3D ROI (500 μm x 50 μm x 15 μm), in between the hippocampus and the entorhinal cortex (with the ROI longitudinal axis perpendicular to the slices longitudinal axis; see Fig..), in controls and tCNTs cultures. The amount of SMI32-positive voxel within each ROI was quantified for each image, and normalized to the overall ROI volume, and all values for all the images from the same condition were then averaged together and plotted. To label the Perforant Pathway, Cholera Toxin subunit B (Thermo-Fisher) was dissolved in PBS at the concentration of 1% [49], and then loaded into a glass pipette which was subsequently mounted on the upright setup headstage and connected to the picospritzer. After reaching the Dentate Gyrus Molecular layer using micromanipulators, the injection was made by the delivering of 3 pulses (20 ms duration) of 20 psi. Cultures was then placed back into the incubator for 24 hours, fixed and stained with anti-mouse Map2 (Invitrogen; 1:400) primary antibody, Alexa 594 goat anti-mouse secondary anotibody (Invitrogen, 1:500) and Hoechst (Invitrogen, 1:1000), and visualized with a Confocal Microscope (Nikon Eclipse Ti-E; 10x and 40x objectives).

Statistics

All values presented are expressed as means ± SD, with n indicating the number of cultures, unless otherwise specified. Statistically significant differences between pairs of data sets were assessed by Student's t test (after validation of variance homogeneity by Levene's test) for parametric data and by the Mann-Whitney U test for nonparametric data. When

multiple groups were compared, One-way ANOVA was used, followed by Bonferroni post hoc analysis. Statistical significance was determined at $p < 0.05$.

Bibliography

[1] Perlmutter JS and Mink JW. Deep Brain Stimulation. Annu Rev Neurosci. (2006) 29: 229–257..

[2] Girgis F, Pace J, Sweet J, and Miller JP. Hippocampal Neurophysiologic Changes after Mild Traumatic Brain Injury and Potential Neuromodulation Treatment Approaches. Front Syst Neurosci. (2016) 10: 8..

[3] Maas AI, Stocchetti N, Bullock R. Moderate and severe traumatic brain injury in adults. Lancet Neurol. (2008) 7(8):728-41.

[4] Finnie JW & Blumbergs PC Traumatic Brain Injury. Vet Pathol (2002) 39:679–689.

[5] Guggenmos DJ, Azin M, Barbay S, Mahnken JD, Dunham C, Mohseni P, Nudo RJ. Restoration of function after brain damage using a neural prosthesis. Proc Natl Acad Sci. (2013) 110(52):21177-82..

[6] Cetin M, Gumru S, Aricioglu F. Nanotechnology Applications in Neuroscience: Advances, Opportunities and Challenges. Bulletin of Clinical Psychopharmacology (2012)22(2):115-20..

[7] Vidu R, Rahman M, Mahmoudi M, Enachescu M, Poteca TD, Opris I. Nanostructures: a platform for brain repair and augmentation. Front Syst Neurosci. (2014) 8:91. .

[8] Lee JK, Baac H, Song SH, Jang E, Lee SD, Park D, Kim SJ. Neural prosthesis in the wake of nanotechnology: controlled growth of neurons using surface nanostructures. Acta Neurochir

Suppl. (2006) 99:141-4..

[9] Wang, M., Mi, G., Shi, D., Bassous, N., Hickey, D., & Webster, T. J. Nanotechnology and Nanomaterials for Improving Neural Interfaces. Adv Funct Mat (2017) 1700905.

[10] Iijima S. Helical microtubules of graphitic carbon. Nature (1991) 354, 56–58..

[11] O'Connell MJ Carbon Nanotubes: properties and applications. CRC press, Taylor e Francis Group (2006)..

[12] Lovat V, Pantarotto D, Lagostena L, Cacciari B, Grandolfo M, Righi M, Spalluto G, Prato M, Ballerini L. Carbon nanotube substrates boost neuronal electrical signaling. Nano Letters (2005) 5, 1107-1110..

[13] Cellot G, Toma F.M, Varley Z.K, Laishram J, Villari A, Quintana M, Cipollone S, Prato M, Ballerini L. Carbon nanotube scaffolds tune synaptic strength in cultured neural circuits: novel frontiers in nanomaterial-tissue interactions. Journal of Neuroscienc.

[14] Fabbro A, Villari A, Laishram J, Scaini D, Toma FM, Turco A, Prato M, Ballerini L. Spinal cord explants use carbon nanotube interfaces to enhance neurite outgrowth and to fortify synaptic inputs. ACS Nano (2012) 6, 2041-2055..

[15] Usmani S, Aurand ER, Medelin M et al. 3D meshes of carbon nanotubes guide functional reconnection of segregated spinal explants. Sci Adv. (2016) 2(7): e1600087.

[16] Bareket-Keren L, Hanein Y. Carbon nanotube-based multi electrode arrays for neuronal interfacing: progress and prospects. Front Neural Circuits. (2013) 9;6:122..

[17] Vidu R, Rahman M, Mahmoudi M, Enachescu M, Poteca TD, Opris I. Nanostructures: a platform for brain repair and augmentation. Front Syst Neurosci. (2014) 8:91. .

[18] Cyril G. Eleftheriou, Jonas B. Zimmermann, Henrik D. Kjeldsen, Moshe David-Pur, Yael Hanein, Sernagora E. Carbon nanotube electrodes for retinal implants: A study of structural and functional integration over time. Biomaterials (2017) 112:108-121..

[19] Vitale F, Summerson SR, Aazhang B, Kemere C, Pasquali M. Neural stimulation and recording with bidirectional, soft carbon nanotube fiber microelectrodes. ACS Nano (2015) 9(4):4465-74..

[20] Aurand ER, Usmani S, Medelin M, Scaini D, Bosi S, B. Rosselli F, Donato S, Tromba G, Prato M, Ballerini L. Nanostructures to Engineer 3D Neural-Interfaces: Directing Axonal Navigation toward Successful Bridging of Spinal Segments. Adv funct Mat (2017) 1.

[21] Cellot G, Cilia E, Cipollone S, Rancic V, Sucapane A, Giordani S, Gambazzi L, Markram H,

Grandolfo M, Scaini D, Gelain F, Casalis L, Prato M, Giugliano M, Ballerini L. Carbon nanotubes might improve neuronal performance by favouring electrical shortcuts. Nat Nanotech (2009): 4(2):126-133.

[22] Shah KA, Tali BA. Synthesis of carbon nanotubes by catalytic chemical vapour deposition: A review on carbon sources, catalysts and substrates. Materials Science in Semiconductor Processing (2016) 41, 67-82.

[23] Chiang W-H, Sankarana RM. Microplasma synthesis of metal nanoparticles for gas-phase studies of catalyzed carbon nanotube growth. Appl. Phys. Lett. (2007) 91, 121503.

[24] Michaelis FB, Weatherup RS, Bayer BC, Bock MC, Sugime H, Caneva S, Robertson J, Baumberg JJ, Hofmann S. Co-catalytic absorption layers for controlled laser-induced chemical vapor deposition of carbon nanotubes. ACS Appl Mater Interfaces. (2014) 6(6):4025.

[25] Bayer BC, Hofmann S, Castellarin-Cudia C, Blume‖ R, Baehtz C, Esconjauregui S, Wirth CT, Oliver RA, C. Ducati C, Knop-Gericke‖ A, Schlögl‖ R, Goldoni A, C. Cepek C, Robertson J. Support−Catalyst−Gas Interactions during Carbon Nanotube Growth on Metallic T.

[26] Morassutto M, Tiggelaara RM, Smithers MA, Gardeniersa GE. Vertically aligned carbon nanotube field emitter arrays with Ohmic base contact to silicon by Fe-catalyzed chemical vapor deposition. Materials Today Communications (2016) 7; 89-100..

[27] Zhang L, Li Z, Tan Y, Lolli G, Sakulchaicharoen N, Requejo FG, Mun BS, Resasco ED. Influence of a Top Crust of Entangled Nanotubes on the Structure of Vertically Aligned Forests of Single-Walled Carbon Nanotubes. Chem. Mater (2006) 18 (23), 5624–5629..

[28] Lee CJ. Park J, Huh Y, Lee JY. Temperature effect on the growth of carbon nanotubes using thermal chemical vapor deposition. Chemical Physics Letters (2001) 343(1-2); 33-38..

[29] Charlier JC. Defects in Carbon Nanotubes. Acc. Chem. Res. (2002) 35(12), 1063–1069..

[30] Costa S, Borowiak-Palen E, Kruszyńska M, Bachmatiuk A, kaleńczuk RJ. Characterization of carbon nanotubes by Raman spectroscopy. Materials Science-Poland. (2008) 26(2) 433-441..

[31] Antunes EF, Lobo AO, Corat EJ, Trava-Airoldia VJ. Influence of diameter in the Raman spectra of aligned multi-walled carbon nanotubes. Carbon (2007) 45(5) 913-921..

[32] Bulusheva LG, Okotrub AV, Kinloch IA, Asanov IP, Kurenya AG, Kudashov AG, Chen X, Song H. Effect of nitrogen doping on Raman spectra of multi-walled carbon nanotubes. phys. stat. sol. (b) (2008) 245(10) 1971–1974. .

[33] Saito R, Grüneis A, Samsonidze GG, et al. Double resonance Raman spectroscopy of single-wall

carbon nanotubes. New J of Physics. (2003) 5:157.1-157.15..

[34] Kim KK, Park JS, Kim SJ, Geng HZ, An KH, Yang CM, et al. Dependence of Raman spectra G band intensity on metallicity of single-wall carbon nanotubes. Phys Rev B (2007) 76:205426,-1–8..

[35] Roeges, N. P. G. A guide to the complete interpretation of Spectra of Organic structures; John Wiley & Sons: Chichester, U.K. 1997.

[36] Long, D. A. Raman spectroscopy; McGraw-Hill, London, U.K., (1997)..

[37] Mattevi C, Wirth CT, Hofmann S et al. In-situ X-ray Photoelectron Spectroscopy Study of Catalyst−Support Interactions and Growth of Carbon Nanotube Forests. J. Phys. Chem. C (2008) 112 (32): 12207–12213..

[38] Hofmann S, Blume R, Wirth CT et al. State of Transition Metal Catalysts During Carbon Nanotube Growth. J. Phys. Chem. C (2009) 113(5): 1648–1656..

[39] Okpalugo TIT, Papakonstantinou P, Murphy H, McLaughlin JAD, Brown, NMD. High resolution XPS characterization of chemical functionalised MWCNTs and SWCNTs. Carbon (2005) 43 (1): 153-161..

[40] Jacobson S, Marcus EM. Neuroanatomy for the Neuroscientist. Springer New York (2008)..

[41] Perederiy JV and Westbrook GL. Structural plasticity in the dentate gyrus - revisiting a classic injury model. Front Neural Circuits (2013) 7: 17..

[42] Vuksic M, Del Turco D, Vlachos A, Schuldt G, Müller CM, Schneider G, Deller T. Unilateral entorhinal denervation leads to long-lasting dendritic alterations of mouse hippocampal granule cells. Exp Neurol. (2011) 230(2):176-85..

[43] Vlachos A, Becker D, Jedlicka P, Winkels R, Roeper J, Deller T. Entorhinal denervation induces homeostatic synaptic scaling of excitatory postsynapses of dentate granule cells in mouse organotypic slice cultures. PLoS One. (2012) 7(3):e32883. .

[44] Lee AC, Wong RK, Chuang SC, Shin HS, Bianchi R. Role of synaptic metabotropic glutamate receptors in epileptiform discharges in hippocampal slices. J Neurophysiol. (2002) 88(4):1625-33..

[45] Puopolo M, Belluzzi O. NMDA-dependent, network-driven oscillatory activity induced by bicuculline or removal of Mg2+ in rat olfactory bulb neurons. Eur J Neurosci. (2001) 13(1):92-102..

[46] Witter MP. The perforant path: projections from the entorhinal cortex to the dentate gyrus.

Prog Brain Res. (2007) 163:43-61.

[47] Jacobson S, Marcus EM. Neuroanatomy for the Neuroscientist. Springer New York (2008).

[48] Witter MP and Amaral DG. Hippocampal formation. In “The rat nervous system” (2004) vol. 3, 3rd edn (ed. PaxinosG), pp. 635–704. Amsterdam, The Netherlands: Elsevier.

[49] Conte WL, Kamishina H, Reep RL. The efficacy of the fluorescent conjugates of cholera toxin subunit B for multiple retrograde tract tracing in the central nervous system. Brain Struct Funct (2009) 213:367–373.

[50] Kitamura T, Pignatelli M, Suh J, Kohara K, Yoshiki A, Abe K, Tonegawa S. Island cells control temporal association memory. Science (2014) 343(6173):896-901..

[51] Edwards SL, Werkmeister JA, Ramshaw JA. Carbon nanotubes in scaffolds for tissue engineering. Expert Rev Med Devices (2009) 6(5):499-505.

[52] Erol O, Uyan I, Hatip M, Yilmaz C, Tekinay AB, Guler MO. Recent advances in bioactive 1D and 2D carbon nanomaterials for biomedical applications. Nanomedicine (2017) 17:30089-8..

[53] Marchesan S, Kostarelos K, Bianco A, Prato M. The winding road for carbon nanotubes in nanomedicine. Materials Today (2015) 18(1):12-19..

[54] Pancrazio JJ. Neural interfaces at the nanoscale. Nanomedicine (Lond). (2008) 3(6): 823–830..

[55] Anguita JV, Cox DC, Ahmad M, Tan YY, Allam J, Silva SRP. Highly Transmissive Carbon Nanotube Forests Grown at Low Substrate Temperature. Adv funct Mater. (2013) 23, 5502–550..

[56] Del Turco D, Deller T. Organotypic entorhino-hippocampal slice cultures--a tool to study the molecular and cellular regulation of axonal regeneration and collateral sprouting in vitro. Methods Mol Biol. (2007) 399:55-66..

[57] Vlachos A, Becker D, Jedlicka P, Winkels R, Roeper J, Deller T. Entorhinal denervation induces homeostatic synaptic scaling of excitatory postsynapses of dentate granule cells in mouse organotypic slice cultures. PLoS One. (2012) 7(3):e32883. .

[58] Ward JW, Wei BQ, Ajayan PM. Substrate effects on the growth of carbon nanotubes by thermal decomposition of methane. Chemical Physics Letters. (2003) 376: 717–725..

[59] Kern W, Puotinen DA. Cleaning solutions based on hydrogen peroxide for use in silicon semiconductor technology. RCA Rev. (1970) 31:187-206..

[60] Gähwiler B. H. Organotypic cultures of neural tissue. Trends in Neuroscience (1988) 11(11) 484-

489.

[61] Mohajerani MH & Cherubini E. Spontaneous recurrent network activity in organotypic rat hippocampal slices. Eur J Neurosci. (2005) 22:107-118..

[62] Fricke R, Cowan WM. An autoradiographic study of the development of the entorhinal and commissural afferents to the dentate gyrus of the rat. J Comp Neurol. (1977) 15;173(2):231-50..

[63] Iijima S. Helical microtubules of graphitic carbon. Nature (1991) 354, 56–58..

[64] Lovat V, Pantarotto D, Lagostena L, Cacciari B, Grandolfo M, Righi M, Spalluto G, Prato M, Ballerini L. Carbon nanotube substrates boost neuronal electrical signaling. Nano Letters (2005) 5, 1107-1110.

Figure Captions.

Figure 1. Morphological and structural characterization of CNTs synthesized by CCVD on transparent substrates.

(a) Top and (b) side SEM views of CNT substrates revealing a random orientation and a vertical alignment of nanotubes, respectively. (c) TEM image of multi-walled nanotubes with different wall number constituting the mat and a particular of an isolated MWCNT (d) showing well-resolved single walls. (e) XPS survey, (f) Raman and C1s core level (g) spectra exhibiting characteristic peaks of CVD grown MWCNTs. In (h) are shown representative optical images of CVD grown CNTs on silicon (left) and on fused silica (right) wafer chip substrate, in which is possible to appreciate the transparency of tCNTs (scale bar: 8 mm).

Figure 2. tCNTs enhance the activity of hippocampal neurons.

(a) representative fluorescent micrographs depicting dissociated primary neurons grown on control substrates (left) or tCNTs substrates (right) stained with βTubIII to see neurons, GFAP to highlight astrocytes and DAPI to stain cell nuclei (Scale bar: 50 μm). As summarized in the plots in (b) we did found a similar density of either neurons and astrocytes in the two conditions. (c) Representative traces of whole cell patch clamp recordings of controls and tCNTs-related neurons. Is evident a significantly higher frequency of PSC current related to the tCNTs condition, as summarized in (d; upper plot), with no major changes concerning the amplitudes of PSCs (d, lower plot).

Figure 3. tCNTs are suitable substrates for the growth of EHCs organotypic cultures.

Representative confocal stitched images showing 8-days-old organotypic EHCs cultures stained with NeuN to label neuronal nuclei and Hoetsch to label cell nuclei. In both entire and lesioned slices, organotypic cultures displayed a similar morphology when grown in control and tCNTs substrates, indicating a comparable health between the two conditions (Scale bar: 500 μm).

Figure 4. tCNTs enhance the EC-DG signal syncronization in EHCs.

(a) Representative sketch depicting the experimental setup concerning field potential extracellular co-recordings performed from the EC (red) and hippocampal DG (black) in entire (left) and lesioned (right) slices in standard Krebs, and relative representative voltage tracings obtained in controls (top) and tCNT (bottom) conditions (scale bar: 10 sec). As shown in (b), no significant different were detected in terms of LFP frequency between the two conditions when slices were superfused with standard extracellular solution. The Bicuculline application seemed to induce a more visible effect in tCNTs entire slices (b, bottom panel), where the LFP frequency is decreased in a similar fashion in EC and EC, while the same drug application seemd to have similar effect concerning the lesioned slices. In (c) is evident how the totality of the voltage signal pairs was found to be synchronized in tCNTs entire slices (bottom) either in standard and Bicuculline-enriched extracellular solution. Concerning the control condition instead, the synchronization between DG and EC was found to be lower, and underwent to a 2-fold increase of its original value (from 43% to 86%) when Bic was added in entire slices. Control related lesioned slices signal synchronization was found to be quite low with respect to tCNTs (11% versus 50%; left panel). This difference was still evident (33 % to 100%) when slices were bathed with Bic (right panel). Note that tCNTs related signals reached the 100% of synchronization even in Bic-superfused lesioned slices, suggesting that a reconnection is established in all cases.

Figure 5. tCNTs induce the sprouting of functionally active fibers into the lesioned area.

To validate the presence of the perforant pathway in our experimental conditions, after injecting the retrograde tracer CTX into the molecular layer of the dentate gyrus (a; top), we found the presence of many CTX-labelled somata into the superficial layer of the MEC (inset), indicating the integrity of this pathway in our experimental model. (b) When we stimulated the PP in entire slices, we always did detect a response in both the DG and deep layers of the EC, either in Controls and tCNTs interfaced cultures (b; top), while in case of lesioned ones we found marked differences between the two conditions (b; bottom): in case of control slices, we detected a response just into the EC in the 50% of case; in another 12.5% of cases just in the DG and in 25% of cases a response was not detected neither into the EC nor the DG. In the remaining 12.5% of cases a response was detected in both areas. As shown in the graph, when we stimulated the PP in t-CNT slices, a response was always present in both areas. (c) Representative confocal images showing the sprouting of SMI32-positive fibers into the lesioned area. As summarized in the plot, cultures grown onto tCNTs dispayed a significantly higher percentage of SMI32-positive volume with respect to controls (scale bar: 100 μm).

Fig.1

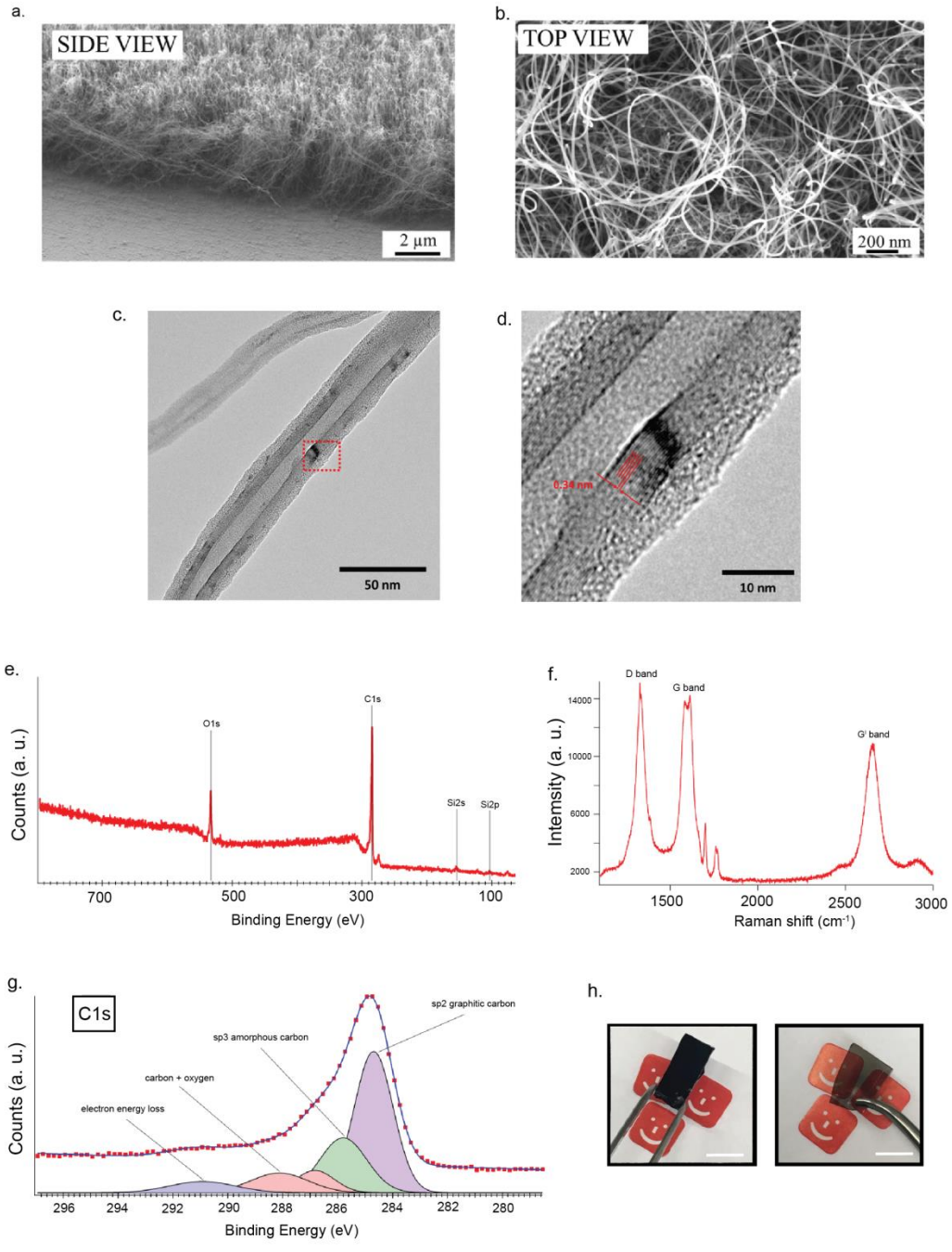
a.
SIDE VIEW
2 µm
b.
TOP VIEW
200 nm
c.
50 nm
d.
0.34 nm
10 nm
e.
O1s
C1s
Si2s
Si2p
Counts (a. u.)
700
500
300
100
Binding Energy (eV)
f.
D band
G band
G' band
Intensity (a. u.)
14000
10000
6000
2000
1500
2000
2500
3000
Raman shift (cm-1)
g.
C1s
sp2 graphitic carbon
sp3 amorphous carbon
carbon + oxygen
electron energy loss
Counts (a. u.)
296
294
292
290
288
286
284
282
280
Binding Energy (eV)
h.

Fig. 2

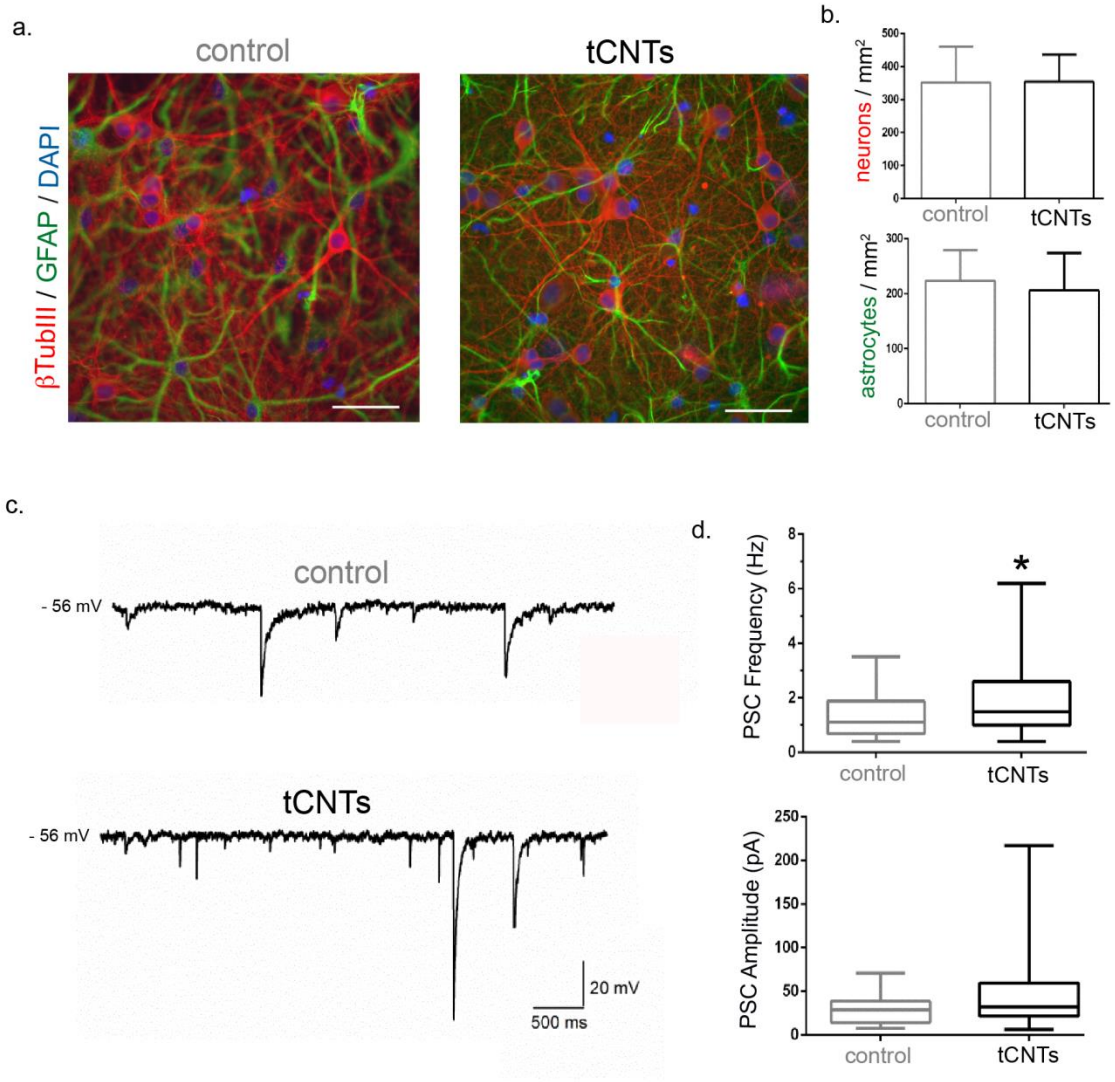
a.
control
tCNTs
βTubIII / GFAP / DAPI
b.
neurons / mm²
astrocytes / mm²
control
tCNTs
c.
control
- 56 mV
tCNTs
- 56 mV
20 mV
500 ms
d.
PSC Frequency (Hz)
PSC Amplitude (pA)
*
control
tCNTs

Fig.3

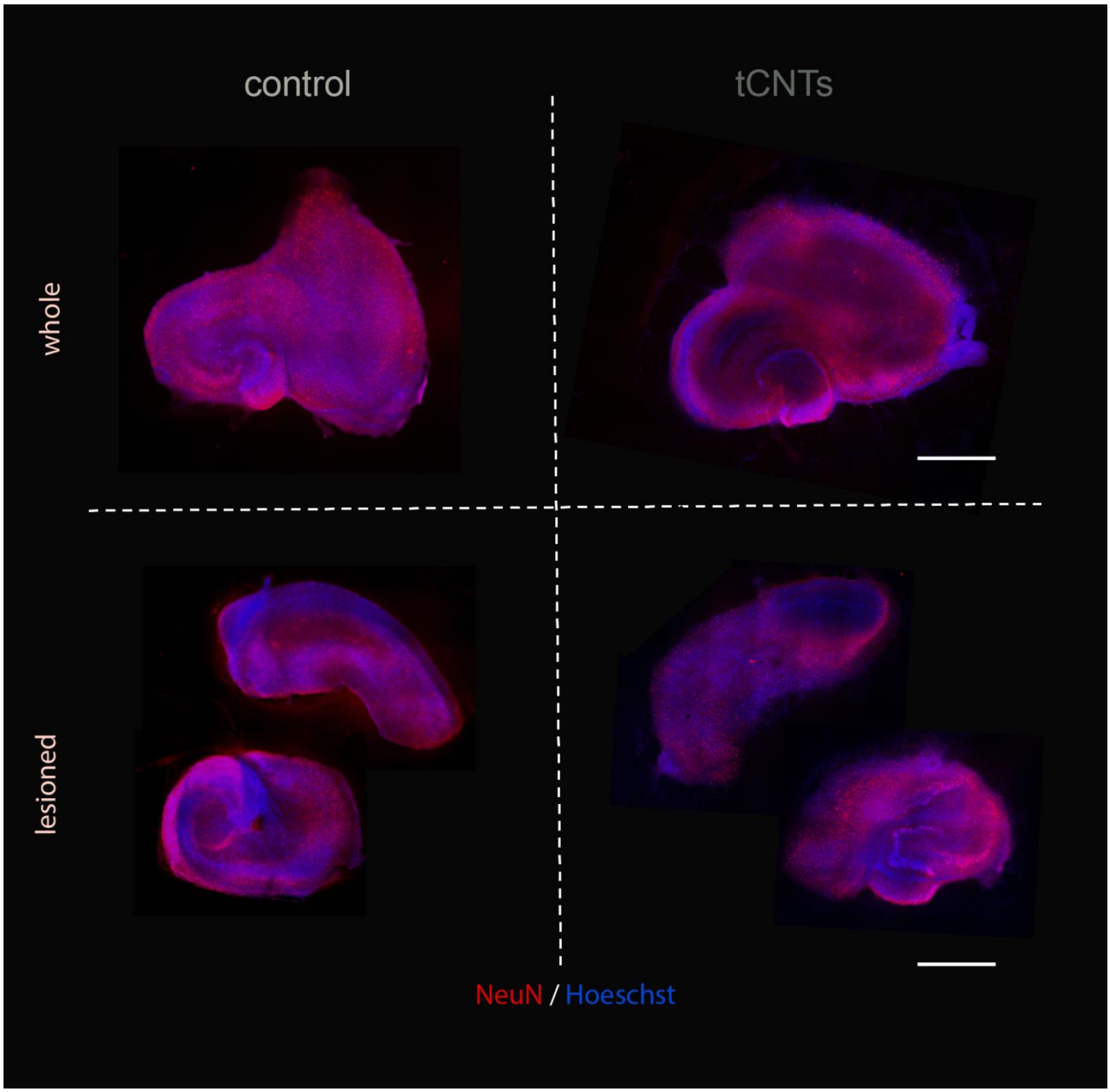

Fig.4

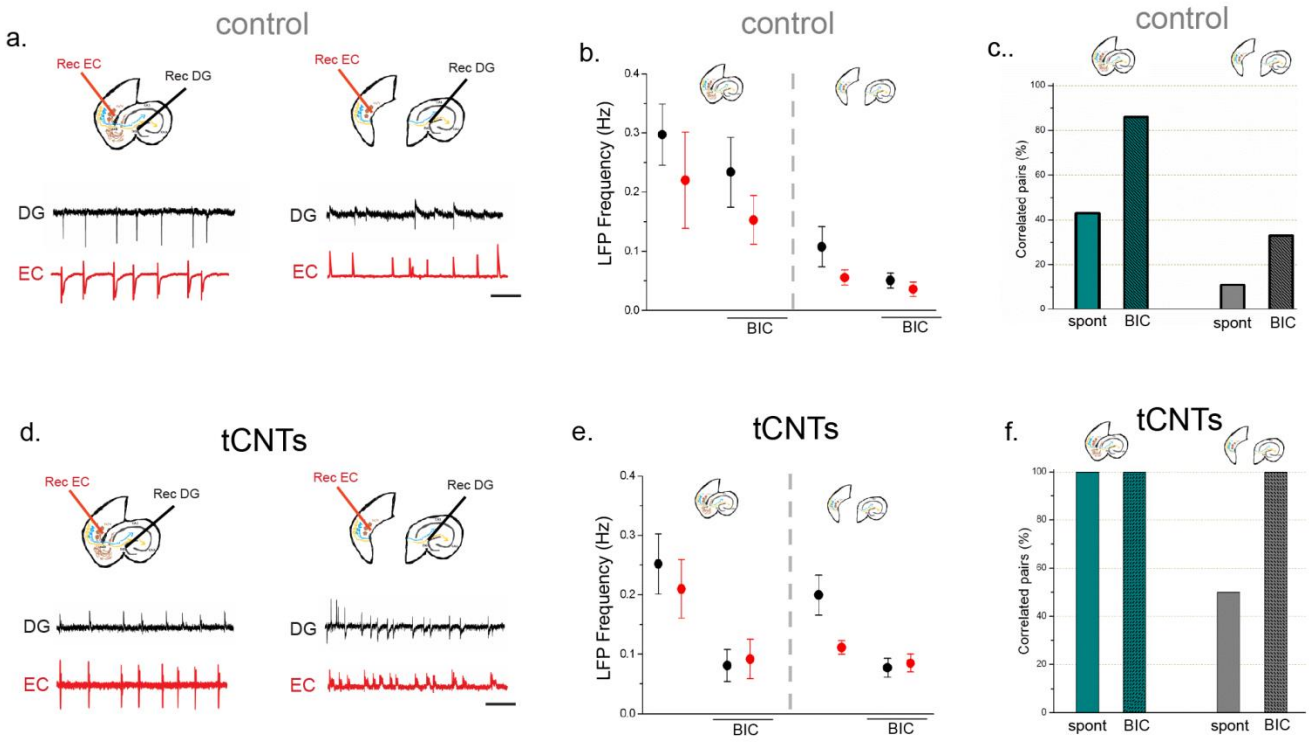
a.
control
Rec EC
Rec DG
DG
EC
b.
control
LFP Frequency (Hz)
BIC
c..
control
Correlated pairs (%)
spont
BIC
d.
tCNTs
e.
tCNTs
f.
tCNTs

Fig.5

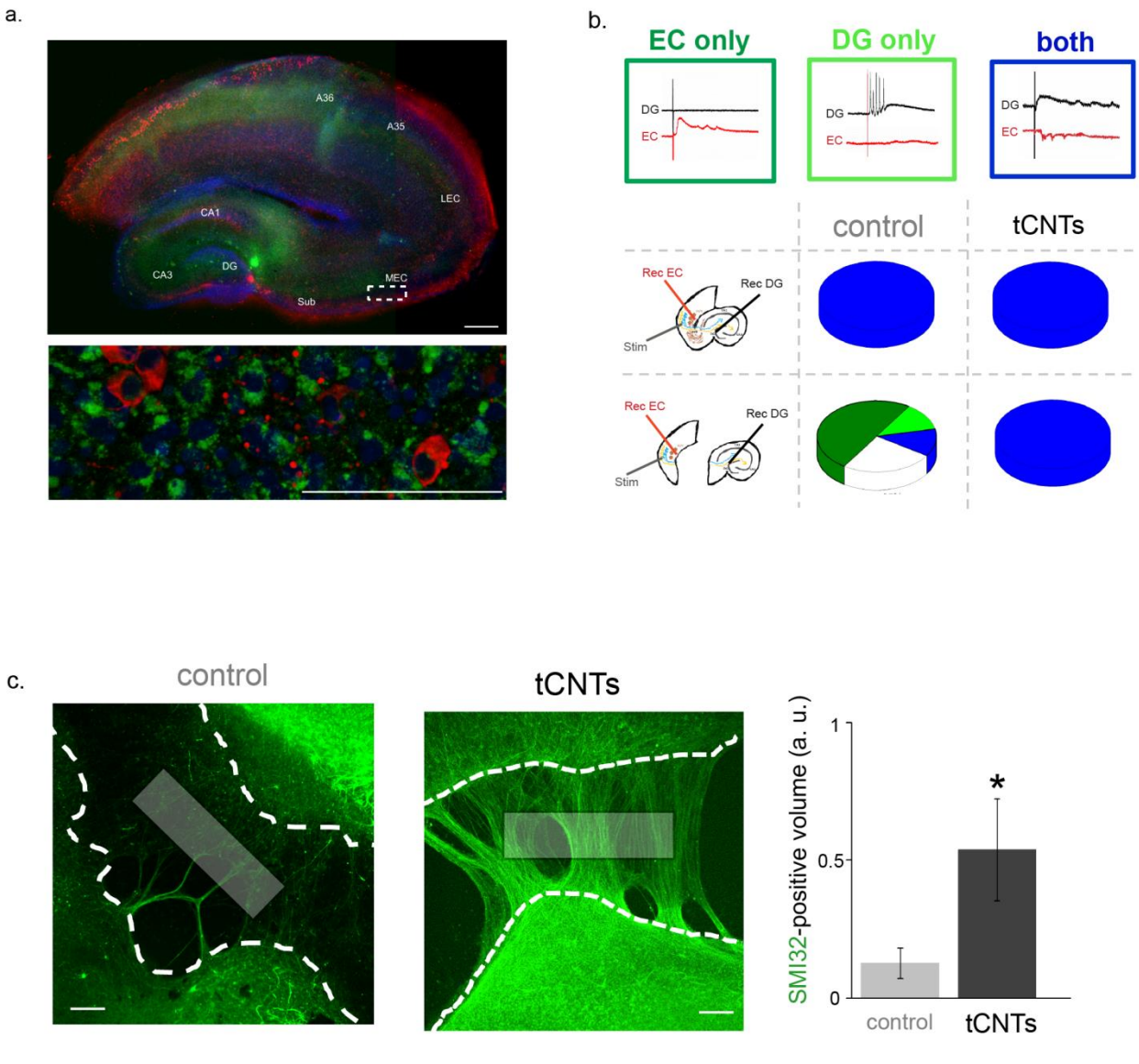
a.
A36
A35
LEC
CA1
CA3
DG
MEC
Sub
b.
EC only
DG only
both
DG
EC
control
tCNTs
Rec EC
Rec DG
Stim
c.
control
tCNTs
SMI32-positive volume (a. u.)
1
0.5
0
*
control
tCNTs

DISCUSSION

In biomedical applications to neurology, the use of implantable devices and prostheses has increased significantly during the last years (Hochberg et al, 2006; Daly & Wolpaw, 2008; Brumberg & Guenther, 2010; Raspopovic et al, 2014; Capogrosso et al, 2016; Bareket et al, 2017). The main goal of these artificial implants is to promote a functional recovery or lessening of symptoms, as is the case in Parkinson disease or in traumatic spinal cord lesions. The recent Nanotechnology-related advances (Cetin et al, 2012) had a huge impact on the amelioration of neural prostheses, by allowing the construction of artificial devices and scaffolds with nano-sized features (Lee et al, 2006; Vidu et al, 2014; Wang et al, 2017). As in most cases the implanted nano-featured devices would need to be interfaced into the foreign body for months or even years (Chapin & Moxon, 2000; Schwartz et al, 2006), a deep characterization and knowledge of the interaction that these are establishing with the neuronal cells and neural tissues is crucial. In this framework, the results I achieved during my PhD work describe the effects which several promising nanomaterials, in particular carbon-based materials, are inducing in neurons, either at the single cell and network level.

In summary, the present study obtained the main following results:

- CNT bi-dimensional substrates are able to inducing specific effects on primary neurons, by a differential regulation and expression of the excitatory presynaptic compartments of chemical synapses. In particular, by an apparent fastening of the neuronal maturation, CNT-interfaced neurons display a significantly higher number of excitatory presynaptic terminals after 8-10 days of growth in vitro. Furthermore, these synapses rely most of their neurotransmission on the so called "recycling pool" of vesicles (Fredj & Burrone, 2009; which are dependent on Action Potentials and the subsequent calcium entry into the pre-synapse), while, at these early stages of maturation, the activity of control-related neurons, is instead linked to the “resting pool” of vesicles (Fredj & Burrone, 2009; that fuse independently of Calcium entry into the presynapse). The synaptic differences between Controls and CNT-interfaced neurons disappear after 3 weeks of in vitro growth (18-22 DIV),

leading to cultures that display a similar regulation and expression of excitatory presynaptic terminals and a comparable synaptic activity. This result is particularly relevant as it indicates that the boosted activity observed in CNT-interfaced neuronal networks, is not reflecting some pathological condition, such as excitotoxic processes associated to several brain disorders such as Schizophrenia (Plitman et al, 2014) or Neurodegenerative Diseases (Salińska et al, 2005), but rather a transient network functional potentiation, that reaches the same plateau of controls after 3 weeks of growth. This is particularly important in a view in which CNTs are used to build up neural implants, as it shows that the boosting regenerative CNT effects do not lead to pathologic conditions upon a long term interfacing.

- Pure bi-dimesional Graphene, a recently synthesized nanomaterial with exclusive physicochemical features (Novoselov et al, 2004), was shown to be a suitable material for the neuronal growth and we demonstrated that it induces a potentiation expressed as a higher frequency of synaptic currents in primary hippocampal networks. This potentiation was not observed neither in Graphite (a material made of overlapping layers of Graphene) nor in Gold (a non carbon-based highly conductive metal). This particular potentiation seems to involve the sequestration of K+ ions onto the Graphene surface in solution, through the non-covalent cation-π interaction (Kumpf & Dougherty, 1993), leading to a potassium gradient close to the plasma membrane, that affected the homeostasis of potassium conductances in Graphene-interfaced neurons, increasing single cell excitability and reflected at the network level into increased occurrence of synaptic events.

- A new kind of CNT-based composite, resulted from a new synthetic process, and characterized by the unusual transparency to the visible light (and therefore more suitable to a variety of biomedical applications), was tested as a substrate for neural growth, and shown to induce regenerating effects on Organotypic Entorhinal-Hippocampal cultures. In particular, cultures lesioned at the subicular level and outdistance roughly to 0.5 mm, displayed a significant increase with respect to controls, either in the signal synchronization and sprouting of their fibers into the lesioned area, indicating the ability of this material to functionally reconnect lesioned areas of the CNS.

Overall, the listed results brought new, previously undescribed insights about the peculiar interactions between neuronal cells and neural tissues with the carbon-based materials CNTs and Graphene, which can be extremely useful to take into account for the forthcoming research studies either *in vitro* and *in vivo*, and which can be considered as a solid background of information for the development of the new generation of implantable neural interfaces and prosthetic devices in medical neuroscience.

BIBLIOGRAPHY

Agster KL, Burwell RD. Hippocmapal and subicular efferents and afferents of the perirhinal, postrhinal, and entorhinal cortices of the rat. Behav Brain Res. (2013) 254: 50-64.

Ahmed El Hady A, Afshar G, Bröking K, Schlüter OM, Geisel T, Stühmer W, Wolf F. Optogenetic stimulation effectively enhances intrinsically generated network synchrony. Front Neural Circuits (2013) 7: 167.

Alivisatos A. P., Andrews A. M., Boyden E. S., Chun M., Church G. M., Deisseroth K., et al. Nanotools for neuroscience and brain activity mapping. ACS Nano (2013) 7, 1850–1866.

Andersen, P. (1975). Organization of hippocampal neurons and their interconnections. In R.L. Isaacson & K.H. Pribram (Eds.) The Hippocampus Vol. I (pp. 155-175), New York, Plenum Press.

Andersen, P. The hippocampus book. (2007) New York: Oxford University Press.

Angle MR, Schaefer AT. Neuronal Recordings with Solid-Conductor Intracellular Nanoelectrodes (SCINEs). PLoS One (2012) 7(8): e43194.

Aurand ER, Sadaf Usmani S, Medelin M, Scaini D, Bosi S, Rosselli FB, Donato S, Tromba G, Prato M, Ballerini L. Nanostructures to Engineer 3D Neural-Interfaces: Directing Axonal Navigation toward Successful Bridging of Spinal Segments. Adv Funct Mat. (2017) 10.1002/adfm.201700550.

Banker GA, Cowan WM. Rat hippocampal neurons in dispersed cell culture. Brain Res. (1977) 13;126(3):397-42.

Bareket L, Barriga-Rivera A, Zapf MP, Lovell NH, Suaning GJ. Progress in artificial vision through suprachoroidal retinal implants. J Neural Eng. (2017) 25;14(4):045002.

Berger M. Nanotechnology: The Future is Tiny. Royal Society of Chemistry (2016).

Bianco A., Kostarelos K., Prato M. Making carbon nanotubes biocompatible and biodegradable. Chem.Commun. (2011) 47, 10182-10188.

Bird CM and Burgess N. The hippocampus and memory: insights from spatial processing. Nature (2008) 9, 182-194.

Bliss TV, Lomo T. Long-lasting potentiation of synaptic transmission in the dentate area of the anaesthetized rabbit following stimulation of the perforant path. J Physiol. (1973) 232(2):331-56.

Blumenthal NR, Hermanson O, Heimrich B, Shastri VP. Stochastic nanoroughness modulates neuron-astrocyte interactions and function via mechanosensing cation channels. Proc Natl Acad Sci. (2014) 111(45):16124-9.

Boghossian A.A., Zhang J., Barone P.W, Reuel N.F., Kim J.H., Heller D.A., Ahn J.H., Hilmer A.J., Rwei A., Arkalgud J.R., Zhang C.T., Strano M.S. Near-Infrared Fluorescent Sensors based on Single-Walled Carbon Nanotubes for Life Sciences Applications. Chemsuschem (2011) 4, 848-863.

Bosi S, Rauti R, Laishram J, Turco A, Lonardoni D, Nieus T, Prato M, Scaini D, and Ballerini L. From 2D to 3D: novel nanostructured scaffolds to investigate signalling in reconstructed neuronal networks. Scientific Reports. (2015) 5:9562.

Boyden ES, Zhang F, Bamberg E, Nagel G, Deisseroth K. Millisecond timescale, genetically targeted optical control of neural activity. Nat Neurosci (2005) 8(9):1263-8.

Brodal, A. Hippocampus and the sense of smell. *Brain* (1947) 70 (Pt 2): 179–222.

Brumberg JS, Guenther FH. Development of speech prostheses: current status and recent advances. Expert Rev Med Devices (2010) 7(5):667-79.

Brus L.. A simple model for the ionization potential, electron affinity, and aqueous redox potentials of small semiconductor crystallites. The Journal of Chemical Physics (1983) 79, 5566.

Bush D, Barry C, Burgess N. What do grid cells contribute to place cell firing? Trends Neurosci. (2014) 37(3):136-45.

Buzea C, Pacheco I, Robbie K. Nanomaterials and nanoparticles: sources and toxicity. Biointerphases. (2007) 2(4):17-71.

Canto CB, Wouterlood FG, Witter MP. What does the anatomical organization of the entorhinal cortex tell us? Neural Plasticity (2008) 2008:381243.

Capogrosso M, Milekovic T, Borton D, Wagner F, Moraud EM, Mignardot JB, Buse N, Gandar J, Barraud Q, Xing D, Rey E, Duis S, Jianzhong Y, Ko WK, Li Q, Detemple P, Denison T, Micera S, Bezard E, Bloch J, Courtine G. A brain-spine interface alleviating gait deficits after spinal cord injury in primates. Nature (2016) 10;539(7628):284-288.

Carballo-Molina OA & Velasco I. Hydrogels as scaffolds and delivery systems to enhance axonal regeneration after injuries. Front Cell Neurosci. (2015) 9: 13.

Carlson AL, Bennett NK, Francis NL, Halikere A, Clarke S, Moore JC, Hart RP, Paradiso K, Wernig M, Kohn J, Pang ZP, Moghe PV. Generation and transplantation of reprogrammed human neurons in the brain using 3D microtopographic scaffolds. Nat Commun. (2016) 7:10862.

Carvalho-de-Souza JL, Treger JS, Dang B, Kent SBH, Pepperberg DR, Bezanilla F. Photosensitivity of neurons enabled by cell-targeted gold nanoparticles. Neuron (2015) 8; 86(1): 207–217.

Cassel JC, Duconseille E, Jeltsch H, Will B. The fimbria-fornix/cingular bundle pathways: a review of neurochemical and behavioural approaches using lesions and transplantation techniques. Prog Neurobiol. (1997) 51(6):663-716.

Cavallo F. Compliant semiconductor scaffolds: building blocks for advanced neural interfaces. Neural Regen Res. (2015) 10(11): 1741–1742.

Cellot G, Cilia E, Cipollone S, Rancic V, Sucapane A, Giordani S, Gambazzi L, Markram H, Grandolfo M, Scaini D, Gelain F, Casalis L, Prato M, Giugliano M, Ballerini L. Carbon nanotubes might improve neuronal performance by favouring electrical shortcuts. Nature Nanotechnology (2009) 4, 126-133.

Cellot G, Lagonegro P, Tarabella G, Scaini D, Fabbri F, Iannotta S, Prato M, Salviati G. PEDOT:PSS Interfaces Support the Development of Neuronal Synaptic Networks with Reduced Neuroglia Response In vitro. Front Neurosci. (2016)14;9:521.

Cellot G, Toma F.M, Varley Z.K, Laishram J, Villari A, Quintana M, Cipollone S, Prato M, Ballerini L. Carbon nanotube scaffolds tune synaptic strength in cultured neural circuits: novel frontiers in nanomaterial-tissue interactions. Journal of Neuroscience (2011) 31, 12945-12953.

Cetin M, Gumru S, Aricioglu F. Nanotechnology Applications in Neuroscience: Advances, Opportunities and Challenges. Bulletin of Clinical Psychopharmacology (2012)22(2):115-20.

Cha C, Shin SR, Annabi N, Dokmeci MR, Khademhosseini A. Carbon-based nanomaterials: multifunctional materials for biomedical engineering. ACS Nano(2013) 7:4, 2891-2897.

Chapin JK, Moxon KA - Neural Prostheses for Restoration of Sensory and Motor Function (2000) Boca Raton: CRC Press (6th ed.)

Chen WH & Lin YW. A substrate scaffold for assessment of nerve regeneration and neurodegenerative diseases. Neural Regen Res. (2015) 10(1): 41–42.

Chen YC, Smith DH, Meaney DF. In-vitro approaches for studying blast-induced traumatic brain injury. J Neurotrauma. (2009) 26(6):861-76.

Chiappini C, De Rosa E, Martinez JO, Liu X, Steele J, Stevens MM, Tasciotti E. Biodegradable silicon nanoneedles delivering nucleic acids intracellularly induce localized in vivo neovascularization. Nat Mater. (2015) 14(5):532-9.

Choi W , Lahiri I, Seelaboyina R & Kang YS. Synthesis of Graphene and Its Applications: A Review. Critical Reviews in Solid State and Materials Sciences (2010) 35:1, 52-71.

Choudhary V, Gupta A. Polymer/Carbon Nanotube Nanocomposites. (2011) Dr. Siva Yellampalli (Ed.).

Clark RE, Broadbent NJ, Squire LR. Hippocampus and Remote Spatial Memory in Rats. Hippocampus. 2005;15(2):260-72.

Colgin LL. Rhythms of the hippocampal network. Nat Rev Neurosci. (2016) 17(4):239-49.

Cooper DR, Nadeau JL. Nanotechnology for in vitro neuroscience. Nanoscale (2009) 1, 183-200.

Daly JJ, Wolpaw JR. Brain-computer interfaces in neurological rehabilitation. Lancet Neurol. (2008) 7(11):1032-43.

Deller T, Adelmann G, Nitsch R, Frotscher M. The alvear pathway of the rat hippocampus. Cell Tissue Res. (1996) 286(3):293-303.

Dresselhaus MS. Fifty years in studying carbon-based materials. Phys scr (2012) T146, 014002.

Fabbro A, Villari A, Laishram J, Scaini D, Toma FM, Turco A, Prato M, Ballerini L. Spinal cord explants use carbon nanotube interfaces to enhance neurite outgrowth and to fortify synaptic inputs. ACS Nano (2012) 6, 2041-2055.

Fabbro A, Scaini D, León V, Vázquez E, Cellot G, Privitera G, Lombardi L, Torrisi F, Tomarchio F, Bonaccorso F, Bosi S, Ferrari AC, Ballerini L, Prato M. Graphene-Based Interfaces Do Not Alter Target Nerve Cells. ACS Nano. (2016) 26;10(1):615-23.

Fernández-Ruiz A, Oliva A, Nagy GA, Maurer AP, Berényi A, Buzsáki G. Entorhinal-CA3 Dual-Input Control of Spike Timing in the Hippocampus by Theta-Gamma Coupling. Neuron (2017) 93, 1213-1226.

Finger, S. Origins of neuroscience: a history of explorations into brain function. (2001). Oxford University Press. p. 286.

Fozdar DY, Lee JY, Schmidt CE, Chen S. Hippocampal neurons respond uniquely to topographies of various sizes and shapes. Biofabrication (2010) 2(3):035005.

Fredj NB, Burrone J. A resting pool of vesicles is responsible for spontaneous vesicle fusion at the synapse. Nat Neurosci. (2009) 12(6):751-8.

Gad P, Choe J, Nandra MS, Zhong H, Roy RR, Tai YC, Edgerton VR. Development of a multi-electrode array for spinal cord epidural stimulation to facilitate stepping and standing after a complete spinal cord injury in adult rats. J Neuroeng Rehabil. (2013) 10:2.

Gähwiler BH, Capogna M, Debanne D, McKinney RA, Thompson SM. Organotypic slice cultures: a technique has come of age. Trends Neurosci. (1997) 20(10):471-7.

Gawad S, Michele Giugliano M, Heuschkel M, Wessling B, Markram H, Schnakenberg U, Renaud P, Morgan H. Substrate Arrays of Iridium Oxide Microelectrodes for in Vitro Neuronal Interfacing. Front Neuroengineering (2009) 2:1.

Giugliano M, Prato M, Ballerini L. Nanomaterial/neuronal hybrid system for functional recovery of the CNS. Drug Discovery Today: Disease Mechanisms. (2008) 5: 37-43.

Goodman RP, Schaap IA, Tardin CF, Erben CM, Berry RM, Schmidt CF, Turberfield AJ. Rapid chiral assembly of rigid DNA building blocks for molecular nanofabrication. Science (2005) 9; 310:1661-5.

Green JD & Arduini AA. Hippocampal electrical activity in arousal. J Neurophysiol. (1954) Nov;17(6):533-57.

Gupta KC, Haider A, Choi Y, Kang I. Nanofibrous scaffolds in biomedical applications. Biomater. Res. (2014) 18(2):27-38.

Hales CM, Rolston JD, Potter SM. How to Culture, Record and Stimulate Neuronal Networks on Micro-electrode Arrays (MEAs). (2010) 39: 2056.

Hales JB, Schlesiger MI, Leutgeb JK, Squire LR, Leutgeb S, Clark RE. Medial entorhinal cortex lesions only partially disrupt hippocampal place cells and hippocampus-dependent place memory. Cell Rep. (2014) 6; 9(3): 893–901.

Harris LD, Graffagnini MJ. Nanomaterials in Medical Devices: A Snapshot of Markets, Technologies and Companies. Nanotech. L. & Bus. (2007) 4, 415-422.

Harrison RH, St-Pierre JP, Stevens MM. Tissue engineering and regenerative medicine: a year in review. Tissue Eng Part B Rev. (2014) 20(1):1-16.

Haziza S, Mohan N, Loe-Mie Y, Lepagnol-Bestel AM, Massou S, Adam MP, Le XL, Viard J, Plancon C, Daudin R *et al*. Fluorescent nanodiamond tracking reveals intraneuronal transport abnormalities induced by brain-disease-related genetic risk factors. Nat Nanotechnol. (2016) 260.

Heidemann M, Streit J, Tscherter A. Investigating Functional Regeneration in Organotypic Spinal Cord Co-cultures Grown on Multi-electrode Arrays. (2015) J Vis Exp. (103): 53121.

Hell, SW, Wichmann, J. "Breaking the diffraction resolution limit by stimulated emission: Stimulated-emission-depletion fluorescence microscopy".*Optics Letters* (1994) 19 (11): 780–782.

Hirsch A. The era of carbon allotropes. Nat Mater. (2010) 9(11):868-71.

Hochberg LR, Serruya MD, Friehs GM, Mukand JA, Saleh M, Caplan AH, Branner A, Chen D, Penn RD, Donoghue JP. Neuronal ensemble control of prosthetic devices by a human with tetraplegia. Nature (2006) 13;442(7099):164-71.

Hosseinkhani M. Mehrabani D, Karimfar MH, Bakhtiyari S, Manafi A, Shirazi R. Tissue Engineered Scaffolds in Regenerative Medicine. World J Plast Surg. (2014) 3(1): 3–7.

Huang F, Shen Q, Zhao J. Growth and differentiation of neural stem cells in a three-dimensional collagen gel scaffold. Neural Regen Res. (2013) 8(4): 313–319.

Iijima S. Helical microtubules of graphitic carbon. Nature (1991) 354, 56–58.

Jacobson S, Marcus EM. Neuroanatomy for the Neuroscientist. Springer New York (2008).

Jaiswal JK, Goldman ER, Mattoussi H, Simon SM. Use of quantum dots for live cell imaging (2004) Nat Methods 1, 73 – 78.

Keefer E.W., Botterman B.R., Romero M.I., Rossi A.F., Gross G.W. Carbon nanotube coating improve neuronal recordings. Nature Nanotechnology (2008) 3, 434-439.

Kitamura T, Inokuchi K. Role of adult neurogenesis in hippocampal-cortical memory consolidation. Mol Brain (2014)19;7:13.

Kitamura T, Pignatelli M, Suh J, Kohara K, Yoshiki A, Abe K, Tonegawa S. Island cells control temporal association memory. Science (2014) 343(6173):896-901.

Kitamura T, Sun C, Martin J, Kitch LJ, Schnitzer MJ, Tonegawa S. Entorhinal Cortical Ocean Cells Encode Specific Contexts and Drive Context-Specific Fear Memory. Neuron (2015) 87(6):1317-31.

Kroto HW, Heath JR, O'Brien SC, Curl RF, Smalley RE. C60: Buckminsterfullerene. Nature (1985) 318(6042), 162-163.

Ku SH, Lee M, Park CB. Carbon-based nanomaterials for tissue engineering. Adv Healthc Mater. (2013) 2(2):244-60.

Kumar S, Ahlawat W, Kumar R, Dilbaghi N. Graphene, carbon nanotubes, zinc oxide and gold as elite nanomaterials for fabrication of biosensors for healthcare. Biosens Bioelectron. (2015) 70:498-503.

Kumpf RA, Dougherty DA. A mechanism for ion selectivity in potassium channels: computational studies of cation-pi interactions. Science. 261, 1708-10 (1993).

Kunze A, Bertsch A, Giugliano M, Renaud P. Microfluidic hydrogel layers with multiple gradients to stimulate and perfuse three-dimensional neuronal cell cultures. Procedia Chemistry (2009) 1(1):369-372.

Lee JK, Baac H, Song SH, Jang E, Lee SD, Park D, Kim SJ. Neural prosthesis in the wake of nanotechnology: controlled growth of neurons using surface nanostructures. Acta Neurochir Suppl. (2006) 99:141-4.

Lee JS, Lipatov A, Ha L, Shekhirev M, Andalib MN, Sinitskii A, Lim JY. Graphene substrate for inducing neurite outgrowth. Biochem Biophys Res Commun. (2015) 1;460(2):267-273.

Lemaire V, Tronel S, Montaron MF, Fabre A, Dugast E, Abrous DN. Long-lasting plasticity of hippocampal adult-born neurons. J Neurosci. (2012) 29;32(9):3101-8.

Li WJ, Tuli R, Okafor C, Derfoul A, Danielson KG, Hall DJ, Tuan, RS. A three-dimensional nanofibrous scaffold for cartilage tissue engineering using human mesenchymal stem cells. Biomaterials (2005) 26(6) 599-609.

Li Z, Hulderman T, Salmen R, Chapman R, Leonard SS, Young SH, Shvedova A, Luster MI, Simeonova PP. Cardiovascular effects of pulmonary exposure to single-wall carbon nanotubes. Environmental Health Perspectives (2007) 115, 377-382.

Lim SH, MAO HQ. Electrospun scaffolds for stem cell engineering. Adv Drug del Rev (2009) 61(12) 1084-1096.

Littlejohn SD. Electrical Properties of graphite nanoparticles in silicone flexible oscillators and electromechanical sensing. Springer. 2014, XV.

Liu MG, Chen XF, He T, Li Z, Chen J. Use of multi-electrode array recordings in studies of network synaptic plasticity in both time and space. Neurosci Bull (2012) 28(4):409–422.

Londono R & Badylak SF. Biologic Scaffolds for Regenerative Medicine: Mechanisms of In vivo Remodeling. Ann Biomed Engin. (2015) 43(3): 577-592.

Lovat V, Pantarotto D, Lagostena L, Cacciari B, Grandolfo M, Righi M, Spalluto G, Prato M, Ballerini L. Carbon nanotube substrates boost neuronal electrical signaling. Nano Letters (2005) 5, 1107-1110.

Lynch MA. Long-term potentiation and memory. Physiol Rev. (2004) 84(1):87-136.

Marie Engelene J. Obien MEJ, Deligkaris K, Bullmann T, Bakkum DJ, Frey U. Revealing neuronal function through microelectrode array recordings. (2014) 8:423.

Mattson MP, Haddon RC, Rao AM. Molecular functionalization of carbon nanotubes and use as substrates for neuronal growth. J Mol Neurosci (2000) 14:175-182.

Mazzatenta A, Giugliano M, Campidelli S, Gambazzi L, Businaro L, Markram H, Prato M, Ballerini L. Interfacing neurons with carbon nanotubes: electrical signal transfer and synaptic stimulation in cultured brain circuits. J. of Neurosci. (2007) 27, 6931-6936.

McMurtrey RJ. Patterned and functionalized nanofiber scaffolds in three-dimensional hydrogel constructs enhance neurite outgrowth and directional control. J Neural Eng. (2014) 11(6):066009.

Menon JU, Jadeja P, Tambe P, Vu K, Yuan B, Nguyen KT. Nanomaterials for Photo-Based Diagnostic and Therapeutic Applications. Theranostics (2013) 3(3): 152–166.

Moser EI, Kropff E, Moser MB. Place cells, grid cells, and the brain's spatial representation system. Annu Rev Neurosci. (2008) 31:69-89.

Nagai Y, Yokoi H, Kaihara K, Naruse K. The mechanical stimulation of cells in 3D culture within a self-assembling peptide hydrogel. Biomaterials (2012) 33(4):1044-51.

Nagai Y., Unsworth L. D., Koutsopoulos S., Zhang S. Slow release of molecules in self-assembling peptide nanofiber scaffold. J. Control. Release (2006) 115, 18–25.

Nagel B, Dellweg H, Gierasch LM. Glossary for chemists of terms used in biotechnology. *Pure & Appl. Chem (1992)* 64,(1)143-168.

Neves G, Cooke SF, Bliss TV. Synaptic plasticity, memory and the hippocampus: a neural network approach to causality. Nat Rev Neurosci. (2008) 9(1):65-75.

Nguyen QT, Schroeder LF, Mank M, Muller A, Taylor P, Griesbeck O, Kleinfeld D. An in vivo biosensor for neurotransmitter release and in situ receptor activity. Nat Neurosci (2010) 13(1):127-132.

Nisbet DR, Rodda AE, Horne MK, Forsythe JS, Finkelstein DI. Neurite infiltration and cellular response to electrospun polycaprolactone scaffolds implanted into the brain. Biomaterials (2009) 30(27):4573-80.

Novoselov KS, Fal'ko VI, Colombo L, Gellert PR, Schwab MG, Kim K. A roadmap for graphene. Nature (2012) 490, 192-200.

Novoselov KS, Geim AK, Morozov SV, Jiang D, Zhang Y, Dubonos SV, Grigorieva IV, Firsov AA. Electric Field Effect in Atomically Thin Carbon Films. Science (2004) 306, 666-669.

O'Brien FJ. Biomaterials & scaffolds for tissue engineering. Materials Today (2011) 14:88–95.

O'Connell MJ Carbon Nanotubes: properties and applications. CRC press, Taylor e Francis Group (2006).

O'Keefe J and Nadel L. The Hippocampus as a Cognitive Map. (1978) Oxford: Oxford University Press.

Obataya I, Nakamura C, Han S, Nakamura N, Miyake J. Nanoscale operation of a living cell using an atomic force microscope with a nanoneedle. Nano Lett. (2005) 5(1):27-30.

O'Keefe J, Dostrovsky J. The hippocampus as a spatial map. Preliminary evidence from unit activity in the freely-moving rat. Brain Res. (1971) 34(1):171-5.

Pantic I, Paunovic J, Dimitrijevic I, Pantic S. Gold nanomaterials in contemporary neurophysiology, neurology and psychiatry research. . Rev. Adv. Mater. Sci. (2015) 40: 257-261.

Perederiy JV and Westbrook GL. Structural plasticity in the dentate gyrus - revisiting a classic injury model. Front Neural Circuits (2013) 7: 17.

Pisanello F, Sileo L, De Vittorio M. Micro- and Nanotechnologies for Optical Neural Interfaces. Front Neurosci. (2016) 10:70.

Plitman E, Nakajima S, de la Fuente-Sandoval C, Gerretsen P, Chakravarty MM, Kobylianskii J, Chung JK, Caravaggio F, Iwata Y, Remington G, Graff-Guerrero A. Glutamate-mediated excitotoxicity in schizophrenia: a review. Eur Neuropsychopharmacol. (2014) 24(10):1591-605.

Prato M, Kostarelos K, Bianco A. Functionalized carbon nanotubes in drug design and discovery. Acc Chem Res. (2008) 41, 60-68.

Pulizzi R, Musumeci G, Van den Haute C, Van De Vijver S, Baekelandt V, Giugliano M. Brief wide-field photostimuli evoke and modulate oscillatory reverberating activity in cortical networks. Sci Rep. (2016) 6:24701.

Ramirez JJ. The role of axonal sprouting in functional reorganization after CNS injury: lessons from the hippocampal formation. Restor Neurol Neurosci. (2001) 19(3-4):237-62.

Raspopovic S, Capogrosso M, Petrini FM, Bonizzato M, Rigosa J, Di Pino G, Carpaneto J, Controzzi M, Boretius T, Fernandez E, Granata G, Oddo CM, Citi L, Ciancio AL, Cipriani C, Carrozza MC, Jensen W, Guglielmelli E, Stieglitz T, Rossini PM, Micera S. Restoring natural sensory feedback in real-time bidirectional hand prostheses. Sci Transl Med. (2014) 5;6(222):222.

Rauti R, Lozano N, León V, Scaini D, Musto M, Rago I, Ulloa Severino FP, Fabbro A, Casalis L, Vázquez E, Kostarelos K, Prato M, Ballerini L. Graphene Oxide Nanosheets Reshape Synaptic Function in Cultured Brain Networks. ACS Nano. (2016) 26;10(4):4459-71.

Robinson JT, Jorgolli M, Shalek AK, Yoon MH, Gertner RS, Park H. Vertical nanowire electrode arrays as a scalable platform for intracellular interfacing to neuronal circuits. Nat Nanotechnol. (2012) 10;7(3):180-4.

Rorden C, Karnath HO. Using human brain lesions to infer function: a relic from a past era in the fMRI age? Nat Rev Neurosci. (2004) 5(10):813-9.

Sahoo SK, Parveen S, Panda JJ. The present and future of nanotechnology in human health care. Nanomedicine (2007) 3(1):20-31.

Salińska E, Danysz W, Łazarewicz JW. The role of excitotoxicity in neurodegeneration. Folia Neuropathol. (2005) 43(4):322-39.

Savage LM, Buzzetti RA, Ramirez DR. The effects of hippocampal lesions on learning, memory, and reward expectancies. Neurobiol Learn Mem. (2004) 82(2):109-19.

Schwartz AB, Cui XT, Weber DJ, Moran DW. Brain-controlled interfaces: movement restoration with neural prosthetics. Neuron (2006) 5;52(1):205-20.

Scoville WB, Milner B. Loss of recent memory after bilateral hippocampal lesions. Journal of Neurology, Neurosurgery, and Psychiatry (1957) 20 (1): 11–21.

Seabra AB, Paula AJ, de Lima R, Alves OL, Durán N. Nanotoxicity of graphene and graphene oxide. Chem Res Toxicol. (2014) 27(2):159-68.

Shah S, Liu JJ, Pasquale N, Lai J, McGowan H, Pang ZP, Lee KB. Hybrid upconversion nanomaterials for optogenetic neuronal control. Nanoscale (2015) 28;7(40):16571-7.

Shepherd JN, Parker ST, Shepherd RF, Gillette MU, Lewis JA, Nuzzo RG. 3D Microperiodic Hydrogel Scaffolds for Robust Neuronal Cultures. Adv Funct Mater. (2011) 21: 47–54.

Silva, Gabriel A. Neuroscience nanotechnology: progress, opportunities and challenges. Nat. Rev. Neurosci. (2006) 7: 65–74.

Smith AM, Mancini MC, Nie S. Bioimaging: second window for in vivo imaging. Nat Nanotechnol. (2009) 4(11):710-1.

Spira ME and Hai A. Multi-electrode array technologies for neuroscience and cardiology. Nat Nanotech (2013) 8, 83-94.

Strange BA, Witter MP, Lein ES, Moser EI. Functional organization of the hippocampal longitudinal axis. Nature (2014) 15, 655-669.

Sun X, Liu Z, Welsher K, Robinson J, Goodwin A, Zaric S, Dai H. Nano-graphene oxide for cellular imaging and drug delivery. Nano Res. (2008) 1, 203-212.

Taniguchi N, "On the Basic Concept of 'Nano-Technology'," Proc. Intl. Conf. Prod. Eng. Tokyo, Part II, Japan Society of Precision Engineering, 1974.

Tsintou M, Dalamagkas K, Seifalian AM. Advances in regenerative therapies for spinal cord injury: a biomaterials approach. Neural Regen Res. (2015) 10(5): 726–742.

Tye KM, Deisseroth K. Optogenetic investigation of neural circuits underlying brain disease in animal models. Nat Rev Neurosci. (2012) 13(4):251-66.

Urban GA. Micro- and nanobiosensors - state of the art and trends. Meas. Sci. Technol. (2009) 20, 1-18.

Usmani S, Aurand ER, Medelin M, Fabbro A, Scaini D, Laishram J, Rosselli FB, Ansuini A, Zoccolan D, Scarselli M, De Crescenzi M, Bosi S, Prato M, Ballerini L. 3D meshes of carbon nanotubes guide functional reconnection of segregated spinal explants. Sci Adv. (2016) 15;2(7):e1600087.

Vallejo-Giraldo , Pampaloni NP, Pallipurath AR, Mokarian-Tabari P, O'Connell J, D. Holmes J, Trotier A,Krukiewicz K, Orpella-Aceret G, Pugliese E, Ballerini L, Kilcoyne M, Dowd E, Quinlan LR, Pandit A, Kavanagh P, Biggs MJP. Preparation of Cytocompatible ITO Neuroelectrodes

with Enhanced Electrochemical Characteristics Using a Facile Anodic Oxidation Process. Adv Funct Mater. (2017) 1605035.

van Strien NM, Cappaert NLM, Witter MP. The anatomy of memory: an interactive overview of the parahippocampal-hippocampal network. Nature (2009) 10, 272-282.

Variola F. Atomic force microscopy in biomaterials surface science. *Phys. Chem. Chem. Phys.* (2015) 17, 2950-2959.

Veloz-Castillo MF, West RM, Cordero-Arreola J, Arias-Carrión O, Méndez-Rojas MA. Nanomaterials for Neurology: State-of-the-Art. CNS Neurol Disord Drug Targets (2016) 10:1306-1324.

Vidu R, Rahman M, Mahmoudi M, Enachescu M, Poteca TD, Opris I. Nanostructures: a platform for brain repair and augmentation. Front Syst Neurosci. (2014) 8:91. .

Vlachos A, Becker D, Jedlicka P, Winkels R, Roeper J, Deller T. Entorhinal denervation induces homeostatic synaptic scaling of excitatory postsynapses of d entate granule cells in mouse organotypic slice cultures. PLoS One. (2012) 7(3):e32883.

Wang CW, Pan CY, Wu HC, Shih PY, Tsai CC, Liao KT, Lu LL, Hsieh WH, Chen CD, Chen YT. In situ detection of chromogranin a released from living neurons with a single-walled carbon-nanotube field-effect transistor. Small. (2007) 3(8):1350-5.

Wang M, Abbineni G, Clevenger A, Mao C, Xu S. Upconversion nanoparticles: synthesis, surface modification and biological applications. Nanomedicine (2011) 7(6):710-29.

Wang, M., Mi, G., Shi, D., Bassous, N., Hickey, D., & Webster, T. J. Nanotechnology and Nanomaterials for Improving Neural Interfaces. Adv Funct Mat (2017) 1700905.

Witter MP and Amaral DG. Hippocampal formation. In "The rat nervous system" (2004) vol. 3, 3rd edn (ed. PaxinosG), pp. 635–704. Amsterdam, The Netherlands: Elsevier.

Witter MP, Naber PA, van Haeften T, Machielsen WC, Rombouts SA, Barkhof F, Scheltens P, Lopes da Silva FH. Cortico-hippocampal communication by way of parallel parahippocampal-subicular pathways. Hippocampus (2000) 10(4):398-410.

Witter MP. The perforant path: projections from the entorhinal cortex to the dentate gyrus. Prog Brain Res (2007) 163, 43-61.

Xinyu Zhu X, Qiao Y, Zhang X, Zhang S, Yin X, Gu J, Chen Y, Zhu Z, Li M, and Shao Y. Fabrication of Metal Nanoelectrodes by Interfacial Reactions. Anal Chem. (2014) 86(14), 7001.

Yin PT, Shah S, Chhowalla M, Lee KB. Design, synthesis, and characterization of grephene-nanoparticle hybrid materials for bioapplications. Chem. Rev. (2015) 115, 2483-2531.

Yu Z, McKnight TE, Ericson MN, Melechko AV, Simpson ML, Morrison B 3rd. Vertically aligned carbon nanofiber arrays record electrophysiological signals from hippoca mpal slices. Nano Lett. (2007) 7(8):2188-95.

Zhang H, Yu M, Xie L, Jin L, Yu Z. Carbon-Nanofibers-Based Micro-/Nanodevices for Neural-Electrical and Neural-Chemical Interfaces. J of Nanomaterials (2012), 280902.

Zhang L, Xia J, Zhao Q, Liu L, Zhang Z. Functional graphene oxide as a nanocarrier for controlled loading and targeted delivery of mixed anticancer drugs. Small (2010) 6, 537-544.

Zhang W, Zhu C, Ye D, Xu L, Zhang X, Wu Q, Zhang X, Kaplan DL, and Jiang X. Porous Silk Scaffolds for Delivery of Growth Factors and Stem Cells to Enhance Bone Regeneration. PLoS One (2014) 9(7): e102371.

Zhao XY, Liu MG, Yuan DL, Wang Y, He Y, Wang DD, Chen XF, Zhang FK, Li H, He XS, Chen J. Nociception-induced spatial and temporal plasticity of synaptic connection and function in the hippocampal formation of rats: a multi-electrode array recording. Mol Pain (2009) 22; 5:55.

Zumdahl SS, Zumdahl SA. Chemistry (9th ed.) Cengage Learning (2014).

APPENDIX

Specific modifications of neuronal threshold by optogenetic (subthreshold) modulations of membrane potential

Sebastian Reinartz, Niccolò P. Pampaloni, Laura Ballerini* and Matthew E. Diamond*

*co-corresponding authors

Synopsis:

Optogenetic excitation/inhibition of neuronal firing, by de- or hyperpolarizing genetically targeted neurons via light-gated ion pumps/channels, is a valuable experimental technique for neuroscience research. By its high temporal precision and cell-type specificity, it constitutes a powerful tool for cognitive neurosciences. Often a specific target brain area is reversibly perturbed in a gain- or loss-of-function manner, in order to study its potential contribution to the perception or cognition of interest. Hereby, usually control experiments are shown, in order to demonstrate specificity in terms of nonexistence of behavioral side effects like e.g. attention or motivation. However, the brain is a highly connected network, consisting of feedback loops, background firing and internal rhythms, just to name a few examples for the complexity. When one of its nodes is suddenly perturbed with a barrage of neuronal firing or with a sudden interruption of ongoing activity (often followed by rebound firing), it is very likely that neighboring nodes are also concerned, possibly even up to a behaviorally relevant extent (Otchy et al., 2015). Ways to use optogenetics for more gentle and local modifications of neuronal excitability, reducing sources of behavioral distraction, are therefore strongly suggested.

Here we studied the aspect of subthreshold modulation of neuronal excitability, transferring existing knowledge from physiology to optogenetics. We further performed a comparison of light induced excitability modifications between intracellularly recorded cultured cortical neurons, Hodgkin-

Huxley model predictions and neurons embedded in rat primary sensory cortex. We performed controlled optogenetic stimulation of single, hChr2(h134) expressing neurons with ramp stimulation, hereby mainly two parameters of the first response spikes are examined: (1) AP-threshold, a functional parameter that describes what voltage is needed to evoke the action potential and (2) maximal slope of spike upstroke, reflecting the number of active sodium channels at the moment of spike initiation, a parameter describing one potential mechanism underlying changes in AP-threshold. Increased action potential threshold and decreased maximal slope indicated a modified neuronal excitability, most likely by a changing number of voltage gated sodium channels (as compared to spontaneously activated spikes). We confirmed this to be a purely neuronal mechanism, by observing similar results when neurons were synaptically isolated from the network.

In another recording session we systematically changed the light onset slopes, by changing the duration to reach the light maximum, we derived the relation between light slope, action potential threshold and spike onset slope. As a possible indicator for excitability that could be more accurately accessed by extracellular recordings e.g. in vivo, we further examined two alternative measures. The supra-linear relation between light slope and spike latencies and the light amplitude/integral necessary for spike initiation, an alternative measure for action potential threshold. These relations were further compared with a Hodgkin Huxley model that includes hChr2(h134).

To transfer these measures to a real functional network, we injected rat primary somatosensory cortex and delivered identical light waveforms, while performing extracellular recordings in anesthetized rats. Considering increased variability due to fluctuations of neuronal excitability due to variations in cortical states and depth of anesthesia levels and the lack of precision of cellular intrinsic measures due to extracellular recordings, the previously identified measures enabled another read out of neuronal excitability.

Preparation of Cytocompatible ITO Neuroelectrodes with Enhanced Electrochemical Characteristics Using a Facile Anodic Oxidation Process

Catalina Vallejo-Giraldo, Niccolò Paolo Pampaloni, Anuradha R. Pallipurath, Parvaneh Mokarian-Tabari, John O'Connell, Justin D. Holmes, Alexandre Trotier, Katarzyna Krukiewicz, Gemma Orpella-Aceret, Eugenia Pugliese, Laura Ballerini, Michelle Kilcoyne, Eilís Dowd, Leo R. Quinlan, Abhay Pandit, Paul Kavanagh, and Manus Jonathan Paul Biggs**

Physicochemical modification of implantable electrode systems is recognized as a viable strategy to enhance tissue/electrode integration and electrode performance in situ. In this work, a bench-top electrochemical process to formulate anodized indium tin oxide (ITO) films with altered roughness, conducting profiles, and thickness is explored. In addition, the influence of these anodized films on neural cell adhesion, proliferation, and function indicates that anodized ITO film cytocompatibility can be altered by varying the anodization current density. Furthermore, ITO-anodized films formed with a current density of 0.4 mA cm^{-2} show important primary neural cell survival, modulation of glial scar formation, and promotion of neural network activity.

1. Introduction

The modification of implantable electrodes for neural stimulation and recording through electrochemical, biochemical, morphological, and topographical functionalization has been a major focus of neural engineering over the past five years.[1,2] A common occurrence following electrode implantation is reactive gliosis and the formation of a glial scar. This encapsulating scar forms at the electrode–tissue interface and accelerates neural loss, increases electrical signal impedance, and thereby compromises the efficacy of a stimulating/recording system in situ.[1] Biomimetic interfaces with multiple functionalities that facilitate stable charge transfer in vivo while promoting enhanced cell interaction, selection, and attachment are critical in chronic neuroelectrode functionality and the development of advanced neural stimulation systems and brain/machine interfaces.[3] In turn, important contributions in organic bioelectronics as neural interface platforms possessing

C. Vallejo-Giraldo, A. Trotier, Dr. K. Krukiewicz,[+] G. Orpella-Aceret, E. Pugliese, Prof. A. Pandit, Dr. M. J. P. Biggs
CÚRAM – Centre for Research in Medical Devices – Galway
Biosciences Research Building
118 Corrib Village, Newcastle, Galway, Ireland
E-mail: manus.biggs@nuigalway.ie

N. P. Pampaloni, Prof. L. Ballerini
Scuola Internazionale Superiore di Studi Avanzati (SISSA)
Via Bonomea, 265, 34136 Trieste, Italy

Dr. A. R. Pallipurath, Dr. P. Kavanagh,[++]
School of Chemistry
NUI Galway
University Road, Galway, Ireland
E-mail: p.kavanagh@qub.ac.uk

Dr. J. O'Connell, Prof. J. D. Holmes, Dr. P. Mokarian-Tabari
Department of Chemistry
University College Cork
Cork, Ireland

Dr. J. O'Connell, Prof. J. D. Holmes, Dr. P. Mokarian-Tabari
Tyndall National Institute
University College Cork
Cork, Ireland

Dr. J. O'Connell, Prof. J. D. Holmes, Dr. P. Mokarian-Tabari
Centre for Research on Adaptive Nanostructures and Nanodevices (CRANN) and AMBER Centre
Trinity College Dublin
Dublin 2, Ireland

Dr. M. Kilcoyne
Carbohydrate Signalling Group
Microbiology
School of Natural Sciences
NUI Galway, University Road, Galway, Ireland

Dr. E. Dowd
Department of Pharmacology, Physiology
NUI Galway
University Road, Galway, Ireland

Dr. L. R. Quinlan
Department of Physiology
NUI Galway
University Road, Galway, Ireland

[+]Present address: Department of Physical Chemistry and Technology of Polymers, Silesian University of Technology, 44-100 Gliwice, Poland
[++]Present address: School of Chemistry and Chemical Engineering, Queen's University Belfast, David Keir Building, Stranmillis Road, Belfast, BT9 5AG, UK

DOI: 10.1002/adfm.201605035

favorable electrochemical properties for neural recording and stimulation have been reported.[4–7]

Ongoing strategies in biomimetic design of the neural interface have focused on morphological, mechanical, and biochemical modification of the electrode–tissue interface to reduce tissue damage and promote electrode integration through device miniaturization, the development of flexible polymer systems, and the localized delivery of antifibrotic or neurotropic chemistries.[8,9] Traditionally, chemically inert conductors such as gold, platinum, and iridium, as well as semiconductors such as silicon, have been widely employed as electrode systems in both clinical and research settings and have been found to perform well under nonchronic settings.[10,11] Recently, however, nonmetallic electrically conducting biomaterials including inherently conducting polymers and polymer composites have been explored as neuroelectrode alternatives in an effort to promote chronic functionality and enhanced biocompatibility.[12,13]

In the field of conductive metal oxide electronics, indium tin oxide (ITO) is one of the most intensively investigated materials because of its relatively low electrical resistivity, its optical transparency, and its thermal stability, making it well-suited for use as an electrode or sensor material.[14] Specifically, ITO thin films have been employed successfully in the fabrication of optoelectronic and electrochromic devices,[15] electroluminescent devices,[16] photovoltaic cells,[17] and waveguide sensors.[18]

Recent studies indicate the potential of electrically conducting ITO thin films for biosensor applications in vitro.[19–25] Selvakumaran et al.[26] demonstrated the efficacy of ITO electrodes as sensing electrodes in vitro for bioassays, and potential physiological measurements. Here it was concluded that ITO offered a compromise between promoting cell growth while adsorbing significantly less protein than titanium control substrates.[22,27] Further, Tanamoto et al.[21] developed micropatterned ITO glass electrode devices to facilitate electrical stimulation of neural cells coupled with fluorescent imaging processes. The device was observed to uniformly stimulate multiple single cells with and the authors noted potential in vivo applications.

It has been shown that ITO can be physically and chemically modified to locally tailor its electrical and optical properties,[28] and, in particular, the modification of ITO electrodes with conductive polymer thin films via electropolymerization techniques has been explored as a method to enhance the electrode conductivity.[29,30] Further, surface treatments such as acid etching[31] and layer-by-layer assembly[32] have been used to modulate and alter the performance of ITO for commercial applications. Electrochemical activation or passivation via the anodic oxidation (anodization process)[33,34] is widely used in biomedical engineering to grow metal oxide dielectrics for electrical devices[35,36] and to obtain protective and decorative films on metallic surfaces to increase corrosion resistance.[37] The experimental conditions, i.e., galvanostatic or potentiostatic anodization deposition, electrolyte composition, and deposition time, facilitate the oxidation of ions at the substrate–solution interface to produce thin-film coatings.[38] Several research groups[39–46] have demonstrated that the anodic oxidation technique can be employed in conjunction with mask strategies for the generation of biologically passive layers or nanofeatures on titanium[39–44] and alumina[45,46] to improve cell adhesion and implant integration. Surface modification of ITO via anodization, however, has not yet been explored as a method to enhance cytocompatibility, cell adhesion, and functionality in implantable systems. Furthermore, the effects of ITO anodization on film electrochemical impedance and topography remain unknown.

In this present comprehensive and systematic study, ITO anodization as a functionalization approach for the generation of cytocompatible and functional thin-film electrodes for potential neural applications is explored for the first time. Anodized ITO thin films were formulated through a facile electrochemical process employing the application of current densities ranging from 0.4 to 43 mA cm^{-2}. Subsequently, the physical, chemical, electrochemical, and cytocompatibility effects of ITO anodization were explored. Our results elucidate important material effects with regard to anodization current densities on ITO film surface morphology, electrochemistry, and cytocompatibility for the generation of neural interfaces with superior electrical and biological characteristics.

2. Results and Discussion

When subjected to anodic[47–51] and cathodic[50–53] polarization, ITO electrodes undergo changes in chemical composition,[47–53] surface morphology,[47,48,50–53] conductivity,[47,48,50–53] and optical transparency.[49–53] Such effects are largely influenced by (i) the electrochemical parameters selected for electrode polarization and (ii) composition of the electrolyte solution.[47–53] For example, polarization at high positive potentials (>1.5 V vs saturated calomel electrode) in aqueous electrolyte can cause substantial structural changes to the ITO electrode.[48] Similarly, polarization in strong acid (1 M HNO_3) or strong base (1 M NaOH) can result in a dramatic reduction in electrochemical activity, electrical conductivity, and optical transparency of the ITO electrode.[53] Such effects are normally attributed to structural and/or chemical changes within the ITO film induced by the polarization process,[47,48] which, under harsh electrochemical conditions, may result in partial or complete dissolution of ITO coating.[47–51]

Here, we report a novel method for the facile fabrication of bioactive ITO substrates with enhanced electrochemical properties as neural interfaces. Due to the detrimental effects on ITO films resulting from anodization in harsh chemical conditions detailed above, we chose to perform the anodization process in a relatively mild electrolyte consisting of 0.01 M phosphate-buffered saline (PBS) solution and 10×10^{-6} M poly(sodium 4-styrenesulfonate) (PSS). Constant current densities of 0.4, 4, and 43 mA cm^{-2} applied for 450 s were used to prepare modified ITO films through anodization in this electrolyte. The optimization process of the current densities employed in this study is indicated in Figure S1 (Supporting Information).

The following sections describe the physical, chemical, electrochemical, and biocompatibility properties of resulting films.

2.1. Physical Characterization of Anodized ITO Films

Systematic studies of thin-film ITO postdeposition processing in optoelectronic device fabrication have focused on the

processing effects on surface roughness and on the generation of defined nanostructures. To a great extent, techniques such as chemical-bath deposition[54] and thermal annealing,[55] respectively, have been utilized to modify film physicochemical properties with resulting films showing considerable morphological changes that translate into the optical transmittance and electrical conductivity. While a number of studies have explored anodization processes to produce microporous titanium oxide films on implant surfaces for orthopedic applications,[56] the impact of anodization on the physical properties of ITO substrates for neural interfaces has not been investigated thus far.

Figure 1A shows representative scanning electron microscopy (SEM) images of anodized ITO films using 0.4, 4, and 43 mA cm^{-2} current densities over a constant time of 450 s, and pristine ITO coated glass as a control substrate. It is interesting to note that pristine ITO films possess a surface morphology composed of a random assembly of nanoparticles that is developed into a nanoparticulate/granular morphology in films anodized under our experimental conditions. The quantification of the degree of nodularity revealed significant differences in nodule diameter when subjected to different deposition current densities. Film growth using higher current densities yielded less-dense, nonuniform films than those of anodized films formed with lower current densities.[57]

Experimentally, pristine ITO films reported a mean particle size of 86 nm, films formed with 0.4 mA cm^{-2} were associated with a mean particle size of 89 nm; and mean particle diameters of 152 and 112 nm were observed in films formed using 4 and 43 mA cm^{-2} current densities, respectively. At 0.4 mA cm^{-2}, the observed nodular distribution was uniform and compact. However, at 4 and 43 mA cm^{-2} current densities, a more clustered grain-like structure and a nonhomogeneous distribution of particles were evident. This trend in distribution was further observed as an increase in porosity percentage in films formed using higher current densities relative to films formed at 0.4 mA cm^{-2} and the pristine ITO coated glass (Figure S2, Supporting Information). This suggests that current deposition strongly affects the processes of surface diffusion of atoms, nucleation, and coalescence of the film growth resulting in different nucleation densities at the surface.[58,59] Noteworthy, a correlation between elastic moduli and porosity[60–62] is inferred, and it can be assumed that anodized ITO films will possess enhanced flexibility due to their high-packing density relative to nonanodized films,[62] an important consideration

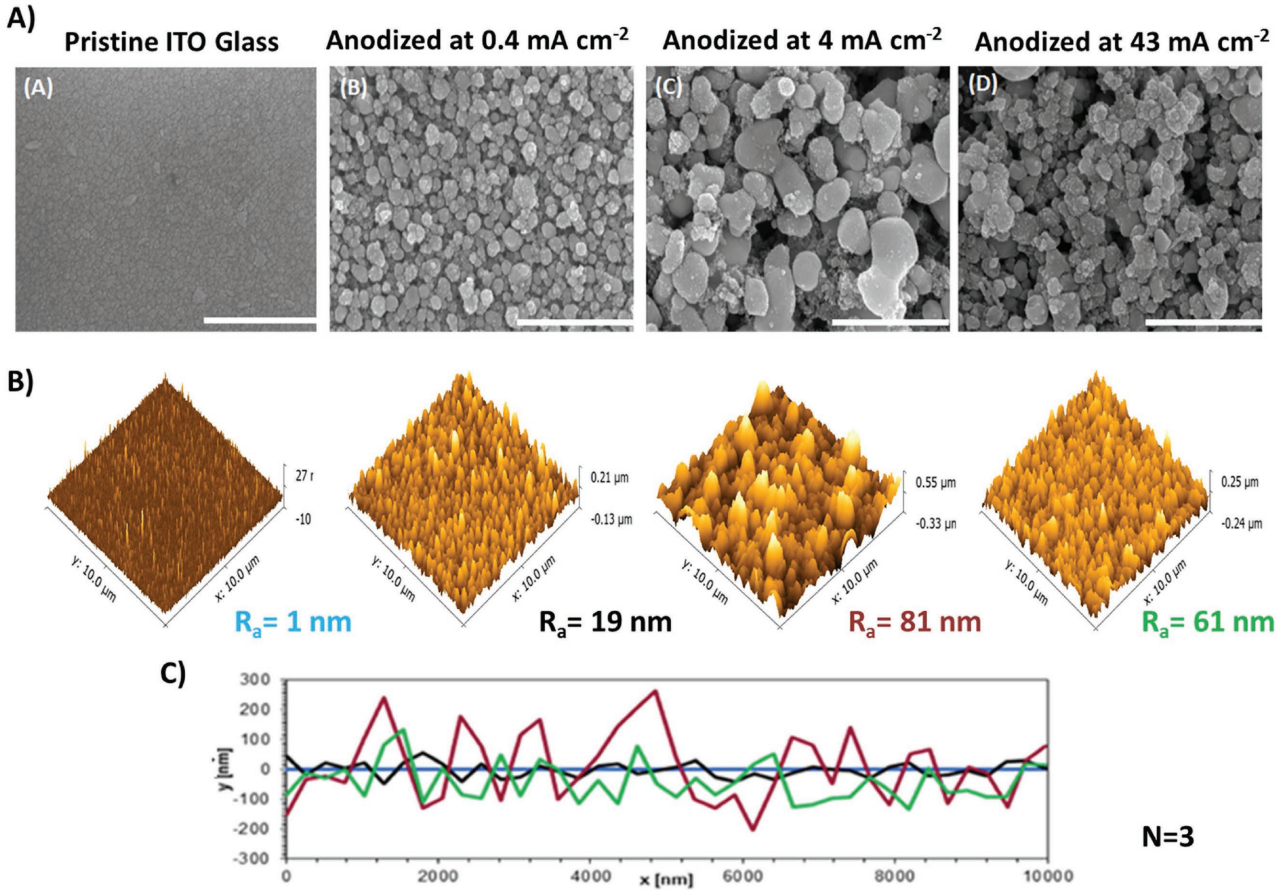

Figure 1. Particle size and distribution are significantly affected by current density. A) Scanning electron micrograms of control pristine ITO coated glass (A) and ITO anodized films electrodeposited with (B) 0.4 mA cm^{-2}, (C) 4 mA cm^{-2}, and (D) 43 mA cm^{-2} current densities. Scale bar = 1 µm. B) Corresponding roughness (R_a) measurements of the pristine ITO glass and the anodized ITO films with different current densities, 0.4 mA cm^{-2}, 4 mA cm^{-2}, and 43 mA cm^{-2}, and representative line profiles C) from each of the films. R_a indicates the mean surface roughness, calculated on 10 μm^2 regions.

in next-generation neuroelectrode design. Interestingly, it was noted that a current density of 0.4 mA cm^{-2} resulted in anodized ITO films with less internal voids.

Anodization processes resulted in significant increases in surface roughness (R_a) relative to pristine ITO films as a function of current density (Figure 1B). Films formed with current densities of 0.4 mA cm^{-2} exhibited an average roughness of 19 nm over 10 μm^2, and an average roughness of 81 and 61 nm when formed at 4 and 43 mA cm^{-2}, respectively. Conversely, pristine ITO films possessed an R_a of 1 nm over 10 μm^2. A similar trend was also observed for mean nodule diameter, which increased from 89 nm in current densities of 0.4 mA cm^{-2} to 152 and 112 nm in films formed with current densities of 4 and 43 mA cm^{-2}, respectively (**Table 1**).

Similarly, an abrupt increase in film thickness was observed in films formed with current densities of 4 and 43 mA cm^{-2} indicating that the maximum rate of anodization deposition is limited by the electrolyte diffusion rate.[57] The limiting current density to attain ≈100% efficiency of film deposition can be determined theoretically by calculating the maximum rate at which the ions diffuse to the cathode. Our data (Table 1) propose that at 4 mA cm^{-2} (under our experimental conditions), the threshold for the limiting current density may have already been met[38,57] and the observed nonlinear increases in particle size, film roughness, and the plateau in film thickness could be indications that films formed using a current density of 4 mA cm^{-2} under our experimental conditions are associated with a decrease in film growth efficiency. Therefore, it can be assumed that between 4 and 43 mA cm^{-2} the diffusion limiting current density for ITO anodization can be found, and that the diffusion kinetics of oxygen and hydrogen at the cathode are insufficient, causing reactions at the anode to stop to conserve electrons.

Similarly, this transition in film thickness was also represented as optical changes to the ITO films that changed from a translucent blue-grey to an opaque dark grey (Figure S3, Supporting Information). It can be anticipated, according to the Drude model,[63] that the changes observed in film morphology derived from the differences in film growth imposed by the explore current densities will impact on the refractive index of films. Optical transmission spectra of the pristine ITO coated glass and the anodized ITO films formed at 0.4, 4, and 43 mA cm^{-2} current densities were performed to quantify film transparency (Figure S4, Supporting Information). The observed trend in optical transmittance of the anodized ITO films formed at higher current densities (4 and 43 mA cm^{-2}) reflects scattering losses as predicted by the effects of film roughness.[64] The aforementioned faster growth observed in films formed at 4 mA cm^{-2} resulted in the decrease in transmittance of these films.

In order to assess the durability and stability of anodized ITO films under physiological conditions, substrates were assessed with an accelerated ageing study that simulated 4 years of implant equivalence in the body (**Figure 2**). Regarding film delamination (Figure 2A) together with consistent high losses in charge storage capacity (CSC), 75% and 74% were observed in films formed with current densities of 4 and 43 mA cm^{-2}, respectively. Conversely, a 55% loss in CSC of ITO films anodized with the lowest current density of 0.4 mA cm^{-2} was observed (Figure 2B). It is interesting to note that pristine ITO glass also underwent a significant diminution in electrical activity with a 96% loss in CSC and with pronounced microcracks observable by SEM.

The effect of thermal ageing on pristine ITO films perceived here was comparable to those presented by Hamasha et al.,[65] who also tested ITO under thermal ageing conditions and showed that films became unstable and demonstrated increased in electrical resistance and physical changes. Current research to improve the stability of ITO electrodes has focused on the deposition of multilayers,[66] of novel transport and luminescent materials[67] such as polymers,[68] and on efficient injection contacts.[69] Conversely, it is reported by Nishimoto et al.[70] that optimal variations in grain-boundary potential caused by oxygen adsorption after annealing TiO_2 structures with ITO can improve thermal stability of pristine ITO. Consequently, surface modifications of thin films of ITO such as the anodization process utilized here may help to explain the enhanced stability observed in anodized films, with the formation of stabilizing oxide layers.[71]

Table 1. Physical properties of anodized ITO films formed with different deposition currents. Values of experimental thickness and mean particle diameter of pristine and anodized films formed with 0.4, 4, and 43 mA cm^{-2} current densities over a constant time of 450 s. The data represent the mean of 15 measurements for film thickness plus >200 measurements for particle diameter. Results are ± SD, $n = 3$.

ITO film	Average thickness [nm]	Mean particle diameter [nm]
Pristine ITO glass	750 ±	86 ± 17
Anodized at 0.4 mA cm^{-2}	109.7 ± 4	89 ± 26
Anodized at 4 mA cm^{-2}	934.5 ± 35	152 ± 78
Anodized at 43 mA cm^{-2}	937.8 ± 47	112 ± 55

2.2. Chemical Characterization

In **Table 2**, the X-ray photoelectron spectroscopy (XPS) survey with the elemental composition of pristine ITO and anodized ITO films using 0.4, 4, and 43 mA cm^{-2} is reported. The XPS survey spectrum of pristine ITO revealed the presence of prominent In, Sn, and O peaks. The atomic percentage for C is also relatively high showing a large presence of atmospheric C on the film surface. Similarly, low-current density anodized samples consisted primarily of In, Sn, and O. The O concentration was observed to increase significantly in anodized ITO films, increasing from 42% O1s atomic% in pristine ITO films to 49.81% in anodized films formed with current densities of 43 mA cm^{-2}. Conversely, the Sn atomic% is reduced in anodized ITO films relative to pristine films, which is reportedly due to the leaching of Sn into the electrolyte during the anodization process.[48]

2.3. Electrochemical Characterization

Figure 3A shows cyclic voltammograms for each of the ITO films in 50 × 10^{-3} M phosphate buffer before and after anodization. Surface charge density was approximated through integration of the charge passed within the cathodic region of voltammetric scans, corresponding to charge densities

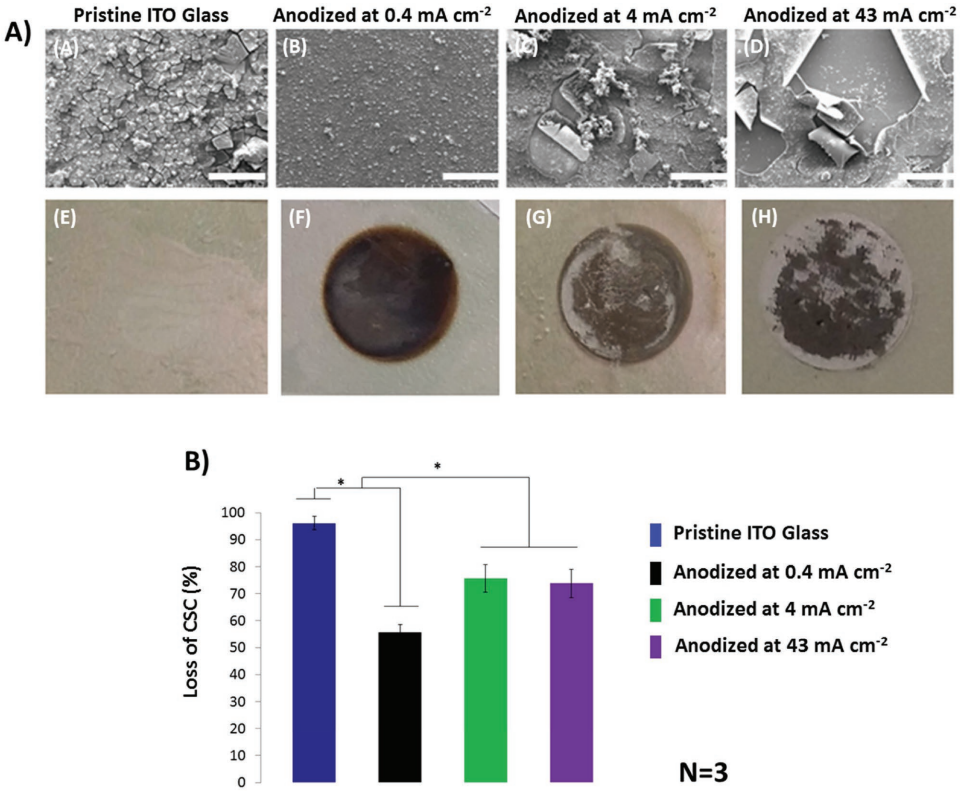

Figure 2. The impact of the accelerated ageing study on durability and electrical stability of the anodized ITO films. A) On top, scanning electron micrograms of control pristine ITO glass (A) and ITO anodized films electrodeposited with (B) 0.4 mA cm^{-2}, (C) 4 mA cm^{-2}, and (D) 43 mA cm^{-2} current densities. Scale bar = 200 µm. After four weeks under biologically relevant ageing, important film delamination was observed on anodized films formed using high current densities (4 and 43 mA cm^{-2}). Partial microcracks were observed in films formed at 0.4 mA cm^{-2} and control ITO. On bottom, corresponding photographs showing the final visual appearance of control and anodized films (E)–(H) after four weeks of ageing study. B) Plot of percentage loss of charge storage capacity (CSC) after four weeks of accelerated ageing study simulating four years of implant equivalence in the body. Important significant differences between the ITO control and the anodized films were observed. The ITO anodized films formed at 0.4 mA cm^{-2} were the most stable films compared to control and to the films formed using high current densities. Results are ± STD, ★ = $p < 0.05$.

of 49, 341, 15, and 15 µC cm^{-2} for pristine ITO films and films subjected to anodization at 0.4, 4, and 43 mA cm^{-2} current densities, respectively (**Table 3**). A large increase in charge density was observed in ITO films subjected to anodization at 0.4 mA cm^{-2}, by almost one order of magnitude, compared to pristine ITO films. This is likely due to the greater surface coverage as indicted by SEM and atomic force microscopy (AFM) analysis. Interestingly, a threefold reduction in charge density was observed for ITO films subjected to anodization at current densities of 4 and 43 mA cm^{-2} compared to the pristine ITO glass (Figure 3A) despite increased surface roughness.

Table 2. XPS analysis of the elemental composition of the pristine ITO and anodized ITO films.

ITO film	Atomic composition [%]			
	In3d	O1s	C1s	Sn3d5
Pristine ITO glass	21.00	42.17	34.62	2.21
Anodized at 0.4 mA cm^{-2}	24.88	43.47	30.34	1.31
Anodized at 4 mA cm^{-2}	23.45	44.53	31.52	1.16
Anodized at 43 mA cm^{-2}	22.75	49.81	26.65	0.78

However, this electrical profile is consistent with the high porosity percentages calculated for these films (Figure S2, Supporting Information). No appreciable difference in charge density was observed in any of the ITO substrates when tested in physiological-like saline solution[72] compared to 50 × 10^{-3} M phosphate buffer solution.

Comparative electrochemical impedance profiles for films are shown in the Bode diagram (Figure 3C) and Nyquist plot (Figure 3D). Within frequency ranges of 10^{-1} to 10^{4} Hz, ITO anodized films formed at a current density of 0.4 mA cm^{-2} displayed the lowest impedance profiles, moderately lower than those recorded for the pristine ITO films and close to the impedance observed for gold coated glass films. This indicates that changes in chemical composition and/or morphology induced by the 0.4 cm^{-2} current density anodization process do not appear to diminish the conductive properties of the ITO electrode. This is significant as alternative electrochemical treatments have been shown to greatly decrease the conductivity of ITO electrodes.[48,50–53] However, an increase in impedance of one order of magnitude was observed for films formed at high current densities (4 and 43 mA cm^{-2}), revealing an inverse relationship between electrical conductivity and the anodization current density applied.

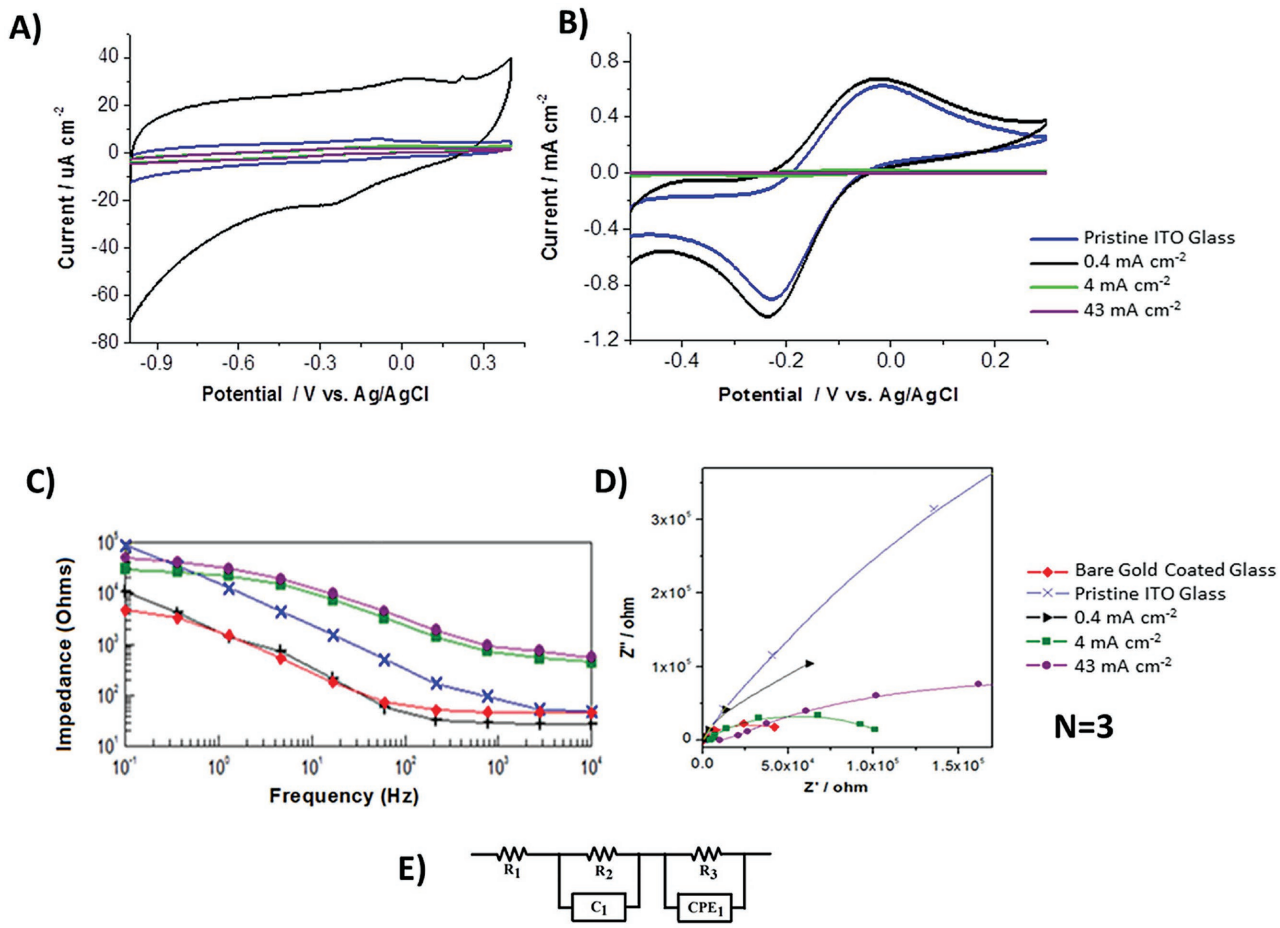

Figure 3. Electrochemical analysis of anodized films. Cyclic voltammograms of ITO (blue) and ITO anodized films formed with current densities; 0.4 mA cm^{-2} (black), 4 mA cm^{-2} (green), and 43 mA cm^{-2} (purple). CVs recorded in 50×10^{-3} M phosphate buffer, A) scan rate 100 mV s^{-1} and in 50×10^{-3} M phosphate buffer containing 2×10^{-3} M $[Ru(NH_3)_6]^{3+}$, B) scan rate 100 mV s^{-1}. C) Bode and D) Nyquist plots comparing the EIS spectra of pristine ITO glass (blue-filled asterisks), bare gold glass (red-filled diamonds), and anodized ITO films formed using 0.4 mA cm^{-2} (black-filled triangles), 4 mA cm^{-2} (green-filled squares), and 43 mA cm^{-2} (purple-filled circles). E) The electrical equivalent circuit used to analyze experimental data.

The experimental data of ITO anodized films were fitted to an equivalent circuit (Figure 3E) consisting of three resistors (R_1, R_2, and R_3), a capacitor (C_1), and a constant phase element (CPE_1), in accordance with previous studies.[73–75] In this circuit, R_1 is the solution resistance; and R_2 and C_1 are associated with space charge layer resistance and space charge layer capacitance, respectively. The double-layer capacitance is denoted as CPE_1 and R_3 is ascribed to the resistance of ITO films (**Table 4**). The simulated data confirmed that the lowest resistance of 8.3 kΩ cm^{-2} for the ITO anodized films formed at a current density of 0.4 mA cm^{-2} when compared with the resistance of 9.8 kΩ cm^{-2} for pristine ITO coated glass. The detrimental effect of high current densities on the conductivity was also observed in the calculated resistance of 22.8 and 209.1 kΩ cm^{-2} for 4 and 43 mA cm^{-2} current densities, respectively.

To further evaluate the electrochemical characteristics of the ITO anodized films, a ruthenium hexamine ($[Ru(NH_3)_6]^{3+}$) redox probe was employed to examine Faradaic redox response

Table 3. Electrochemical characteristics of ITO anodized films. Non-Faradaic charge density evaluated from cathodic region of cyclic voltammograms recorded in 50×10^{-3} M phosphate buffer at 0.1 V s^{-1} scan rate (potential range: –1 to 0.4 V vs Ag/AgCl). Faradaic charge density and peak current density (i_{pa}) evaluated from voltammograms recorded in 50×10^{-3} M phosphate buffer containing 2×10^{-3} M $[Ru(NH_3)_6]^{3+}$ at 0.1 V s^{-1} scan rate.

ITO film	Non-Faradaic charge density [μC cm^{-2}]	Faradaic charge density [mC cm^{-2}]	$E^{o\prime}$ [V]	i_{pa} [mA cm^{-2}]	D_o [cm^2 s^{-2}]
Pristine ITO	49	1.43	–0.13	0.62	4.62×10^{-6}
Anodized at 0.4 mA cm^{-2}	341	1.45	–0.13	0.67	8.37×10^{-6}
Anodized at 4 mA cm^{-2}	15	0.04	–0.14	0.02	6.92×10^{-9}
Anodized at 43 mA cm^{-2}	15	–	–	–	–

Table 4. Summary of the calculated resistance values (R_3) for each of the anodized ITO films after equivalent circuit analysis.

ITO film	Resistance (R_3) [kΩ cm^{-2}]
Pristine ITO glass	9.8 ± 0.3
Anodized at 0.4 mA cm^{-2}	8.3 ± 0.6
Anodized at 4 mA cm^{-2}	22.8 ± 2.6
Anodized at 43 mA cm^{-2}	209.1 ± 9.2

within a biologically relevant potential range (–0.4 to +0.2 V vs Ag/AgCl) (Figure 3B). With pristine ITO films, $[Ru(NH_3)_6]^{3+}$ undergoes a one electron redox reaction (redox potential ($E^{o'}$) = –0.13 V vs Ag/AgCl), yielding an anodic peak current (i_{pa}) of 0.62 mA cm^{-2} and a Faradaic charge density of 1.3 mC cm^{-2} (Table 3). A slight increase of i_{pa} and Faradaic charge density is observed with ITO films formed through anodization at 0.4 mA cm^{-2}, possibly due to the increased surface roughness. This shows that although the non-Faradaic charge density is greater with these films, the increased surface roughness does not translate into a greater electrochemically active surface area than that of the relatively smooth nonanodized ITO film. Kraft et al.[48] observed a similar response using $[Fe(CN)_6]^{3-}$ as a redox probe, where non-Faradaic current (charge density) increased after ITO electrode anodization while Faradaic current remained essentially constant. A large decrease of i_{pa} and Faradaic charge density is evident in ITO films subjected to anodization with current densities greater than 0.4 mA cm^{-2}, accompanied by a slight decrease in $E^{o'}$ of ≈10 mV for the $Ru^{3+/2+}$ redox couple (Table 3). The difference in $E^{o'}$ may result from variation in chemisorption sites within the electrode film, which can influence redox probe stability.[76] The voltammetric response observed for ITO films anodized at 43 mA cm^{-2} is characteristic of a highly resistive surface with no evidence of heterogeneous electron transfer between the electrode and the redox probe.[77]

Scan rate studies (Figure S5, Supporting Information) revealed a linear dependence of i_{pa} versus $\nu^{1/2}$ (ν = scan rate) for all ITO films (with the exception of ITO anodized films formed with current densities of 43 mA cm^{-2}), indicative of a semi-infinite planar diffusional response described by the Randles–Sevcik equation.[78] Diffusion coefficients (D_0), evaluated from the linear portion of i_{pa} versus $\nu^{1/2}$, are shown in Table 3. D_0 values in the order of 10^{-6} cm s^{-1} were calculated for $[Ru(NH_3)_6]^{3+}$ at both pristine ITO and ITO films formed through anodization at 0.4 mA cm^{-2} in a phosphate buffer. Again, a decrease of D_0, by approximately three orders of magnitude, is evident for ITO films subjected to anodization with current densities of 4 and 43 mA cm^{-2}, further corroborating the insulating nature of films prepared at anodizing current densities greater than 0.4 mA cm^{-2}.

Interestingly, the presence of the PSS ionomer was critical for the anodization process and ITO thin films subjected to anodic oxidation under ambient conditions in a 0.01 M phosphate-buffered saline solution were associated with a linear increase in impedance profile as a function of current density (Figure S6, Supporting Information).

2.4. Biological Characterization

Nanoscale signaling modality has been shown to have a profound effect on cell viability, proliferation, and on cell attachment in the material's space.[79–81] Because the application of different current densities for the anodization of ITO films resulted in defined nanoscale morphological changes, the cellular interfacial response has been analyzed based as a function of roughness. With this in mind, the effects of films formed at 0.4, 4, and 43 mA cm^{-2} current densities, which in order exhibit an average of roughness of 19, 81, and 61 nm, respectively, on human neuroblastoma SH-SY5Y cell adhesion and proliferation were assessed in vitro. These were then compared to pristine ITO coated glass with an experimental average roughness of 1 nm (**Figure 4**A). After periods of 1, 7, and 14 d, cells were stained with calcein (live) and ethidium homodimer (dead) to establish cell viability. All experimental and control films were nontoxic to SH-SY5Y cells. However, significant differences were observed at day 14 with respect to cell viability. Cells grown on films with the lowest roughness profile (formed at the lowest current density 0.4 mA cm^{-2}; R_a = 19 nm over 10 μm^2) maintained 86% viability relative to control films at day 1 (Figure 4B). Similarly, when analyzed with alamarBlue Assay by 24 h (Figure 4C), the SH-SY5Y population cultured on anodized ITO films was comparable to cells cultured on control pristine ITO coated glass. While by days 7 and 14 cells cultured on all experimental anodized films demonstrated a marked decreasing trend in metabolic activity, the anodized films with 19 nm roughness (formed at 0.4 mA cm^{-2} current density) showed an overall significant higher metabolic activity of 87% by day 7 and 78% by day 14, respectively, compared to 61 and 81 nm films' roughness profiles and pristine ITO control substrates. Overall, anodized ITO films possessing an R_a 81 nm (the highest roughness profile) showed a significant decrease in metabolic activity relative to cells cultured on control ITO coated glass and on anodized films with 19 nm roughness.

These results are similar to those of Fan et al.[82] In their work, they have reported on the cell proliferation of neural cells cultured on silicon wafers possessing different levels of surface roughness. It was concluded that the Si wafers with surface R_a ranging from 20 to 50 nm promoted a significantly higher cell proliferation. Conversely, on surfaces with an R_a less than ≈10 nm and on rough surfaces with R_a above 70 nm, cell metabolic activity was reported to be significantly lower. It is noteworthy that even though cell proliferation and viability depend on cell type and substrate composition, it is apparent that neurons do not readily attach on excessively smooth (R_a = 10 nm) or rough surfaces (R_a = 250 nm).[83]

Tissues can be described as complex nanoscale composites that impact morphological and mechanical features to the resident cellular constituents. Previous studies show that nanotopography influences cellular function and focal adhesion (FA) formation in vitro[79,84] and may be employed to modulate the dynamic interface between materials and cell/tissues. With an awareness of this, cell attachment to the anodized ITO films was quantified through immunofluorescent labeling of the FA associated protein paxillin[85] (**Figure 5**A–D). At day 1, cells cultured on all experimental films and control pristine ITO glass were associated with an overall average of ≈14 focal adhesions

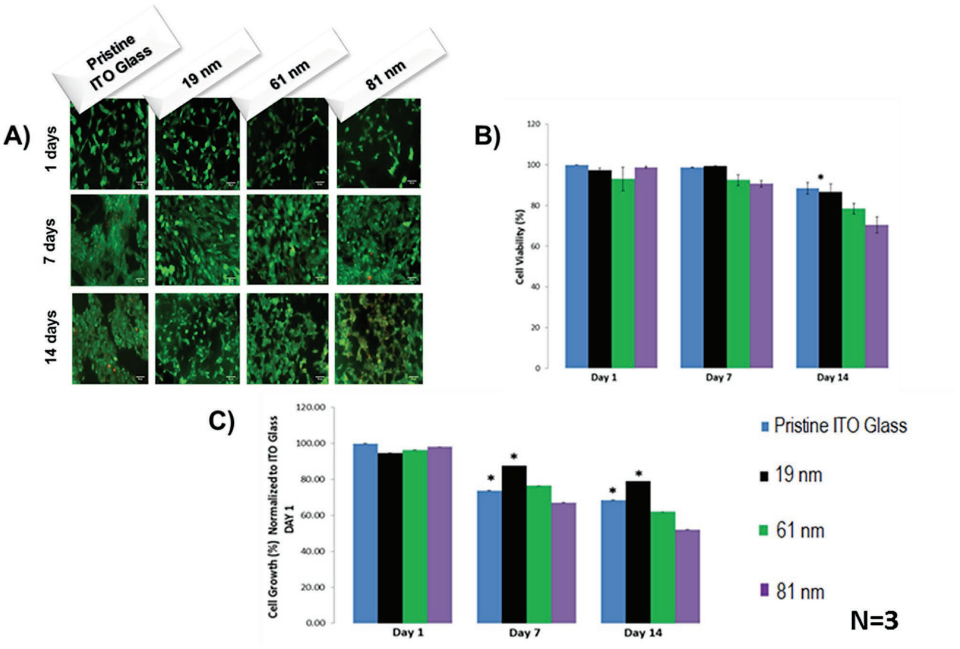

Figure 4. Cytocompatibility analysis of anodized ITO films of different roughness (R_a) formed by varying the current density. A) Fluorescent images of SH-SY5Y cells following 1, 7, and 14 d in culture on anodized films displaying 19, 61, and 81 nm over 10 μm^2 (R_a) roughness relative to pristine ITO control (R_a 1 nm over 10 μm^2). Green, live; red, dead. Bar = 50 μm. B) A significant ($p < 0.05$) decrease in cell viability was observed in anodized films with an average roughness of 61 and 81 nm relative to control and 19 nm film roughness. C) Metabolic activity of SH-SY5Y cells compared with pristine ITO coated glass control as measured by the alamarBlue Assay ($p < 0.05$), $n = 3$. Metabolic activity was significantly elevated in cells cultured on anodized ITO films with 19 nm roughness relative to anodized films with 61 and 81 nm roughness, respectively, by days 7 and 14. Results are ± STD, ★ = $p < 0.05$.

per cell. By day 7, SH-SY5Y cells cultured on pristine ITO control presented a significant increase in FA numbers per cell, an average of 25 focal adhesions per cell, compared to all the experimental anodized ITO films with an average number of 17 FAs per cell. Interestingly, trends in FA numbers were reversed in cells cultured on the pristine ITO control group by day 7, which demonstrated a significant reduction in FA number by day 14 (Figure 5E). Conversely, previous studies have reported a disruption to cell adhesion by nanorough surfaces with similar roughness profiles[79,86] and a decrease in cell viability; however,

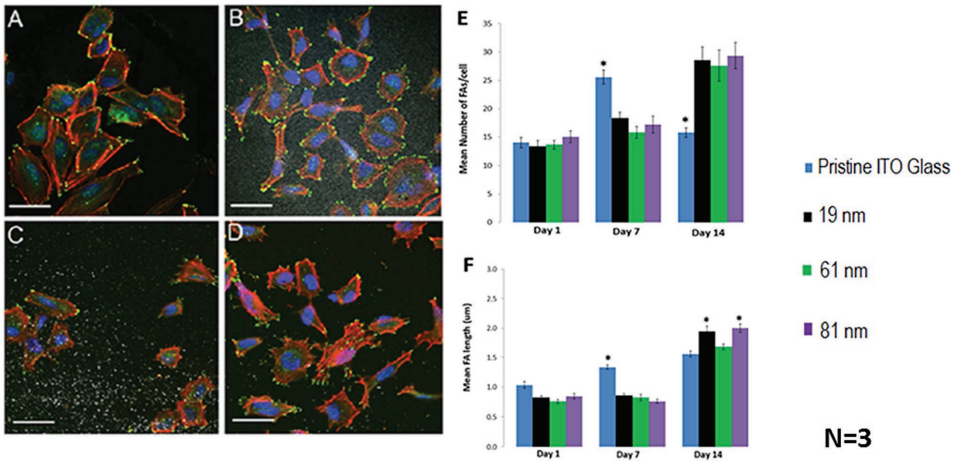

Figure 5. Focal adhesion formation of SH-SY5Y cell grown roughness. A–D) Immunofluorescent imaging was employed to quantify FA length and number in cells cultured on pristine ITO coated glass and experimental anodized films of different roughness (green: paxillin, red: actin; blue: nucleus, bar: 40 μm). E) Cells cultured on control ITO coated glass generated less FA complexes over time, while this trend was reversed in cells on experimental anodized ITO films of all roughness. SH-SY5Y cells grown on 19 and 81 nm roughness of anodized films were associated with a significant increase in FA length relative to cells cultured on pristine ITO coated glass ($R_a = 1$ nm). F) There was a significant reduction in cells cultured on 61 nm roughness compared to the cells grown on 19 and 81 nm experimental roughnesses. For all analysis, results are ± STD, ★ = $p < 0.05$.

FA quantification was not performed in these studies. Specifically, it was noted by Brunetti et al.[79] that cellular adhesion was significantly increased on regions of low (smooth) roughness.

Independent of the surface roughness, it was interesting to note an increased number of FAs in SH-SY5Y cells cultured on all anodized films relative to SH-SY5Y cells cultured on pristine ITO coated glass by day 14.[87] We hypothesize that the enhanced number of FA observed in SH-SY5Y cells cultured on anodized ITO films relative to pristine ITO may be as a result of the anodization process inducing differential protein adsorption.[88,89] Studies into the influence of surface chemistry on protein adsorption through etching and deposition techniques,[90] plasma treatment,[91] and anodization processes[92] indicate enhanced extracelular matrix (ECM) protein adsorption as a function of oxygen content,[88,93,94] also observed here in anodized ITO films.

Similarly, FA length was observed to be significantly greater in cells cultured on pristine ITO control substrates than in cells cultured on anodized films by day 7. By day 14, the FA length in the experimental anodized films with the lowest and highest roughness profiles (19 and 81 nm) was significantly higher than the length of FAs in cells cultured on pristine ITO control substrates (Figure 5F). A significant reduction in FA length was noted, however, in cells cultured on R_a film roughness of 61 nm over 10 μm^2. This reduction in FA reinforcement may be related to the particle diameter and nanofeatures with lateral dimensions of ≈100 nm that have been shown to be disruptive to integrin clustering,[84,95] an effect which is lost by reducing or increasing the feature dimensions, an effect also demonstrated here.

To gain further insight into cell adhesion, the length of the FAs was subgrouped in focal complexes (FXs) measuring <1 µm in length and FAs proper, measuring between 1 and 5 µm. FXs were most abundant in cells cultured on all experimental roughnesses and pristine ITO coated glass substrates on days 1 and 7. By day 14, cells cultured on anodized ITO films with roughness of 19, 61, and 81 nm over 10 μm^2 demonstrated reduced FX frequency, and a similar FA distribution profile with lengths ranging from 1 to 4.5 µm. However, cells cultured on control ITO substrates were associated with a reduction in FA frequency (**Figure 6**). It was interesting to note that over a period of 14 d in culture, cells demonstrated a progressive shift from nascent and unstable focal complexes to more stable focal adhesions. Hence, it can be inferred that the influence of film roughness is a predominant factor in the observed increase in focal adhesion frequency together with the concept of increased oxygen content to protein adsorption owing to the anodization process.

In order to assess the potential functional response of neuronal populations to implanted anodized ITO thin-film devices in vitro, and the potential for induction of a reactive astrocyte phenotype, the functional response of a primary ventral mesencephalic (VM cells) coculture was assessed via an in-house protein microarray assay. Spotted antibodies for proteins associate with astrocyte reactivity, cell adhesion, and mechanotransduction utilized in this study are outlined in Table S1 (Supporting Information). Antibodies were printed at a range of concentrations (0.1–1 mg mL^{-1}) and assessed for retained function and optimal print concentration by incubation with a fluorescently labeled protein lysate from VM cells cultured for 21 d on all anodized films and pristine ITO control (Figure S8, Supporting Information).

Owing to the construction of the gliosis antibody microarray, an unsupervised clustering of all experimental films normalized by control pristine ITO was performed (**Figure 7**). This analysis clearly defined a group between the anodized films with nanoroughness of 61 and 81 nm, respectively, and a single cluster for the films formed with the lowest roughness profile of 19 nm (formed at 0.4 mA cm^{-2} current density); sharing only 1% similarity with the rest of the experimental substrates. As gliosis is dependent on the bioelectrochemical as well as physicomechanical properties of the implanted material it was remarkable to notice that the resulting roughness factor of the anodized films was predominant on the differential intensity expression of the antibodies evaluated.

The hallmarks of glial scar formation are multifactorial; in the developed antibody microarray gliosis was studied from the diverse and interwoven response of microglia and astrocytes,[96,97] and from the changes of transient calcium currents that affect overall homeostasis and astrocytes reactivity.[98] Overall, ITO anodized films formed with current densities of 0.4 mA cm^{-2} (films with 19 nm roughness) showed significant downregulation of the gliosis response relative to VM populations cultured on other anodized ITO films. Specifically, downregulation in the intensity of OX42/Iba1 (microglia), glial-fibrillary acidic protein (GFAP), and Nestin (reactive astrocytes) was observed.

A recent study by Kim et al.[99] has shown that coupled to the increase in GFAP expression as main maker for reactive

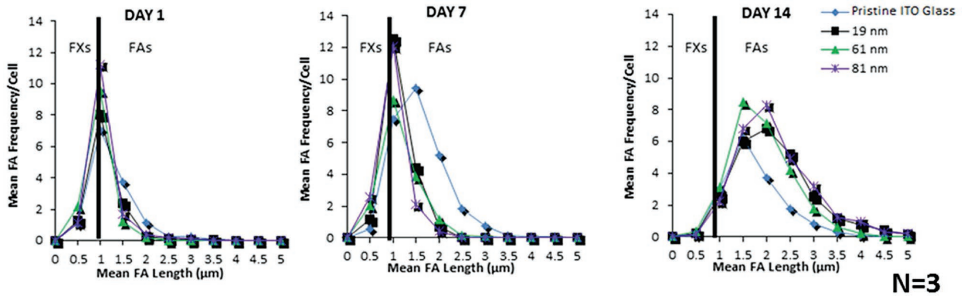

Figure 6. Focal adhesions were subgrouped into focal adhesions (FAs) proper and nascent focal complexes (FX). FXs were the predominant adhesion complex subtype observed on all anodized ITO films and the pristine ITO coated glass up to day 7. However, FXs were displaced by the FA subtype by day 14 in cells cultured on all experimental and control materials. A significant increase in the mean number of focal adhesions per cell on all of the experimental anodized ITO films compared to control pristine ITO group was observed on day 14, $n = 3$.

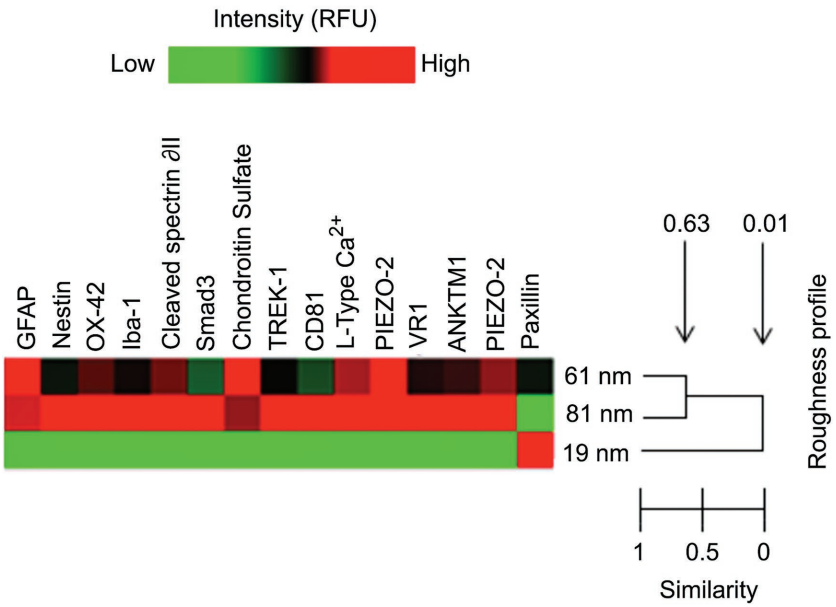

Figure 7. Unsupervised clustering of all experimental anodized films normalized by control pristine ITO. This analysis clearly defined a group between the anodized films with nanoroughness of 61 and 81 nm, respectively, and a single cluster for the films formed with the lowest roughness profile of 19 nm; sharing only 1% similarity with the rest of the experimental substrates. The gliosis response of the films formed with 0.4 mA cm^{-2} current density, which exhibit the lowest roughness profile of 19 nm, showed a remarkable intensity downregulation of reactive astrocytes, microglia and calcium influx markers. The resulting roughness factor of the anodized films was predominant on the differential intensity expression of the antibodies evaluated.

astrocyte reactivity.[106] Moreover, downregulation in protein markers for gliosis such as Smad3,[107] chondroitin sulfate[108] and the TRP[109] family channels such as VR1[110] and ANKTM1[111] proteins linked to inflammation and the attenuated gliosis response were observed in VM cells cultured on ITO films anodized with 0.4 mA cm^{-2}.

In order to validate cell studies performed with SH-SY5Y cells migration proteins such as CD 81 (TAPA) and paxillian were also concurrently assessed in VM populations. CD 81 is a member of the tetraspan family of proteins and is involved both in cell adhesion and the machinery of migration[112] and in relation to glial scar formation, CD 81 has been found to have a defined relation to reactive astrocytes expression. Critically, previous studies have shown that upregulation of CD 81 is a prominent characteristic of glial scar formation.[113,114] Moreover observed downregulation in the expression of CD 81 and upregulations in the expression of paxillin are in accordance with observed modulation to FA formation in SH-SY5Y cells and suggest that the roughness of anodized ITO films has an effect on focal adhesion frequency and cell adhesion.

astrocytes, further reactivity can be fully characterized by the expression of cleaved spectrin αII. Downregulations in cleaved spectrin αII were also observed in VM populations cultured on ITO anodized films formed with current densities of 0.4 mA cm^{-2} relative to cells cultured on other experimental and control substrates, again indicating the reduced potential of these films to induce a reactive astrocyte phenotype.[99]

Interestingly, cleaved spectrin αII is sensitive to calpain-mediated proteolysis, and calpains have been shown to play a central role in the neuroprotection of the CNS and neuron calcium influx[100,101] changes in which may mediate the onset of reactive gliosis.

Cleaved spectrin αII protein is directly linked to the regulation of intracellular Ca^{2+} concentrations, and it was noted that together with the downregulation of this protein, only VM cells cultured on films formed with 19 nm roughness (formed at 0.4 mA cm^{-2} current density) exhibited a low expression of L-type Ca^{2+} and the mechano-gated ion channel PIEZO 2. These observations are intriguing as an upregulation in voltage-gated calcium channels such as L-type Ca^{2+} has been known to induce reactive astrogliosis.[98] Furthermore, the calcium regulator mechanosensitive protein PIEZO 2 is known to play a role in the regulation of calcium permeability, which may relate to cell membrane damage.[102–104] It is of importance to indicate the observed downregulation of TREK 1 expression on ITO films anodized with 0.4 mA cm^{-2} and that optimal function of astrocytes homeostasis is mediated by K^+ channels[105] such as TREK 1, which has been shown to help set the negative resting membrane potential of astrocytes and regulate

2.5. Functional Characterization

The ability of anodized ITO to interface neuronal circuit formation was subsequently explored via patch-clam analysis. In particular, due to the favorable electrochemical and phenotypical responses of VM cells to these anodized films the functional response was explored using explanted primary neurons on ITO anodized at the lowest current density (0.4 mA cm^{-2}) via two functional indicators: network formation and synaptic activity.[115] Rat hippocampal cells, from which primary neuronal cultures were grown and maintained for 8 to 10 d on ITO anodized films formed at a current density of 0.4 mA cm^{-2}, were compared to control cultures grown on poly-L-ornithine coated glass coverslips. Hippocampal neuron maturation and viability were assessed using single-cell recordings (see subsection "*Electrophysiological Recordings*" in the Experimental Section). Visually identified neurons from the two culture groups were patch clamped under voltage clamp modality to measure the cell passive membrane properties that are known indicators of neuronal health.[116] These parameters (input resistance and membrane capacitance) did not differ ($P = 0.221$ and $P = 0.369$ for input resistance and cell capacitance, respectively) when measured in the two culture conditions (see bar plots in **Figure 8**C). We investigated synapse formation and activity after in vitro growth of neurons by measuring the occurrence of spontaneous postsynaptic currents (PSCs) in both culture groups. The appearance of PSCs provided clear evidence of functional synapse formation, which is a widely accepted index of network efficacy.[115]

Figure 8A shows representative current tracings of the recorded electrical activity. PSC amplitude and frequency were measured from neurons grown in control and 0.4 mA cm^{-2} anodized ITO films. As summarized in the bar plots of Figure 8B, these values were not statistically different ($P = 0.988$ and $P = 0.247$, amplitude and frequency, respectively) in the two groups of cultures and were consistent with those measured in other studies testing the permissive nature of manufactured interfaces.[117] The impact on cells of the modified substrate is, therefore, negligible. In Figure 8D, the cellular composition of control and anodized ITO film hippocampal cultures is shown, assessed by immunofluorescence markers[118] for astrocytes (GFAP) and neurons (β-tubulin III). It was observed both β-tubulin III and GFAP immunoreactive cells in all growing conditions (Figure 8D left and right panels) and both cell groups were represented in a proportion that is comparable in all experimental groups (quantified by measuring the cell density, bar plot in Figure 8E; $P = 0.415$, 30 visual fields per condition, three different culture series). Thus cell survival and the global network size were not affected by ITO anodized film formed at current density of 0.4 mA cm^{-2}.

To assess the ability of ITO anodized films formed at a current density of 0.4 mA cm^{-2} to transfer sufficient charge for cellular depolarization, primary cultures of VM cells were grown on films for 60 d and stimulated with biphasic pulses of 2 V cm^{-2}, 0.1 s duration at a frequency of 0.2 Hz. Cells were observed to generate calcium transients in response to the stimulus via 0.4 mA cm^{-2} anodized ITO films, while the same stimulus did not elicit any response in pristine ITO control cultures. Representative traces of changes in background subtracted Fluo4 fluorescence intensity from individual regions of interest were acquired (**Figure 9**) (representative videos of the stimulation via 0.4 mA cm^{-2} (Video S1, Supporting Information) and pristine ITO controls (Video S2, Supporting Information) using VM cells are available in the Supporting Information). Moreover, calcium transients were also visible when using primary hippocampal neurons, cultured on 0.4 mA cm^{-2} anodized ITO films (Figure S9, Supporting Information).

3. Conclusion

Here we employed a range of current densities for the anodization of ITO in an aqueous cytocompatible electrolyte and investigated the effects of anodization current density on ITO electrochemical, physical, and cytocompatibility properties. Furthermore we assessed anodization as a methodology for the formulation of neural interface materials with a focus on reduced cellular reactivity and enhanced neural stimulation capacity.

This work provides a useful benchmark for anodization conditions for subsequent studies with neural microelectrodes, micropatterning, and biochemical functionalization. It was observed that anodization offers the ability to modify ITO films with differential properties for charge transfer and resistivity may provide a facile approach to the deposition of electrode coatings with differential regions of charge conductance and cellular function capacities. It can be hypothesized that anodization with varying current densities may be employed to deposit insulator and charge carrier regions on a single electrode system, providing cytocompatible and functional coatings for implantable thin-film ITO devices.

4. Experimental Section

Anodic Oxidation of ITO: The anodic oxidation of ITO was conducted under ambient conditions in a solution of 10×10^{-6} M PSS (Sigma-Aldrich, Ireland, 70 000 g mol^{-1} M_W) prepared in a 0.01 M PBS solution with a platinum foil as a counter electrode (cathode). The electrolyte solution was placed in an in-house fabricated electrochemical cell, connected to a Princeton Applied Research Potentiostat/Galvanostat model 2273 controlled with Power Suite software. Pristine ITO coated glass slides were purchased from Diamond Coatings, UK. These were provided as thin films sputtercoated onto glass substrates with a nominal thickness of 750 nm and a sheet resistivity of 8–10 Ohms sq^{-1}. Pristine ITO coated glass slides were individually cleaned in acetone, dried with a stream of nitrogen, and moved to a desiccating chamber to remove moisture for 24 h prior to use. Galvanostatic anodization was performed applying constant current densities of 0.4, 4, and 43 mA cm^{-2} over a constant time of 450 s to pristine ITO coated glass. A schematic representation of the anodization process is presented in Figure S10 (Supporting Information).

Physical Characterization—Surface Morphology: SEM was carried out using a Hitachi S-4700 Cold Field Emission Gun Scanning Electron Microscope. The SEM images were taken using an accelerating voltage of 15 kV and spot current of 10 µA. Gold sputtering was carried out before testing the samples using an EMSCOPE SC500 to deposit 10 nm of gold.

AFM was performed to analyze the roughness of the samples. All measurements were taken on a Veeco Dimension 3100 AFM using TESPA Tips (NanoWorld) (Si < 8 nm tip radius, 42 N m^{-1} spring constant, 320 kHz nominal resonance frequency), in tapping mode over an area of 10 and 10 µm^2, respectively, with a 0.5–1 Hz scan rate.

Transmission Electron Microscopy (TEM) was performed using an H-7000 electron microscope to analyze inner particle distribution of the films. The samples were fixed into Epon base low viscosity resin (Agar Scientific R1078) so as to release the samples from the glass surface slide and be embedded in the resin. Thereafter, all samples were sectioned at 100 nm thickness and collected on Formvar-carbon 200 mesh copper grids (Agar Scientific—62200N-200 Square Mesh Nickel 3.95 mm). Images were taken at 75 kV with direct magnification of 20 000×.

Physical Characterization—Thickness Measurements: The thickness of the anodized films was measured using a Zygo Newview 100 surface profilometer controlled by MicroPlus software. A pattern of bright and dark lines–fringes was created as incoming light was split from the limited region between the anodized film and the pristine ITO glass. This pattern difference was translated to calculate the height information, resulting in the thickness of the film. The size of the testing area was 1.6 cm^2.

Physical Characterization—UV–Visible Spectroscopy: The optical transmittance of the ITO coated glass and the anodized films was assessed by using a Thermo Scientific Varios-Kan Flash microplate reader at the visible-light wavelengths (400–800 nm).

Physical Characterization—Stability and Durability through Accelerated Ageing Study: The stability of the pristine ITO glass and the anodized ITO films was determined using a long-term passive degradation through accelerated ageing study. Following the ASTM international guidelines for accelerated aging of medical devices[119] as well as the procedure detailed by Green et al.[120] and Hukins et al.[121] the experimental parameters were determined using Equation (1)

$$t_{37} = t_T \times Q10^{(T-37)/10} \quad (1)$$

where t_{37} is the simulated time at 37 °C, t_T shows time samples are placed at the elevated temperature, T is the elevated temperature, and $Q10$ is the accelerated factor equal to 2.0 as per the ASTM specification.

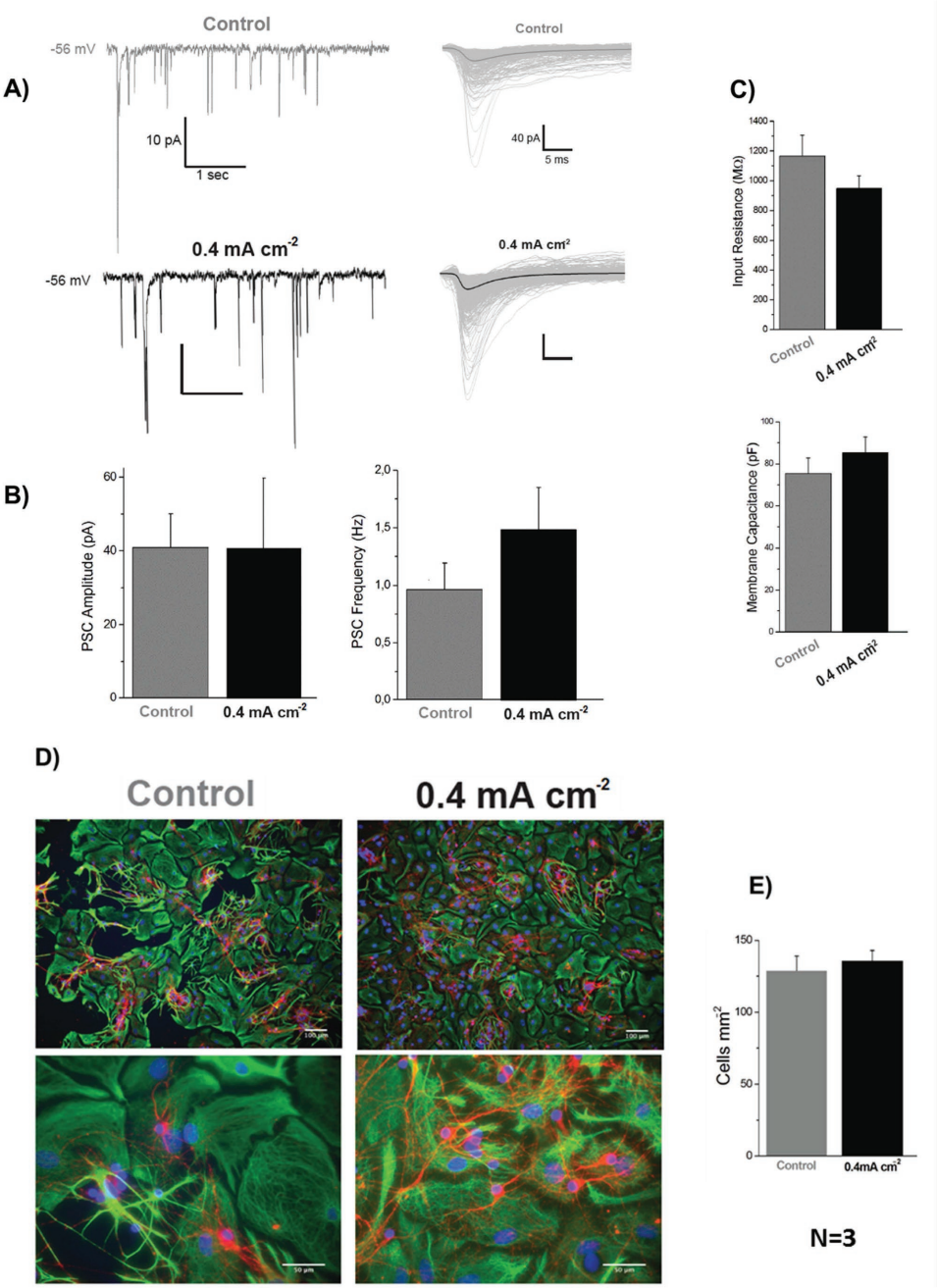

Figure 8. Synaptic network formation on anodized film formed at a current density of 0.4 mA cm^{-2}. A) Left, current tracings from two sample neurons (in grey control and in black anodized film) showing heterogeneous postsynaptic currents (PSCs; inward deflections) recorded at a holding potential of –56 mV. Right, Superimposed traces show isolated PSCs recorded from control (top; the average is superimposed in grey) and 0.4 mA cm^{-2} (bottom; the average is superimposed in black) neurons. B) Bar plots summarize PSC amplitude (left) and PSC frequency (right) values. Although not statistically significant, on anodized films PSC frequency was slightly higher (0.96 ± 0.65 Hz in controls and 1.48 ± 0.97 Hz in anodized films, $n = 8$ and $n = 7$, respectively), while the average values for PSC amplitude were similar (40.8 ± 25.9 pA controls and 40.5 ± 50.7 pA in anodized films). C) Bar plots summarize the values measured for the input resistance (top, 1195 ± 368 MΩ controls and 946 ± 229 MΩ anodized films) and membrane capacitance (bottom, 75 ± 20 pF controls and 85 ± 19 pF anodized films). D) Fluorescent micrographs of immune-labeled cultures, control (left) and anodized films (right), at low (top panels, objective 10×) and high (bottom panels objective 40×) magnifications. Neurons are visualized by anti β-tubulin III, in red, glial cells by anti-GFAP, in green, and nuclei are visualized by Hoechst, in blue. E) The plots summarize neuronal (left) and glial (right) densities in all conditions.

Three experimental replicas for each group were placed in an oven at 95 °C and immersed in 0.9% saline for four weeks simulating 1560 d (four years) of implantation. Cyclic voltammetry was performed before and after the ageing study and used to calculate the percentage of loss in CSC. SEM pictures were taken after the ageing study to show morphological changes. The SEM sample preparation and imaging were performed following the details in the subsection "*Physical Characterization—Surface Morphology*" of this section.

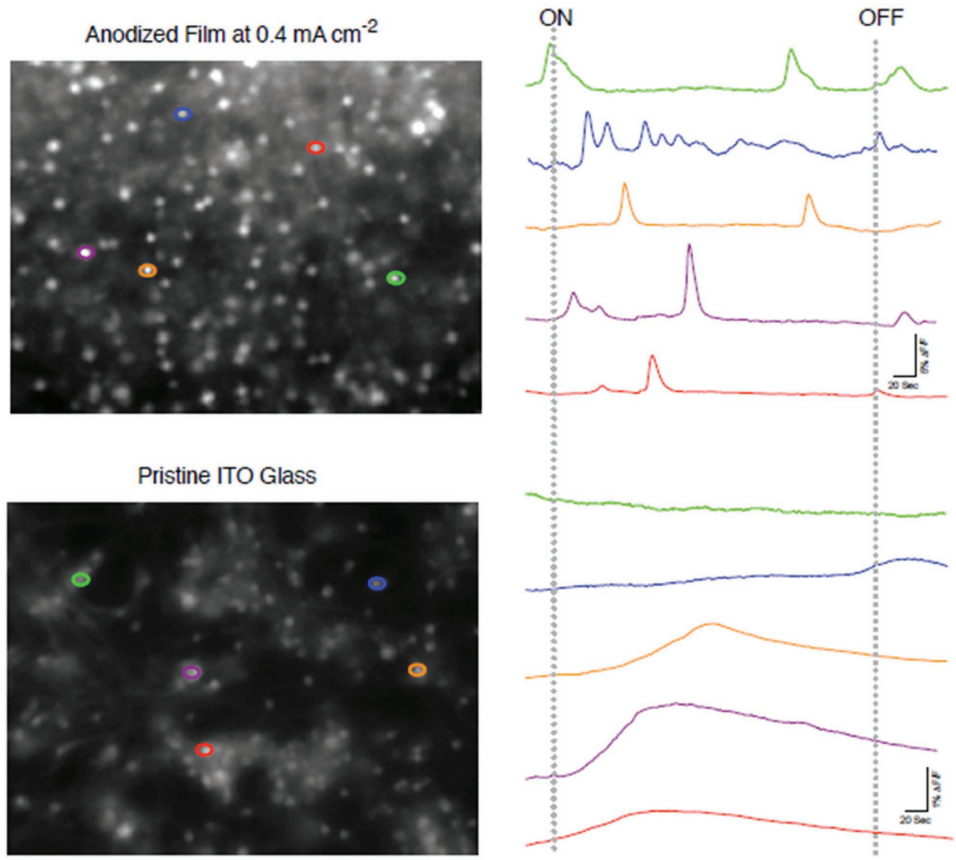

Figure 9. Calcium imaging and substrate stimulation. Left snapshots of representative fields of VM cells grown on anodized ITO film formed at 0.4 mA cm^{-2} (top) and control pristine ITO glass (bottom) and stained with calcium-sensitive fluorescent probe Fluo-4. Five regions of interest (ROI) per images were selected (highlighted in different colors), each representing a single neuron. Right, fluorescence tracings show the appearance of Ca^{2+} episodes, calcium events were measured from the relative ROI in the corresponding recording filed in both conditions (each cell is identified by the color). Stimulation was delivered to the films as biphasic voltage pulses (2 V cm^{-2}, 0.1s pulse, 0.2 Hz). Dashed lines highlight the corresponding evoked calcium response in both groups. Note that all selected cells displayed calcium transients in response to the stimulus in the 0.4 mA cm^{-2} condition, while the same stimulus did not elicit any responses in control cultures.

Chemical Characterization: XPS spectra were acquired on an Oxford Applied Research Escabase XPS system equipped with a CLASS VM 100 mm mean radius hemispherical electron energy analyzer with a triple-channel detector arrangement in an analysis chamber with a base pressure of 5.0×10^{-10} mbar. Survey scans were acquired between 0 and 1100 eV with a step size of 0.7 eV, dwell time of 0.5 s, and pass energy of 100 eV. Core level scans were acquired at the applicable binding energy range with a step size of 0.1 eV, dwell time of 0.5 s, and pass energy of 50 eV averaged over 50 scans. A non-monochromated Mg-kα X-ray source at 200 W power was used for all scans. All spectra were acquired at a take-off angle of 90° with respect to the analyzer axis and were charge corrected with respect to the C 1s photoelectric line by rigidly shifting the binding energy scale to 285 eV. Data were processed using CasaXPS software where a Shirley background correction was employed and peaks were fitted to Voigt profiles. To ensure accurate quantification, atomic sensitivity factors were taken from the instrument spectrum acquisition software and manually input into the data processing software.

Electrochemical Characterization—Electrochemical Measurements: Cyclic voltammetry was performed using a CH Instruments 620 series potentiostat. Measurements were recorded in a custom-made electrochemical cell (2 mL volume) containing the pristine ITO coated glass as working electrode (1.6 cm^2), an Ag/AgCl reference electrode (3 M KCl) (Bioanalytical Systems), and a platinum foil counter electrode (Goodfellow) in 50×10^{-3} M phosphate buffer solution (pH 7.8) or saline solution.[72] Prior to measurements, solutions were purged with N_2 to avoid O_2 reduction at low potentials (<–0.4 V vs Ag/Ag/Cl).

Electrical impedance spectroscopy (EIS) was performed using a Princeton Applied Research Potentiostat/Galvanostat model 2273 running with Power Suite software with a four-electrode setup as described in ref. [12]. Briefly, the signal was to the anodized films with a surface area of 1.6 cm^2, along with a platinum foil counter-electrode (CE) and controlled by a saturated Ag/AgCl reference electrode. An AC sine wave of 40 mV amplitude was applied with 0 V DC offset. The impedance magnitude and phase angle were calculated at 1, 10, 100, 1000, and 10 000 Hz, as it is reported that most of the neural cell communication occurs between 300 Hz and 1 kHz.[122]

Values were presented on Bode and Nyquist plots and compared to those of a pristine ITO coated glass slide and to bare gold coated glass. The data fitting analysis was performed using EIS Spectrum Analyzer 1.0 software.

Biological Characterization—Cell Culture: The human neuroblastoma cell line SH-SY5Y was cultured in Dulbecco's modified Eagle's medium nutrient mixture F12 (DMEM/F12) medium and supplemented with 10% fetal bovine serum, 1% penicillin/streptomycin (PS), and all-*trans* retinoic acid (RA) at a final concentration of 10×10^{-6} M for differentiation into a neuronal phenotype. Immunofluorescence micrographs showing the neuronal phenotype of SH-SY5Y as a response to RA supplementation are shown in Figure S7 (Supporting Information).

To control the surface area of culture, the pristine ITO coated glass and the anodized films were placed in customized silicone Ace O-rings with wall dimension of 1.78 mm and internal diameter (I.D) of 10.8 mm and were sealed around the borders of the surface area with silicone elastomer (Sylgard 184). The materials were placed in six well culture plates and sterilized by 100% ethanol for 2 h, and subsequently washed repeatedly with Hank's balanced salt solution (HBSS) and incubated overnight at 37 °C, 5% CO_2 for neural cell culture. A quantity of 50 000 or 2000 cells cm^{-2} was plated on each film, and then 200 µL of the culture medium was added to each well, and changed with fresh media every day for a period of 1, 7, or 14 d. Control Thermanox Plastic Coverslips with 13 mm diameter (NUNC brand products) were also bonded with silicone Ace O-rings as above.

Primary hippocampal cultures were prepared from 2 to 3 d postnatal (P_2–P_3) rats as previously reported by Cellot et al.[115] Briefly, hippocampi were dissected and enzymatically digested. Cells were plated on poly-L-ornithine coated glass coverslips (control) or on anodized ITO substrates formed at 0.4 mA cm^{-2} current density. Coverslips were placed in petri dishes and cultured in serum-containing medium in a 5% CO_2-humidified incubator for 8–10 d. Cell morphology was analyzed by immunofluorescence experiments and epifluorescence microscopy to gain insights into cell health and shape. Briefly, cell densities were quantified at 20× (0.5 NA) magnification using a DM6000 Leica microscope (Leica Microsystems GmbH, Wetzlar, Germany), with random sampling of visual fields (713 × 532 µm).

Cell Culture—Ethical Statement: All experiments were performed in accordance with the European (EU) guidelines (2010/63/UE) and Italian law (decree 26/14) and were approved by the local authority veterinary service and by our institution (SISSA-ISAS) ethical committee. Every effort was made to minimize animal suffering and to reduce the number of animals used. Animal use was approved by the Italian Ministry of Health, in accordance with the EU Recommendation 2007/526/CE.

Primary cultures of VM neurons were obtained from the mesencephalon of embryonic Sprague-Dawley rats according to methods previously described by Vallejo-Giraldo et al.[12] Briefly, the ventral mesencephalon was dissected from embryonic 14 d rat brains and then mechanically dissociated with a pipette, until the tissue was dispersed. Cells were grown in a humidified atmosphere of 5% CO_2 at 37 °C and culture in media (Dulbecco's modified Eagle's medium/F12, 33 × 10^{-3} M D-glucose, 1% L-glutamine, 1% PS, 1% fetal calf serum (FCS), supplemented with 2% B27). The pristine ITO glass and the anodized films were cultured for 21 d in six well culture plates and sterilized in 70% ethanol for 2 h, and subsequently washed repeatedly with HBSS. They were then rinsed three times with deionized (DI) water and left to dry overnight. A quantity of 50 000 cells cm^{-2} was plated on each film, and then 3 mL of the culture medium was added to each well and changed with fresh media every 2 d for a period of 21 d.

Biological Characterization—Metabolic Analysis: The alamarBlue Assay (Life Technologies, UK) was used to assess cell metabolism and was carried out at days 1,7, and 14. For this purpose, 10% of the alamarBlue solution was added to the culture media, in accordance with the provided protocols. Sample absorbance was measured in a 96-well plate at 544 excitation and 590 emission wave lengths using a Thermo Scientific Varios-Kan Flash microplate reader.

Biological Characterization—Immunofluorescent Labeling: Indirect double-immunofluorescent labeling was performed to visualize focal adhesion sites. SH-SY5Y cells on experimental and control substrates were fixed with 4% paraformaldehyde and 1% of sucrose for 15 min at room temperature (RT) at each time point. Once fixed, the samples were washed with PBS and permeabilized with buffered 0.5% Triton X-100 within a buffered isotonic solution (10.3 g sucrose, 0.292 g NaCl, 0.06 g MgCl2, 0.476 g (4-(2-hydroxyethyl)-1-piperazineethanesulfonic acid) HEPES buffer, 0.5 mL Tri-ton-X-100, in 100 mL water, pH 7.2) at 4 °C for 5 min. Nonspecific binding sites were blocked with 1% bovine serum albumin (BSA) in PBS at 37 °C for 5 min and subsequently incubated for 2 h with a 1:100 concentration anti-vinculin (Rb mAb to Paxillin (Y113) (Life Technologies, 1:100). Samples were washed three times with 0.05% Tween 20, PBS and then incubated for 1 h in the secondary antibody Alexa Fluor 488 goat anti-Rabbit IgG (H+L) (Life Technologies, 1:100) combined with rhodamine-conjugated phalloidin (Life Technologies, 1:100) to stain F-actin. Nonspecific charges (e.g., remaining aldehyde) were neutralized with 0.5% Tween 20/PBS (5 min ×3) to minimize background labeling. Samples were mounted on microscope cover slides and counterstained with SlowFade Gold antifade reagent with 4′,6-diamidino-2-phenylindole (DAPI) for nuclear staining.

For immunofluorescence experiments on primary hippocampal neurons, cultures were fixed with 4% formaldehyde (prepared from fresh paraformaldehyde) in PBS for 60 min at RT and then washed in PBS. The samples were permeabilized with 0.3% Triton-X-100 and subsequently incubated with primary antibodies for 30 min at room temperature, washed with PBS and incubated with secondary antibodies for 45 min. Cultures were then mounted in Vectashield (Vector Laboratories) on 1 mm thick microscope slides. To visualize neurons, rabbit anti β-tubulin III, 1:250 (Sigma), primary antibody was used and Alexa 594 goat anti-rabbit secondary antibody, 1:500 (Invitrogen); to visualize astrocytes mouse anti GFAP 1:250 (Sigma) primary antibody was used and Alexa 488 goat anti-mouse secondary antibody 1:500 (Invitrogen), and Hoechst 1:10 000 (Invitrogen) was used to visualize cell nuclei.

Expression of dopamine by the presence of tyrosine hydroxylase (TH) in human neuroblastoma cell line SH-SY5Y cultures was evaluated by indirect double-immunofluorescent labeling as detailed for the visualization of focal adhesion sites in this section. SH-SY5Y cells on experimental and control ITO substrates were incubated for 2 h with a 1:1000 concentration anti-Anti- TH (MAB318, Merck Millipore, 1:1000) washed three times with 0.05% Tween 20, PBS and then incubated for 1 h in the secondary antibody Alexa Fluor 488 (Life Technologies, 1:1000) combined with rhodamine-conjugated phalloidin (Life Technologies, 1:100) to stain F-actin. Samples were mounted on microscope cover slides and counterstained with SlowFade Gold antifade reagent with DAPI for nuclear staining.

Biological Characterization—Microscopy and Image Analysis: After immunostaining, samples were viewed with an Olympus IX 81 fluorescence microscope with filters for fluorescein isothiocyanate (FITC) (excitation 490 nm; emission 520 nm), Texas Red (excitation 596 nm; emission 615 nm), and DAPI (excitation 358 nm; emission 461 nm). At least 20 randomly selected images at 60× magnification were taken from each test group and the control group. The total number of focal adhesion points per cell and their length were quantified by direct scoring with a 4-pixel-wide line on the FITC channel as previously described in ref. [81] using ImageJ software (National Institutes of Health, USA) (Figure S11, Supporting Information).

Cell densities were quantified at 20× (0.5 NA) magnification using a DM6000 Leica microscope (Leica Microsystems GmbH, Wetzlar, Germany), with random sampling of seven to ten fields (713 × 532 µm; control and anodized film, $n = 3$ culture series).

Protein Antibody Microarray—Protein Extraction: For protein extraction and collection, samples were carefully placed on ice and the cells were washed twice with cold PBS 1X. After the complete aspiration of cold PBS 1X, 100 µL of cold lysis buffer was added. The lysis buffer was composed of radioimmunoprecipitation (RIPA) lysis buffer (Sigma) supplemented with 1% of protease inhibitors (Life Science-Roche) and 1% of phosphatase inhibitors cocktails I & III (Sigma). Thereafter, the adherent cells were scraped off using Corning cell scrapers (Sigma) and then the cell suspension was gently transferred into microcentrifuge tubes and placed on ice. Microcentrifuge tubes were centrifuged for 15 min at 14 000 rpm at 4 °C, and afterward gently removed from the centrifuge and placed on ice. Without disturbing the pellet, the supernatant was carefully aspirated and placed in a fresh clean tube, kept on ice, and stored at –80 °C to be quantified. The pellet was discarded.

Protein Antibody Microarray—Protein Quantification: Protein quantification of the pristine ITO glass and the ITO anodized films was done using Bio-Rad Protein Assay Dye Reagent (#5000006). As per manufacturer's instructions, the dye working solution was prepared and filtered in a concentration of 1:4 in distilled water followed by the preparation of protein standard BSA at concentrations of 0.25, 0.5, 0.75,

and 0.9 mg mL^{-1}. After this, 5 µL of each BSA standard and sample solution were mixed in a clean, dry tube together with 250 µL of dye working solution. This solution was vortexed and incubated for 5 min at RT and finally read using NanoDrop 8000 software with the Protein Bradford module.

Protein Antibody Microarray—Construction of Gliosis Antibody Microarray: Nexterion slide H microarray slides were purchased from Schott AG (Mainz, Germany). Alexa Fluor 555 carboxylic acid succinimidyl ester was obtained from Life Technologies (Carlsbad, CA, USA).

Protein samples were labeled with Alexa Fluor 555 carboxylic acid succinimidyl ester according to manufacturer's instructions. Excess label was removed and buffer was exchanged with PBS, pH 7.4, by centrifugation through 3 kDa molecular weight cutoff filters. Absorbance at 555 and 280 nm was measured for labeled samples and calculations were performed according to manufacturer's instructions using an arbitrary extinction coefficient of 100 000 and molecular mass of 100 000 to enable quantification of relative protein concentration and label substitution efficiency.

All commercial antibodies (Table S1, Supporting Information) were buffer exchanged into PBS and quantified by bicinchoninic acid (BCA) assay.[123] Antibodies were diluted to print concentration in PBS and printed in six replicates on Nexterion H amine reactive, hydrogel coated glass slides using a SciFLEXARRAYER S3 piezoelectric printer (Scienion, Berlin, Germany) under constant humidity (62% +/− 2%) at 20 °C. Each feature was printed using ≈1 nL of diluted antibody using an uncoated 90 µm glass nozzle with eight replicated subarrays per microarray slide. After printing, slides were incubated in a humidity chamber overnight at room temperature to facilitate complete conjugation. The slides were then blocked in 100×10^{-3} M ethanolamine in 50×10^{-3} M sodium borate, pH 8.0, for 1 h at room temperature. Slides were washed in PBS with 0.05% Tween 20 (PBS-T) three times for 2 min each wash followed by one wash in PBS, dried by centrifugation (470 × g, 5 min), and then stored with desiccant at 4 °C until use.

Incubations were carried out in the dark. Microarray slides were incubated essentially as previously described.[124] Initially, one labeled sample was titrated (2.5–15 µg mL^{-1}) for optimal signal-to-noise ratio and all samples were subsequently incubated for 1 h at 23 °C at 5 µg mL^{-1} in Tris-buffered saline (TBS; 20×10^{-3} M Tris-HCl, 100×10^{-3} M NaCl, 1×10^{-3} M CaCl2, 1×10^{-3} M MgCl2, pH 7.2) with 0.05% Tween 20 (TBS-T). All microarray experiments were carried out using three replicate slides. Alexa Fluor 555 labeled healthy rat brain lysate (5 µg mL^{-1}) and soybean agglutinin lectin (10 µg mL^{-1}) were incubated in two separate subarrays on every slide to confirm retained antibody performance and printing, respectively (Figure S8, Supporting Information). After incubation, slides were washed three times in TBS-T for 2 min per wash, once in TBS and then centrifuged dry as above. Dried slides were scanned immediately on an Agilent G2505 microarray scanner using the Cy3 channel (532 nm excitation, 90% photomultiplier tubes (PMT), 5 µm resolution) and intensity data were saved as a .tif file. Antibody microarrays were verified to remain active for at least 2 weeks after printing and all incubations were carried out within that timeframe.

Data extraction from .tif files was performed essentially as previously described.[124] Data were normalized to the mean of three replicate microarray slides (subarray-by-subarray using subarray total intensity, n = 3, 18 data points). Unsupervised hierarchical clustering of normalized data was performed using Hierarchical Clustering Explorer v3.0 (http://www.cs.umd.edu/hcil/hce/hce3.html) using the parameters no prefiltering, complete linkage, and Euclidean distance. Statistical analysis was performed as detailed in subsection "*Calcium Imaging and Substrate Stimulation*".

Electrophysiological Recordings: Single whole-cell recordings were obtained at RT with pipettes (5–7 MΩ) containing (in $\times 10^{-3}$ M): 120 K gluconate, 20 KCl, 10 HEPES, 10 ethylene glycol-bis(beta-aminoethyl ether)-N,N,N′,N′-tetraacetic acid (EGTA), 2 $MgCl_2$, 2 Na_2ATP, pH 7.3; osmolarity was adjusted to 300 mOsm. The extracellular solution contained (in $\times 10^{-3}$ M): 150 NaCl, 4 KCl, 1 $MgCl_2$, 2 $CaCl_2$, 1 $MgCl_2$, 10 HEPES, 10 glucose (all Sigma), pH 7.4. Coverslips with cultures were positioned in a Perspex chamber mounted on an inverted microscope (Eclipse TE-200, Nikon, Japan). Data were collected by Multiclamp 700B patch amplifier (Axon CNS, Molecular Devices) and digitized at 10 kHz with the pClamp 10.2 acquisition software (Molecular Devices LLC, US). The spontaneous synaptic activity was recorded clamping the membrane voltage at −56 mV holding potential (not corrected for liquid junction potential, which was 14 mV). All recorded events were analyzed offline with the AxoGraph 1.4.4 (Axon Instrument) event detection software (Axon CNS, Molecular Devices).

Calcium Imaging and Substrate Stimulation: Stimulation of anodized films formed at 0.4 mA cm^{-2} was performed with two different primary cultures: primary cultures of VM neurons and primary hippocampal neurons.

Changes in intracellular calcium (Ca^{2+}_I) primary cultures of VM neurons were measured as described previously.[12] Briefly, cells grown on pristine ITO glass as a control and on ITO anodized films formed at 0.4 mA cm^{-2} were loaded with the calcium-sensitive fluorescent probe Fluo-4 AM (Life Technologies) (5×10^{-6} M in dimethyl sulfoxide (DMSO)) for 30 min at 37 °C, washed, followed by 30 min at 37 °C in the dark. After dye loading was completed, cells were bathed in culture media (Dulbecco's modified Eagle's medium/F12, 33×10^{-3} M D-glucose, 1% L-glutamine, 1% PS, 1% FCS, supplemented with 2% B27) and transferred to a custom built chamber that allowed electrical stimulation to be applied directionally to the films. Stimulation was achieved by the delivery of biphasic voltage pulses, using a software controlled constant voltage stimulator connected to the chamber via Pt contacts. The chamber was mounted on the stage of a Zeiss Axiovert 200 inverted microscope. The microscope was equipped with a 10 position Orbit I filterwheel (Improvision), for excitation (488 nm) and emission (510 nm low-pass (LP) filter). The emission light was collected every second with an Orca 285 camera (Hamamatsu). The system was controlled by the Openlab system version 5.5. Changes in Ca^{2+}_I in response to external electrical stimulation were expressed as changes in background subtracted fluorescence intensity expressed as $\Delta F/F_0$ (F_0 is the baseline fluorescence level and ΔF is the rise over baseline).

For Ca^{2+} imaging experiments using primary hippocampal neurons, cultures were loaded with cell permeable Ca^{2+} dye Oregon Green 488 BAPTA-1 AM (Molecular Probes) in DMSO (Sigma-Aldrich) with a final concentration of 4×10^{-6} M for 20 min at 37 °C in the cell culture incubator.[118] The samples were then placed in a recording chamber mounted on an inverted microscope (Nikon TE-200) where they were continuously superfused at RT with the extracellular solution (see subsection "*Electrophysiological Recordings*"). Cultures were observed with a 20× objective (0.45 NA, PlanFluor, Nikon). Images (1024 × 1024 pixels) were acquired continuously for 7 min (at 6.67 frame s^{-1}) by a Hamamatsu Orca-Flash 4.0 digital camera, exciting the $Ca^{2\pm}$ dye with a 488 nm wavelength light generated by a mercury lamp. Excitation light was separated from the light emitted from the sample using a 395 nm dichroic mirror and ND filter (1/16). Images of emitted fluorescence >480 nm were displayed on a color monitor controlled by an integrating imaging software package (HC Image, Hamamatsu) using a personal computer. Recorded images were analyzed offline with the Clampfit software (pClamp suite, 10.2 version; Axon Instruments). Intracellular Ca^{2+} transients were expressed as fractional amplitude increase ($\Delta F/F_0$, where F_0 is the baseline fluorescence level and ΔF is the rise over baseline); the onset time of neuronal activation determined by detecting those events in the fluorescence signal that exceed at least five times the standard deviation of the noise. For stimulation, voltage stimuli were delivered using a Constant Voltage Isolated Stimulator (DS2A-Mk.II, Digitimer, England) connected to silver electrodes through insulated silver wires. One electrode was placed in contact with the upper part of the anodized film formed at 0.4 mA cm^{-2} or glass (control) sample in a dry environment; the reference electrode was in the extracellular solution. Under such conditions, neurons could only be extracellularly stimulated through the electrolyte-anodized film interface. During Ca^{2+} imaging recording session, 500 ms long high voltage was delivered (1/60 s).

Statistical Analysis: All data presented here were confirmed using at least three replicates for each of the test groups and control group.

The results are expressed as the mean of the values ± standard error of the mean. One-way ANOVA followed by a Bonferroni test was performed to determine the statistical significance ($p < 0.05$), unless otherwise stated.

For the hippocampal cultures electrophysiology and immunofluorescence analysis, all values from samples subjected to the same experimental protocols were pooled and expressed as mean ± SD with n = number of cells, unless otherwise specified. Where not otherwise indicated, statistically significant differences between data sets were assessed by Student's t-test (after validation of variances homogeneity by Levene's test) for parametric data at a minimum significance level of $p < 0.05$.

Supporting Information

Supporting Information is available from the Wiley Online Library or from the author.

Acknowledgements

This research was supported in part by a research grant from the Science Foundation Ireland (SFI) and was cofunded under the European Regional Development Fund under Grant Number 13/RC/2073. M. J. P. Biggs is also an SFI, Starting Investigator SIRG COFUND fellow (Grant No. 11/SIRG/B2135). The authors would like to acknowledge the Advanced Materials and BioEngineering Research (AMBER) and the Science Foundation Ireland (SFI) for funding through SFI-AMBER (Grant No. SFI 12/RC/2278 AMBER). The authors would like to acknowledge the joint funding received from the Irish Research Council through IRC New Foundation Scheme/Nano Surface project, the NUI Galway microscopy suite, and David Connolly for microscopy support. The authors are grateful to Pierce Lalor and Ruther Levey for help in the TEM analysis.

Received: September 27, 2016
Revised: January 16, 2017
Published online:

[1] C. Vallejo-Giraldo, A. Kelly, M. J. Biggs, *Drug Discovery Today* **2014**, *19*, 88.
[2] G. M. Durand Dm, E. Krames, *J. Neural Eng.* **2014**, *11*, 020201.
[3] A. Zhang, C. M. Lieber, *Chem. Rev.* **2016**, *116*, 215.
[4] K. Svennersten, K. C. Larsson, M. Berggren, A. Richter-Dahlfors, *Biochim. Biophys. Acta* **2011**, *1810*, 276.
[5] K. C. Larsson, P. Kjall, A. Richter-Dahlfors, *Biochim. Biophys. Acta* **2013**, *1830*, 4334.
[6] R. Owens, P. Kjall, A. Richter-Dahlfors, F. Cicoira, *Biochim. Biophys. Acta* **2013**, *1830*, 4283.
[7] D. T. Simon, E. O. Gabrielsson, K. Tybrandt, M. Berggren, *Chem. Rev.* **2016**, DOI: 10.1021/acs.chemrev.6b00146, *116*, 13009.
[8] T. D. Kozai, N. B. Langhals, P. R. Patel, X. Deng, H. Zhang, K. L. Smith, J. Lahann, N. A. Kotov, D. R. Kipke, *Nat. Mater.* **2012**, *11*, 1065.
[9] D. Mantione, I. Del Agua, W. Schaafsma, J. Diez-Garcia, B. Castro, H. H. Sardon, D. Mecerreyes, *Macromol. Biosci.* **2016**, *16*, 1227.
[10] S. F. Cogan, *Annu. Rev. Biomed. Eng.* **2008**, *10*, 275.
[11] Rose LSRaTL, *Neural Prostheses: Fundamental Studies*, Prentice Hall, Englewood Cliffs, NJ **1990**.
[12] C. Vallejo-Giraldo, E. Pugliese, A. Larranaga, M. A. Fernandez-Yague, J. J. Britton, A. Trotier, G. Tadajon, A. Kelly, I. Rago, J. R. Sarasua, E. Dowd, L. R. Quinlan, A. Pandit, M. J. Biggs, *Nanomedicine (Lond)* **2016**, *11*, 2547.
[13] H. Zhou, X. Cheng, L. Rao, T. Li, Y. Y. Duan, *Acta Biomater.* **2013**, *9*, 6439.
[14] O. J. Gregory, Q. Luo, E. E. Crisman, *Thin Solid Films* **2002**, *406*, 286.
[15] B. W. Faughnan, R. S. Crandall, *Top. Appl. Phys.* **1980**, *40*, 181.
[16] L. J. Meng, C. H. Li, G. Z. Zhong, *J. Lumin.* **1987**, *39*, 11.
[17] J. R. Bellingham, A. P. Mackenzie, W. A. Phillips, *Appl. Phys. Lett.* **1991**, *58*, 2506.
[18] B. J. Luff, J. S. Wilkinson, G. Perrone, *Appl. Opt.* **1997**, *36*, 7066.
[19] A. C. Weitz, M. R. Behrend, N. S. Lee, R. L. Klein, V. A. Chiodo, W. W. Hauswirth, M. S. Humayun, J. D. Weiland, R. H. Chow, *J. Neurophysiol.* **2013**, *109*, 1979.
[20] A. C. Weitz, M. R. Behrend, A. K. Ahuja, P. Christopher, J. Wei, V. Wuyyuru, U. Patel, R. J. Greenberg, M. S. Humayun, R. H. Chow, J. D. Weiland, *J. Neural Eng.* **2014**, *11*, 016007.
[21] R. Tanamoto, Y. Shindo, N. Miki, Y. Matsumoto, K. Hotta, K. Oka, *J. Neurosci. Methods* **2015**, *253*, 272.
[22] Q. Qiu, M. Sayer, M. Kawaja, X. Shen, J. E. Davies, *J. Biomed. Mater. Res.* **1998**, *42*, 117.
[23] S. Petronis, M. Stangegaard, C. B. Christensen, M. Dufva, *Biotechniques* **2006**, *40*, 368.
[24] Y. Nashimoto, Y. Takahashi, T Yamakawa, Y. S. Torisawa, T. Yasukama, T. ITO-Sasaki, M. Yokoo, H. Abe, H. Shiku, H. Kambara, T. Matsue, *Anal. Chem.* **2007**, *79*, 6823.
[25] M. L. Guo, J. H. Chen, X. B. Yun, K. Chen, L. H. Nie, S. Z. Yao, *Biochim. Biophys. Acta: Gen. Subjects* **2006**, *1760*, 432.
[26] J. Selvakumaran, M. P. Hughes, J. L. Keddie, D. J. Ewins, *Eng. Med. Biol. Soc. Ann.* **2002**, 261, DOI: 10.1109/Mmb.2002.1002326.
[27] H. Pluk, D. Stokes, B. Lich, B. Wieringa, J. Fransen, *J. Microsc -Oxford.* **2009**, *233*, 353.
[28] C. M. Bowers, A. A. Shestopalov, R. L. Clark, E. J. Toone, *ACS Appl. Mater. Interfaces* **2012**, *4*, 3932.
[29] B. Wei, J. Liu, L. Ouyang, C. C. Kuo, D. C. Martin, *ACS Appl. Mater. Interfaces* **2015**, *7*, 15388.
[30] J. Arjomandi, D. Raoufi, F. Ghamari, *J. Phys. Chem. C* **2016**, *120*, 18055.
[31] C. J. Huang, Y. K. Su, S. L. Wu, *Mater. Chem. Phys.* **2004**, *84*, 146.
[32] P. K. H. Ho, M. Granstrom, R. H. Friend, N. C. Greenham, *Adv. Mater.* **1998**, *10*, 769.
[33] J. L. Robinson, P. F. King, *J. Electrochem. Soc.* **1961**, *108*, 36.
[34] N. Cabrera, N. F. Mott, *Rep. Prog. Phys.* **1948**, *12*, 163.
[35] S. W. Cho, J. G. Jeong, S. H. Park, M. H. Cho, K. Jeong, C. N. Whang, Y. Yi, *Appl. Phys. Lett.* **2008**, *92*, 213302.
[36] G. R. T. Schueller, S. R. Taylor, E. E. Hajcsar, *J. Electrochem. Soc.* **1992**, *139*, 2799.
[37] C. Blawert, W. Dietzel, E. Ghali, G. L. Song, *Adv. Eng. Mater.* **2006**, *8*, 511.
[38] M. V. Diamanti, B. Del Curto, M. Pedeferri, *J. Appl. Biomater. Biomech.* **2011**, *9*, 55.
[39] L. E. Mcnamara, T. Sjostrom, K. E. Burgess, J. J. Kim, E. Liu, S. Gordonov, P. V. Moghe, R. M. Meek, R. O. Oreffo, B. Su, M. J. Dalby, *Biomaterials* **2011**, *32*, 7403.
[40] H. Tsuchiya, J. M. Macak, A. Ghicov, L. Taveira, P. Schmuki, *Corros. Sci.* **2005**, *47*, 3324.
[41] A. Ghicov, H. Tsuchiya, J. M. Macak, P. Schmuki, *Electrochem. Commun.* **2005**, *7*, 505.
[42] S. Mahshid, A. Dolati, M. Goodarzi, M. Askari, *Nanotechnology (General) -217th Ecs Meeting* **2010**, *28*, 67.
[43] T. Tian, X. F. Xiao, R. F. Liu, H. D. She, X. F. Hu, *J. Mater. Sci.* **2007**, *42*, 5539.
[44] S. Bauer, S. Kleber, P. Schmuki, *Electrochem. Commun.* **2006**, *8*, 1321.
[45] E. E. L. Swan, K. C. Popat, C. A. Grimes, T. A. Desai, *J. Biomed. Mater. Res., Part A* **2005**, *72A*, 288.
[46] T. R. B. Foong, A. Sellinger, X. Hu, *ACS Nano* **2008**, *2*, 2250.
[47] G. Folcher, H. Cachet, M. Froment, J. Bruneaux, *Thin Solid Films* **1997**, *301*, 242.
[48] A. Kraft, H. Hennig, A. Herbst, K. H. Heckner, *J. Electroanal. Chem.* **1994**, *365*, 191.

[49] Y. Shao, X. Xiao, L. Y. Wang, Y. Liu, S. D. Zhang, *Adv. Funct. Mater.* **2014**, *24*, 4170.
[50] E. Matveeva, *J. Electrochem. Soc.* **2005**, *152*, H138.
[51] M. Senthilkumar, J. Mathiyarasu, J. Joseph, K. L. N. Phani, V. Yegnaraman, *Mater. Chem. Phys.* **2008**, *108*, 403.
[52] L. Liu, S. Yellinek, I. Valdinger, A. Donval, D. Mandler, *Electrochim. Acta* **2015**, *176*, 1374.
[53] J. Stotter, Y. Show, S. H. Wang, G. Swain, *Chem. Mater.* **2005**, *17*, 4880.
[54] R. Castro-Rodriguez, A. I. Oliva, V. Sosa, F. Caballero-Briones, J. L. Pena, *Appl. Surf. Sci.* **2000**, *161*, 340.
[55] G. Kavei, A. M. Gheidari, *J. Mater. Process. Technol.* **2008**, *208*, 514.
[56] C. Yao, T. J. Webster, *J. Nanosci. Nanotechnol.* **2006**, *6*, 2682.
[57] J. F. Vanhumbeeck, J. Proost, *Corros. Rev.* **2009**, *27*, 117.
[58] A. Paul, J. Wingbermuhle, *Appl. Surf. Sci.* **2006**, *252*, 8151.
[59] A. Facchetti, M. H. Yoon, T. J. Marks, *Adv. Mater.* **2005**, *17*, 1705.
[60] S. Lee, J.-Y. Kwon, D. Yoon, H. Cho, J. You, Y. T. Kang, D. Choi, W. Hwang, *Nanoscale Res. Lett.* **2012**, *7*, 18.
[61] M. Asmani, C. Kermel, A. Leriche, M. Ourak, *J. Eur. Ceram. Soc.* **2001**, *21*, 1081.
[62] K. Zeng, F. Zhu, J. Hu, L. Shen, K. Zhang, H. Gong, *Thin Solid Films* **2003**, *443*, 60.
[63] A. Solieman, M. A. Aegerter, *Thin Solid Films* **2006**, *502*, 205.
[64] M. Montecchi, R. M. Montereali, E. Nichelatti, *Thin Solid Films* **2001**, *396*, 262.
[65] M. M. Hamasha, T. Dhakal, K. Alzoubi, S. Albahri, A. Qasaimeh, S. Lu, C. R. Westgate, *J. Disp. Technol.* **2012**, *8*, 385.
[66] C. W. Tang, S. A. Vanslyke, *Appl. Phys. Lett.* **1957**, *51*, 913.
[67] E. I. Haskal, *Synth. Met.* **1997**, *91*, 187.
[68] H. Jung, W. Chung, C. H. Lee, S. H. Kim, *J. Nanosci. Nanotechnol.* **2012**, *12*, 5407.
[69] E. Haskal, A. Curioni, P. Seidler, W. Andreoni, *Appl. Phys. Lett.* **1997**, *71*, 1151.
[70] N. Nishimoto, Y. Yamada, Y. Ohnishi, N. Imawaka, K. Yoshino, *Phys. Status Solidi A* **2013**, *210*, 589.
[71] A. Turak, InTech, Dewetting Stability of ITO Surfaces in Organic Optoelectronic Devices, in *Optoelectronics—Advanced Materials and Devices*, **2013**, Ballato, S.L.P.a.J.M. ., DOI:10.5772/3463.
[72] X. F. Wei, W. M. Grill, *J. Neural Eng.* **2009**, *6*, 046008.
[73] T. Bejitual, K. Ramji, A. Kessman, K. Sierros, D. Cairns, *Mater. Chem. Phys.* **2012**, *132*, 395.
[74] M. Serantoni, V. J. Cunnane, *J. Electroanal. Chem.* **2003**, *548*, 49.
[75] L. Hung-Ji, L. Der-Yuh, W. Jenq-Shinn, Y. Chu-Shou, C. Wu-Ching, L. Wei-Hsuan, W. Jyh-Shyang, *Jpn. J. Appl. Phys.* **2009**, *48*, 04C122.
[76] C. Donley, D. Dunphy, D. Paine, C. Carter, K. Nebesny, P. Lee, D. Alloway, N. R. Armstrong, *Langmuir* **2002**, *18*, 450.
[77] R. G. Keil, *J. Electrochem. Soc.* **1986**, *133*, 1375.
[78] A. J. F. Bard, *Electrochemical Methods: Fundamentals and Applications*, Wiley, New York **1980**.
[79] V. Brunetti, G. Maiorano, L. Rizzello, B. Sorce, S. Sabella, R. Cingolani, P. P. Pompa, *Proc. Natl. Acad. Sci. USA* **2010**, *107*, 6264.
[80] M. Buttiglione, F. Vitiello, E. Sardella, L. Petrone, M. Nardulli, P. Favia, R. d'Agostino, R. Gristina, *Biomaterials* **2007**, *28*, 2932.
[81] M. J. Biggs, R. G. Richards, S. Mcfarlane, C. D. Wilkinson, R. O. Oreffo, M. J. Dalby, *J. R. Soc. Interface* **2008**, *5*, 1231.
[82] Y. W. Fan, F. Z. Cui, S. P. Hou, Q. Y. Xu, L. N. Chen, I. S. Lee, *J. Neurosci. Methods* **2002**, *120*, 17.
[83] S. P. Khan, G. G. Auner, G. M. Newaz, *Nanomedicine* **2005**, *1*, 125.
[84] M. J. P. Biggs, R. G. Richards, N. Gadegaard, R. J. McMurray, S. Affrossman, C. D. W. Wilkinson, R. O. C. Oreffo, M. J. Dalby, *J. Biomed. Mater. Res., Part A* **2009**, *91A*, 195.
[85] M. D. Schaller, *Oncogene* **2001**, *20*, 6459.
[86] M. H. Kim, M. Park, K. Kang, I. S. Choi, *Biomater Sci-Uk* **2014**, *2*, 148.
[87] K. Kang, M. H. Kim, M. Park, I. S. Choi, *J. Nanosci. Nanotechnol.* **2014**, *14*, 513.
[88] G. Sriram, P. Patil, M. P. Bhat, R. M. Hegde, K. V. Ajeya, I. Udachyan, M. B. Bhavya, M. G. Gatti, U. T. Uthappa, G. M. Neelgund, H. Y. Jung, T. Altalhi, M. D. M. Kurkuri, *J. Nanomater.* **2016**, *2*, 24.
[89] B. Wälivaara, B.-O. Aronsson, M. Rodahl, J. Lausmaa, P. Tengvall, *Biomaterials* **1994**, *15*, 827.
[90] S. W. Myung, Y. M. Ko, B. H. Kim, *Jpn. J. Appl. Phys.* **2014**, *53*, 11R. B.01.
[91] N. Recek, M. Jaganjac, M. Kolar, L. Milkovic, M. Mozetič, K. Stana-Kleinschek, A. Vesel, *Molecules* **2013**, *18*, 12441.
[92] A. Sharma, A. J. Mcquillan, L. A. Sharma, J. N. Waddell, Y. Shibata, W. J. Duncan, *J. Mater. Sci.: Mater. Med.* **2015**, *26*, 221.
[93] Z. Bai, M. J. Filiaggi, R. J. Sanderson, L. B. Lohstreter, M. A. Mcarthur, J. R. Dahn, *J. Biomed. Mater. Res., Part A* **2010**, *92*, 521.
[94] W. Shi, Y. Shen, D. Ge, M. Xueb, H. Caoa, S. Huanga, J. Wangc, G. Zhangc, F. Zhangc, *J. Membr. Sci.* **2008**, *325*, 801.
[95] M. J. Biggs, R. G. Richards, M. J. Dalby, *Nanomedicine* **2010**, *6*, 619.
[96] I. P. Karve, J. M. Taylor, P. J. Crack, *Br. J. Pharmacol.* **2016**, *173*, 692.
[97] A. Tykhomyrov, A. Pavlova, V. Nedzvetsky, *Neurophysiology* **2016**, *48*, 54.
[98] M. Burgos, M. D. Pastor, J. C. Gonzalez, J. R. Martinez-Galan, C. F. Vaquero, N. Fradejas, A. Benavides, J. M. Hernández-Guijo, P. Tranque, S. P. K. Calvo, *Glia* **2007**, *55*, 1437.
[99] J. H. Kim, S. J. Kwon, M. C. Stankewich, G. Y. Huh, S. B. Glantz, J. S. Morrow, *Exp. Mol. Pathol.* **2016**, *100*, 1.
[100] S. Du, A. Rubin, S. Klepper, C. Barrett, Y. C. Kim, H. W. Rhim, E. B. Lee, C. W. Park, G. J. Markelonis, T. H. Oh, *Exp. Neurol.* **1999**, *157*, 96.
[101] J. Liu, M. C. Liu, K. K. W. Wang, *Sci. Signaling* **2008**, *1*, re1.
[102] V. S. Sajja, E. S. Ereifej, P. J. Vandevord, *Neurosci. Lett.* **2014**, *570*, 33.
[103] B. Coste, J. Mathur, M. Schmidt, T. J. Earley, S. Ranade, M. J. Petrus, A. E. Dubin, A. Patapoutian, *Science* **2010**, *330*, 55.
[104] A. E. Dubin, M. Schmidt, J. Mathur, M. J. Petrus, B. Xiao, B. Coste, A. Patapoutian, *Cell Rep.* **2012**, *2*, 511.
[105] M. Olsen, *Methods Mol. Biol.* **2012**, *814*, 265.
[106] X. Wu, Y. Liu, X. Chen, Q. Sun, R. Tang, W. Wang, Z. Yu, M. Xie, *J. Mol. Neurosci.* **2013**, *49*, 499.
[107] Y. Wang, H. Moges, Y. Bharucha, A. Symes, *Exp. Neurol.* **2007**, *203*, 168.
[108] M. Pekny, M. Pekna, *Biochim. Biophys. Acta: Mol. Basis Disease* **2016**, *1862*, 483.
[109] A. Ellis, D. L. Bennett, *Br. J. Anaesth.* **2013**, *111*, 26.
[110] J. B. Davis, J. Gray, M. J. Gunthorpe, J. P. Hatcher, P. T. Davey, P. Overend, M. H. Harries, J. Latcham, C. Clapham, K. Atkinson, S. A. Hughes, K. Rance, E. Grau, A. J. Harper, P. L. Pugh, D. C. Rogers, S. Bingham, A. Randall, S. A. Sheardown, *Nature* **2000**, *405*, 183.
[111] G. M. Story, A. M. Peier, A. J. Reeve, S. R. Eid, J. Mosbacher, T. R. Hricik, T. J. Earley, A. C. Hergarden, D. A. Andersson, S. W. Hwang, P. McIntyre, T. Jegla, S. Bevan, A. Patapoutian, *Cell* **2003**, *112*, 819.
[112] E. Tejera, V. Rocha-Perugini, S. Lopez-Martin, D. Pérez-Hernández, A. I. Bachir, A. R. Horwitz, J. Vázquez, F. Sánchez-Madrid, M. Yáñez-Mo, *Mol. Biol. Cell.* **2013**, *24*, 261.
[113] B. K. Song, G. R. Geisert, F. Vázquez-Chona, E. E. Geisert, *Neurosci. Lett.* **2003**, *338*, 29.
[114] J. D. Peduzzi, T. B. Grayson, F. R. Fischer, E. E. Geisert Jr., *Exp. Neurol.* **1999**, *160*, 460.
[115] G. Cellot, F. M. Toma, Z. K. Varley, J. Laishram, A. Villari, M. Quintana, S. Cipollone, M. Prato, L. Ballerini, *J. Neurosci.* **2011**, *31*, 12945.

[116] J. S. Carp, *J. Neurophysiol.* **1992**, *68*, 1121.
[117] A. Fabbro, D. Scaini, V. Leon, E. Vázquez, G. Cellot, G. Privitera, L. Lombardi, F. Torrisi, F. Tomarchio, F. Bonaccorso, S. Bosi, A. C. Ferrari, L. Ballerini, M. Prato, *ACS Nano* **2016**, *10*, 615.
[118] S. Bosi, R. Rauti, J. Laishram, A. Turco, D. Lonardoni, T. Nieus, M. Prato, D. Scaini, L. Ballerini, *Sci. Rep.* **2015**, *5*, 9562.
[119] ASTM, Standard Guide for Accelerated Aging of Sterile Barrier Systems for Medical Devices, *In F1980-07*, **2011**, ASTM International, Conshohocken, PA.
[120] R. A. Green, R. T. Hassarati, L. Bouchinet, C. S. Lee, G. L. Cheong, J. F. Yu, C. W. Dodds, G. J. Suaning, L. A. Poole-Warren, N. H. Lovell, *Biomaterials* **2012**, *33*, 5875.
[121] D. W. Hukins, A. Mahomed, S. N. Kukureka, *Med. Eng. Phys.* **2008**, *30*, 1270.
[122] R. A. Green, N. H. Lovell, G. G. Wallace, L. A. Poole-Warren, *Biomaterials* **2008**, *29*, 3393.
[123] P. K. Smith, R. I. Krohn, G. T. Hermanson, A. K. Mallia, F. H. Gartner, M. D. Provenzano, E. K. Fujimoto, N. M. Goeke, B. J. Olson, D. C. Klenk, *Anal. Biochem.* **1985**, *150*, 76.
[124] J. Q. Gerlach, M. Kilcoyne, L. Joshi, *Anal. Methods* **2014**, *6*, 440.